

| | |
|----------------------|---|
| Title | Hollow core photonic crystal fibre as a viscosity and Raman sensor |
| Authors | Horan, Laura E. |
| Publication date | 2013 |
| Original Citation | Horan, L. E. 2013. Hollow core photonic crystal fibre as a viscosity and Raman sensor. PhD Thesis, University College Cork. |
| Type of publication | Doctoral thesis |
| Rights | © 2013, Laura E. Horan. - http://creativecommons.org/licenses/by-nc-nd/3.0/ |
| Download date | 2025-01-13 21:44:00 |
| Item downloaded from | https://hdl.handle.net/10468/1438 |

Hollow Core Photonic Crystal Fibre as a Viscosity and Raman Sensor

Laura Elizabeth Horan
BSc
105398053



NATIONAL UNIVERSITY OF IRELAND, CORK

FACULTY OF SCIENCE

DEPARTMENT OF PHYSICS

**Thesis submitted for the degree of
Doctor of Philosophy**

October 2013

Supervisors: Dr Fatima C. Garcia Gunning
Dr Albert A. Ruth

Head of Department/School: Prof John McInerney

Research supported by IRCSET

Contents

| | |
|--|-----------|
| Abstract | v |
| Acknowledgements | vii |
| List of Publications | viii |
| List of Figures | ix |
| List of Tables | xiv |
| 1 Introduction | 1 |
| 2 Fundamentals Background | 8 |
| 2.1 Hollow Core Photonic Crystal Fibre | 9 |
| 2.1.1 Photonic Band Gap Effect | 11 |
| 2.1.2 Liquid Filled Fibres | 13 |
| 2.1.3 Altering the End-Facet of the Fibre | 18 |
| 2.1.4 Modal Properties of Liquid Filled Fibre | 18 |
| 2.2 Viscosity | 19 |
| 2.2.1 Current Capillary Viscometers | 21 |
| 2.3 Determination of Viscosity | 23 |
| 2.3.1 Description of Forces | 24 |
| 2.3.2 Derivation of the Liquid Velocity Equation | 28 |
| 2.3.3 Estimating Viscosity from Liquid Velocity | 29 |
| 2.4 Raman Spectroscopy | 30 |
| 2.4.1 Vibrational Raman Scattering Theory | 31 |
| 2.4.2 Liquid Core Fibre for Raman Scatter Collection | 33 |
| 2.4.3 Raman Scatter Collection with Hollow Core Photonic Crystal Fibre | 33 |
| 2.5 Summary | 37 |
| 3 Microscope Analysis of Liquid Filling Capillaries | 39 |
| 3.1 Experimental Set-up | 40 |
| 3.1.1 Fibre Specifications | 41 |
| 3.1.2 Radius Estimation | 41 |
| 3.2 Images of the Capillary Filling | 43 |
| 3.3 Characterisation of Capillaries Filling with Water | 44 |
| 3.3.1 First Filling Results | 45 |
| 3.3.2 Second and Subsequent Filling Results | 46 |
| 3.3.3 Contact Angle Estimation | 47 |
| 3.3.4 Surface Analysis of the Silica Capillaries | 48 |
| 3.4 Capillary Filling with Propan-1-ol | 49 |
| 3.5 Summary | 51 |
| 4 Optical Fibre Viscometer | 52 |
| 4.1 Optical Analysis | 53 |
| 4.1.1 Alignment of the Short Fibre Sample with the System | 54 |
| 4.1.2 Observations of the Optical Transmission Changes During Filling | 56 |

| | | |
|----------|--|------------|
| 4.1.3 | Choice of Fibre and Laser Source | 58 |
| 4.1.4 | The Viscometer Set-up | 59 |
| 4.1.5 | Temperature Control | 62 |
| 4.2 | Timing Measurements and Error Analysis | 64 |
| 4.2.1 | Determination of the Start and End Filling Times | 64 |
| 4.2.2 | Repeat Filling Tests with Laser Set-Up | 70 |
| 4.2.3 | Fitting of Experimental Data to the Model | 71 |
| 4.2.4 | Error Estimation | 72 |
| 4.3 | Optical Fibre Viscometer Applications | 73 |
| 4.3.1 | Propan-1-ol | 73 |
| 4.3.2 | Glucose and Fructose | 79 |
| 4.3.3 | Observations for Saline Solutions | 82 |
| 4.4 | Summary | 83 |
| 5 | Optical Transmission Properties of Liquid Filled Hollow Core Photonic Crystal Fibres | 85 |
| 5.1 | Light Transmission Experiments | 86 |
| 5.1.1 | Adaptation of the Experimental Set-Up for Liquid Filled Fibres | 89 |
| 5.1.2 | Measurement Procedure | 90 |
| 5.1.3 | Selective Core Filling | 93 |
| 5.2 | Experimental Results | 94 |
| 5.2.1 | Mapping Distribution of an Empty HC-1060 | 95 |
| 5.2.2 | Mapping Distribution of Liquid Filled HC-1060 | 97 |
| 5.2.3 | Measurements with a Shack-Hartmann Wavefront Sensor | 101 |
| 5.3 | Numerical Aperture of Liquid Filled Fibres | 104 |
| 5.4 | Summary | 105 |
| 6 | Viscometer Integrated with Raman Scatter for Simultaneous Analysis | 107 |
| 6.1 | Experimental Set-up | 108 |
| 6.2 | Proof of Principle Results for Solutions of Glucose | 111 |
| 6.3 | Tests with Other Bio-Fluids | 115 |
| 6.4 | Post Analysis of Dynamic Raman Scatter | 118 |
| 6.5 | Summary | 120 |
| 7 | Raman Scatter in Hollow Core Photonic Crystal Fibre | 122 |
| 7.1 | Experimental Apparatus | 123 |
| 7.1.1 | Fibre and Pump Laser Selection | 124 |
| 7.1.2 | Background Spectra of Fibres and Preparation of Spectra | 127 |
| 7.1.3 | Comparison of Raman Collection Efficiency in Core Filled and Fully Filled Fibre States | 128 |
| 7.1.4 | Practical Fibre Length | 129 |
| 7.2 | Applications Using Core Only Filled Hollow Core Photonic Crystal Fibre | 131 |
| 7.2.1 | Mono-Saccharides: Glucose and Fructose | 131 |
| 7.3 | Other Applications | 138 |

| | | |
|----------|---|------------|
| 7.3.1 | Glucose and Lactate | 138 |
| 7.3.2 | Creatinine and Urea | 140 |
| 7.3.3 | Interstitial Fluids | 141 |
| 7.4 | Summary | 143 |
| 8 | Conclusions | 144 |
| 8.1 | Future Work | 147 |
| A | List of Symbols and Acronyms | 149 |
| B | Derivation of the Liquid Flow Velocity Model | 152 |
| C | Data Sheets | 156 |

I, Laura Elizabeth Horan, certify that this thesis is my own work and I have not obtained a degree in this university or elsewhere on the basis of the work submitted in this thesis.

Laura Elizabeth Horan

Abstract

This PhD thesis investigates the application of hollow core photonic crystal fibre for use as an optical fibre nano litre liquid sensor. The use of hollow core photonic crystal fibre for optical fibre sensing is influenced by the vast wealth of knowledge, and years of research that has been conducted for optical waveguides. Hollow core photonic crystal fibres have the potential for use as a simple, rapid and continuous sensor for a wide range of applications.

In this thesis, the velocity of a liquid flowing through the core of the fibre (driven by capillary forces) is used for the determination of the viscosity of a liquid. The structure of the hollow core photonic crystal fibre is harnessed to collect Raman scatter from the sample liquid. These two methods are integrated to investigate the range of applications the hollow core photonic crystal fibre can be utilised for as an optical liquid sensor.

Understanding the guidance properties of hollow core photonic crystal fibre is forefront in dynamically monitoring the liquid filling. When liquid is inserted fully or selectively to the capillaries, the propagation properties change from photonic bandgap guidance when empty, to index guidance when the core only is filled and finally to a shifted photonic bandgap effect, when the capillaries are fully filled. The alterations to the guidance are exploited for all viscosity and Raman scattering measurements.

The concept of the optical fibre viscosity sensor was tested for a wide range of samples, from aqueous solutions of propan-1-ol to solutions of mono-saccharides in phosphate buffer saline. The samples chosen to test the concept were selected after careful consideration of the importance of the liquid in medical and industrial applications. The Raman scattering of a wide range of biological important fluids, such as creatinine, glucose and lactate were investigated, some for the first time with hollow core photonic crystal fibre.

This thesis is dedicated with love to my wonderful parents, Tony and Julie
Horan

Acknowledgements

The undertaking of a PhD study can never be credited to one person, but rather to a team of people, who kindly offer their help, time, support, guidance, their experience and their knowledge. I wish to offer my heartfelt and gracious thankfulness to many people who have been key to many aspects of this work. This thesis would not have reached this stage without the kind help and support of everyone I have met and worked with during my PhD study.

I would like to first thank Dr. Fatima C. Garcia Gunning for presenting me the opportunity to work with her and the Photonic Systems Group in Tyndall National Institute. Without her guidance, support and endless patience, this project would never have been realised. Thank you for always believing in me, even when I didn't.

I would also like to thank my co-supervisor Dr. Albert A. Ruth for his guidance, advice and support throughout my PhD, for offering laboratory space to work in University College Cork and supplying equipment to facilitate the study of Raman spectroscopy.

Thank you to all the people in Tyndall National Institute and University College Cork, that I have met during my time here, and have helped me throughout my PhD studies. Thank you to Dr. Bob Manning, Prof. Andrew Ellis, Dr. Denise Gabuzda, Dr. Paul Galvin, Dr. Patricia Vazquez, Galvin Khara and Eileen Hurley for invaluable help and discussions throughout my studies and thesis preparation. A special thank you to my fellow PhD students, who shared with me all the highs and lows of this PhD journey. Thank you to Monika Rutowska for helping me in the initial stages of the thesis work and to Jiadi Lu for help with Labview programming. Without your help, this project would have been much more challenging. You both created a wonderful and enjoyable lab atmosphere to work in. Thank you also to CAPPA and Dr. Milosz Przyjalgoski for allowing me the use of their laboratory space and their equipment. I wish to also thank Dr. Florian English and Dr. Kris Rowland for generously offering their time and knowledgeable expertise for the preparation of this thesis.

To all my friends and the UCC Squash Club, thank you for keeping me happy, healthy and for all the great times we've shared and memories made, I'll never forget this amazing time.

Finally a special thank you to my parents, who without their constant emotional support, none of this would have been possible. Thank you for always reassuring me, and listening to me in times of doubt and celebrating with me in times of happiness. Thank you for always thinking of me, and being there for me. You are my inspiration.

List of Publications

Journal Publications

L. E. Horan, A. A. Ruth, and F. C. G. Gunning, “Hollow core photonic crystal fiber based viscometer with raman spectroscopy,” *Journal of Chemical Physics*, vol. 137, p. 224504 (12pp), 2012.

Conference Papers

L. E. Horan and F. C. G. Gunning, “Hollow core photonic crystal fiber as a viscosity sensor,” in *Proceedings of SPIE, 22nd International Conference on Optical Fiber Sensors*, Beijing, vol. 8421, pp. 8421–140, 2012.

L. E. Horan, M. Rutowska, A. D. Ellis, F. C. G. Gunning, “Investigations to use hollow core photonic crystal fibres for glucose monitoring in blood plasma”, *Photonics Ireland*, Dublin, 2011.

L. E. Horan, G. Khara, M. Rutowska, A. D. Ellis, F. C. G. Gunning, “Potential monitoring of glucose in blood plasma using hollow core photonic crystal fibres”, in *Proceedings of SPIE, 21st International Conference on Optical Fiber Sensors*, Ottawa, vol. 77533W, pp. 7753-177, 2011.

M. Rutowska, L. E. Horan, F. C. G. Gunning, “Photonic crystal fibres: selective filling delays”, *Proceedings of IEEE, European Conference on Lasers and Electro-Optics and the European Quantum Electronics Conference (CLEO-EQEC Europe)*, Munich, vol. CH3, 2009.

Patent Applications

M. Rutowska, L. E. Horan, G. Khara, F. C. G. Gunning, “Nano-scale viscometer device”, Patent Application applied for in the US (US20120236302-A1) (16th March 2012), the UK (GB1104547.3) (18th March 2011) and in Ireland (IE2012/0133) (13th March 2012).

List of Figures

| | | |
|------|---|----|
| 1.1 | Schematic of a standard optical fibre end facet, and a diagram of total internal reflection | 1 |
| 1.2 | Example schematic of optical fibres used for sensing of samples for a standard optical fibre, a tapered optical fibre and a hollow core photonic crystal fibre. | 3 |
| 1.3 | A selection of graphs from the thesis that highlight the main results achieved using hollow core photonic crystal fibre for viscosity and Raman studies. | 6 |
| 2.1 | Schematic of a hollow core photonic crystal fibre (courtesy of NKT Photonics A/S) labelling the pitch (Λ), core defect diameter (D) and the capillary diameter (d). | 9 |
| 2.2 | Examples of hollow core photonic crystal fibres; HC-2000, HC-1060, HC-633, HC-540. Images courtesy of NKT Photonics A/S. | 10 |
| 2.3 | Schematic of the photonic band gap effect in one and two dimensional cases of silica/air waveguides. | 12 |
| 2.4 | Schematic of the two dimensional cross section of HC-PCF, which demonstrates how the refractive index changes for the three filled states (a) empty, (b) liquid core filled and (c) fully filled. | 14 |
| 2.5 | Two dimensional schematic demonstrating light guidance in liquid filled hollow core photonic crystal fibres. | 14 |
| 2.6 | Near-field CCD images of empty and liquid filled hollow core photonic crystal fibre. | 15 |
| 2.7 | Plot of the shift in central wavelength guided by the photonic bandgap effect versus the refractive index, estimated using the scalar equation. | 16 |
| 2.8 | Examples of guidance with a broadband supercontinuum source for the HC-1060 when empty, core filled and fully filled, demonstrating the modal properties of the hollow core photonic crystal fibre. | 19 |
| 2.9 | Schematic of the parabolic velocity flow profile of a Newtonian liquid within a capillary channel. | 20 |
| 2.10 | Schematic of laminar and turbulent flow in a capillary. | 23 |
| 2.11 | Schematic of the forces acting on the flow of liquid through a capillary in the (a) vertical and (b) horizontal configurations, with respect to the \hat{z} direction of liquid flow. | 25 |
| 2.12 | Schematic of the cohesive and adhesive forces between the internal molecules of a liquid and the surface walls. | 25 |
| 2.13 | Schematic of the cohesion (red) and adhesion (green) forces in liquids for a contact angle $\theta < 90^\circ$ (a) and $\theta > 90^\circ$ (b). | 26 |
| 2.14 | Plot of the filling model for the time taken to fill a length of capillary. | 28 |
| 2.15 | Schematic of Stokes Raman and Anti-Stokes Raman for a molecule. | 31 |
| 2.16 | Diagram demonstrating the definition of a steradian of radius r and area πr^2 | 36 |
| 2.17 | Schematic of Raman generation within a liquid filled HC-PCF. | 36 |

| | | |
|------|--|----|
| 3.1 | Nikon microscope and experimental set-up to view the end-facet of a hollow core photonic crystal fibre. | 40 |
| 3.2 | Images taken with the Nikon Eclipse ME600 of the cross section of the HC-1550 and HC-1060. | 41 |
| 3.3 | Gaussian distribution of radius measurements for HC-1060. . . . | 42 |
| 3.4 | Images showing dynamic filling of a 6 cm HC-PCF (HC-1060) with water. (a) 0 s (b) 104 s (c) 111 s (d) 134 s (e) 174 s. | 43 |
| 3.5 | Images showing the dynamic filling of a 4.4 cm HC-1550 with water. (a) 0 s (b) 4 s (c) 25 s (d) 27 s (e) 30 s (f) 49 s. | 44 |
| 3.6 | First filling times of 2 - 6 cm lengths of empty HC-1550, compared to the theoretical model (black line). | 45 |
| 3.7 | Second filling times of 2 - 6 cm HC-1550, compared to the theoretical model (black line). | 46 |
| 3.8 | Time plotted against the number of fillings, for multiple fillings of two HC-1550 fibre segments 4.3 ± 0.1 cm with distilled water, timed by the microscope method. | 47 |
| 3.9 | Plots of time versus filling number for HC-1550 filled repeatedly with Propan-1-ol for lengths of (top left) 33 mm, (top right) 38 mm, (bottom left) 44 mm, and (bottom right) 45 mm. | 50 |
| 3.10 | Dependence of the viscosity of propan-1-ol over a temperature range of 270 - 345 K. | 50 |
| 4.1 | Set-up of the supercontinuum source, featuring a Q - switched Nd:YAG laser source, a $\times 40$ focusing lens and a highly non-linear 20 m solid core PCF (SC-05-1060). | 53 |
| 4.2 | Typical transmission spectrum of the supercontinuum source 500 - 1750 nm, measured with an optical spectrum analyser. | 54 |
| 4.3 | Schematic of the alignment set-up for the HC-PCF segment, utilising a SC source and a CCD camera, along with a motorised xyz alignment stage. | 54 |
| 4.4 | Thorlabs DCU223C Camera pixel sensitivity to wavelength, figure courtesy of Thorlabs - Inc. | 55 |
| 4.5 | Transmission spectra of 10 cm HC-1060 fibre for three different filling states: empty (red), core filled (green) and fully filled (blue). | 56 |
| 4.6 | Transmission spectra (500 - 1450 nm) of the SC source (black), the transmission of the SC source through the experimental system (blue), and the loss of the system (dashed green line). Resolution 10 nm. | 57 |
| 4.7 | Near field images of the HC-1060 while dynamically filling with a liquid and guiding a supercontinuum source. | 58 |
| 4.8 | Schematic of experimental set-up for the optical fibre viscometer. | 60 |
| 4.9 | Image of the actual viscometer set-up. | 60 |
| 4.10 | The response curve of the photo-diode to wavelength, courtesy of Thorlabs - Inc. | 61 |

| | | |
|------|--|----|
| 4.11 | Schematic of temperature control system for the HC-PCF segment, featuring a copper reservoir fitted with a lid for the liquid, and a copper plate to heat the fibre. Both parts were heated using a peltier element, controlled with a P.I.D, not seen here. | 63 |
| 4.12 | Images of the temperature control system from the top (left) and from the side (right), showing the positions of the thermistors. | 63 |
| 4.13 | Voltage change with time measured by the PD for a HC-1060 fibre (11.4 cm) during the filling process with a 0.5 M aqueous glucose solution, for the transmission of a HeNe (632.8 nm) laser source. | 65 |
| 4.14 | Close-up plot of the fluctuation of voltage signal measured by the PD after the core is filled while the capillaries are filling. | 66 |
| 4.15 | A selection of modes generated within the core of the fibre and captured using a CCD during the dynamic filling of a HC-1060 with water. | 67 |
| 4.16 | Example plots of transmission profiles of the 632.8 nm laser source during dynamic capillary filling. | 68 |
| 4.17 | Comparison of laser sources 532 nm and 632.8 nm for viscosity measurements. | 69 |
| 4.18 | Dried fibre filling experiments. | 71 |
| 4.19 | Experimental data for (a) 0.01 M aqueous glucose and (b) 0.001 M aqueous glucose solutions (red squares) plotted to the capillary filling model (black line). | 72 |
| 4.20 | Graph indicating start point (a) by a red circle and core filling point (b) by a red circle for all velocity measurements. | 73 |
| 4.21 | Surface tension data for binary solutions of propan-1-ol and water in the range of 20 to 25 ° Celsius. Dotted line is the fitting of Equation (4.4) to the data from literature (black circles). | 76 |
| 4.22 | Viscosity estimations of aqueous propan-1-ol made by the optical fibre viscometer compared to results available from the literature. | 77 |
| 4.23 | Viscosity estimation results obtained with the optical fibre viscometer for PBS solutions of glucose and fructose for different concentrations ranging from 10^{-4} - 1 M. | 82 |
| 5.1 | Schematic of experimental set-up to map the transmission of a broadband source across the micro-structure of the hollow core photonic crystal fibre. | 87 |
| 5.2 | Schematic of a simple lens, showing the positions of the object distance, image distance and focal length. | 88 |
| 5.3 | Figure showing the position of the object and image formation using a lens | 90 |
| 5.4 | Diagram demonstrating the shift of the image as the lens position is changed. | 91 |
| 5.5 | Schematic to demonstrate the calculation of the step size of the image, as the lens is moved in steps | 92 |

| | | |
|------|---|-----|
| 5.6 | Images of an empty HC-1060 transmitting the full SC source when (a) the image is centred with the PH and (b) when the lens is shifted by 20 μm , resulting in a change in the image position with respect to the PH. The PH is shown as a black circle at the centre of both images. | 93 |
| 5.7 | Images of all three filling states (empty, core filled and fully filled) and guidance properties of HC-1060, taken with a Nikon Eclipse Microscope $\times 500$ magnification. | 93 |
| 5.8 | Image of a HC-1060, where the external capillaries have been collapsed using a fusion splicer, leaving the core channel open. . . | 94 |
| 5.9 | Data mapping of the wavelength propagation distribution over the cross section of the HC-PCF in dBm from the OSA, for an empty HC-1060. | 96 |
| 5.10 | Data mapping of the wavelength propagation distribution over the cross section of the HC-PCF in mW from the OSA, for an empty HC-1060. | 97 |
| 5.11 | Contour plots in dBm of the mapping distribution of wavelength transmission for the core only filled and fully filled HC-1060. . . | 98 |
| 5.12 | Contour plots of the transmission mapping distribution of the core only filled and fully filled HC-1060 in units of mW, normalised to the peak power. | 99 |
| 5.13 | Gaussian distribution of the guidance mechanisms for the core only filled and fully filled fibres. | 100 |
| 5.14 | A schematic of the Shack-Hartmann wavefront sensor, from Thorlabs Inc., and the response curve of the CCD to wavelengths. . . | 102 |
| 5.15 | Plots of the wavefront transmission of a 532 nm laser source and a 632.8 nm laser source for the core filled and fully filled states. . . | 103 |
| 6.1 | Set-up for the integrated Raman viscometer. | 108 |
| 6.2 | Graphs depicting the calibration of the pixel array for the CCD camera in spectrometer. | 110 |
| 6.3 | Transmission signal measured by a PD for a 532 nm pump source when a HC-1060 was filling with a 1 M aqueous glucose solution. . . | 111 |
| 6.4 | Sequential Raman spectra of a HC-1060 filling with 1 M aqueous glucose solution. | 112 |
| 6.5 | Raman signal generation over time for 542 nm and 654 nm compared to the PD signal. | 113 |
| 6.6 | Comparison of the Raman spectra for the three filled states (empty, core filled and fully filled) of 1 M aqueous glucose solution in HC-1060. | 114 |
| 6.7 | The integrated PD measurement and Raman count measurement for an aqueous solution of 0.3 M urea and 0.05 M creatinine. . . | 115 |
| 6.8 | Comparison of the Raman spectra for the three filled states of an aqueous solution of 0.3 M urea and 0.05 M creatinine in HC-1060. . . | 116 |
| 6.9 | The integrated PD measurement and Raman count measurement for an aqueous solution of 50 mM lactate and 10 mM glucose. . . | 117 |

| | | |
|------|---|-----|
| 6.10 | Comparison of the Raman spectra for the three filled states of an aqueous solution of 50 mM lactate and 10 mM glucose in HC-1060. | 118 |
| 6.11 | Spectrum of 1 M aqueous glucose, compiled using data for the dynamic measurement of Raman scatter from Figure 6.5. | 119 |
| 6.12 | Spectra of a mixture of 0.3 M urea and 0.05 M creatinine in aqueous solution (a) and a mixture of 0.05 M lactate and 0.01 M glucose in aqueous solution (b). These spectra are compiled from the results for all the spectra collected as seen in Figure 6.8 for 800 s (a) and Figure 6.10 for 380 s (b). | 120 |
| 7.1 | Schematic of the Raman signal backscatter detection set-up. . . | 124 |
| 7.2 | Image of the set-up for Raman signal backscatter detection. . . | 124 |
| 7.3 | Transmission spectra of the HC-1060 in three filled states to the SC source. | 125 |
| 7.4 | Comparison of Raman scatter at 3500 cm^{-1} generated under similar conditions with a 532 nm laser and a 632.8 nm laser. | 126 |
| 7.5 | Raman spectra of the aqueous solution and silica of the fibre. . . | 127 |
| 7.6 | Comparison of collection efficiencies of two fibre filling states. . . | 128 |
| 7.7 | Raman scatter count plotted against increasing length of HC-PCF fibre segments. | 129 |
| 7.8 | HC-PCF vs cuvette measurement for 1 M (a) glucose and (b) fructose. | 132 |
| 7.9 | Comparison of Raman spectra for (a) 0.3 M, (b) 0.6 M, (c) 1.25 M and (d) 2.5 M concentrations of aqueous glucose solutions. . . | 133 |
| 7.10 | The Raman count for increasing in molecular concentration of aqueous glucose solutions. | 135 |
| 7.11 | Comparison of Raman spectra for 1 M glucose (red) and fructose (blue), in the region $500 - 1500\text{ cm}^{-1}$. Differences in the vibrational structure of the mono-saccharide molecules are seen here. | 135 |
| 7.12 | Comparison of 0.05 M aqueous glucose and fructose Raman spectra, to identify solutions of mixed molecules. | 137 |
| 7.13 | Investigation of lactate and glucose Raman spectra within a core only filled HC-1060. | 139 |
| 7.14 | Raman spectra of creatinine and urea at physiological concentrations. | 141 |
| 7.15 | Raman spectra of interstitial fluids at physiological concentrations. | 142 |

List of Tables

| | | |
|-----|--|-----|
| 3.1 | Specifications for HC-1060 and HC-1550. | 41 |
| 3.2 | Data for initial fillings of HC-1550 with distilled water. | 48 |
| 4.1 | Binary solutions of propan-1-ol ¹ in water ² used in the experimental viscosity measurements for the optical fibre viscometer proof-of-concept. | 74 |
| 4.2 | Experimental data of velocity and viscosity for aqueous solutions of Propan-1-ol ¹ | 76 |
| 4.3 | Results from literature for solutions of propan-1-ol ¹ in water ² | 78 |
| 4.4 | Experimental data of velocity and viscosity for PBS solutions of glucose and fructose. | 80 |
| 4.5 | Viscosity values from literature for mono-saccharides glucose and fructose in solution with water. | 81 |
| 5.1 | Comparison of the Shack-Hartmann method and PH method, using the FWHM of the transmission distribution to analyse the transmission of the guided wavelength for the core filled and fully filled fibres. | 104 |
| 7.1 | Table of properties for core filled and fully filled HC-1060 with water. | 125 |
| 7.2 | SNR comparison for a 10 cm HC-PCF, acquisition time 60 s and a 1 cm cuvette, acquisition time 600 s. | 133 |
| 7.3 | SNR comparison for 0.3 M, 0.6 M, 1.25 M and 2.5 M aqueous glucose solutions in core filled HC-PCF, acquisition time 20 s. | 134 |
| 7.4 | SNR comparison for 0.1 M aqueous glucose solution, 0.1 M aqueous fructose solution and a mixture of 0.05 M glucose and 0.05 M fructose in aqueous solution, for a number of wavenumbers, verifying the presence of both species in the mixture, for a core filled HC-PCF, for an acquisition time of 20 s. | 138 |

Chapter 1

Introduction

The transport of light within a waveguide has been widely studied since it was first observed in the 19th century, resulting in the fabrication of silica waveguides in the 20th century, known as optical fibres. An optical fibre is structured to have a cylindrical core with a higher refractive index than the surrounding cladding, allowing the fibre to guide light by the mechanism of total internal reflection. The difference in refractive index between the core and cladding is usually on the order of 1 %. A schematic of a standard optical fibre, and the guidance mechanism is shown in Figure 1.1.

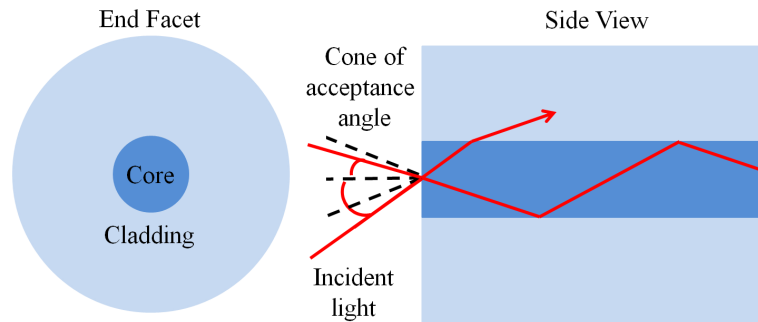


Figure 1.1: Schematic of a standard optical fibre end facet (left) indicating the core region with a material of high refractive index (blue) and the surrounding silica cladding of lower refractive index (light blue). The side view of a standard optical fibre (right) demonstrates the launching of light (red) to the fibre, at an angle within the cone of acceptance (black dashed line), which results in guidance within the fibre by total internal reflection. A light ray with an angle greater than the cone of acceptance undergoes refraction at the core interface, and results in the non guidance of the ray.

In Figure 1.1, light (red lines) that is launched to the fibre within a range of angles

(depicted by the black dashed lines), will propagate along the fibres length. Light launched at an angle greater than this range shall be refracted and scattered to the surrounding cladding. The critical angle that determines the range of acceptance angles for propagation, is defined by Snell's law [1].

Silica is chosen to fabricate these waveguides, due to its attractive optical transmission properties of low absorption and high purity, combined with its high mechanical strength, and flexibility. The guidance properties of a standard optical fibre can be theoretically modelled, by solving the wave equation for cylindrical co-ordinates, using the Bessel functions [2]. These solutions predict the modal properties, the boundary conditions, and the properties of guided and evanescent fields within the fibre.

Optical fibres were initially developed for the delivery of light for communications, however, optical fibres have also been utilised for sensing applications for over four decades [3]. Traditionally optical fibre sensors have been used to measure strain [4, 5, 6], temperature [7] and pressure [8] by observing changes in the intensity, phase, polarisation and wavelength of the guided light. Applying the fibre to an interferometer set-up [9], or writing a grating to the fibre [10], are among many of the techniques where optical fibres are used for sensing. There are many review papers that describe in detail the history and physical applications of optical fibres to sensing [11, 12, 13, 14]. Optical fibre sensors have only begun to become commercially competitive with traditional and well established sensors, despite the benefits associated with optical fibre sensors, such as the optical sensitivities that can be offered and their potentially compact structure.

Optical fibre sensors enable simple, rapid and continuous monitoring, with the benefits of low loss light delivery, long interaction lengths and the ability to excite and capture light signals. Many optical fibre sensing applications are aimed towards industry, oil and gas, construction and also to a smaller extent the food industry and bio-medical sector. At the 15th International Conference on Optical Fibre Sensors 2003 (OFS 15), the percentage of papers that were submitted in the area of bio-sensing was 2.4%, while temperature, pressure and strain represented the majority at 55% [12]. However, with the recent advances in micro and nano fibres [15], surface plasmon resonance [16], and biological techniques [17], optical fibres have been increasingly applied to the area of bio-sensing and medical diagnostics [18, 19], as their vast potential has been realised.

In biological and chemical sensing, the function of optical fibre sensors is to guide and transport light, which excites the molecules at the delivery point, and is

used to measure refractive indices of the liquid sample, or is used to record the absorption and transmission properties of the sample. Light interacts with the molecules when the sample is placed within the optical field of the fibre. A sample can be placed at the terminal of an optical fibre to interact with the optical field, as demonstrated schematically in Figure 1.2 (a). Optical fibres have also been post-processed to improve interaction of molecules with the evanescent field, which is the component of the optical field that permeates outside the boundaries of the optical fibre core. Interaction with the evanescent field (an electromagnetic field that undergoes exponential decay with distance from the silica/air boundary) is achieved by tapering the fibre, as demonstrated in Figure 1.2 (b). In this schematic, the sample has a much larger area over which to interact with the evanescent field. However, tapering the fibre to such small diameters (approximately 1 - 100 μm) [15, 20, 21], weakens the structural properties of the optical fibre. To overcome this, the placement of the sample within the guided optical field, without disrupting the guidance mechanism or weakening the structure of the fibre, has the potential to be a competitive and powerful sensing system. Hollow core photonic crystal fibres provide such a structure for fibre optic sensing, as seen in Figure 1.2 (c). An example of its cross section is shown in Figure 1.2 (d).

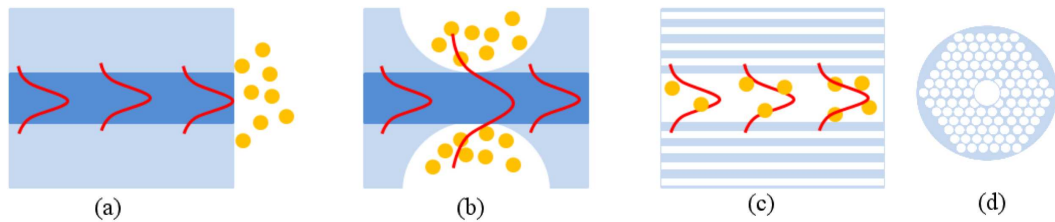


Figure 1.2: Example schematic of optical fibres used for sensing of samples for (a) a standard optical fibre, (b) a tapered optical fibre, (c) a hollow core photonic crystal fibre and the cross section of a hollow core photonic crystal fibre (d). The light blue indicates the presence of silica (refractive index 1.45) and the blue indicates the presence of doped silica of higher refractive index. The red curves display the optical field within the fibre, the yellow circles indicate the liquid sample and molecules. In (a) the sample interacts with the optical field when it exits the fibre at the end facet. In (b) the optical field interacts with the sample, via the evanescent field, which can be visualised by the exaggerated extension of the pulse decay (pictured in red) at the thinnest part of the structure. In (c) the guided optical field and sample occupy the same space, allowing the optical field to interact with the sample within the fibre.

Hollow core photonic crystal fibre have been developed and optimised for the delivery of low loss light [22, 23, 24, 25, 26]. However many review papers have

been published on the wide range of potential applications of hollow core photonic crystal fibre [27, 28]. Since their conception hollow core photonic crystal fibres have been recognised as an ideal device for liquid and gas sensing [29]. The use of micro-structured optical fibres for medical and liquid sensing in particular is an important field of research [30]. The large overlap between the liquid sample and the optical field in hollow core photonic crystal fibre results in enhanced signal detection [31], when compared with the standard optical fibre and tapered fibres, seen in Figure 1.2. The benefits of choosing a hollow core photonic crystal fibre for bio-sensing, rather than traditional cuvettes (a vial with clear sides, used to hold a sample for spectroscopic measurements) or standard optical fibres, is that hollow core photonic crystal fibre allow long interaction lengths with the optical field. They also only require nano litre volumes of sample and offer the potentially cheap production of new fibre for sensors. The uniform hollow capillaries allow the introduction of gases and liquids to the structure of the fibre [32] and allow light to be guided by the photonic band gap effect (which shall be discussed in Chapter 2) in air or through the sample, allowing a strong interaction between the electromagnetic wave and the samples [31, 33, 34, 35]. There are many reviews of using hollow core photonic crystal fibre for bio-sensing such as for gas sensing [36, 37, 38], for the detection of bio-molecules [39, 40, 41], and in biomedical investigations [42].

There is a wide scope of applications for optical sensing, and one significant research area is in glucometers. Diabetics must monitor their glucose levels throughout the day. This creates a need for a reliable and repeatable way to determine glucose levels in blood. For the diagnosis and testing of diabetes, monitoring the levels of glucose in blood requires highly sensitive, highly accurate detection, with a low level of invasiveness [43]. Normal glucose levels are between 4 - 9 mM. These levels tend to rise and fall throughout the day, particularly after eating. Glucose levels that are chronically higher or lower than these figures indicate hyperglycaemia or hypoglycaemia. Measurements need to be completed within a small time period as glucose decays at a measurably rapid rate once a blood sample has been taken from a vein. Typically enzymes that are specific to glucose, such as glucose oxidase and hexokinase are used to detect the presence of glucose. Glucometers utilize μL samples of blood that react with an enzyme electrode containing glucose oxidase. The re-oxidation creates an electric current that can be measured [44]. A method for continuous, non-invasive measuring is required and desired for diabetes patients.

The determination of the Raman spectra from biologically interesting fluids is

a potentially powerful technique that can be used for real time monitoring and non-invasive measurements of glucose concentration. Interstitial fluids from the skin and saliva from the mouth [45] can be taken from the body in a virtually non-invasive manner, when compared with the extraction of blood from a vein. Saliva is a promising non-invasive option, as saliva in patients with diabetes has been shown to have a different composition when compared to healthy patients [45, 46, 47]. There are a variety of methods for non-invasive glucose monitoring, such as surface enhanced Raman spectroscopy, fluorescence and photo-acoustics, reviewed by [48, 49, 50].

With consideration of these applications, hollow core photonic crystal fibre can be potentially used to address the need for sensitive glucose detection by monitoring the change in the viscosity of liquid, and to analyse the Raman spectra of biological samples, by collecting the scatter in long lengths of hollow core photonic crystal fibre. In this thesis it is shown that it is possible to determine the viscosity of aqueous glucose solutions over a wide range of concentrations from 10^{-4} - 1 M, and to probe the Raman spectra of the samples within the capillaries of the fibre. Furthermore, the collection of Raman scatter will be shown to improve with increased fibre length, thus improving the detection resolution of the system.

The main results of this shall be the implementation of a multi-analytical viscometer and Raman sensor using the hollow core photonic crystal fibre. In this thesis, it is shown for the first time that hollow core photonic crystal fibres can be used for the measurement of viscosity, and it is also shown that selectively core only filled fibres with long lengths can be used to collect the Raman scatter of molecules present in interstitial fluids. A selection of the main results are shown in Figure 1.3.

Thesis Chapter Outline

The chapters and contents of this thesis are organised in the following way:

Chapter 2: Fundamentals Background

This chapter comprises the fundamental background information on the hollow core photonic crystal fibre, viscosity of liquids, and Raman scatter within liquid filled fibres. The guidance properties of hollow core photonic crystal fibre are discussed for both the empty and filled states. The fundamentals of insertion of a liquid into a hollow core photonic crystal fibre are discussed. A model for the determination of the viscosity of a liquid from capillary flow is outlined from first

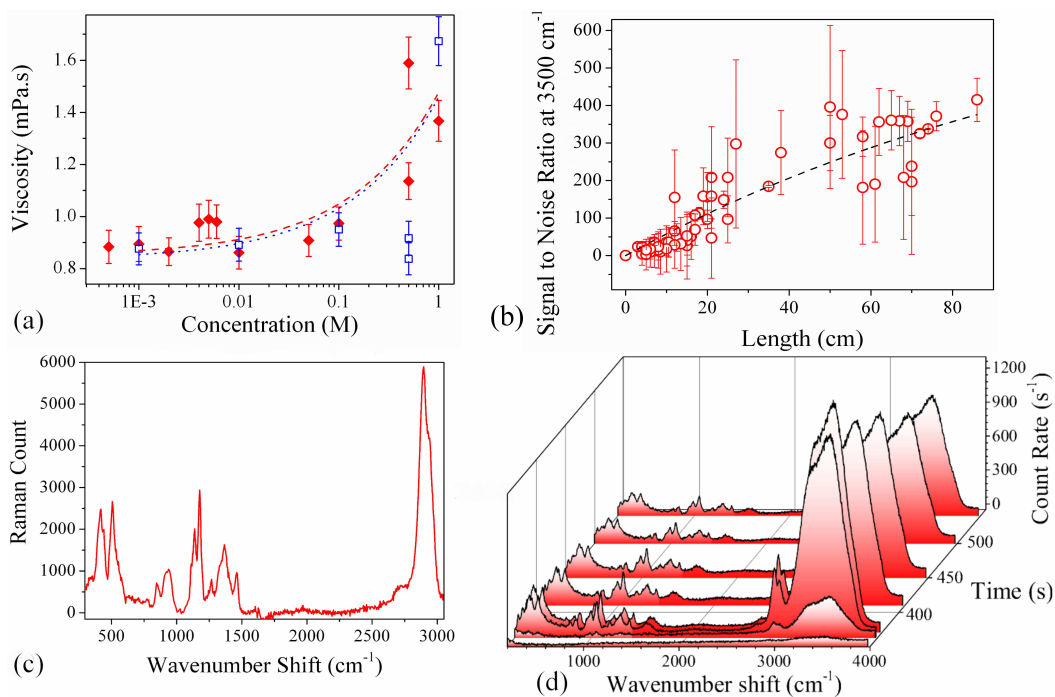


Figure 1.3: A selection of graphs from the thesis that highlight the main results for using hollow core photonic crystal fibre for viscosity and Raman studies. Plot (a) shows the viscosity results for solutions of glucose (red) and fructose (blue) in PBS (10^{-4} - 1 M), tested with 10 - 12 cm lengths of fibre (Section 4.3.2). Plot (b) shows the increase in Raman count for water core hollow core fibres as the fibre length increases from 0.03 - 0.86 m (Section 7.1.4). Plot (c) shows the Raman spectra of 2.5 M glucose, taken with an integration time of 20 s (Section 7.2.1). Plot (d) shows a selection of Raman spectra taken from a dynamically filling hollow core photonic crystal fibre, which shows the rise and decay in counts as the capillaries fill (Section 6.2).

principles for the hollow core photonic crystal fibre. The collection of Raman scatter within a liquid core fibre are discussed and compared to hollow core photonic crystal fibre in the final section.

Chapter 3: Microscope Analysis of Liquid Filling Capillaries

The pattern of filling for a hollow core photonic crystal fibre by capillary action is examined using a microscope. The model for viscosity determination is tested using this method for water and propan-1-ol.

Chapter 4: Optical Fibre Viscometer

The microscope method for the determination of viscosity is changed to an optical method that is repeatable and temperature controlled. The system is tested for glucose and fructose solutions, and propan-1-ol solutions, and compared to

results available in the literature.

Chapter 5: Optical Transmission Properties of Liquid Filled Hollow Core Photonic Crystal Fibre

The light guidance properties of the empty, liquid core and fully liquid filled fibre are tested to determine how the propagation changes in each state. A cross section of the fibre structure that comprises the core and cladding is analysed and tested using a pinhole method and a Shack-Hartmann wavefront sensor. The results are used to characterise the numerical aperture of both filling states of the fibre.

Chapter 6: Viscometer Integrated with Raman Scatter for Simultaneous Analysis

A method of measuring the Raman scatter of the liquid molecules within the fibre and the viscosity simultaneously is integrated to test the fibres potential as a multi-analytical sensor.

Chapter 7: Raman Scatter in Hollow Core Photonic Crystal Fibre

The use of liquid core hollow core photonic crystal fibre is examined for the collection of Raman scatter. Liquids of interest in bio-sensing are examined, such as interstitial fluids, glucose and lactate solutions and urea and creatinine solutions.

Chapter 8: Conclusions

The final chapter outlines all the main results of the thesis, and the conclusions that can be taken from the experimental results. Finally, future work is proposed and briefly discussed.

Chapter 2

Fundamentals Background

This chapter reviews some of the extensive literature and previous work that has been published in the field of optical sensing with hollow core photonic crystal fibres (HC-PCF). The background information covers three topics that are investigated experimentally in this thesis, and is divided as follows: the guidance of light in HC-PCF when empty and during its filled states, the measurement of the flow velocity during the filling of the silica capillaries of the HC-PCF and its relationship with the viscosity of the liquid, and finally Raman scatter generation and collection within liquid filled fibres.

The first section describes the photonic band gap (PBG) effect in optical fibres by drawing a conceptual understanding of the periodic dielectric structure. The literature discussing the understanding of the guidance properties of these unique fibres shall be outlined, and reviewed for the cases of air-core, liquid core and fully liquid filled HC-PCF.

The second section comprises a review of the physical parameters of viscosity, surface tension and hence flow dynamics that should be considered in the filling process of the internal capillaries of the fibre. The application of capillaries for the measurement of liquid viscosity is discussed, and currently commercially available capillary viscometers are reviewed. The model of capillary flow as a function of viscosity with time is outlined.

The final section briefly describes the phenomenon of Raman scatter. This is an inherently weak process, and one way of increasing the Raman signal is to increase the volume of the sample and the number of molecules available to generate Raman scatter. Previous investigations using long lengths of Teflon fibres are discussed, along with the more recent application of using HC-PCF as a tool for

Raman signal collection.

2.1 Hollow Core Photonic Crystal Fibre

Confinement of light waves in an artificial two or three dimensional PBG material has been a subject of interest since the mid 1980s with preliminary investigations reported by John [51] and Yablonovitch [52, 53]. Confining light in this manner controls the propagation properties with a phenomenon other than total internal reflection, used in standard optical fibres and waveguides [54]. This concept was proposed first for use in two dimensional optical silica waveguides in 1995 [29, 55, 56]. The cross section of the fibre resembled a two dimensional periodic crystal, and was composed of stacked silica capillaries, centred around a core defect.

In 1999, guidance by the PBG effect was theoretically and experimentally demonstrated to provide confinement of light in the hollow core of an air-silica optical fibre [57, 58, 59, 60]. The principle of trapping and guiding light waves in air instead of silica, created promising applications for optical fibres, that could not be achieved in traditional standard optical fibre. The subsequent development and advancement of these fibres from their theoretical beginnings [61] and investigations for their experimental fabrication [25, 62] has been reported in many reviews [63, 64, 65].

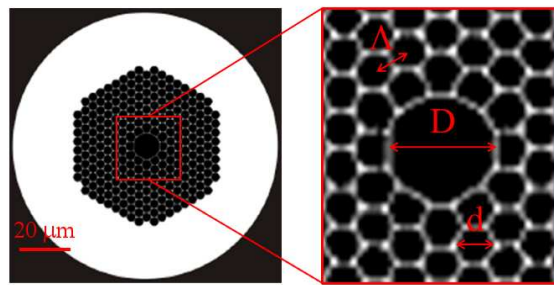


Figure 2.1: Schematic of a HC-PCF (courtesy of NKT Photonics A/S). Right is a magnified image of the core, labelling the pitch (Λ), core defect diameter (D) and the capillary diameter (d).

HC-PCF (as shown in Figure 2.1) use a two dimensional air-silica cladding of hollow capillaries, arranged around a central defect in the lattice. The optical waveguide can confine and propagate wavelength bands along the defect core of the fibre using the PBG effect [66]. PBG optical fibres are present in many forms: solid and hollow core, with a variety of holey claddings including; periodic

hexagonal structure, kagome lattice, and suspended core fibre. Each of these types have been extensively investigated, and allow PCF to be tailored for a wide range of applications. This thesis will focus on the use of HC-PCF. The HC-PCF permits very low loss guidance of light through the air core of the fibre, high power delivery without risk of damage to the fibre, unique dispersion properties, they have lower non-linearity and potentially lower transmission loss.

A selection of typical HC-PCFs is seen in Figure 2.2. The images indicate the core (with radius D) and micro-structure regions of the fibre. The diameter of the capillaries of the micro-structured region is typically on the scale of the wavelengths that will be guided within the core defect.

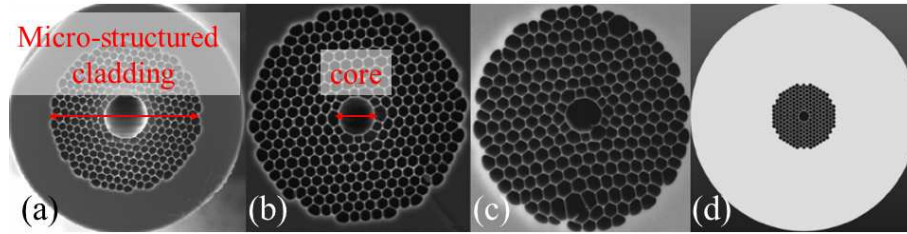


Figure 2.2: Examples of hollow core photonic crystal fibres, images courtesy of NKT Photonics A/S. (a) HC-2000, with the micro-structured cladding region indicated in red. (b) HC-1060, with the core region indicated in red, (c) HC-633, (d) HC-540. The number indicates the wavelength of the primary bandgap.

HC-PCF have many applications in sensing as discussed in the literature [35, 67, 68, 69, 70, 71, 72, 73]. The brief review of sensors in this section outlines that optical fibre sensors are used to monitor gases, liquids, temperature, strain and pressure. HC-PCF are beneficial for optical sensing as liquid samples can be inserted into the capillaries. HC-PCF allow light to be guided only within the hollow core of the fibre. This allows a large overlap between the electromagnetic field and the sample inserted into the capillaries [33], provided that the PBG guidance conditions still hold after the filling. Filling the core of the fibre, or filling the entire fibre, changes the wavenumber of the guided light and therefore changes the bandgaps that the light can access. Figure 1.2 in Chapter 1, shows a range of optical fibre sensing schematics, highlighting the advantage of using HC-PCF. In the case of HC-PCF, there will be a greater overlap between the sample and the optical field, in comparison to other fibre optical sensors, such as tapered fibres which rely on the evanescent field only.

In order to harness the unique HC-PCF structure as an optical liquid sensor, first a complete understanding of the initial PBG and the dynamic behaviour

of liquid flow inside the capillaries must be achieved. The effect of the liquid upon the guidance properties shall be described in the theory in the following section, and investigated experimentally in Chapters 4 for dynamic fluid flow, and in Chapter 5 for two static filling profiles of the HC-PCF; core filled only and fully filled.

2.1.1 Photonic Band Gap Effect

The PBG arises from the phenomenon of interference and resonance effects within the silica-air structure. The review paper by Jin [74] opens with a short paragraph of the PBG effect, which explains succinctly the guidance mechanism in HC-PCF.

“A PBG refers to a range of wavelength λ within which light propagation is prohibited. The opening of a PBG depends on the longitudinal component of the wave-vector or the propagation constant k_z , which is related to the effective refractive index n_{eff} by $k_z = 2\pi n_{eff} / \lambda$. A PBG may be closed for $k_z = 0$ (i.e. in plane) but opens up for $k_z > 0$ (i.e. out of plane)(...). If the hollow core supports an optical mode within one of the PBGs, this mode will be confined to the core region and propagate along the fibre with low loss.”

A photonic crystal supports modes over specific bands of wavelengths. The spectral window between these bands is defined as the “photonic bandgap”. PBG guidance in HC-PCF can exist when the guided light is of a wavelength within the bandgap, it cannot be supported in the photonic crystal cladding, and is reflected back to the defect hollow core of the fibre [54, 75]. The defect allows modes of forbidden light to exist within the air-silica dielectric. These modes are defined by the propagation constant β , where $\beta = n_{eff}k$ ($k = 2\pi/\lambda =$ wave number, $n_{eff} =$ effective refractive index). The propagation constant in relation to the guidance of light in a waveguide is shown in Figure 2.3 (a). The range of propagation constants that are allowed or forbidden to propagate in the guidance region depend on the wavelength of the light and the bandgap. This is schematically demonstrated using a vectorial wavenumber ray model in Figure 2.3 (a).

In a one dimensional case, when light is incident on an infinite structure with a periodically alternating refractive index, as seen in Figure 2.3 (b), some light will

be reflected at the interfaces, due to the Bragg condition [54] and Fresnel reflection, while the residual light will be able to transmit through the one dimensional structure. This structure is similar to the cross section of a HC-PCF. In the case of a HC-PCF, when light is guided by the PBG effect, it is guided within the core of the fibre and it is unable to propagate within the cladding material, if the light falls within a specific range of β values [57]. A guided mode can then be present within the core of the fibre [66, 76], if it is possible that a resonance mode can be excited within that space. This is demonstrated schematically for a two dimensional structure in Figure 2.3 (c). A fundamental mode will be trapped within the core as it will not be possible for this mode to propagate within the capillaries of the cladding due to the PBG. The mode allowed to propagate through the air core comprise the constructively interfering reflected rays at the core. Higher order modes with low β values, that can fit into the capillaries leak away into the cladding of the fibre. Figure 2.3 (d) shows the distribution of the light intensity over a two dimensional cross section of the HC-PCF, demonstrating that the guided light is confined to the hollow core only.

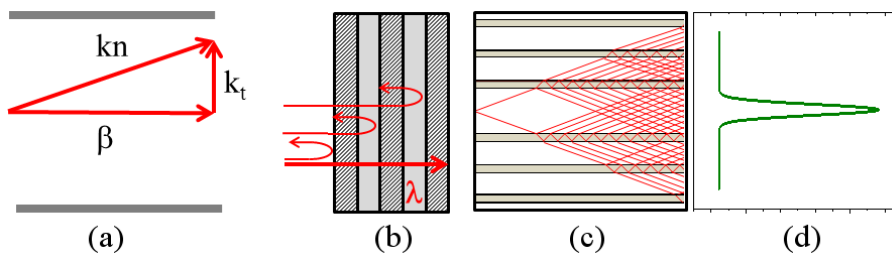


Figure 2.3: Schematic of PBG effect in a silica/air waveguide. (a) Beta (propagation constant). (b) Bragg reflectance in a one dimensional optical plate. (c) PBG effect in a two dimensional structure. (d) Confinement of the guided mode to the core defect.

There are many theories to explain this effect, such as mode coupling theory [63], anti-resonance theory [77] and solutions to Maxwell's equations in a periodic dielectric medium [75, 78, 79]. Many different methods and models are used to study the propagation characteristics of PCF [80, 81], such as the effective index model [82], plane wave expansion method [83], beam propagation method [84], finite element method [85, 86] and super cell method [81]. These typically require complex mathematical functions, and long calculation and simulation times, and can be found extensively in the literature. The general theory of propagation in PCFs is beyond the scope of this thesis and here the focus is on understanding the general behaviour of how light propagates within the HC-PCF only, particularly for the liquid filled cases.

The optical guidance properties of HC-PCF are best understood using the component of the wave vector, β , along the fibre axis, as shown in Figure 2.3 (a). The value of the propagation constant determines whether the light is present or evanescent in any part of the waveguide. The PBG of the periodic structure of the PCF can be estimated from Maxwell's equations and used to determine which frequencies can propagate within the core of the fibre. Results are normally presented using a propagation diagram, known as band-edge or finger-plot diagrams, indicating where the light is evanescent (unable to propagate). The axis are usually labelled $\beta\Lambda$ and $\omega\Lambda/c$. This concept resembles the electronic bandgap in semi-conductors.

2.1.2 Liquid Filled Fibres

As discussed previously, one of the advantages of using HC-PCF for liquid sensing is that liquids can be inserted into the silica capillaries of the fibre. Confinement of liquids within the internal core of the fibre allows an increase in the overlap between the optical field and liquid for sensing [33, 87]. The experimental insertion of liquids into the narrow capillaries (1-10 μm) is discussed in Section 4.1.4.

The insertion of liquids to the hollow spaces in HC-PCF will result in a change in the guidance mechanism of the optical fibre. This is due to a change in refractive index within the internal structure from air ($n = 1$) to that of the liquid (n_{liquid}). A schematic diagram of the refractive index change across a two dimensional section of the HC-PCF is shown in Figure 2.4. In (a) the grey areas represent the silica capillary walls of the micro-structure, and the white spaces are the air filled areas. The black dashed line is a guide to show how the refractive index changes over the cross section of the HC-PCF from the average refractive index of the micro-structured cladding.

Depending on the selection of capillaries that are filled, the propagation properties can be changed. If the core only of the fibre is filled, as depicted in figure 2.4 (b), guidance occurs via index guiding [33] as the core has a much higher refractive index than the combined average index of the cladding, represented by the black dashed line. A small selection of capillaries in the cladding surrounding the core can also be filled to tailor the propagation properties of the fibre [88, 89]. When the entire structure is fully filled with a liquid, as shown in Figure 2.4 (c), the original guidance mechanism of the PBG shifts to shorter wavelengths, depending on the refractive index contrast. This occurs only when all the hollow

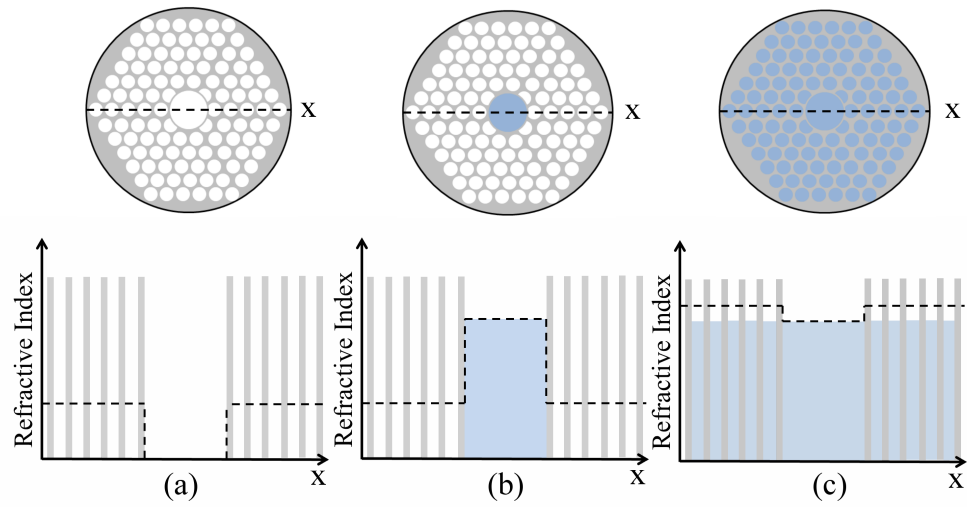


Figure 2.4: Schematic of the two dimensional cross section of HC-PCF, which demonstrates how the refractive index changes for the three filled states (a) empty, (b) liquid core filled and (c) fully filled. The inserts above each figure display the HC-PCF when empty, core filled and fully filled respectively, with the dashed line showing the cross section that is used to analyse the changes in refractive index. The grey areas indicate the silica of the HC-PCF, the blue areas represent the liquid filling. The black dashed lines in the two dimensional cross sections below the images of the HC-PCF are a guide to demonstrate how the refractive index changes across the two dimensional structure.

capillaries exhibit a uniform change in refractive index, and the initial conditions for guidance are re-established, with the exception that the refractive index contrast is now lower [90, 91].

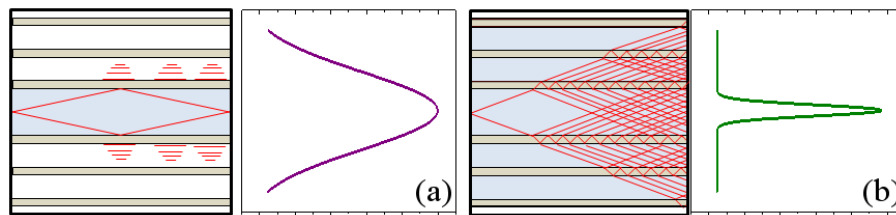


Figure 2.5: Schematic of guidance in liquid filled HC-PCF for (a) index guiding in core filled fibres and (b) PBG guidance in fully filled fibres.

The two schemes of light propagation within the liquid filled fibres are demonstrated in Figure 2.5. The results of this are discussed further in Chapter 5. Figure 2.5 (a) demonstrates index guidance in a liquid core filled fibre. Figure 2.5 (b) demonstrates PBG guidance in a fully liquid filled fibre. The light is more strongly confined to the core for the fully filled case, due to guidance by the shifted PBG effect.

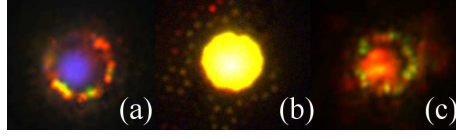


Figure 2.6: Near-field CCD images of a broadband source (400 - 1700 nm) in empty and liquid filled HC-PCF (HC-1060, purchased from NKT Photonics A/S) for (a) PBG in an empty fibre (b) index guiding in a core filled fibre and (c) PBG guidance in a fully filled fibre.

The difference in guidance between the PBG and index guiding can also be demonstrated by looking at the near field images of the end facet of the HC-PCF with a CCD camera. In Figure 2.6, the HC-PCF when (a) empty, (b) core filled and (c) fully filled is shown when guiding a broadband light source. For (a) and (c) which demonstrate PBG guidance, light is mainly confined to the core of the fibre, with some higher order modes and surface modes in the silica cladding [92]. For the index guiding case, (b), the guidance is spread throughout the core, demonstrating strong confinement due to the refractive index contrast between the core and the cladding.

Fully Liquid Filled Fibres

To predict the change in propagation properties of the HC-PCF upon the complete filling of all the hollow capillaries by a liquid, the vectorial equations that determine the original PBG, as discussed in Section 2.1.1, may be assumed to be scalar [91]. This simplification is due to the assumption that the inclusion of liquids to the capillaries of the fibre will result in a low index contrast [91], as long as $n_{liquid} < n_{silica}$. The scalar wave equation is used to determine the shift in PBG from the original guided wavelength, λ_0 , to a new guided wavelength λ . This is defined by the equation [91]

$$\lambda = \lambda_0 \left[\frac{1 - \left(\frac{n_{liquid}}{n_{silica}}\right)^2}{1 - \left(\frac{n_{air}}{n_{silica}}\right)^2} \right]^{\frac{1}{2}} \quad (2.1)$$

where n_{air} is the refractive index of air, n_{silica} is the refractive index of silica and n_{liquid} is the refractive index of the liquid inserted to all the capillaries of the HC-PCF. This was shown for heavy water in 2006 by Antonopoulos et al. [93] and for fructose solutions in 2006 by Cox et al. [94] and for a range of other experimental uses in the literature [95]. By using the scalar equations to determine the approximate shift in PBG with the insertion of liquids, the fibre can be tailored with the internal refractive index to guide a range of wavelengths in the visible region. The shift in PBG with refractive index, with respect to the

initial PBG guided wavelength is shown in Figure 2.7. This figure describes the approximate change in guided wavelength in a commercially available HC-1550 and HC-1060 HC-PCF (purchased from NKT Photonics A/S), with respect to the refractive index change from $n_{air} = 1$ to $n_{liquid} > 1$. For a liquid with a refractive index close to water $n_{liquid} \approx 1.33$, the PBG for the HC-1550 would shift to 850 nm, while the PBG for the HC-1060 would shift to 580 nm.

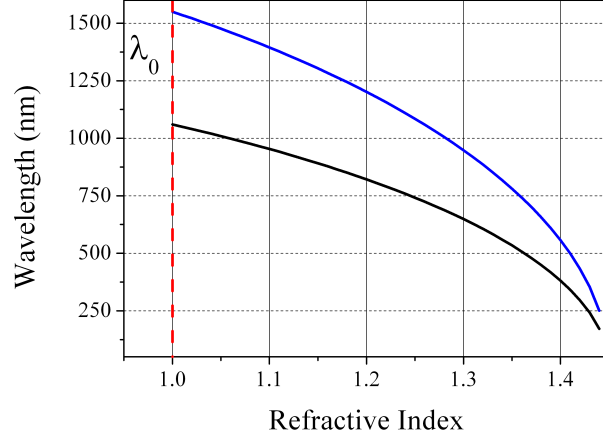


Figure 2.7: Shift in central wavelength guided by the PBG, estimated using the scalar equations. The shift is demonstrated for two commercially available fibres, HC-1550 (blue) and HC-1060 (black).

Liquid Core Only Fibres

When only the core of the fibre is selectively filled with a liquid, the guidance properties differ from the PBG effect. The filling of the core, results in an area of high refractive index, surrounded by a cladding with a lower average refractive index. The contrast between refractive index is higher ($\Delta n > 0.1$) than for standard optical fibre ($\Delta n \sim 0.01$). This larger contrast in refractive index results in the strong confinement of light to the core of the fibre, above a certain wavelength threshold [96], defined by the refractive index of the filling liquid and the average refractive index of the air-silica. For this reason, the guidance properties of these liquid core fibres cannot be solved using the standard solution to a cylindrical waveguide, as this assumes that the contrast is very low, $\Delta n \approx 0.01$ [97].

HC-PCF can be analysed with methods similar to the standard optical fibres, which propagate light via total internal reflection, using an effective index model [55, 98]. For a fundamental mode to exist in the core of the fibre, the propagation constant must be less than kn_{core} , where k is the wavevector and n_{core} is the refractive index of the core. These fibres can be compared analogously to standard optical fibres, using the V parameter to determine the number of modes that can

propagate within the core [99]. The V parameter is used in standard optical fibre to determine whether the fibre is single or multi-mode, and is given by:

$$V = \frac{2\pi R}{\lambda} \sqrt{n_{core}^2 - n_{eff}^2} \quad (2.2)$$

where R is the core radius of the standard fibre. For photonic crystal fibre, this can be replaced with the pitch of the micro-structure cladding (Λ) [98]. Depending on the parameters of the fibre, and the ratio of the micro-structure capillary diameter to the pitch, the fibre can be endlessly single mode, or can propagate a range of higher order modes within the high index core, depending on the fibre structure [100]. Mortensen discussed in his paper [79] that when the ratio between the capillary diameter (d) and pitch becomes greater than 0.42, the fibre becomes multi-mode. As the ratio increases, higher order modes can be trapped and available to propagate within the core of the fibre [64]. Thus light of fundamental and higher order modes is strongly guided and do not leak to the silica cladding.

The index guiding in the liquid core allows the fibre to guide light in the visible range, and to allow the sample to be probed in the visible regime [101]. This is an attractive optical property for sample sensing. Liquid core fibres also present guidance by the original PBG, as the cladding structure is not affected by the presence of liquid, and this is demonstrated in [102, 103]. This hybrid guidance is attractive for a wide range of sensing purposes [89]. A good theoretical review of water core index guiding HC-PCF can be found in [33, 74], which include fingerplot diagrams indicating the index guiding regime and the original PBG still present in the capillary micro-structure. This is also observed experimentally in Chapter 5.

To determine the average refractive index of the micro-structured cladding, the fraction of air filled space in the HC-PCF to silica filled space can be determined [82]. The average refractive index of the cladding structure can be calculated by:

$$n_{avg} = \sqrt{fn_{air}^2 + (1-f)n_{silica}^2} \quad (2.3)$$

where f is the air filling fraction, given by [28] for a triangular lattice

$$f = \frac{\pi \left(\frac{d}{\Lambda}\right)^2}{2\sqrt{3}} \quad (2.4)$$

A typical f value for commercially available HC-PCF, such as the HC-1060 (NKT

Photonics A/S) is $> 90\%$. The air filling fraction is determined by considering the lattice of the micro-structure. The average refractive index of the micro-structured cladding decreases, as the ratio of the capillary diameter to the pitch increases [33].

The calculation of the effective index can also be compared to a perfect conductor [33], and determined using this method for fundamental modes and higher order modes within the core filled HC-PCF, with the equation

$$n_{eff}^2 = n_{core}^2 - a_i \left(\frac{\lambda}{R} \right)^2 \quad (2.5)$$

where a_i is a parameter that determines the mode generated for the wavelength confined in the liquid core filled fibre.

2.1.3 Altering the End-Facet of the Fibre

In order to tailor the filling of the capillaries of HC-PCF, the structure must be pre-processed before the introduction of liquids. The literature shows many methods to selectively fill the capillaries of a HC-PCF. The majority involve the blocking the capillaries at one of the end-facets. This can be achieved using a number of methods, such as collapse of the external capillaries by heating [32, 101, 104, 105], injecting a curable polymer [106], or side access [107]. Fibres may also be preprepared using chemical methods to prepare the surfaces by silanization [108] or to create a hydrophobic surface [109]. The collapsing method was used in these experiments, and will be discussed in Section 5.1.3.

2.1.4 Modal Properties of Liquid Filled Fibre

HC-PCF fibres are designed to support guidance of the fundamental mode over a long distance due to the PBG effect. This can be demonstrated in a segment of HC-PCF by launching light at the fundamental bandgap within the hollow core of the fibre. This is demonstrated in Figure 2.8. The first image (a) in Figure 2.8 is the HC-1060 (seen previously in Figure 2.2), indicating the core and micro-structured cladding region. (b) Shows the propagation of the fundamental mode, at a wavelength 1060 nm within the core of an air-silica HC-1060, exhibiting a Gaussian-like profile, referred to as an LP_{01} mode. (c) Depicts a higher order mode, generated by changing the alignment of the fibre from the optimum position

to a non-optimum position, and generates the LP_{11} mode. When the fibre is filled with a liquid however, guidance properties change as described in Section 2.1.2. Figure 2.8 (d-e) show a water core and fully water filled fibre propagating a full broadband source. The initial fundamental mode at 1060 nm has been replaced with broad guidance in the visible regime.

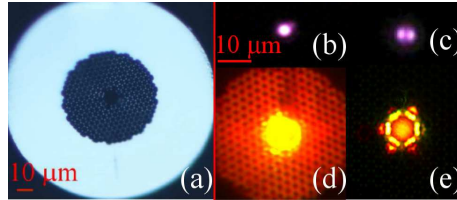


Figure 2.8: Examples of guidance with a full broadband supercontinuum source for the HC-1060 when empty (b-c), core filled (d) and fully filled (e). (a) Depicts the micro-structure of the HC-1060 using a Nikon microscope (magnification $\times 500$), and (c) shows the generation of a higher order mode LP_{11} within the core of the fibre at 1060 nm, generated by changing the alignment of the fibre from the optimum at (b).

As the HC-PCF fills dynamically with a liquid, modal interference occurs in the core of the fibre. This is observed experimentally in the experiments described in Chapter 4, viewed in real time using a CCD camera (30 frames/s) and significantly impacts the collection of Raman scattered light as described in Chapters 6 and 7. This is due to the competing schemes of guidance and the changes in refractive index between the three media of air, silica cladding and filling liquid in the HC-PCF. The liquid interior creates a dynamic medium for the propagation of light but also results in a constant state of modal competition within the fibre, due to the fluid nature of the liquid.

The next section shall discuss the property of viscosity, which is examined in Chapters 3 and 4, where the HC-PCF is tested for its use as an optical fibre viscometer. Currently available capillary viscometers are discussed in terms of their uses in industry and medical diagnostics, the volume of samples they require and their performance. This is compared to our patent for an optical fibre viscometer using HC-PCF [110].

2.2 Viscosity

Viscosity is a property that describes the resistance of a liquid to flow, or the friction between the liquid layers, when the liquid is acted on by an external

force, such as gravity. The resistance or friction results in shear stress (force, F per unit area, A) between the layers. A liquid flows in a discrete set of layers, each featuring a different velocity. In a capillary, layers at the walls will have a lower velocity than those at the centre of the capillary. This stress is proportional to the rate of flow velocity between the two layers. The property of viscosity was first proposed by Isaac Newton when he theorised that the shear stress a liquid undergoes is proportional to the velocity gradient $\partial u / \partial y$ of the fluid:

$$\frac{F}{A} = \mu \frac{\partial u}{\partial y} \quad (2.6)$$

where μ is the viscosity, u is the velocity of the liquid layer, F is the force, and A is the area that the force acts upon. If the velocity profile is linear in the above equation, the liquid is defined as Newtonian, and the viscosity will remain constant where the temperature and pressure is unchanged.

When liquid flows through a cylindrical pipe, the shape of the flow profile can be determined using the Navier-Stokes equations. By changing the variables of the Navier-Stokes equations to cylindrical coordinates, and solving for fluid flow in the z -direction, the shape of flow can be deduced to be parabolic. The viscosity flow profile is shown schematically in Figure 2.9 as a parabolic flow in the z -direction. Changes in pressure will not affect the viscosity, but an increase in temperature will result in a decrease in viscosity. The absolute viscosity is very sensitive to temperature changes, modelled by the Arrhenius equation [111]. In non-Newtonian fluids the relationship between velocity and shear stress is non-linear.

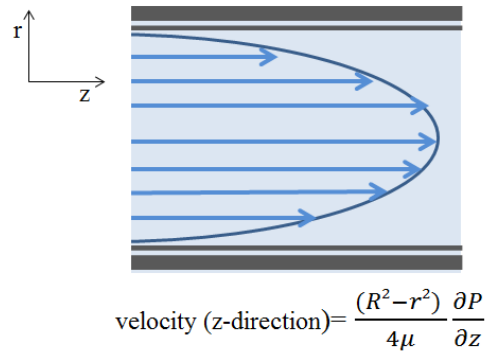


Figure 2.9: Schematic of the parabolic velocity flow profile of a Newtonian liquid within a capillary channel, where R is the radius of the capillary.

One of the key features of modelling liquid flow in capillaries is the determination of the viscosity of a liquid from the flow profile. It has been studied extensively

with many models, where most models derived the viscosity from the initial equation described by Washburn in 1921 [112]. This study investigated the capillary action of a liquid in a porous material, and suggested a new way to measure viscosities using this phenomenon. This relationship describes the time taken for a liquid to flow through a porous material, considering standard conditions of room temperature and pressure, and for a Newtonian liquid. The Washburn equation is given by:

$$L^2 = \frac{\sigma R t}{4\mu} \quad (2.7)$$

where L is the length of the capillary, t is the time taken to fill, R is the diameter of the capillary, σ is the surface tension and μ is the viscosity.

The determination of the viscosity of a liquid when it is mixed with solutes and solvents is more complex. Adding solutes to a liquid tend to increase or decrease the surface tension and viscosity. Many models have been derived for different solutions and suspensions, as reviewed by Rutgers [113]. These models usually predict the viscosity behaviour up to a concentration of 0.2 M. Some empirical models use the Einsteinian formula: $\mu_{rel} = 1 + k.c$ [114], where k is a factor of the molecules in solution and c is the concentration of the molecules, logarithmic formulae or power formulas such as the Jones Doyle formula equation [115, 116]

$$\frac{\mu}{\mu_0} = 1 + A c^{\frac{1}{2}} + B c \quad (2.8)$$

The parameters A and B in both cases refer to the concentrations of solute in the solvent and physical characteristics of each liquid solution.

2.2.1 Current Capillary Viscometers

The flow of liquid through capillary tubes via the phenomenon of capillary action, due to the existence of cohesion and adhesion forces between the liquid molecules and the capillary walls, is a fundamental topic of study, and is forefront in many events such as tear duct drainage, wicking and hydrology and is a key consideration in many applications in engineering, industry, biology and medical diagnostics.

Viscosity is an important parameter, and is used in many applications to control liquid flow velocity and to determine chemical concentrations. The measurement of the viscosity of blood plasma [117] is used to determine pathological diseases [118, 119, 120] and to measure the viscosity of DNA [121]. In industry, viscosity

can determine the concentration of sugars [122], in food production [123], it can be used to control the flow velocity of chemicals in industry production and is an important parameter for the manufacture of paints, inks and other products [124]. Micro-channels for the transport and mixing of liquids, and lab on chip applications have recently become an important study, and require precise viscosity measurements of very low volumes of liquid in comparison to industry applications. Therefore the determination of viscosity is important in bio-chip designs [125].

There are many different types of commercial viscometers available, such as rotating viscometers (which measure torque), falling sphere viscometers (based on Stoke's law), Ostwald viscometers (u-tube viscometers) and capillary tube viscometers, among many others such as bubble, slit and vibrational viscometers. Current commercially available capillary viscometers require volume samples of 1-10 ml, are bulky and require a measurement time on the scale of minutes. Many viscometers have complex designs and chambers in order to determine the viscosities of Newtonian and non-Newtonian fluids.

Capillary tube viscometers have been proven to be inexpensive, easy to use and construct, easy to maintain at a constant temperature and can compensate for the end facet and wall effects. These can be made to hold sample volumes of 1 ml or less, depending on the length and radii of the tubes. However the measurement of viscosity requires constant monitoring of the meniscus level. Micro-capillary viscometers have been fabricated and investigated for use in biomedical studies and for other liquids [119], but require CCD cameras to track the meniscus of the liquid as it travels through the channels. This arrangement requires 600 nL of liquid, with a measurement time on a scale of a few minutes. Other viscometers of the same type measure the viscosity of non-Newtonian fluids continuously, [118], but still require volumes in the mL range. Recently, a lab on chip viscometer has been published in literature with the ability to measure 30 nL samples [126].

In this thesis, HC-PCF are studied for use as a capillary viscometer. These fibres have the advantage that they do not require constant monitoring of the meniscus level by a CCD camera and they are capable of measuring viscosity of 10 nL samples of liquid, which has potential applications in medical diagnostics. They are chemically inert, and have the capability of being light weight and highly portable. This analysis shall be discussed in Chapters 3 and 4.

2.3 Determination of Viscosity

The theory that will be outlined in this section, is based on the Lucas-Washburn equation, which was applied by Nielsen et al [32, 127] to liquid flow within the capillary channels of HC-PCF. The Lucas-Washburn equation describes the time it takes for a liquid to flow through a capillary as being proportional to the square of the length of capillary segment [112], and is frequently used in capillary flow models [128, 129, 130, 131]. Other models which base their analysis on the rise of liquid by capillary action also demonstrate similar theoretical results to those derived from Lucas-Washburn [132, 133, 134]. The equation of Nielsen shall be examined further to extract useful information about the physical parameters of liquid viscosity and surface tension from the flow of liquid through the silica capillaries of the HC-PCF.

The analysis and mathematics are simplified by taking some basic assumptions in our model. First, the liquid flow is assumed to have a constant velocity, and does not take into account that the liquid begins to flow from rest ($v = 0$). Due to the average length of fibre (~ 10 cm) that is used in these experiments, the time taken for the liquid to accelerate from rest to its average velocity was negligible when compared to the total time taken to fill the capillary length.

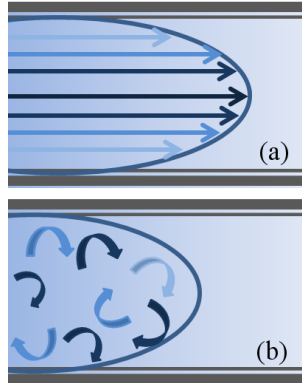


Figure 2.10: Schematic of (a) laminar and (b) turbulent flow in a capillary.

The flow is assumed to be laminar. The Reynolds number is a dimensionless coefficient that determines the state of liquid flow as it changes from laminar to turbulent (shown schematically in Figure 2.10 for laminar and turbulent flow in a capillary), as a ratio of inert to viscous forces. For liquid flow through the silica tubes, the ratio is calculated from the fluids physical parameters of density (ρ),

mean velocity (v) and dynamic viscosity (μ), and the capillary diameter (d).

$$Re = \frac{\rho v d}{\mu} \quad (2.9)$$

Values of the Reynolds number above 2000 define liquids that are in the transient process before turbulent flow (<4000). Values of flow below 2000 exhibit laminar flow. The fluids reported in this study always exhibit laminar flow. For water, the Reynolds number never exceeds 0.01 v , and this condition is similar for all other liquids studied in this thesis, resulting in laminar flow through the capillaries of the HC-PCF. To increase the Reynolds number, pressure could be applied to one end of the HC-PCF. In the experimental process outlined in this thesis, pressure was not applied, and the analysis of flow under this mode of operation can be neglected.

All liquids used in the experimental measurements are assumed to be Newtonian and have a constant viscosity (at constant temperature) that will not change upon the application of pressure or constraint to the liquid.

2.3.1 Description of Forces

Our model, as per Nielsen et al. [32] and Sreekantath et al. [135], considers the sum of all forces acting on the liquid inside the capillary to determine the flow profile. The summation of all forces, can be related to Newton's second law.

$$\sum \vec{F} = \frac{d(m\vec{v})}{dt} \quad (2.10)$$

Four main forces are considered to be acting on the liquid. The capillarity force (F_c) and the force due to pressure difference (F_P) between the two ends of the capillary encourages the flow of liquid into the capillary. The frictional force (F_f) of the walls and the gravitational force (F_g) act against the flow of the liquid through the capillaries. Each force acts in the \vec{z} direction, which is the direction of flow if the liquid.

$$\sum \vec{F} = \vec{F}_c + \vec{F}_g + \vec{F}_f + \vec{F}_P \quad (2.11)$$

The application of forces to the flow of liquid through the capillary is shown in Figure 2.11 for the vertical (a) and horizontal (b) configurations. In the vertical configuration, the forces due to pressure difference and capillary action are active in the positive \vec{z} direction, while the forces of gravity and friction are active in

the opposite \hat{z} direction. For the horizontal case, the gravity force changes to be active in the negative \hat{y} direction, and so this term is neglected when considering a horizontal capillary.

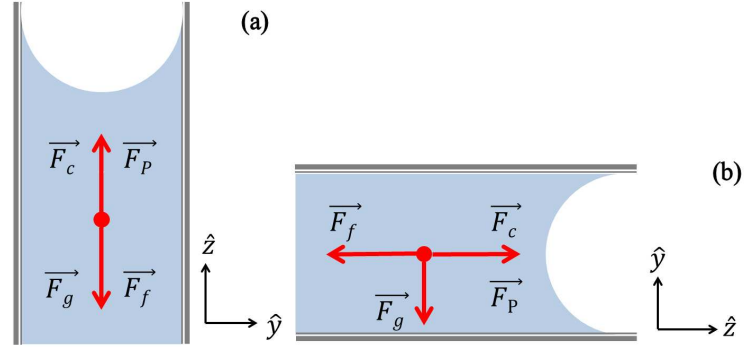


Figure 2.11: Schematic of the forces acting on the flow of liquid through a capillary in the (a) vertical and (b) horizontal configurations, with respect to the \hat{z} direction of liquid flow.

Herein, each of the forces are derived from first principles.

(i) Capillary Force

A liquid forms a contact angle with a solid surface, resulting from the inter-molecular interactions, and forces of adhesion and cohesion between the liquid and solid. The adhesive forces cause the liquid to spread along the solid surface, while cohesive forces within the liquid molecules cause the liquid to adopt a state of minimum contact with the surface. This is shown schematically in Figure 2.12. In this figure, the molecules of the liquid are shown as blue circles that are attracted by cohesive forces to the surrounding near molecules (red bonds) and are attracted to the solid capillary walls by adhesive forces (green bonds).

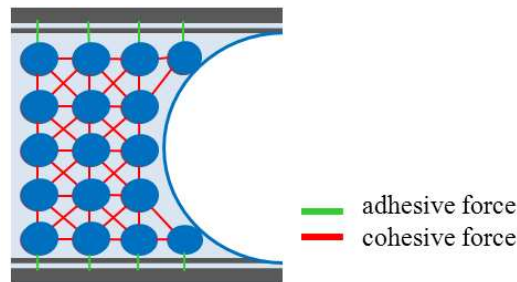


Figure 2.12: Schematic of the cohesive and adhesive forces acting between the molecules in the liquid and the walls of the capillary.

The glass used in the case of HC-PCF capillaries is a high energy surface, allowing liquids to adopt a small contact angle, which allows the surface to undergo wetting by the liquid. Depending on the value of the contact angle, the liquid can be drawn into the capillaries or pushed away from the capillary walls. A schematic of this is shown in Figure 2.13. In Figure 2.13 (a), the contact angle is $\theta < 90^\circ$, showing that the molecules are attracted by adhesive forces to the walls (green arrows in insert), and that the liquid flows up through the capillary by the phenomenon capillary action. In Figure 2.13 (b), $\theta > 90^\circ$, and the molecules are not attracted to the capillary walls, shown in the insert by the green arrows directed away from the walls. In this case, liquid is repelled from the capillary, and pushed away from the surface walls.

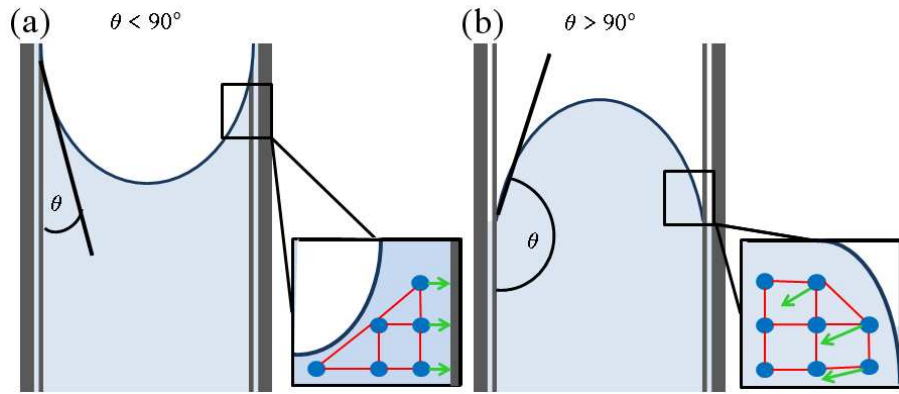


Figure 2.13: Schematic of the cohesion (red) and adhesion (green) forces in liquids for a contact angle $\theta < 90^\circ$ (a) and $\theta > 90^\circ$ (b).

From the capillary equation [136]

$$L = \frac{2\sigma \cos\theta}{\rho g R}, \quad (2.12)$$

where σ is surface tension of the liquid, θ is the contact angle between the capillary walls and the liquid, ρ is the density of the liquid, g is gravity, and R is the capillary radius. Multiply across by πR .

$$L\pi R = \frac{2\sigma \cos\theta}{\rho g R} \pi R \quad (2.13)$$

Let the volume for a cylinder be $V = \pi R^2 L$.

$$V\rho g = 2\pi R\sigma \cos\theta \quad (2.14)$$

Where, $F_c = V\rho g$. Introduce the term $\sigma' = \sigma \cos \theta$.

$$L\pi R = \frac{2\sigma'}{\rho g R} \pi R \quad (2.15)$$

(ii) Gravitational Force

Taken from Newton's second law, when a body is under the influence of the force of gravity only

$$F_g = mg = -\pi \rho g R^2 L(t) \quad (2.16)$$

for t = time, and where $m = \pi R^2 L \times \rho$, volume \times density.

(iii) Frictional Force

The flow of liquids within a circular capillary is described by the Poiseuille equation, which is dependent on the pressure difference between both ends of the capillary, the liquid's viscosity, and the inner radius of the capillary tube. This equation is valid for liquids undergoing laminar flow.

From Poiseuille's equation of flow:

$$\Delta P_P = \frac{8Q\mu L}{\pi R^4} \quad (2.17)$$

with the volumetric flow rate $Q = v(t)A$, where $v(t)$ is the velocity, and A is the cross sectional area. Pressure is a ratio of the magnitude of the force to the area its acts over, giving

$$\frac{F}{\pi R^2} = \frac{8v(t)A\mu L}{\pi R^4} \quad (2.18)$$

The cross sectional area of the cylinder is assumed to be that of a circle for simplicity, so that $A = \pi R^2$. Substituting this into the above equation gives:

$$F_f = -8\pi\mu L(t)v(t) \quad (2.19)$$

(iv) Pressure

From the definition of pressure described above, $\Delta P = \frac{F}{A}$, then:

$$F_P = \Delta P \pi R^2 \quad (2.20)$$

2.3.2 Derivation of the Liquid Velocity Equation

The above four forces are summed together using Newton's second law. Gravity is a negligible condition due to scale of radius considered when using a HC-PCF (which is less than 5×10^{-6} m), and thus the term can be removed from the sum. It is also negligible in the experiments that will be outlined, as the fibre was filled in the horizontal position. Thus the final relationship between the length of the capillary and time for filling is [32]

$$L(t)^2 = \frac{At}{B} + \frac{Ae^{-Bt}}{B^2} - \frac{A}{B^2} \quad (2.21)$$

where $A = 4\sigma\cos\theta/\rho R$ and $B = 8\mu/\rho R^2$. A full derivation of Equation (2.21) can be found in Appendix B. This relationship is seen in Figure 2.14, where the time required to fill a capillary of length L and of radius $5 \mu\text{m}$ is plotted. The liquid used in the theoretical plot is water with parameters of 1.002 mPa.s for viscosity, 1000 kg/m³ for density and 0.072 N/m for surface tension.

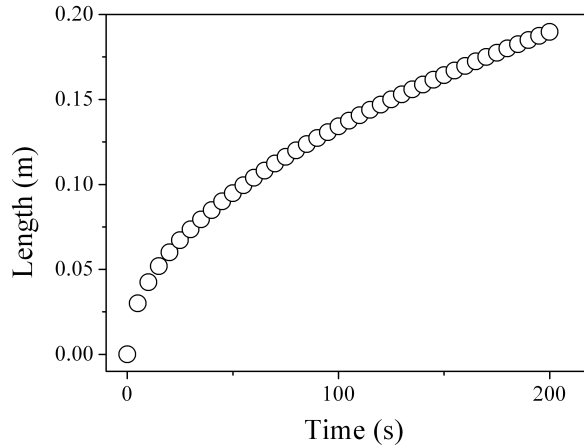


Figure 2.14: Nielsen's model of time taken to fill a length of capillary.

It is assumed that $e^{-Bt} \ll 1$, for values of B greater than 10,000, which is true when considering the dimensions of the capillaries and the parameters of the fluids that will be considered in this thesis. Equation (2.21) can now be solved

using a quadratic formula to give the result

$$\frac{A}{B} = \frac{L^2}{t} \quad (2.22)$$

Considering the constants A and B , defined earlier, the fraction gives the ratio of surface tension to viscosity

$$\frac{A}{B} = \frac{\sigma'R}{2\mu} \quad (2.23)$$

This allows the average velocity of the liquid flow through a length of capillary to be related to the viscosity of the fluid (μ), surface tension (σ), radius (R) and length (L) of the capillary, and the time (t) required to fill the capillary length.

$$v = \frac{L}{t} = \frac{\sigma'R}{2L\mu} \quad (2.24)$$

Equation (2.24) shall be used in the experiments to relate the average liquid velocity to the physical parameters of viscosity and surface tension to characterise liquid samples. The length of a HC-PCF segment can be measured to an accuracy of 0.5 mm, and experimentally the filling can be timed to an accuracy of 0.5 s to determine the average velocity of a liquid sample.

2.3.3 Estimating Viscosity from Liquid Velocity

To calculate the viscosity of the liquid samples, the ratio from Equation (2.24) needs to be separated into its individual components of surface tension and viscosity. This will allow the average velocity of liquid flow to be associated to a viscosity value. The value of the surface tension must be found separately to the velocity estimations. The surface tension of a liquid can be calculated by theoretical or experimental methods. For the purposes of this thesis, the surface tensions of all liquids were calculated theoretically.

The surface tension for common liquids such as water is precisely known for a wide range of temperatures and pressures. When using these liquids, the known value for surface tension can be used with Equation (2.24) and used to solve for the viscosity. When considering the surface tension of solutions, the complexity of the equation for the surface tension depends on the solute and solvent used. In general, the parameters of the solvent are known and available from literature, but the effect of adding a solute is not as well defined, but can be estimated. For the purposes of this thesis, a simple surface tension equation was used which

was valid for all liquid solutions considered. For simple saccharides dissolved in aqueous solutions the relationship between the concentration and surface tension is linear, and described by [137]:

$$\sigma' = (\sigma_w + \frac{\Delta\sigma}{\Delta C}C)\cos(\theta) \quad (2.25)$$

where σ_w is the surface tension for the solvent, C is the concentration of the solute, with a constant $\frac{\Delta\sigma}{\Delta C}$ ($\frac{Nm^{-1}}{M}$) for the solute, referring to the change in surface tension with respect to the change in concentration. To calculate the contact angle of the solvent meniscus with the capillary walls, the optical fibre viscometer system was calibrated with the solvent. Using $C = 0$, the value of σ_w from literature and the value of σ' found from Equation (2.24) is used in Equation (2.25) to find $\cos(\theta)$. This formula and contact angle are used to find all values of surface tensions for a range of solutions of different concentrations.

2.4 Raman Spectroscopy

When an electromagnetic wave is incident on a medium; a gas or a liquid, the presence of molecules in the medium results in scattering of the wave, caused by the induction of a dipole or a multipole moment in the molecule. In the majority of cases the scattering is elastic (Rayleigh scattering) where there is no change of energy to the wave from its interaction with the medium. Occasionally, the molecule will scatter light at a different frequency than the incident photon (Raman scatter), where a change in energy takes place in the wave and the medium. The generation of inelastic scatter, or Raman scatter, can be explained classically or by using quantum mechanics [138, 139, 140]. The Raman scatter is a weak process, with a photon conversion efficiency of 10^{-18} [141, 142]. After the scattering process, the emitted photons can have frequencies that are greater (anti-Stokes) or smaller (Stokes) than the initial frequency of the exciting light. The change in frequency of the emitted photons is based on a change in the vibrational energy levels of the molecule or atom. This provides information on the vibrational states of a molecule which are unique, based on the molecular structure.

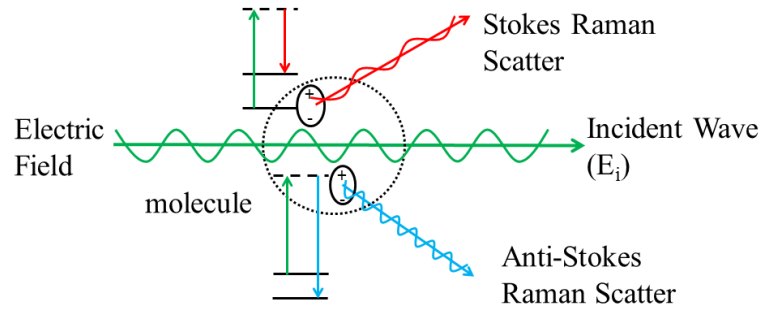


Figure 2.15: Elastic and inelastic scatter of electromagnetic radiation (green) from molecules. The inelastically scattered light is denoted as Stokes Raman (red) and Anti-Stokes Raman (blue).

2.4.1 Vibrational Raman Scattering Theory

A schematic of the Raman scatter process is shown in Figure 2.15. An electromagnetic wave is incident on a molecule (black dotted circle), which scatters light elastically and inelastically. The generation of Stokes Raman is shown in red, and the Anti-Stokes is shown in blue. The model describing Raman scatter assumes that a photon with initial energy $\hbar\omega$, excites a molecule to a virtual state, exchanging energy with the molecule in the process, and resulting in the scattered photon possessing less energy, leaving the molecule in a vibrationally excited state [143]. This process is called Stokes Raman scattering. If however, the molecule is already in a vibrationally excited state, the interaction with the incident photon will result in the molecule falling to a lower energy state, and increasing the energy of the photon, resulting in Anti-Stokes Raman scattering. This second process is generally weaker than Stokes Raman due to the decreased population of thermally excited vibrational states in comparison to the ground state.

The scattered light (of wavelength λ , in units nm) is generally defined by the wavenumber, $\tilde{\nu} = \lambda^{-1}$. Raman scatter is measured as a function of wavenumber shift $\Delta\tilde{\nu}$ (in units of cm^{-1}) from the incident wavelength, λ_0 (nm), to the shifted wavelength, λ (nm):

$$\Delta\tilde{\nu}(\text{cm}^{-1}) = \left(\frac{1}{\lambda_0(\text{nm})} - \frac{1}{\lambda(\text{nm})} \right) 10^7 \quad (2.26)$$

Raman scatter, known as Raman lines, are observed at energy shifts corresponding to vibrational states of the scattering molecules. The spectra of vibrational states is unique to each molecule, depending on its structure and symmetry and can be used for the identification of the molecular species [144]. This fact is used

in Chapters 6 and 7. Spectra are generally plotted for the wavenumber shift, in units of cm^{-1} , as seen in all spectra contained in this thesis.

A classical theory of Raman scatter concerns the polarisability, α , of a molecule, under the influence of a harmonically changing external electromagnetic field. The electric field strength of an electromagnetic wave fluctuates with time, $E = E_o \cos(2\pi\nu_o t)$, inducing a time dependent electric dipole moment.

$$\vec{P}(t) = \alpha \vec{E}(t) = \alpha E_o \cos(2\pi\nu_o t) \quad (2.27)$$

The nuclear displacement of the molecule vibrating with a frequency ν_m can be described by $q = q_o \cos(2\pi\nu_m t)$. Assuming small displacements, the polarisability can be expanded using Taylor's polynomial:

$$\alpha = \alpha_o + \left(\frac{\partial\alpha}{\partial q}\right)_o dq_o + \dots \quad (2.28)$$

This results in a classical approximation of the induced electric dipole moment:

$$\vec{P} = \alpha_o E_o \cos(2\pi\nu_o t) + \left(\frac{\partial\alpha}{\partial q_o} \frac{q_o E_o}{2}\right) \{ \cos[2\pi(\nu_o - \nu_m)t] + \cos[2\pi(\nu_o + \nu_m)t] \} \quad (2.29)$$

[138] where the first term on the right hand side describes the elastic scatter, the second term describes the time dependence of the inelastic Stokes Raman, and the third term describes the time dependence of the inelastic Anti-Stokes Raman. These equations are a classical treatment of Raman scattering, and do not specify the probability of occurrence for Stokes Raman or anti-Stokes Raman. When a quantum approach is used to determine the occurrence of the phenomenon of Raman scattering, the probability of Stokes Raman scattering is much higher than anti-Stokes Raman scattering, due to the fact that statistically, a larger number of molecules will inhabit the ground state, for Stokes Raman, while a lower number will inhabit an excited state for anti-Stokes Raman.

The intensity of the scattered light depends on the population of vibrational ground states, the intensity of the incident radiation and the dependence of the polarisability components on nuclear displacements. From scattering theory the intensity of the scattered electromagnetic wave is proportional to the polarisability, α of the molecule and the wavelength, λ , as defined in the equation:

$$I = \frac{I_0 8\pi^4 \alpha^4}{\lambda^4 r^2} (1 + \cos^2(\phi)) \quad (2.30)$$

Where, r is the radius of the molecule, I is the intensity of the scattered wave, I_0 is the intensity of the incoming wave, and ϕ is the angle between the incident and scattered light wave. The classical theory exhibits a λ^{-4} dependence of the scattering intensity.

2.4.2 Liquid Core Fibre for Raman Scatter Collection

The collection of the weak signal of Raman scatter in liquids or gases can be greatly enhanced, by employing a hollow core optical fibre to increase the interaction length, in comparison to measurements with standard set-ups, for example cuvettes. Samples can be placed within hollow core optical fibre waveguides filled with liquid, which can guide light over a long length by the mechanism of index guiding. This increases the sample volume over which Raman signal can be generated and collected. These types of waveguides were first fabricated in 1972 by Walrafen [145] and used by Schwab and McCreery [146] for Raman spectroscopy to generate a 3000 time relative enhancement in Raman signal compared to standard cuvette methods. The waveguides feature a hollow centre that could be liquid filled and allowed the propagation of pump light by total internal reflection along the core. Initially, materials such as fused quartz were used, which has a high refractive index (1.493), restricting the liquids that could be used and resulting in lossy propagation.

Due to the limitations of the high refractive index of glass, other polymers, such as amorphous fluoropolymers were investigated for their use as low refractive index capillary tubes. This resulted in the use of Teflon AF 2400 for the manufacture of capillary tubes with a hollow core in the range of μm with a refractive index of 1.29 [147]. However, these waveguides exhibit higher loss than their silica counterparts. A more optimal choice for Raman signal collection with liquid core fibres, is a liquid filled HC-PCF.

2.4.3 Raman Scatter Collection with Hollow Core Photonic Crystal Fibre

Since their conception, HC-PCFs have been proposed as optimum devices for enhanced optical sensing, and have been applied to the area of Raman spectroscopy in recent years [103, 148, 149, 150, 151]. HC-PCF can enhance the collection of Raman scatter, due to their guidance properties [103, 152], fabrication and surface

preparation. A number of fibre types have been investigated for this principle, such as micro-structured fibre and fibres that have been chemically prepared with nano-particles for surface enhanced Raman spectroscopy. The focus of this review are HC-PCFs. The principle of Raman collection in core filled only fibres is similar to the liquid core fibres discussed previously. When the HC-PCF are prepared, such that only the core is liquid filled, and the surrounding capillaries remain air filled, the numerical aperture and collection angle is greatly increased, thus increasing the collection of Raman scatter within the liquid core.

The introduction of liquids to the core of HC-PCF allows a wide range of liquids to be investigated [153]. Selectively filling the core of the HC-PCF and allowing the micro-structure to remain unfilled can enhance the Raman signal by 100 times [150, 154]. Liquid is selectively infiltrated to the core only by collapsing the micro-structure cladding of one end-facet of the HC-PCF, closing access to the capillaries and allowing liquid to fill the core, as reported in the literature [154]. Light is focused into the uncollapsed end and the Raman backscatter is collected from the infiltrated liquid sample. Other set-ups have collapsed both ends of fibre to ensure uniform filling inside the core. This leads to a decrease in the intensity of guided light emitted from the fibre, due to the effect of collapsing the external capillaries and altering the otherwise uniform micro-structure at the end point of the HC-PCF [155]. Due to the advantages of using liquid core fibres for enhanced sensing, they have been utilised widely in fluorescence [156] and Raman [147] measurements.

The Raman signal obtained from liquid samples can be further enhanced by the addition of metal colloidal structures to the liquid analyte and to the silica walls of the HC-PCF. To add these metal surfaces to the core of LC-PCF, noble metal nano particles were employed to enhance the Raman signal [150, 151, 154]. These particles are mixed in with the solution to be investigated, which typically contains DNA, hemoglobin or protein [157]. Nano particles have many properties that can be utilised for sensing and can also be used for fluorescence labelling [158].

For a hollow optical fibre, the Raman signal that can be expected to be generated over the length is estimated by:

$$I_R \propto I_L \sigma_s D \Omega_0 L \quad (2.31)$$

where I_R is the intensity of the spontaneous Raman signal, I_L is the intensity

of the pump laser coupled to the fibre, σ_s is the Raman cross section of the molecule, D is the number density of the sample, Ω_0 is the solid angle over which the Raman signal can be collected from inside the capillary fibre and L is the length of the fibre over which Raman signal is collected. This equation gives an estimation of Raman signal in the forward scattering direction. However, the attenuation and absorption of the pump laser through the medium must also be taken into account. The pump laser should decay as $I_L e^{-\alpha_L}$, where α_L is the loss coefficient and in this case not only takes into account the absorption of the liquid, but also the residual loss of light to the silica capillaries of the fibre, for a given wavelength: $\alpha_L = \alpha_{liquid}(\lambda) + \alpha_{fibre}(\lambda)$. The enhancement factor for Raman scatter collection for a variety of configurations, such as forward and back-scattering signal collection is derived and outlined in Altkorn et al. [159]. This paper describes in detail the equations of most efficient length for liquid core fibres, and the confinement of light within the channel.

There are two parameters to consider when tailoring a fibre for its collection efficiency, its numerical aperture (NA) and its internal diameter (d). The internal diameter determines the volume of sample per unit length that can be contained within the fibre. It also determines the guidance properties of the fibre. The numerical aperture is a function of the difference in the refractive index of the core and cladding of the fibre, and is associated with the solid angle (steradian) of scattered Raman signal that the fibre will collect. This relationship is therefore:

$$\Omega \cong \pi(NA)^2 = \pi(n_{core}^2 - n_{cladding}^2) \quad (2.32)$$

The critical angle which defines the solid angle about which Raman scattered light can be collected within a liquid core fibre is estimated by the refractive index change between the core and the cladding, denoted by Δn .

$$\theta_c \approx \sqrt{\frac{2\Delta n}{n_{liquid}}} \text{radians} \quad (2.33)$$

where n_{liquid} is the refractive index of the liquid. From Equation (2.33) it can be assumed that the greater the difference in refractive index between the core and the cladding, the greater the collection angle of Raman scatter within the liquid core. The schematic of the solid angle collection within a unit sphere is shown in Figure 2.16. From the figure, it is apparent that the steradian can have a value between $0 \leq \Omega \leq 4\pi$.

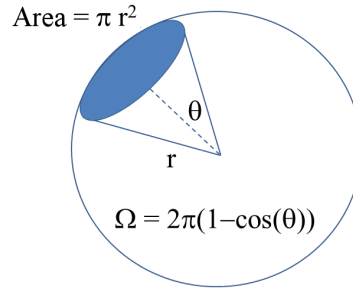


Figure 2.16: Diagram demonstrating the definition of a steradian of radius r and area πr^2 .

The solid angle of Raman scatter in the cone that the fibre can collect, is determined using the equation

$$\Omega = \int \int_S \sin\theta d\theta d\vartheta \quad (2.34)$$

for a cone of signal, with an numerical aperture of $n_{air} \sin\theta$, the solid angle guided by the optical waveguide is $\Omega = 2\pi(1 - \cos\theta)$ (Figure 2.16). Applying this theory to the liquid core fibre, the area over which the collection of Raman scatter can occur is shown in Figure 2.17.

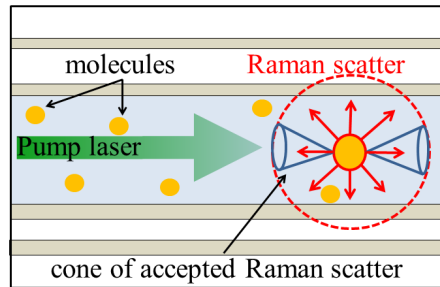


Figure 2.17: Schematic of Raman generation within a liquid filled HC-PCF. The green pump laser (originating from the left) is incident on the molecules (yellow circles) within the fibre and generates spontaneous Raman scatter that is isotropic (shown in red). Scatter that falls within the cone of collection (shown in blue), specified by the numerical aperture of the fibre, or the PBG can be propagated to the end facet points of the HC-PCF.

To consider the collection of Raman signal within the length of the cylinder, the amount of isotropically scattered light that can be collected at each small length segment of the cylinder, due to the numerical aperture of the fibre must be considered. The intensity of Raman signal collected with respect to length is expressed by:

$$I_R = \frac{I_L \sigma_s \Delta L}{\pi r^2} \quad (2.35)$$

where I_R is the intensity of the collected Raman scatter, I_L is the intensity of the

pump laser incident on the sample at a certain length inside the cylinder fibre, r is the radius of the fibre, σ_s is the Raman scatter cross section coefficient and is dependent on the molecule, and ΔL is the illuminated length. This is divided by the area of the hollow cylinder, to determine the intensity of the collected Raman scatter per unit area. This equation determines the efficiency of the forward scattering Raman collection configuration.

For HC-PCF which are collapsed at one end to facilitate core only filling, thus resulting in a change in the guidance properties at this point, collecting Raman signal in a back scattering system may result in better collection efficiency. Therefore the optimum length for collection in the backward scattering direction is determined to be [159]:

$$I_R = \frac{I_L K}{2\alpha_s} (1 - e^{-2\alpha_s L}) \quad (2.36)$$

where, I_R is the Raman intensity measured from the fibre, I_L is the intensity of the pump laser, α_s is the loss of the system, due to the absorbance of the liquid in the fibre core, and the loss of the fibre and L is the fibre length. The constant K is a function of the Raman cross section, the numerical aperture of the liquid core fibre and the number of Raman active molecules per unit volume. The most practical length can be estimated to be $0.5/\alpha_s$, by considering Equation (2.36), for the value of $L = 2\alpha_s$ [159]. This is the length of lossless fibre that will give the same signal generation as an infinite length of lossy fibre considered for Raman scattering collection. The maximum Raman intensity that can be obtained by a liquid core fibre is $I_{Rmax} = I_L K / 2\alpha_s$, as the value of $2\alpha_s L$ goes to infinity. This shall be used in Chapter 7, to determine the practical length of fibre for Raman scatter collection.

2.5 Summary

This chapter covers the theoretical background information that is required for the subsequent experimental chapters in this thesis. The first part covered the PBG effect in HC-PCF, and gave a schematic description of how the guidance changes once liquids are introduced to the interior of the fibre. The important literature that details the development of HC-PCF theoretically and experimentally is referred to. The next section described the viscosity of liquids, and the importance of the determination of this parameter in industry and medical di-

agnostics. An extensive review of capillary viscometers available commercially, and current research in the development of nano litre capillary viscometers is presented. A filling model for capillary flow in HC-PCF was derived to determine the velocity from liquid flow. Subsequently the determination of a liquids viscosity from the flow velocity was shown and derived. The final section discussed Raman spectroscopy and the use of liquid filled fibres to enhance the collection of the isotropic scatter of Raman signal from liquids. The recent developments of using HC-PCF for Raman signal collection is reviewed and described in detail for a backscattering collection configuration.

Chapter 3

Microscope Analysis of Liquid Filling Capillaries

This chapter will analyse the filling of the capillaries contained within the micro-structure of a hollow core photonic crystal fibre (HC-PCF), using a microscope to continually monitor one end-facet.

In Section 2.3.2, a capillary filling model, based on the Lucas-Washburn equation, was presented. The model was solved to estimate the time for a liquid, with density (ρ), viscosity (μ) and surface tension (σ), to fill a capillary with dimension of length (L) and radius (R). The model can be applied to the capillaries of HC-PCF to estimate the average filling velocity, by measuring the filling time and fibre length. The advantage of using HC-PCF are the small volumes of sample required and quick filling times. This information can subsequently be used to determine its viscosity.

To test this model using segments of HC-PCF, a microscope was used to monitor one of the end facets of short fibre segments (< 10 cm), while the other end was dipped into a beaker with the liquid under test, and the time required to fill the capillaries was recorded. This chapter presents the experimental set-up and results observed with water and propan-1-ol. These samples feature different molecular chemistries that are expected to affect the filling results differently in both cases, due to presence of SiO^- defects in the silica composition of the capillary walls.

3.1 Experimental Set-up

An optical microscope (Nikon Eclipse ME600) shown in Figure 3.1 (a), was used to image the end-face of HC-PCF segments using a $\times 50$ objective and $\times 10$ eyepiece. The fibre was positioned vertically under the objective using a specially machined receptacle that was designed to hold a fibre clamp (purchased from Fujikura, with a $150\text{ }\mu\text{m}$ channel, FH - 40 - 150) securely on the microscope stage, as shown in Figure 3.1 (b). The HC-PCF segment was then placed in the fibre clamp, which secured the fibre and enabled the end-facet to remain in position at the focal point of the microscope objective throughout the measurement. The other end of the HC-PCF was able to hang freely, to facilitate the introduction of liquids to the capillaries.

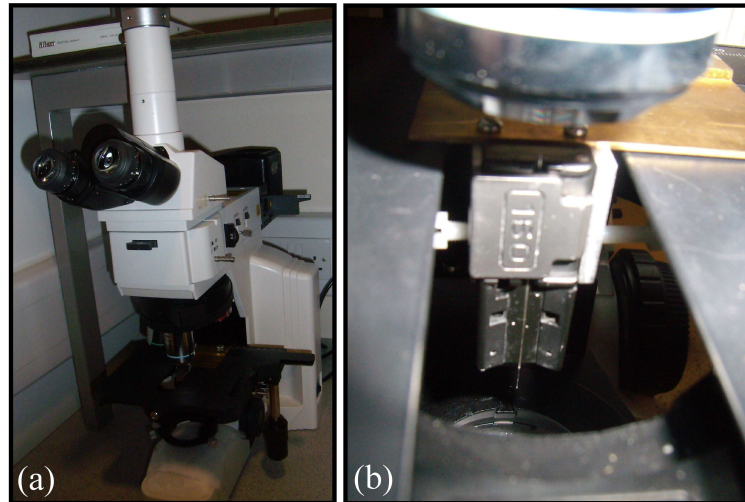


Figure 3.1: Image of the Nikon Eclipse ME600 (a) used to view the end-facet of HC-PCF, featuring a close up in (b) of the microscope stage and the fibre within a fibre clamp, positioned vertically under the objective. Liquid was introduced to the free end of the fibre to determine the HC-PCF filling dynamics.

The fibre segments were prepared by removing 2 cm of the acrylate coating material from both ends of the HC-PCF segment using a Fujikura jacket stripper HJS - 02 - 80. Both ends were then cleaved using a Fujikura high precision fibre cleaver (CT-32), and inspected for quality and possible contamination before measurements. This ensured that the capillaries were not blocked by residual particles from handling the fibre during the preparation process. The interior surface of the capillaries was not prepared chemically before the insertion of liquids.

3.1.1 Fibre Specifications

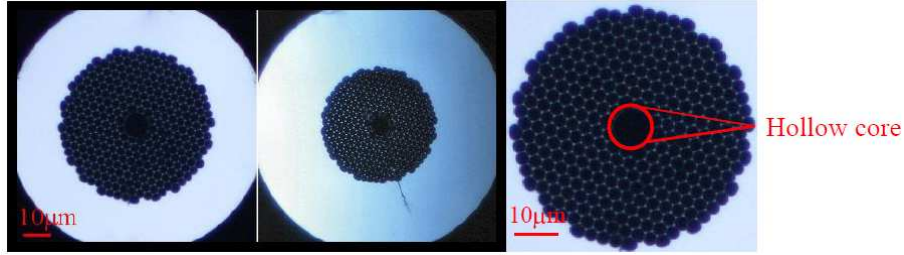


Figure 3.2: Images taken with the Nikon Eclipse ME600 microscope of the end facets of a HC 1550 (left) and HC 1060 (middle). A schematic showing the selection of the fibre core to determine the radius is shown on the right.

Two examples of HC-PCF were considered to test the optical fibre viscometer. These were the HC-1060 and HC-1550 fabricated by and purchased from NKT Photonics A/S, Denmark. These fibres are depicted in Figure 3.2 and the specifications are outlined in Table 3.1, and in Appendix C. Both of these fibres feature a core diameter within the micrometer scale, surrounded by a micro-structure of capillaries. These fibres have two different primary bandgaps (1060 and 1550 nm respectively), however this should not affect the microscope analysis of the filling dynamics, as this relies only on the reflection of light from the end facet of the fibre when the capillaries are filled.

Table 3.1: Specifications for HC-1060 and HC-1550.

| Type | Wavelength | HC Diameter | Cladding Diameter | NA |
|---------------|------------|------------------|-------------------|------------|
| HC-1060 [160] | 1060 nm | 10 μm | 50 μm | ~ 0.2 |
| HC-1550 [161] | 1550 nm | 11 μm | 70 μm | ~ 0.2 |

3.1.2 Radius Estimation

The fabrication process to draw HC-PCF, is known to result in fluctuations in the radius of the fibres core radius. The actual radius of the fibre may differ from that given in the data sheet [160, 161], over the drawn fibre length. The core is not perfectly circular, instead it is constructed by the removal of seven silica rods, resulting in the formation of a twelve sided unsymmetrical dodecagon. For this reason, the diameter and error of the fibre core is estimated by analysing the end facet cross sections of thirty seven microscope images of HC-1060, using a software package (NIS Elements BR 3.0). The microscope software was calibrated to provide accurate measurements of the core radius. To measure the radius, the

HC-1060 hollow core was fitted by the software with a circle, which calculated the radius.

The mean radius (μ_{mean}) for all images was estimated to be $4.61 \mu\text{m}$, with a standard deviation (σ_{dev}) calculated to be

$$\sigma_{dev} = \sqrt{\frac{\sum_{i=1}^N (x_i - \mu_{mean})^2}{N}} = 0.17 \mu\text{m} \quad (3.1)$$

where x_i is the value of each individual radius, and N is the number of radii values. The estimated values of the radius were fitted to a Gaussian distribution with equation

$$F(x; \mu_{mean}, \sigma_{dev}^2) = \frac{1}{\sqrt{2\pi\sigma_{dev}^2}} e^{-\frac{1}{2} \frac{(x-\mu)^2}{\sigma_{dev}^2}} \quad (3.2)$$

and the distribution is shown in Figure 3.3. The red circles are data points for the radius estimated by the microscope software, and the red dashed line is the Gaussian fit for Equation (3.2), with the dashed black vertical lines indicating the σ_{dev} (68 % of the data set) and $2\sigma_{dev}$ (95 % of the data set) error. All values for the estimated radius fall within $2\sigma_{dev}$ of the mean, with an error of $\pm 0.34 \mu\text{m}$. Taking into account the uncertainty associated with the core shape of the HC-PCF not being ideally circular in practice, the estimation of the error for the fibre radius was assumed to be $\pm 0.5 \mu\text{m}$.

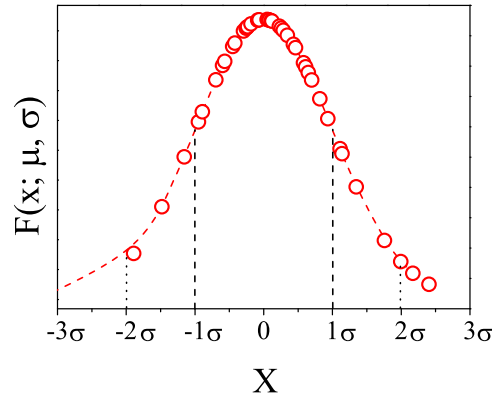


Figure 3.3: Normalised Gaussian distribution of the radius measurements for HC-1060, with a mean of $\mu_{mean} = 4.62 \mu\text{m}$ and standard deviation of $\sigma_{dev} = 0.17 \mu\text{m}$.

3.2 Images of the Capillary Filling

The microscope images of the filling pattern were used to predict the dynamic optical guidance properties of the HC-PCF, over the time period of its filling. The images of the HC-PCF end-face were captured by the Nikon microscope camera, collected using a Nikon Digital Sight DSU2 and viewed using Nikon Elements BR 3.0. The filling of the capillaries was recorded by capturing the images at a rate of 5 frames/s. To perform the timing measurement, the image path to the camera was blocked until the end of the fibre was inserted into the water. The image was then unblocked and a sequence of images was captured by the program. A capillary was deemed to be filled when the image of a capillary changed from dark to bright, indicating the reflection of the focused microscope light from the surface of the liquid.

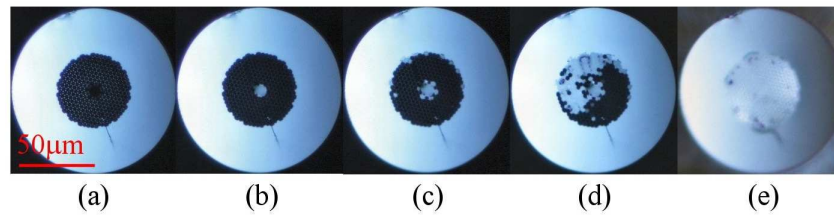


Figure 3.4: Images showing dynamic filling of a 6 cm HC-PCF (HC-1060) with water. (a) 0 s (b) 104 s (c) 111 s (d) 134 s (e) 174 s.

A sequential set of microscope images is displayed in Figure 3.4 which depict the filling process observed for a 6 cm HC-1060. The first image displays the cross section of an empty HC-1060, before filling with a liquid. Distilled water was then introduced to the opposite end of this fibre segment (not shown here). The second image shows the core filled with a liquid, while the surrounding capillaries remain empty. The core of the fibre always fills faster, as it has a larger radius. The capillaries surrounding the core of the fibre usually fill first, once the core has filled. Subsequently the rest of the capillaries in the cladding fill in an arbitrary fashion. The remaining images show the filling of the capillaries at different time stages.

This pattern could also be seen using a 4.4 cm HC-1550. A sequential set of images for HC-1550 filling with distilled water is shown in Figure 3.5. The results are similar to the HC-1060 and it is expected that all fibre segments will fill in this pattern, depending on cleave quality and the liquid used.

To characterise the response of the sensor to filling, samples of different lengths

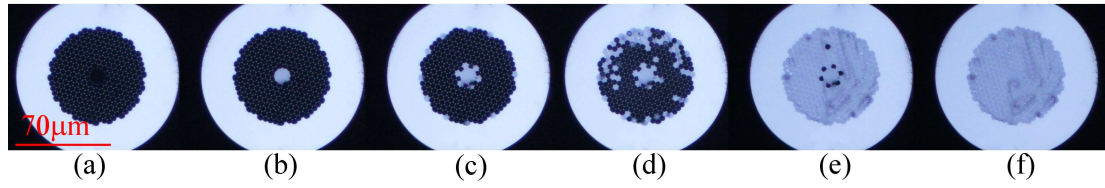


Figure 3.5: Images showing the dynamic filling of a 4.4 cm HC-1550 with water.
(a) 0 s (b) 4 s (c) 25 s (d) 27 s (e) 30 s (f) 49 s.

were tested and compared to our filling model. These experiments shall be detailed in the following sections.

3.3 Characterisation of Capillaries Filling with Water

Water was chosen as the test liquid, as it is a common solvent in industry applications due to its attractive polar properties and its ability to form hydrogen bonds. It is also ubiquitous in the life sciences and biomedical fluids. For this reason, the physical properties of water and solutions of alcohols and other solutes in water have been extensively studied with many results available in literature. Therefore there is a broad depth of literature that the results obtained in this thesis can be compared against. This is discussed in detail in Chapter 4.

In Section 3.2, it was shown that using the microscope, it was possible to observe the end facet of the fibre, showing that the core fills first each time, followed by the capillaries of the micro-structure in a sequence pattern depending on the capillary radius and cleave quality of the end-facet. For these measurements, there are two reference points for timing the filling; the point where the liquid is inserted to the capillaries, and the point where the end facet under observation by the microscope fills. The error associated with the timing measurements is large due to the ambiguity of the start point which is not monitored by the microscope directly, but instead relied on human efficiency and response time, resulting in an error of ± 1 s. The microscope software recorded 5 frames per second of the fibres end facet, resulting in an error for the determination of the filling of the capillaries of ± 0.2 s. The error in timing is more prevalent for shorter fibre lengths, of 4 cm or less, where the error in time can attribute to a 8 % systematic error. As a result of this, all error associated with each measurement in the following section is displayed on the y-axis, and the error bar on the x-axis is too small to be seen at the scales chosen (error for length measurements is ± 0.05 mm).

3.3.1 First Filling Results

A range of HC-1550 fibre lengths from 2 - 6 cm were timed while filling with distilled water. This data (red squares) is displayed in Figure 3.6 where the length of the fibre segment used is plotted on the x-axis and the time taken to fill the core only is plotted on the y-axis. This figure also includes the theoretical model from Eq. (2.24) represented by the black line. This model was calculated for water and HC-1550 using data available for water ($\mu = 0.001002$ Pa.s, $\sigma = 0.072$ N/m, $\rho = 1000$ kg/m³, $R = 5.5 \pm 0.5$ μ m).

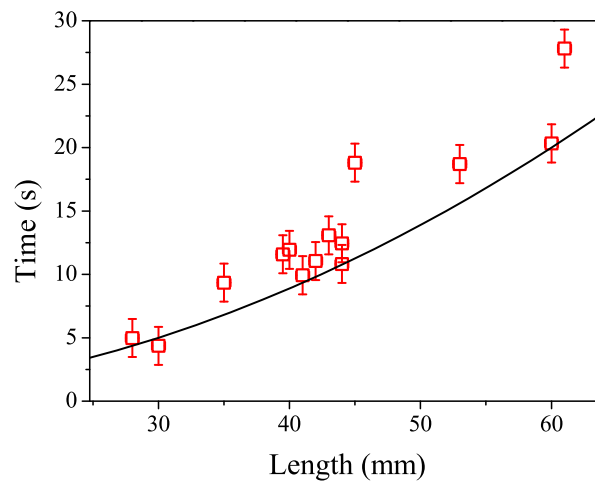


Figure 3.6: First filling times of 2 - 6 cm lengths of empty HC-1550, compared to the theoretical model (black line).

Figure 3.6 shows that the experimental data did not trend with the model proposed in Chapter 2. The experimental results show consistently longer filling times and there is a large fluctuation of results from the theoretical model [162]. This deviation from the expected results can be explained with several experimental uncertainties and non-optimal experimental design. The contact angle used for the model, between the capillary walls and the meniscus of the water was assumed to be 0° . This assumption may be incorrect and will be investigated further in Section 3.3.3. Furthermore, the experiments were not carefully insulated from fluctuations in temperature, which can cause additional measurement error. The microscope objective focuses light on the fibres tip, and generates heat at this point which will decay over the fibres length, resulting in temperature gradients and hence in a change in the liquid flow velocity. Viscosity is a temperature sensitive parameter, that can easily fluctuate, and generally increases exponentially with decreasing temperature [111].

3.3.2 Second and Subsequent Filling Results

After the initial filling measurements, the water was removed from the fibres using a clean syringe and plastic connectors. By pushing air at a pressure of 137 kPa (1.37 atm) to one end of the fibre via the syringe, water was pushed out of the capillaries. The syringe was not sealed to the fibre, and therefore the majority of the air escaped, however, enough air was pushed through the capillaries to remove the water, without damaging the internal micro-structure. The fibres were subsequently refilled in a similar fashion to that previously described, and timed using the microscope.

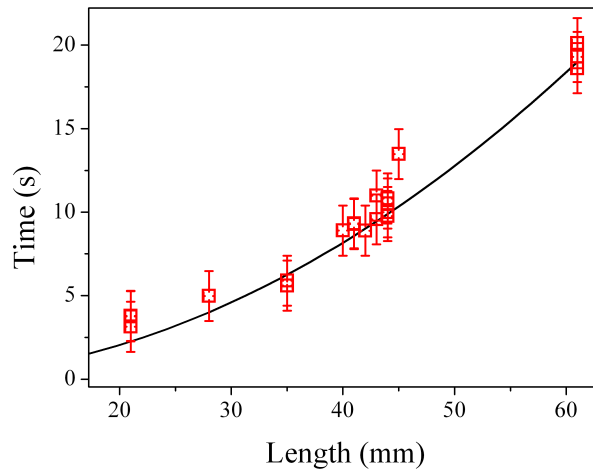


Figure 3.7: Second filling times of 2 - 6 cm HC-1550, compared to the theoretical model (black line).

The results (red squares) for the second filling are displayed in Figure 3.7, and are compared to the theoretical model (black line). The fluctuations in the time measurements were reduced, in comparison to Figure 3.6, where the results trend to the predictions of the model, with respect to experimental error and temperature fluctuations. These measurements did not include temperature control or make any attempt to protect the fibre from external temperature changes. Therefore, the improvements indicate that the initial filling changes the contact angle of the meniscus to the internal capillary walls, approaching 0° . One explanation may be attributed to a change in the surface chemistry of the silica after pre-filling, which is discussed further in Section 3.3.4.

Subsequent fillings of the same fibre segment were carried out to understand and estimate an optimum sequence of fillings (Figure 3.8). For the same segment of fibre, the filling times became shorter getting closer to the estimations of the capillary model. This is usually evident after 2 - 3 fillings. This theory was tested

extensively for two fibre samples, both of length $\sim 4.3 \pm 0.1$ cm. Each segment was filled over ten times, and the results are depicted in Figure 3.8. Clearly in both cases and within experimental error, the filling times (red squares) approached the model estimation (black line) by increasing the number of fillings. Neither of the samples were protected from temperature fluctuations. It can be concluded that when filling the fibre with water, in order to ensure that the contact angle between the meniscus and silica wall is close to 0° , the fibre walls should be pre-wetted with a film of liquid. The implications of this change in surface are discussed further in Section 3.3.3 and Section 3.3.4.

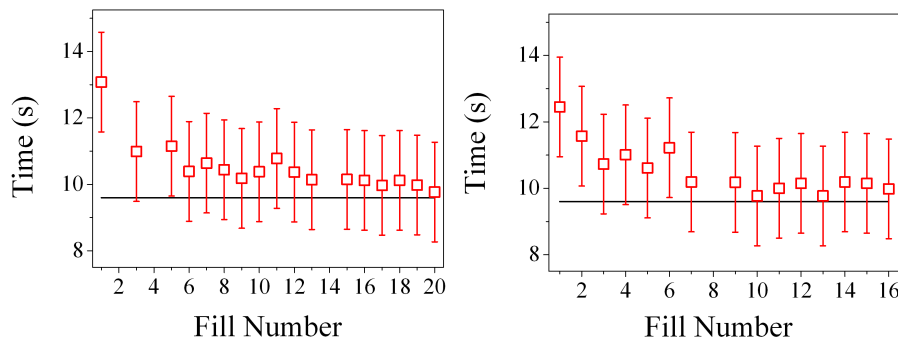


Figure 3.8: Time plotted against the number of fillings, for multiple fillings of two HC-1550 fibre segments 4.3 ± 0.1 cm with distilled water, timed by the microscope method.

3.3.3 Contact Angle Estimation

The estimations for the first filling times described previously assumed that the contact angle between the silica walls and the meniscus of water was 0° . While this can be assumed for the pre-filled fibres that have a thin film of wetting layer on the silica walls, this cannot be assumed for the dry fibres. From the graphs in Figure 3.8 and the results in Figure 3.7, it is clear that the assumption that the contact angle is 0° is a good approximation for capillaries that have been filled at least three times. The assumption however does not hold for a dry silica surface.

At 20° Celsius, it is known that the viscosity of water is 1.002 mPa.s, hence the time measurement and the viscosity value can be used to estimate the contact angle. A series of results is shown in Table 3.2, where the contact angle is estimated to vary from 22 to 56° , with an average of 39° . This is assumed by comparing $\cos(\theta) = (\text{viscosity water})/(\text{measured viscosity})$ for dry fibre samples. Note that the large differences may also be associated with a change in viscosity due to temperature variations, particularly for filling longer fibre lengths. A 1°

Celsius variation in temperature can induce a change in viscosity of 0.02 mPa.s, which would result in an over/under estimation in θ by $\pm 3^\circ$.

Table 3.2: Data for initial fillings of HC-1550 with distilled water.

| Water Room temp. | Length (m) | Time (s) | Velocity (m s ⁻¹) | Viscosity (mPa.s) | cos θ |
|---------------------|---------------|-------------|----------------------------------|----------------------|------------------------|
| | 0.045 | 18.81 | 0.00239 | 1.79 | 56° |
| | 0.061 | 27.81 | 0.00219 | 1.45 | 46° |
| | 0.053 | 18.7 | 0.00283 | 1.29 | 39° |
| | 0.028 | 4.98 | 0.00562 | 1.23 | 36° |
| | 0.040 | 11.94 | 0.00335 | 1.44 | 46° |
| | 0.039 | 11.58 | 0.00344 | 1.44 | 46° |
| | 0.043 | 13.08 | 0.00329 | 1.37 | 43° |
| | 0.044 | 12.45 | 0.00353 | 1.24 | 37° |
| | 0.041 | 9.93 | 0.00413 | 1.14 | 29° |
| | 0.044 | 10.82 | 0.00407 | 1.08 | 22° |
| | 0.060 | 20.33 | 0.00295 | 1.09 | 24° |
| | 0.035 | 9.35 | 0.00374 | 1.48 | 47° |
| | 0.042 | 11.05 | 0.00381 | 1.21 | 34° |
| | | | | | Average θ : 39° |

Different liquids can be expected to have a different contact angles, and therefore a calibration of the sensor with the liquid of interest must be performed before viscosity tests. However in this thesis, the majority of liquids of interest are water-based and therefore, this analysis needs only to be performed once for aqueous solutions.

3.3.4 Surface Analysis of the Silica Capillaries

The surface structure and composition of the internal walls of the fibre have a strong influence on the filling delay. The silica structure can be described like a crystal [163], and consists of a regular four ring pattern, with three ring defects, due to the fabrication process [164, 165]. The three ring defect results in a hanging bond, O_2^- [166, 167], and thus makes the surface of the capillaries hydro-phillic. The presence of the defects is seen in the Raman spectra of the silica. In Section 7.1.2, the Raman spectra of silica is shown, as a broad vibration from $\sim 250 - 550 \text{ cm}^{-1}$. This broad vibration is due to the silica structure. There also exists a sharp vibrational band at 550 cm^{-1} , which is though to be due to the three ring silica defect [164].

The defects encourage the flow of water through the capillaries, but also slows it

initially, as the dry silica wall undergoes a bonding process with the silica defects and the OH water bonds. However once these bonds have been made, they are not broken by the syringe drying method, possibly due to the low pressure used to extract the liquid with the syringe. After the first filling, the interior walls of the fibre are left with a residual thin film of water. Thus future fillings undergo less resistance as the liquid travels through the capillaries. Over multiple fillings, the capillary surface accumulates a complete wetting film, resulting in a reduction in fill times that trend with the capillary viscosity model. Therefore repeat fillings result in a change in contact angle between the meniscus of the liquid and the capillary walls.

When liquids are used to fill the fibres that do not contain polar bonds, the hydro-philic nature and hence long initial filling times are expected to not be present. To verify this analysis, fibres are filled repeatedly with propan-1-ol and the results described in the following section.

3.4 Capillary Filling with Propan-1-ol

Propan-1-ol ($\text{CH}_3\text{CH}_2\text{CH}_2\text{OH}$) is a primary alcohol, meaning that the OH hydroxyl group is attached to a carbon atom. To test the fibres response to an alcohol, lengths of HC-1550 were filled with pure propan-1-ol. Prior to measurements, the propan-1-ol underwent filtration to remove impurities. The filling was timed using the microscope method as outlined previously.

Figure 3.9 shows the results of four different segments of HC-1550 filled repeatedly with propan-1-ol. Within experimental error all results trend to estimated values from the model with $\mu = 0.00196$ Pa.s, $\sigma = 0.026$ N/m, $\rho = 785$ kg/m³, $\theta = 0^\circ$, as described in Section 2.3.2. The black line is the expected filling time estimated by the model and the red squares are the data points with associated 1.5 s error. The time for the first filling of propan-1-ol tends to be too long or too short by a range of ± 1.5 s. This discrepancy in times was due to temperature fluctuations in the fibre, and temperature affects from the surrounding air environment.

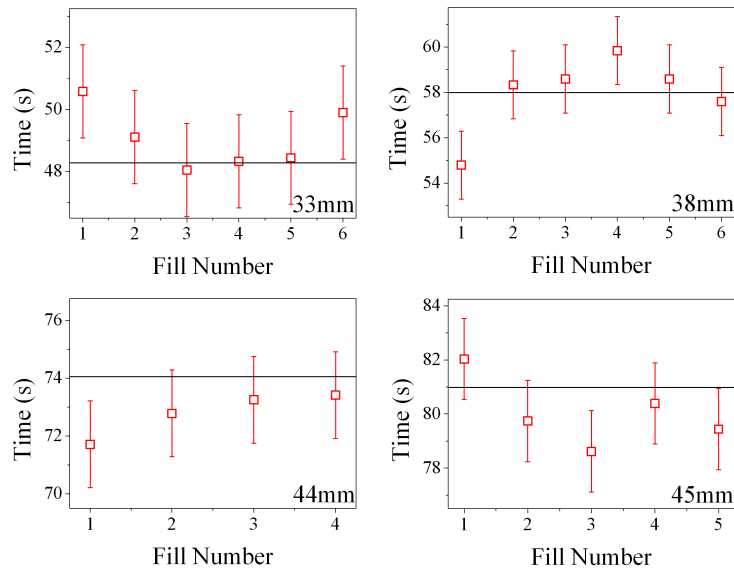


Figure 3.9: Plots of time versus filling number for HC-1550 filled repeatedly with Propan-1-ol for lengths of (top left) 33 mm, (top right) 38 mm, (bottom left) 44 mm, and (bottom right) 45 mm.

As discussed previously, increases in temperature decrease the viscosity, causing the liquid velocity to increase. The behaviour of the viscosity of propan-1-ol with temperature is plotted in Figure 3.10. These values (black circles) are taken from literature [168, 169], and show that for increasing temperature, the viscosity of propan-1-ol at around room temperature will vary by 0.5 mPa.s. This result indicates that the insulation of the system from temperature fluctuations is needed to optimise the experimental method, and will be discussed in Chapter 4, where the measurement of viscosity with HC-PCF is optimised.

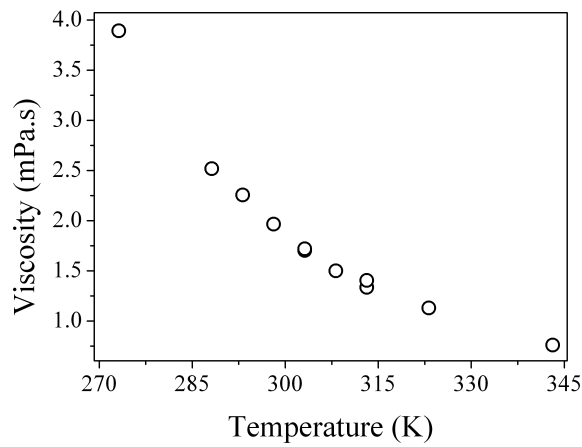


Figure 3.10: Dependence of the viscosity of propan-1-ol over a temperature range of 270 - 345 K.

3.5 Summary

This chapter verifies the filling pattern that occurs for HC-PCF, which is that the core, having a larger radius, will fill before the capillaries. The filling of capillaries with water is then tested to determine if the results approach to the model derived in Chapter 2. It was found that several fillings are required to approach the models estimation. These tests verify that the model requires the additional parameter of a contact angle to be featured in the estimations for the viscosity with the HC-PCF viscosity sensor. If the initial contact angle between the walls of the capillary and meniscus are featured in the filling model, all results will trend with the viscometer, allowing the determination of the viscosity of a fluid.

The main conclusions from this chapter can be summarised as follows:

- HC-PCF fill under capillary action in a pattern that results in the core filling first, followed by the capillaries in the periodic micro-structure.
- For water, the fibre segment must undergo multiple fillings before the filling time trends with the theoretical model.
- The contact angle between the meniscus and the capillary walls must be included in the filling model.

To improve experimental accuracy, the temperature dependence of the viscosity will need to be considered and controlled for accurate measurements. The timing method will also need to be improved to provide more than two points to detect the fill time. A dynamic measurement of liquid filling is required to quantify the liquid flow process. Finally, the microscope method is rather bulky, and to further the application of the HC-PCF as a viscometer, a new experimental method needs to be implemented, which will be described in Chapter 4.

Chapter 4

Optical Fibre Viscometer

This chapter describes in detail the optimisation of the experimental set-up and investigatory measurements performed with the hollow core photonic crystal fibre (HC-PCF), optical fibre viscometer. The experiments were designed to verify the mathematical model and concept outlined in Chapter 2 and to improve the measurement system outlined in Chapter 3. The new set-up scheme for the timing and monitoring of liquid flow within the fibre resulted in a 60 % improvement in the reduction of error in the time measurement. This also results in an enhanced sensitivity in the estimation of the liquids viscosity and overall error estimation. The set-up in this chapter is superior to that described in Chapter 3, as the liquid flow was monitored in real time, rather than at the start and stop points only. A laser source was utilised to detect the dynamic liquid flow within the capillaries of the HC-PCF. A large data set was acquired to determine the filling time. The system implemented a heating element to increase the fibre temperature to a few degrees above room temperature in order to overcome fluctuations from the environmental surroundings. Finally, for all measurements of solvents, the optical fibre viscometer was pre-calibrated with the solvent to determine the contact angle of the meniscus with the silica capillary walls.

The viscometer was tested with a variety of liquids of interest in biomedical and industrial applications. Propan-1-ol was used to characterise the response of the sensor to alcohols, as already discussed and utilised in Chapter 3. Glucose and fructose diluted in water or phosphate buffer saline (PBS), over a wide range of concentrations (10^{-4} - 1 M) was used to calibrate the sensors response to viscosity changes. These chemicals are ubiquitous in the bio-medical and food industries and are therefore appropriate choices for viscosity studies.

The optical fibre viscometer proposed here has the capability to be portable, sensitive to changes in viscosity and is chemically inert. The concept has been detailed in a patent application, by Horan et al. in the US (US20120236302-A1) (16th March 2012) [110], the UK (GB1104547.3) (18th March 2011) and in Ireland (IE2012/0133) (13th March 2012) as a capillary viscometer for the analysis of nano litre liquid samples. This chapter will demonstrate the concept, implementation, testing and merits of this invention.

4.1 Optical Analysis

A supercontinuum (SC) source (500 - 1750 nm) was fabricated “in-house” and used to study the dynamic change in the HC-PCF light propagation properties during filling, as discussed in Section 4.1.2, and subsequently for alignment purposes of each empty optical fibre viscometer sample. It consisted of a Q-switched Nd: YAG laser source (JDSU, wavelength 1064 nm, 0.55 ns pulse width, 6.85 kHz pulse repetition rate), followed by a focusing lens ($\times 40$, NA 0.65) to launch the laser light to a 20 m highly non-linear fibre (Blaze Photonics SC-05-1060, core diameter 2 μm), as shown in Figure 4.1. The output was collected by a $\times 40$ infinity correction lens and collimated. The set-up for the SC source is shown in Figure 4.1.

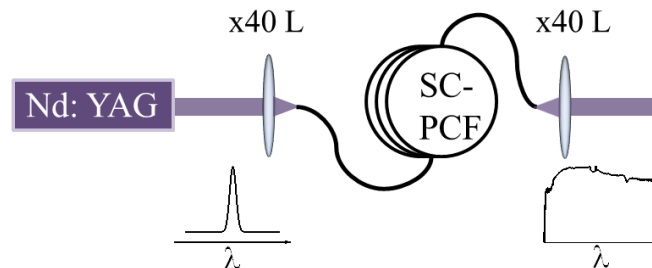


Figure 4.1: Set-up of the supercontinuum source, featuring a Q - switched Nd: YAG laser source, a $\times 40$ focusing lens and a highly non-linear 20 m solid core PCF (SC-05-1060). Inset are the plots for the pump laser (left) and SC spectrum generated (right).

A typical output spectrum is shown in Figure 4.2, ranging from 500 - 1750 nm (limited by the wavelength range of the optical spectrum analyser used Ando AQ-6315E, 350 nm – 1750 nm, resolution 10 nm, and sweep time 2.5 s).

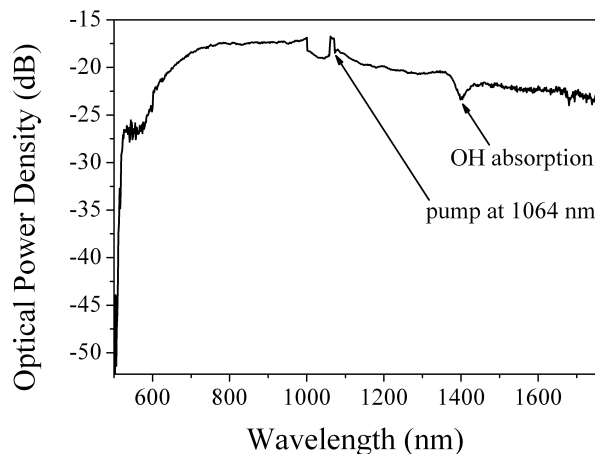


Figure 4.2: Typical transmission spectrum of the supercontinuum source 500 - 1750 nm, measured with an optical spectrum analyser with a resolution of 10 nm.

4.1.1 Alignment of the Short Fibre Sample with the System

In order to analyse the liquid flow through the HC-PCF using the system, the SC source beam was focused to the HC-PCF segment by a $\times 40$ infinity corrected objective lens. The fibre segment was clamped and held in place on an xyz positioning stage, controlled by a motorised nano-position controller (Newport NanoPZ PZC200 controller). The terminal of the fibre was clamped to a fixed short stage (3 cm in length). The clamp on this stage could be replaced with a reservoir to insert liquid to the fibre to analyse the optical properties of the HC-1060 during liquid flow, as will be discussed in Section 4.1.5. The set-up is shown schematically in Figure 4.3.

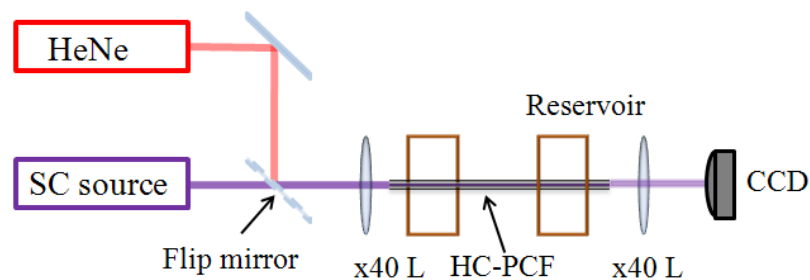


Figure 4.3: Schematic of the alignment set-up for the HC-PCF segment, utilising a SC source and a CCD camera, along with a motorised xyz alignment stage.

The light output from the fibre was collected utilising a $\times 40$ objective lens, which collimated the output light and directed the beam to a Thorlabs CCD camera

(DCU223C, colour CCD camera (1024×768 pixels), sensor Sony ICX204AK, with area $4.76 \text{ mm} \times 3.57 \text{ mm}$, 30 frames/ s). The camera was connected via a universal serial bus (USB) 2.0 to a computer and controlled by the Thorlabs DX software program. The camera's pixel sensitivity to wavelength is shown in Figure 4.4.

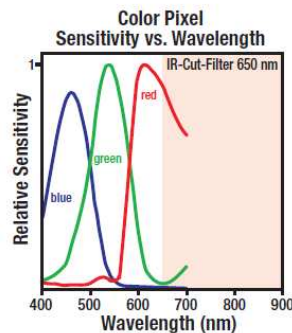


Figure 4.4: Thorlabs DCU223C Camera pixel sensitivity to wavelength, figure courtesy of Thorlabs - Inc.

The camera is responsive to wavelengths in the visible region. However, wavelengths in the infrared region were also detected by the CCD and were displayed as a pink colour, by the software program. The sensitivity of the camera to infrared wavelengths was significantly reduced in comparison to wavelengths in the visible region, as shown in Figure 4.4. The software was optimised to detect the wavelengths in the infrared region by decreasing the frame rate and increasing the contrast.

Precise alignment of the HC-1060 was implemented by filtering the SC source with a bandpass filter (Thorlabs 1050-10, central wavelength = $1050 \pm 2 \text{ nm}$, full width half maximum = $10 \pm 2 \text{ nm}$). This allowed only wavelengths around 1050 nm, close to the fibre's primary PBG to be launched to the HC-1060 segment, enabling the fibre to be aligned using the motorised stage, and by monitoring the output of the fibre with the CCD. When aligned, the fundamental mode of the PBG was able to propagate through the hollow core of the fibre.

The optical free space experimental set-up is schematically illustrated in Figure 4.8. Two sources are utilised in the experiment for (a) the alignment of the HC-PCF segment, facilitated by the SC source and (b) the velocity measurement of the liquid flowing through the capillaries, facilitated by the 632.8 nm HeNe source. This is described in more detail in Section 4.1.4.

4.1.2 Observations of the Optical Transmission Changes During Filling

From the study of the filling profiles of the HC-1060 and HC-1550 in Chapter 3, three distinct filling states can be achieved; empty, core filled and fully filled. The three distinct filling stages show three very different light guiding properties, as described in Chapter 2, which is examined in more detail here.

The output spectrum of the HC-PCF, HC-1060 was measured using an optical spectrum analyser (OSA), when the SC source was launched to the fibre, to demonstrate the changes in light guiding properties for the three different filling states of the fibre. The results are presented in Figure 4.5. Inset in the figure from right to left are images of the fibre tip when empty, core filled and fully filled with water, referring to the red spectrum (air filled fibre), green spectrum (water core fibre) and blue spectrum respectively (fully filled fibre).

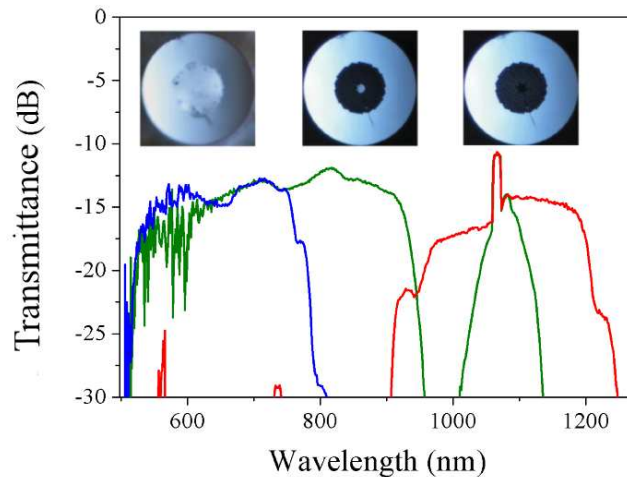


Figure 4.5: Transmission spectra of 10 cm HC-1060 fibre for three different filling states: empty (red), core filled (green) and fully filled (blue).

The red spectrum represents light guiding by the original PBG (see the insert in Figure 4.7 (b)), with a maximum at 1060 nm, and a secondary band at ~ 735 nm, as expected [170]. The green spectrum was recorded when only the core was filled, and where index guiding is the dominant guiding mechanism (see the insert in Figure 4.7 (d)). This transmission exhibits two distinct peaks: the first, at 1060 nm, relates to the original PBG determined by the cladding micro-structure, and secondly a broadband guidance centred at ~ 810 nm, due to index guiding mechanism. This broadband guidance had a 3 dB (equivalent to a full width half maximum) and a 20 dB bandwidth of at least 150 nm and 440 nm

respectively, and the spectrum is clipped at lower wavelengths due to the non-optimal condition of the SC source used (see Figure 4.2). The blue spectrum was measured when the entire fibre was fully filled, with a shifted PBG at ~ 750 nm (Figure 4.7 (e-f)), and 3 dB and 20 dB bandwidth of at least 100 nm and 280 nm respectively, taking into consideration the lower wavelength clipping.

The experimental set-up of the system has a wavelength dependent loss associated with it that affects the determination of the spectral transmission band of the fibre. In Figure 4.6, the direct output of SC source (black trace) as detected by an optical spectrum analyser was compared to the same source when transmitted through the lenses and reservoir of the system (blue trace). The loss attributed to the lens and reservoir system is outlined by the green dashed line. The SC source has a cut off around 500 nm. The spectrum received at the distal end of the fibre is therefore a combination of the filtered source and the propagation properties of the HC-PCF.

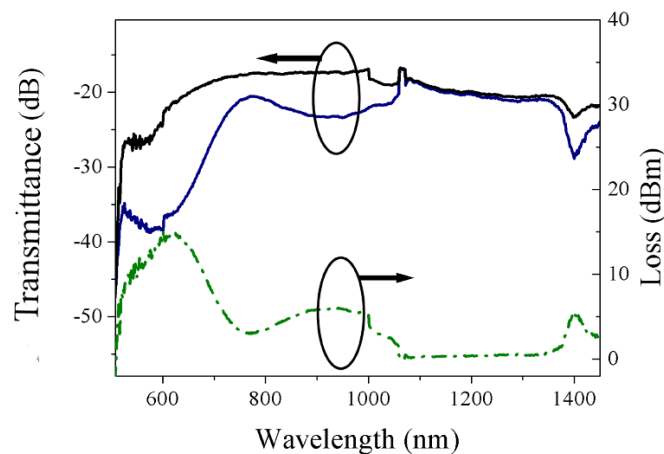


Figure 4.6: Transmission spectra (500 - 1450 nm) of the SC source (black), the transmission of the SC source through the experimental system (blue), and the loss of the system (dashed green line). Resolution 10 nm.

Description of the Change in Guidance Properties, Using the Near Field CCD Images, During the Filling of the Fibre

The optical properties of light guidance will change as the fibre is filled with a liquid. A selection of the real time images can be seen in Figure 4.7, and is further described in this section. These images are the near field CCD images of the end facet of the HC-PCF inserted into the liquid filled reservoir, and are taken during the filling process. The spectrum transmitted was the full SC source. The images of the CCD verify that propagation properties change dynamically over the filling time, depending on the number and pattern of capillaries filled.

Initially at $t = 0$ s, only light at wavelengths within the original PBG, centred around 1060 nm was guided as the reservoir was empty (Figure 4.7 (b)). Note that, due to the wavelength specifications of the CCD, shown in Figure 4.4, the infrared components of the light are usually shown as violet/pink colour. During the filling, the laser side of the fibre, which was still empty, scatters and leaks light of wavelengths outside the PBG, and at the detector side of the fibre, which is partially filled, some of the visible light scattered is confined back to the core either by index-like guiding (as the core fills faster) or by the PBG shift (Figure 4.7 (c)). Eventually, after 114 s (Figure 4.7 panel (d)), the core is fully filled, and the image from the CCD was saturated as index-like guiding mechanism allows for a broad range of wavelengths across the visible and near infrared range to be propagated (as shown in the green spectra in Figure 4.5). After 340 s (not shown in Figure 4.7), all capillaries were filled, and a PBG shift was observed. To illustrate the PBG shift, bandpass filters centred at 500 nm and 650 nm (with a full width half maximum (FWHM) of 10 nm) were mounted at the fibres input. Figure 4.7 (e) and (f) confirm the propagation of these wavelengths as expected by the PBG shift.

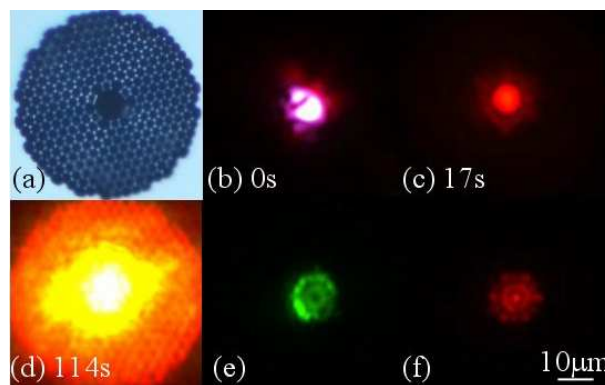


Figure 4.7: Near field images of the HC-1060 during dynamic filling with a liquid for an SC source launched to the fibre. (a) shows the cross section of a HC-1060 taken with a Nikon microscope, (b-f) shows the near field images of the HC-1060 when (b) empty, (c) during the filling of the core, (d) when the core is fully filled and (e-f) when the core and capillaries are fully filled.

4.1.3 Choice of Fibre and Laser Source

The insertion of liquids to the capillaries shifts the guidance band from the original PBG to shorter wavelengths, as discussed in Chapter 2 and seen in Section 4.1.2. The PBG shift that occurs when the internal refractive index of the air filled

capillaries is changed can be calculated using the scalar equations, Equation (2.1) outlined in Chapter 2. In the previous section, the propagation bands of the three filling states of the HC-1060 were shown and discussed in Figure 4.5. By examining the data, it is evident that the choice of laser will result either in a decay of guidance while filling, or an increase in guidance (not taking into account losses).

The scheme chosen for the viscosity measurements was no-guidance to guidance, utilising a wavelength source in the visible region of the electromagnetic spectrum. Wavelengths in the near infrared are absorbed by the aqueous solutions used to fill the capillaries of the HC-PCF. The optimum laser for this measurement must be within the region where water is the least opaque (~ 500 nm). However, HC-1060 has a secondary PBG at ~ 700 nm. A laser close to this wavelength is expected to be partially guided within the silica struts when the fibre is empty. This will allow verification that the fibre is optimally aligned, whereas a source that is completely unguided initially may result in alignment error.

The laser source chosen for experimental measurements was a HeNe (continuous wave (cw), 1 mW, 632.8 nm). By using this as the laser source, the filling of the core and/or all capillaries of a HC-1060 fibre could be monitored through the light propagation changes from no-guidance to index guidance and then shifted PBG, which is demonstrated in Figure 4.7. The HeNe output wavelength of 632.8 nm falls outside the PBG of the empty fibre, and thus was initially not propagated within the core, but could be seen confined within the silica struts surrounding the core. Residual scatter from the micro-structure is also confined to the outer silica cladding, and is detected initially by the experimental set-up. Once the fibre core is filled, and guidance shifts to index guiding, and light from the laser source is guided within the fibre core. This combination was selected as an optimum for the liquids investigated in this thesis, however, many variations and combinations of fibre and laser can prove useful for different applications.

4.1.4 The Viscometer Set-up

To ensure optimum alignment when the fibre is inserted into a reservoir, first the output of the sample was clamped to a 3 cm fixed stage to align the fibre utilising the CCD camera. After alignment, the fixed 3 cm stage at the fibres output was removed and replaced with another 3 cm stage with the reservoir attached to it, and this is shown in Figure 4.8 and Figure 4.9. The terminal of

the fibre was inserted into a reservoir ($3\text{ cm} \times 2.5\text{ cm}$), designed to hold the fibre horizontally in line with the xyz stage, by a series of plastic connectors (Kinesis) to prevent leakage of liquid during and after the filling of the fibre. The fibre segment (diameter 0.22 mm) was inserted into a piece of blue tubing (F-228, length 1.1 cm and external diameter 1.6 mm and internal diameter 0.25 mm). This tubing section was placed inside an adapter (P-882, internal diameter 1.6 mm) with a screw end that could be fixed to the reservoir. The specifications of the reservoir are discussed in detail in Section 4.1.5.

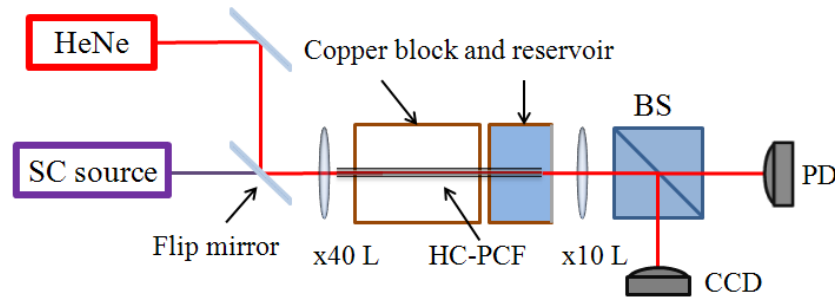


Figure 4.8: Schematic of experimental set-up for the optical fibre viscometer.

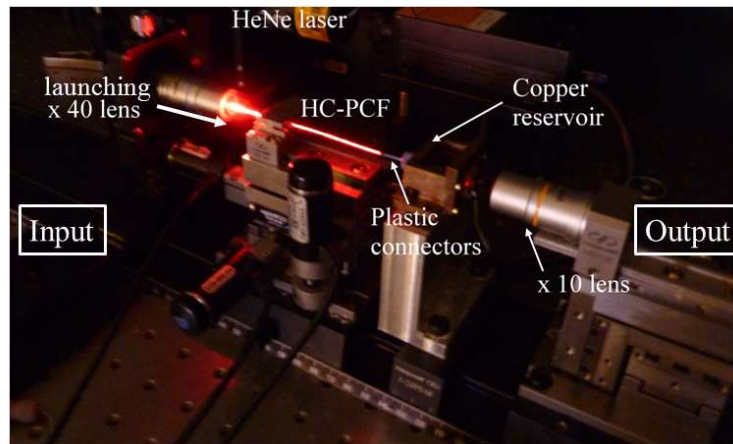


Figure 4.9: Actual set-up of the optical fibre viscometer, used to estimate the measurement of the liquid viscosity. The HC-1060 is illuminated with a HeNe laser source, and the image is taken during a filling measurement.

Fibre segments of 10 to 12 cm in length were used for the experiments. The fibre tips had their cladding jacket removed, 2 cm from each end, in order to allow cleaving of the ends for better light coupling. The chosen lengths were long enough to enable accurate optical alignment, and yet short enough to limit the measurement time and to prevent excessive temperature variations.

The flip mirror was raised to direct the HeNe laser to the HC-1060 segment,

which had been previously aligned to the system using the SC. To detect the propagation changes, the output of the fibre was collimated with a $\times 10$ infinity corrected lens. The collimated beam passed through a 50/50 beam splitter placed after the collection lens to allow the signal to be monitored by a photo-diode (PD) and a CCD camera simultaneously during filling. The CCD camera monitored the dynamic filling of the fibre with near field images recorded via USB 2.0 (with the collection of images optimised by the Thorlabs DX software for the HeNe source at 30 frames/s). The images were saved by the software as a film that depicts the change in propagation mechanism of the fibre as the capillaries were filled. The PD detected the power of the light transmitted from the terminal of the fibre over time.

The PD (Thorlabs SM05PD1A- cathode grounded) had a large detection area of 13 mm^2 and was sensitive over a broad wavelength region (between 350 - 1100 nm), with the maximum sensitivity at 980 nm, as shown in Figure 4.10. The photo-diode was connected via a BNC connector coaxial cable to a National Instruments portable DAQ (NI USB-6218, 400 ksamples/s), connected by USB 2.0 to the computer. A 50Ω load resistor was connected between the anode and ground port of the DAQ. The total load, on the PD was $R_L = 50 \Omega$. The data was collected using a Labview program, which recorded the voltage measured by the photo-diode as a function of time.

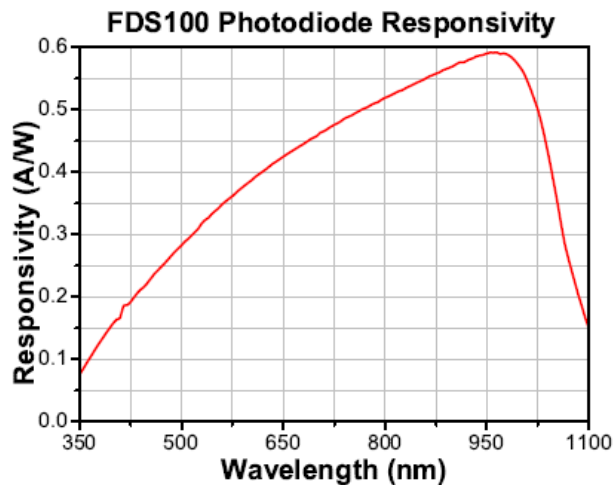


Figure 4.10: The response curve of the photo-diode to wavelength, courtesy of Thorlabs - Inc.

From Figure 4.10, it can be estimated that, at 632.8 nm, the PD had a responsivity of 0.4 A/W. Voltage measurements from the photo-diode can be recalculated to measure the light power transmitted by the HC-PCF. This is performed using a

simple equation:

$$P = \frac{V}{\Re(\lambda) \times R_L} \quad (4.1)$$

where P is the power measured by the PD, $\Re(\lambda)$ is the wavelength dependent conversion efficiency in units (A/W) and R_L is the resistive load. This formula is used to estimate the transmission properties of the filling fibre, over time.

4.1.5 Temperature Control

Viscosity is a temperature dependent property, tending to decrease with increasing temperature in a non linear manner [111]. Thus, the set-up proposed here had to incorporate a temperature control system in order to minimise temperature fluctuations within the set-up and environment. As the liquid enters the fibre from the reservoir and travels through its length the liquid is vulnerable to fluctuations in ambient temperature. The HeNe source for example could cause heating of the silica and liquid. The coefficient of thermal expansion for silica is $\alpha_{bulk} = 5.5 \times 10^{-7} \text{ K}^{-1}$, and thus the expected change in length per 1 K change in temperature for a 12 cm fibre (using $\Delta L = L_0 \alpha_{bulk} \Delta T$) is $6.6 \times 10^{-8} \text{ m}$. The effect of temperature on the fibre length is negligible, in comparison to the influence of temperature on the viscosity. The source power was maintained at less than 1 mW for all measurements to minimise this effect, using a set of neutral density filters. Other sources of temperature change originated from uncontrollable temperature effects from the surrounding open air environment.

In order to prevent temperature influences from the surrounding environment, the fibre and reservoir were heated during the experiments. The temperature control system featured two thermo-electric cooled peltier elements controlled using a P.I.D. controller. The system was split into two parts. One section controlled the temperature of the liquid within the reservoir. The other controlled the temperature fluctuations along the fibre length that was external to the reservoir. The schematic of our temperature control system is shown in Figure 4.11.

The reservoir comprised a rectangular copper enclosure measuring $3 \times 2.5 \text{ cm}$, with a copper lid, depicted in Figure 4.11 and Figure 4.12, to maintain a uniform temperature within the liquid. It had a small, circular polymethyl methacrylate (PMMA) window (thickness 0.1 cm, diameter 0.5 cm) at the output end in order to allow the transmitted light to be monitored. The reservoir was maintained at a constant temperature by a Thorlabs TED 200C temperature controller which

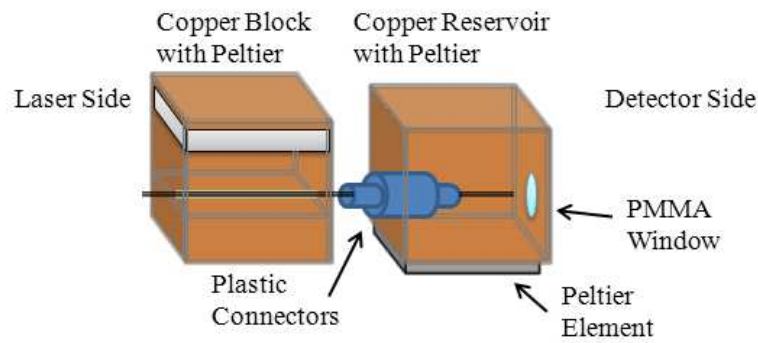


Figure 4.11: Schematic of temperature control system for the HC-PCF segment, featuring a copper reservoir fitted with a lid for the liquid, and a copper plate to heat the fibre. Both parts were heated using a peltier element, controlled with a P.I.D, not seen here.

supplied current to a peltier element and monitored the temperature at the side of the copper reservoir with a thermistor (20 k Ω) and some heat transfer paste. The peltier element was positioned under the reservoir to ensure even distribution of heat throughout the liquid. The thermistor was embedded into the side of the copper reservoir, seen in Figure 4.12, to monitor the temperature of the system. The P.I.D controls of the TED 200C were optimised to allow the reservoir to reach a stable temperature of 29° Celsius within a few minutes, and to maintain that temperature to within ± 0.1 ° Celsius.

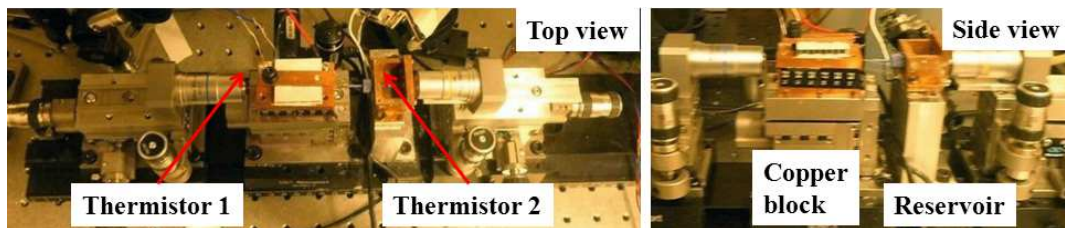


Figure 4.12: Images of the temperature control system from the top (left) and from the side (right), showing the positions of the thermistors.

The xyz optical positioning stage that held the fibre was fitted with a 5 cm long copper casing. The casing consisted of two plate sections (a top and a bottom plate) that fitted around the fibre, as shown in Figure 4.11. A trench in the bottom plate allowed the fibre to sit within two copper plates, without the weight of the plates affecting the fibre. The temperature was monitored by a thermistor positioned just above the groove where the fibre was held in place (Figure 4.11). A peltier heating element was connected to the top plate to ensure an even distribution of temperature throughout the copper casing. This is also depicted in Figure 4.12. The current in the peltier element was controlled by a Newport 350B temperature controller. The P.I.D settings were optimised so that

the plate would heat the fibre to a constant temperature of $29 \pm 0.1^\circ$ Celsius.

The limit of the temperature accuracy for the system was $\pm 0.1^\circ$ Celsius, and was the best that could be achieved with this preliminary set-up, in order to prove the principle of the viscometer. This system was not ideal, as two separate temperature controllers were used to control the temperature of one system. However, as the temperature of a liquid increases, the fluctuations in viscosity decrease, as discussed in this section, which allows our measurements to retain their accuracy, even if there are small overall fluctuations in temperature. The experiments here demonstrate a proof-of-concept for the optical fibre viscometer. For a real prototype, the entire system would need to be insulated. To further insulate the fibre from temperature fluctuations, the environmental conditions surrounding the apparatus should be carefully controlled, by using a standard temperature and pressure chamber, that would shield the experiment from temperature fluctuations, and other external effects. These careful precautions were not applied to the experimental set-up and the error associated with this is taken into account in the estimations of the viscosity in Section 4.3.

4.2 Timing Measurements and Error Analysis

This section describes the method for the determination of the filling time from the output collected by the PD, and describes the measurement process. The experimental set-up has already been outlined in Section 4.1. The preliminary data measurements are compared with the capillary model and the statistical error of the process is established.

4.2.1 Determination of the Start and End Filling Times

A characteristic filling curve for a velocity measurement is displayed in Figure 4.13. The initially decreasing signal in Figure 4.13 is caused by the insertion of the liquid to the reservoir. This causes refraction of the exiting beam to the PD, resulting in a change in the output alignment of the fibre. Upon meeting the liquid interface, the laser guidance is expected to be scattered, resulting in a significant decay in output signal to the photo-diode detector. The signal remains at an almost constant level for the majority of the capillary filling time after the initial signal drop. This first drop is defined as the filling start point and is set as t_{int} .

For a brief time period, before the core of the fibre is fully filled, a very rapid increase in transmission is observed. The peak of the increase in transmission is defined as the point where the core of the fibre has been fully filled. After this point the transmission remains virtually constant. It is sufficient to capture the core filling time in order to determine the average velocity for the viscosity analysis. Nevertheless, as the filling continues in the fibre cladding capillaries, modal competition within the core is observed until the capillaries are completely filled (after 900 s, for this particular fibre length and test sample). Note that the signal at the start is not zero, as there was no attempt to block the scattered light confined to the solid outer cladding of the fibre from the PD.

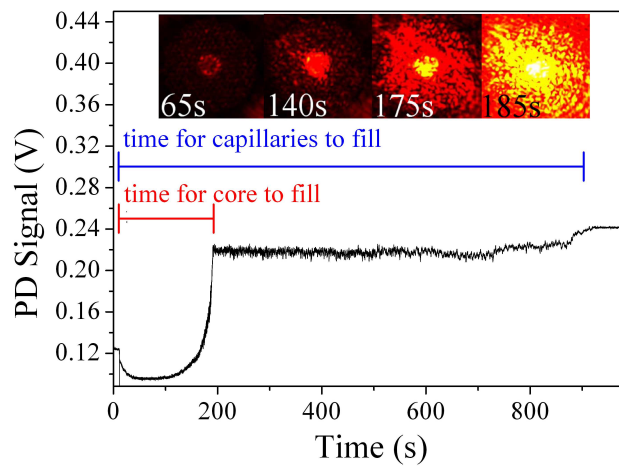


Figure 4.13: Voltage change with time measured by the PD for a HC-1060 fibre (11.4 cm) during the filling process with a 0.5 M aqueous glucose solution, for the transmission of a HeNe (632.8 nm) laser source.

The fibre (11.4 cm) in Figure 4.13 was filled with a 0.5 M aqueous glucose solution. The transmission of the HeNe laser over the filling time of the fibre is represented by the signal of the PD in units of voltage. Insets show the near-field images of the output of the HC-PCF, captured by the CCD camera sequentially over the filling process at $t = 65$ s, 140 s, 175 s and at $t = 185$ s, where the core is almost fully filled. The core can clearly be seen in the centre of the images, throughout the sequence. The timing measurements for the start and end point were taken when the initial drop in signal occurs at $t_{int} \sim 10$ s, indicating the addition of liquid to the reservoir. The end point, when the core is filled, is the point where the signal reaches a maximum at ~ 190 s. A closer inspection of this plot reveals some interesting observations of the HC-PCF once the core is filled. After 190 s, the signal undergoes large fluctuations of ± 0.01 V, corresponding

to a laser power fluctuation of 0.02 mW (estimated using Equation (4.1)). These fluctuations continue until the entire fibre has been fully filled with the liquid. Then the fluctuation in transmission voltage changes to 0.003 V or 0.006 mW, which can be attributed to the experimental set-up and alignment issues.

The large fluctuation in signal during the capillary filling is due to the modal competition that was observed in the core of the fibre by the CCD camera during this time period, and was previously discussed in Chapter 2 and shown in Figure 4.15. The section of data from ~ 180 s to ~ 1000 s is further investigated and is displayed in Figure 4.14. This figure shows clearly the point where the core fills, the fluctuation in signal during the capillary filling immediately after this point, and finally the increase in signal and the reduction in signal fluctuation when the fibre and all the capillaries are completely liquid filled after 800 s.

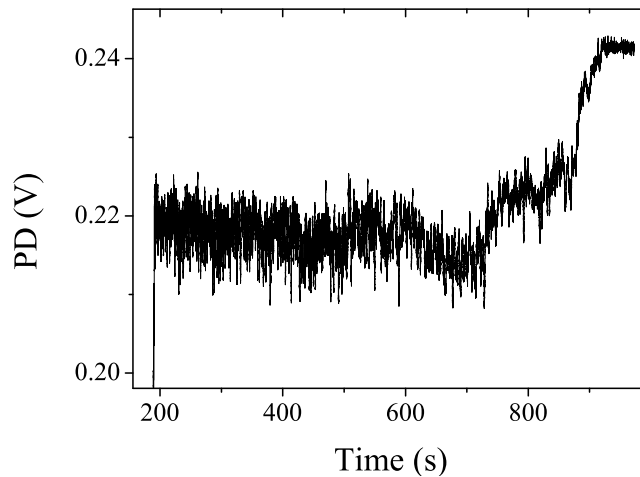


Figure 4.14: Close-up plot of the fluctuation of voltage signal measured by the PD after the core is filled while the capillaries are filling.

Figure 4.15 depicts the modal competition at 632.8 nm and 650 nm, that occurs in the core of the fibre when the core has filled and the micro-structure surrounding the core is undergoing filling. The CCD camera in this case was too slow to identify between individual modes, and instead picks out the spatially resolved modal distribution of the fibre end that changes during the dynamic filling. It is clear that the modes are not fundamental or Gaussian in nature. The top row shows the modes of the 650 nm source, depicting a broad mode in (a), an LP_{11} in (b) and a superposition of higher order modes in (c). The middle and bottom rows show the modal competition for the 632.8 nm HeNe laser. Figure 4.15 (e) shows an LP_{11} mode. Figure 4.15 (f-h) shows a central bright spot, and surrounding ring, similar to an LP_{02} mode. These pictures represent the modes

available for the light to couple to within the liquid state fibres.

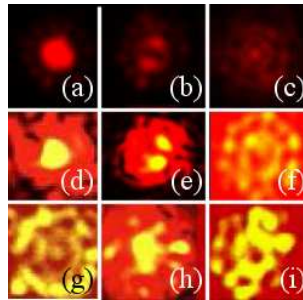


Figure 4.15: A selection of modes generated during the dynamic filling of a HC-1060 with water, guiding the SC source filtered 650 nm bandpass filter (top row) and a 632.8 nm HeNe laser (middle and bottom rows). The modal competition can clearly be seen by the superposition of higher order modes within the liquid core of the HC-PCF.

The PD plot in Figure 4.13 gives an example of one typical filling profile, under optimum conditions of alignment and temperature control. Figure 4.16 displays the transmission graphs of four measurements that were not quite optimum, but instead typical results of these experiments. These graphs demonstrate how measurements with non-optimum alignment can change due to experimental error. Figure 4.16 (a) shows a broad fluctuation in the voltage measurements at the decay section of the transmission between 20 - 100 s, due to an error in the focusing of the signal to the PD detector with the $\times 10$ lens. As such, the point where the core fills is not as well defined as in Figure 4.13, which results in a larger error estimate for the core filling time measurement. Figure 4.16 (b) experiences a decay in signal after the core fills, in contrast to the optimum measurement, which should remain steady or increasing after this point. This is due to error in the initial alignment of the fibre to the HeNe laser. However, once the capillaries are filled, the signal rises and remains steady, as expected. Figure 4.16 (c) displays a transmission plot where the signal decays quickly and then recovers after the filling of the core. The reason for this drop cannot be attributed to alignment, but may be caused due to leakage of fluid between the capillaries at the fibre end facet (at the laser input) due to a non-optimum cleave. Figure 4.16 (d) experiences a drop in signal after the filling of the core, which, like Figure 4.16 (b) can be attributed to alignment error.

From the non-optimum alignment results for the filling profiles of HC-PCF, it is clear that alignment changes the shape of the characteristic curve. However the start and finishing point are always clearly defined for slight alignment errors. For greater alignment errors, the start and finishing points will not be clearly

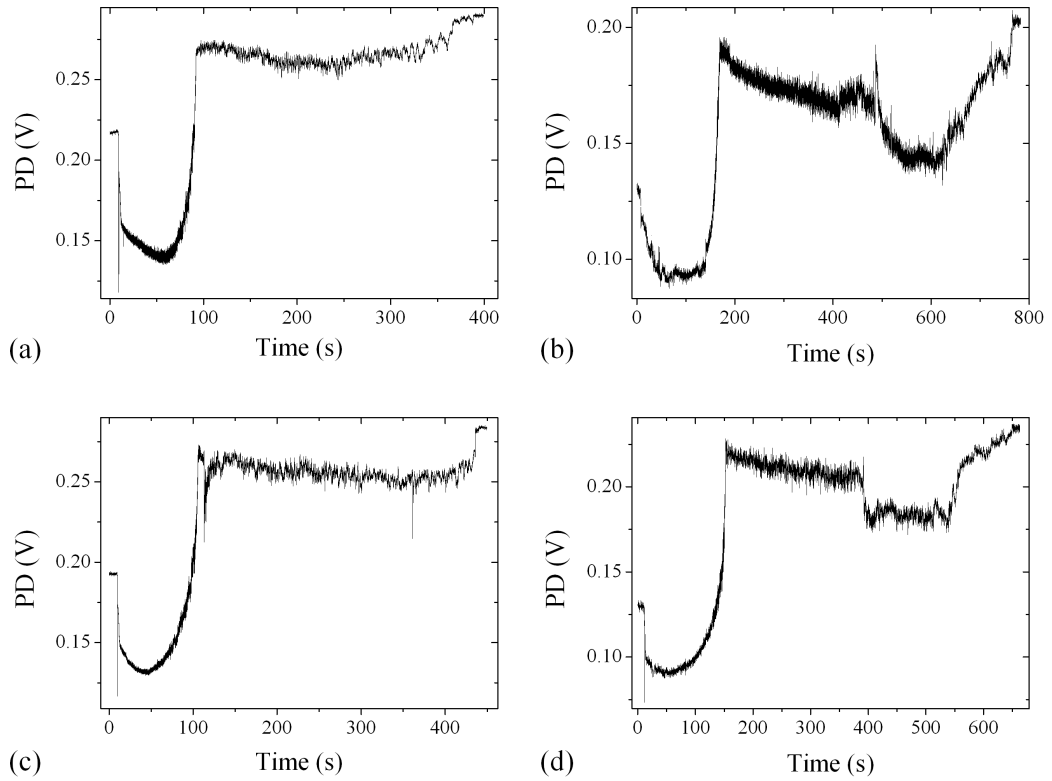


Figure 4.16: Example plots of transmission profiles of the 632.8 nm laser source during dynamic capillary filling.

defined, and a measurement cannot be taken.

To verify that the 632.8 nm source was optimum for this experiment, in comparison to other short wavelength sources, a second laser source at 532 nm (continuous wave, frequency doubled ND: YAG, 4 mW) was also used to measure the filling properties of a HC-PCF. This wavelength is positioned outside the secondary PBG, and will not be guided within the micro-structure, unlike the 632.8 nm light source. Instead, all light from the 532 nm would be scattered to the solid cladding of the HC-PCF.

Two 15.5 cm segments of HC-1060 were prepared, as previously described in Section 4.1. Both lasers were kept at powers below 1 mW, and both experiments were performed in the same fashion as described in this chapter. One fibre was aligned to the system with the 632.8 nm source and tested with a solution of 50 mM aqueous glucose. The 632.8 nm source was then replaced with the 532 nm source, and a new 15.5 cm HC-1060 was aligned to the system using the SC source. The measurement was repeated with the same solution. The results for the filling measurements are shown in Figure 4.17 for the 532 nm source (left

in green) and for the 632.8 nm source (right in red). The results show that, due to the initial non-guidance of the 532 nm source (left), initial alignment is much more difficult to achieve, and thus the measurement results in an unsteady transmission. After the core is filled, there is a sudden decay in signal. The 632.8 nm source transmission spectra (right) is more stable, and the point where the core fills retains the voltage signal measured by the PD.

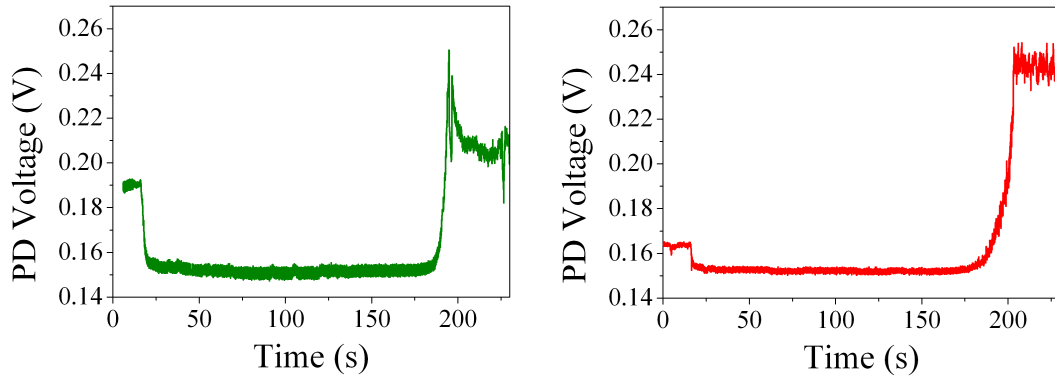


Figure 4.17: Comparison of laser sources 532 nm (left) and 632.8 nm (right) for viscosity measurements, using a 50 mM aqueous glucose solution and two 15.5 cm HC-1060 segments.

The time over which the PD signal is increasing for the core filling is also different for the two sources. The 632.8 nm source rise time occurs in 30 s, while the 532 nm rise time occurs in 10 s. This results in a more defined core filling time for the 532 nm source. Taking into account the guidance properties of the two sources, the 632.8 nm source was observed to be more suited to measurements with this type of HC-PCF, due to the initial guidance within the secondary PBG, allowing a more efficient alignment of the fibre.

This section examined the filling profile of the HC-PCF as seen by the PD for a 632.8 nm laser source. The start and end points of the filling could be clearly defined using the PD trace. The 632.8 nm measurement was compared to the same measurement with a 532 nm source. It was found that the 532 nm source had a much shorter trace for the time where the PD signal was increasing as the core filling nears completion. The alignment, mis-alignment and its effect on the characteristic filling trace was examined with several measurements. It was seen that slight misalignment will not effect the determination of the core filling, but the signal will drop after the filling of the core, during the filling of the capillaries. This drop does not occur for an accurately aligned fibre.

4.2.2 Repeat Filling Tests with Laser Set-Up

To determine the fibres re-usability as a sensor, tests were performed on pre-filled fibres. This test was to determine if the measurements for time could be repeated using a pre-filled fibre that had been dried before reuse.

Repeatedly filling the same fibre sample has been shown previously in Chapter 3 for the microscope set-up. The repeat fillings changed the filling times required for a liquid sample within the HC-PCF, due to the hydrophilic change to the properties of the surface of the internal silica walls of the HC-PCF. The initial filling deposits a thin non-uniform wetting layer on the walls of the capillaries, that remains after the bulk volume of liquid has been removed from the capillaries, by the syringe method described in Chapter 3. This thin film alters the propagation properties of the fibre, and prevents guidance by the original PBG effect.

The repeat filling analysis was performed with the set-up shown in this chapter. In this case light launched to the input of the pre-filled fibre is scattered and no output is seen. Although once filled, the fibre sample would guide certain wavelengths, the accuracy of the start filling time was lost due to the initial scattering. The residue of liquid that is left as a wetting layer on the walls of the capillaries prohibits guidance of the laser through the fibre, and therefore accurate alignment cannot be facilitated. All light directed to the fibre undergoes scattering, and guidance is not promoted in any part of the micro-structure. This also prohibits the determination of the initial start point for the filling, as the time is measured by an initial drop in signal as liquid enters the capillaries.

To overcome the loss of guidance within the micro-structure and as a further experiment to characterise the fibres reuse-ability, the pre-filled fibres were dried in an oven overnight at 100 ° Celcius. After the drying, the fibres were allowed to cool and were examined under the microscope for signs of liquid still remaining on the silica walls. The fibre was then placed in the set-up. If the capillary walls of the fibre had dried thoroughly, the original PBG would be present once again, and alignment would be facilitated by the SC source.

Figure 4.18 graphs the results for the first filling velocity (red circles) using the laser set-up and the second filling velocity (black squares) with the laser set-up, with the two lines fitted as guides to the eye. The repeat tests for these fibres resulted in much longer filling times and therefore slower velocities than were recorded for the very first filling of the fibre. As the original PBG is present in these fibres, it is concluded that the drying process removes a greater portion of

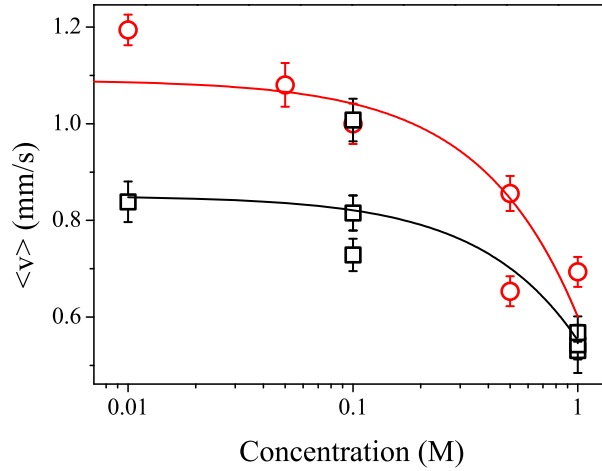


Figure 4.18: First fibre filling (red circles) and second filling (black circles) using oven drying method. The second filling shows a longer fill time than the first, due to over dehydration of the oven dried fibre.

liquid from the capillaries than for the first measurements. The drying of HC-PCF at high temperatures clearly breaks the OH bonds between the wetting layer and the silica, as discussed in Section 3.3.4, and can further cause dehydration of the fibre that was not present for the first filling. Drying the fibre at 100 ° Celsius restores the internal capillaries of the fibre to their original state.

As a result of these experiments, measurements with the optical fibre viscometer were performed once with each fibre segment. For each measurement a new piece of fibre was used to prevent cross contamination with the samples, and to maintain the original PBG.

4.2.3 Fitting of Experimental Data to the Model

The quality of the experimental data in Chapter 3 was established by comparing the results to the model derived in Chapter 2. Here the same analysis was repeated for 0.01 M and 0.001 M aqueous glucose solutions. The data for Figure 4.19 (a) was measured for HC-1060 filled with 0.01 M solutions. The model was calculated with the surface tension (σ) derived from [137], where density was assumed to be 1000 kg/m³ and μ derived from [115] using data from [171, 172, 173, 174], which will be discussed further in the mono-saccharide application Section 4.3.2. The data for Figure 4.19 (b) for 0.001 M aqueous glucose was compared to the capillary model, with parameters taken from the literature quoted as before for Figure 4.19 (a). The error bars were estimated by determining the error in the

measurement of the length of the fibre, and the error in the recording of the time for filling. This is discussed in Section 4.2.4. The error bars are included in both graphs in Figure 4.19, and the data points show good agreement with the filling model, for the first fillings of all the HC-1060 segments.

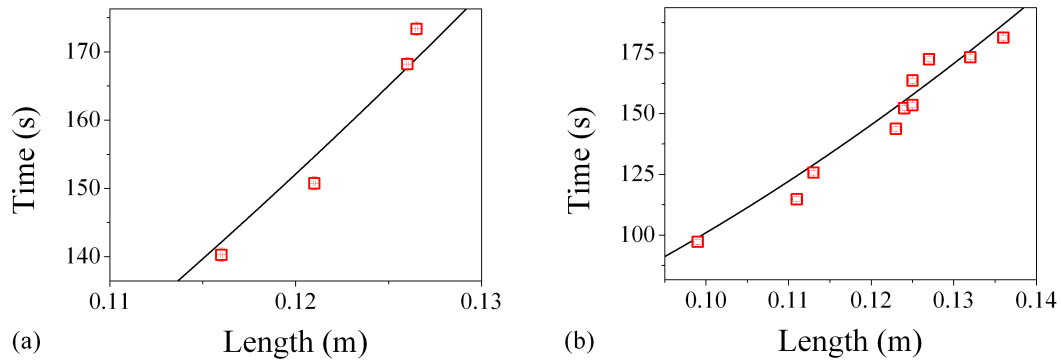


Figure 4.19: Experimental data for (a) 0.01 M aqueous glucose and (b) 0.001 M aqueous glucose solutions (red squares) plotted to the capillary filling model (black line).

These experimental results for 0.01 M and 0.001 M aqueous glucose solutions show good agreement with the model, estimating the contact angle to be 60° , by pre-calibrating the fibre with the solvent, water.

4.2.4 Error Estimation

There are two main error sources in the measurements for the velocity of the liquid flow. The first is the determination of the fibre length. Sections of HC-PCF were cut by hand from a 20 m reel of fibre. Once the fibre was prepared by cleaving both ends, the fibre was kept straight and the length was measured using a high precision ruler, accurate to 0.5 mm. The second source of experimental error comes from the time uncertainty. The start and end points of the filling is very clearly defined from the PD results, as shown in Figure 4.16 and Figure 4.20. The start time is usually indicated by a drop in signal. The exact core filling time is ambiguous, as the increase in signal is more gradual. In this case, the exact point of filling is defined as the inflection point on the curve where the slope changes value. The PD system recorded data at a rate of 50 points per second. The amount of data points needed to observe a change in the slope was 20, and therefore the estimated time error for this point was 0.5 s.

To determine the error for the viscosity measurements, the additional parameters of core radius and temperature fluctuations are required. The error in the

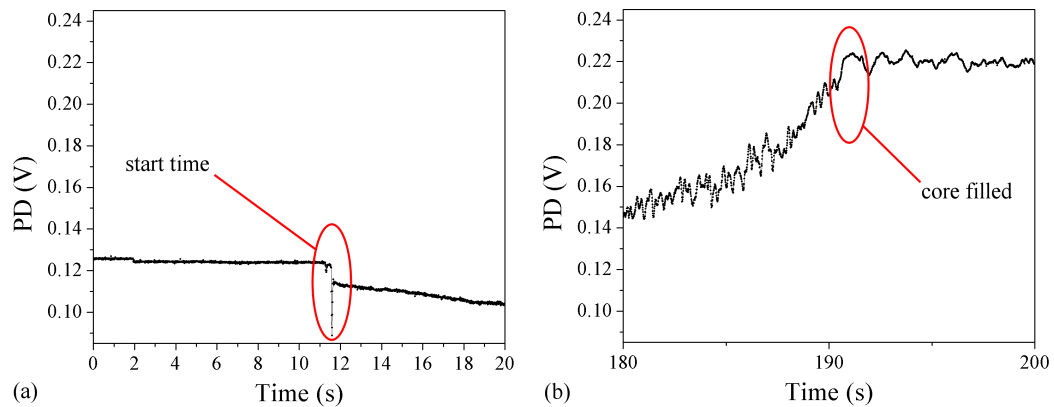


Figure 4.20: Graph indicating start point (a) by a red circle and core filling point (b) by a red circle for all velocity measurements.

measurement of the core has been previously discussed in Chapter 3. For the viscosity, an additional error is attributed to the $\pm 0.1^\circ$ Celsius fluctuation in the P.I.D temperature control system. For example, in water, the viscosity is expected to fluctuate by 0.01 mPa.s for every 0.1° Celsius change in temperature. This fluctuation is included in the error estimates for all data discussed in this thesis.

4.3 Optical Fibre Viscometer Applications

The optical fibre viscometer was characterised and tested with samples that are of importance in industrial applications and medical diagnostics. Propan-1-ol over a range of mole fractions in aqueous solution was examined to verify the sensors response to a solvent miscible in water. Glucose and fructose solutions in phosphate buffer solution (PBS) were examined to quantify the sensors response to viscous liquids and common sugary solutions.

4.3.1 Propan-1-ol

Propan-1-ol and other alcohols are commonly used in the chemical and food processing industry. The viscosity measurement of these liquids is of paramount importance for careful monitoring of production processes. This motivation led to the testing of binary solutions of propan-1-ol and water in this section with the optical fibre viscometer. To the best of our knowledge, it is the first time that propan-1-ol solutions are investigated for viscosity analysis using HC-PCF.

As discussed in Chapter 3, the filling process of the silica capillaries is disrupted by liquids with OH bonds, due to defects present in the fused silica. This slows the flow of liquid, resulting in a longer filling time that can be compensated for by estimating the angle between the meniscus and the capillary wall. The filling of HC-PCF with pure propan-1-ol has been observed in Chapter 3, to have a filling time that agrees with the model derived in Chapter 2. Therefore propan-1-ol is expected to have a 0° contact angle with the capillary walls. Our experimental viscosity results determined by the optical fibre viscometer method, outlined previously in this chapter, will be compared to the data from literature, which utilises other commercially available viscometers. The mass fraction where the contact angle becomes 0° can then be established for our experimental data.

To quantify the response of the sensor to a chemical, miscible in water, aqueous solutions of propan-1-ol, over a mass fraction range of 0 to 1 were tested with the optical fibre viscometer. The mass fraction is calculated using the formula:

$$x_1 = \frac{m_1}{m_1 + m_2} \quad (4.2)$$

where m_1 is the mass of the solute, in this case propan-1-ol, and m_2 is the mass of the solvent, water in this case. Solutions of propan-1-ol and water for testing with our optical fibre viscometer were made up in the ratio of masses displayed in Table 4.1. The propan-1-ol was first filtered to remove impurities using a syringe filter. When propan-1-ol is added in small mass quantities to water, the contact angle between the silica and meniscus is expected to reduce to 0° . The point where this angle turns shall be investigated in this section, utilising a number of solutions with low mass fractions of propan-1-ol.

Table 4.1: Binary solutions of propan-1-ol¹ in water² used in the experimental viscosity measurements for the optical fibre viscometer proof-of-concept.

| Mass Propan-1-ol ¹ (m_1) | Mass Water ² (m_2) | Mass Fraction (x_1) |
|---|-----------------------------------|-------------------------|
| (g) | (g) | |
| 0 | 10 | 0 |
| 0.032 | 10 | 0.003 |
| 0.4 | 9.76 | 0.04 |
| 0.67 | 9 | 0.07 |
| 1.536 | 5.76 | 0.21 |
| 3.36 | 6.31 | 0.35 |
| 10 | 0 | 1 |

The experimental measurements were performed as described in Section 4.1.4, with the exception that the system was not temperature controlled, and all mea-

measurements were recorded at room temperature. The data from the PD signal was then used to estimate the time of filling as described in Section 4.2.1. The time and length values of the results were used to estimate the solutions velocity, $v = L/t$. The value for each experimental measurement solution used, in terms of mass fraction is displayed in Table 4.1.

The surface tension for each solution is required to estimate the viscosity of the binary solutions of propan-1-ol and water. This data is readily available in literature [175, 176, 177], and is plotted as a function of mass fraction in Figure 4.21. The surface tension can be estimated by considering a linear function of the liquids in the binary solution [178]

$$\sigma = \sigma_1 x_1 + \sigma_2 x_2 \quad (4.3)$$

where σ_1 is the surface tension of the solvent (water) and σ_2 is the surface tension of the solute (propan-1-ol), x_1 and x_2 are the mass fractions of the solvent and solute respectively. This relationship can be expressed as a function of the mass fraction of the solute only, and is shown in Equation (4.4), with a correction factor based on the mass fraction of the solute, with fitting constants A and B.

$$\sigma = \sigma_1 - (\sigma_1 - \sigma_2)x_2 \left[\frac{1 + A(1 - x_2)}{1 + B(1 - x_2)} \right] \quad (4.4)$$

This model is fitted to the data from literature in Figure 4.21 with a black dotted line. This fitting was used to determine the surface tension for each of the solutions (outlined in Table 4.1) tested experimentally with the optical fibre viscometer.

The mixture of alcohols with water results in a homopolar mixture, that decreases the surface tension with increased concentration of alcohols. The data from literature (black circles in Figure 4.21 [175, 176, 177]) indicates that the surface tension of water reduces rapidly for less than 0.1 mass fraction of propan-1-ol. After the solution has been changed to 0.2 mass fraction of propan-1-ol, the surface tension of the binary solution is almost constant, suggesting that propan-1-ol is highly miscible in water, and that the addition of very small quantities of alcohols reduces the surface tension of water quite significantly. It is therefore expected that above 0.1 mass fraction, the contact angle between the meniscus and the silica walls is 0 °.

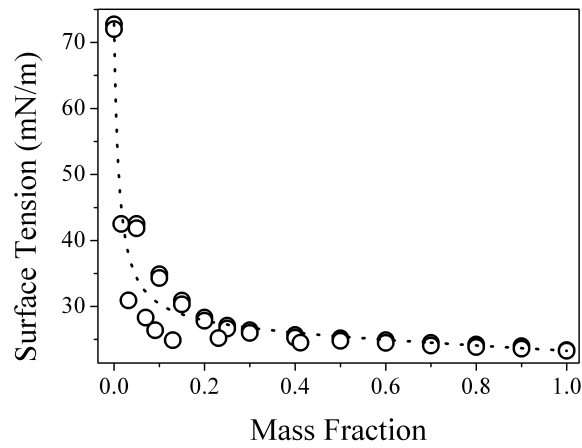


Figure 4.21: Surface tension data for binary solutions of propan-1-ol and water in the range of 20 to 25 ° Celsius. Dotted line is the fitting of Equation (4.4) to the data from literature (black circles).

Table 4.2: Experimental data of velocity and viscosity for aqueous solutions of Propan-1-ol¹.

| Mass Fraction (x_1) | Length m | Velocity mm s^{-1} | Surface Tension N/m | Viscosity mPa.s | Angle |
|----------------------------|-------------|--------------------------------|------------------------|--------------------|-------|
| 0 | 0.126 | 0.784 | 0.072 | 1.02 | 45° |
| 0.003 | 0.165 | 0.546 | 0.068 | 1.34 | 45° |
| 0.003 | 0.156 | 0.804 | 0.068 | 0.96 | 45° |
| 0.003 | 0.135 | 0.603 | 0.068 | 1.48 | 45° |
| 0.003 | 0.135 | 0.487 | 0.0681 | 1.83 | 45° |
| 0.003 | 0.169 | 0.478 | 0.068 | 1.49 | 45° |
| 0.003 | 0.156 | 0.444 | 0.068 | 1.73 | 45° |
| 0.003 | 0.147 | 0.479 | 0.068 | 1.71 | 45° |
| 0.003 | 0.146 | 0.467 | 0.068 | 1.76 | 45° |
| 0.04 | 0.165 | 0.254 | 0.041 | 2.44 | 0° |
| 0.04 | 0.151 | 0.311 | 0.041 | 2.18 | 0° |
| 0.04 | 0.12 | 0.427 | 0.041 | 2.01 | 0° |
| 0.04 | 0.147 | 0.313 | 0.041 | 2.23 | 0° |
| 0.04 | 0.149 | 0.364 | 0.041 | 1.89 | 0° |
| 0.07 | 0.151 | 0.563 | 0.037 | 1.09 | 0° |
| 0.07 | 0.14 | 0.599 | 0.037 | 1.16 | 0° |
| 0.07 | 0.136 | 0.639 | 0.037 | 1.06 | 0° |
| 0.07 | 0.129 | 0.664 | 0.037 | 1.08 | 0° |
| 0.21 | 0.106 | 0.291 | 0.028 | 2.58 | 0° |
| 0.35 | 0.114 | 0.256 | 0.026 | 1.95 | 0° |
| 1 | 0.123 | 0.784 | 0.023 | 1.93 | 0° |

The viscosity for each solution tested experimentally was then calculated using Equation (2.24), using the velocity of the flow and the surface tension for each solution. The results are outlined in Table 4.2, which also states the contact angle assumed for each solution. Above 0.003, the solutions were assumed to have a 0° contact angle. This assumption was made based on the observations from fitting the experimental data to the data available from literature [175, 176, 179, 180] and also the change in surface tension that occurs as the fraction of propan-1-ol is increased in the binary solution.

The data for the estimated viscosity measured by the optical fibre viscometer and the data available from literature [175, 176, 179, 180] are plotted in Figure 4.22 for a range of mass fractions of propan-1-ol in water. In Figure 4.22 (a) the estimated viscosity of each solution measurement through the fibre is plotted in blue half-filled circles with respect to the mass fraction (including error bars). In Figure 4.22 (b) the mean viscosity values from Table 4.2 from 0 to 0.1 mass fraction (blue open circles) are plotted with the data from literature (black open symbols). The error is estimated by taking the mean square error. These results trend with the data from the literature, within the error bars.

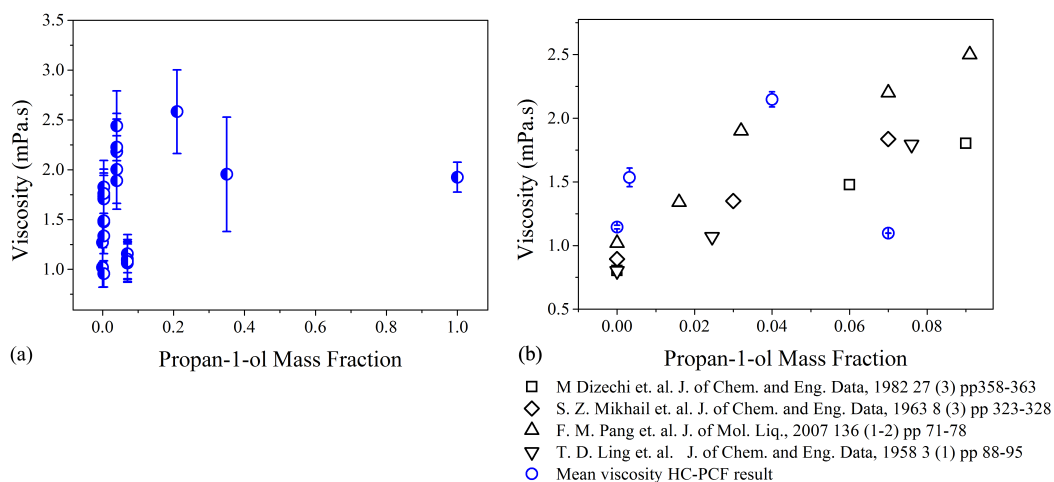


Figure 4.22: (a)Viscosity results from 0 - 1 of propan-1-ol to water mass fraction, measured by the HC-PCF optical viscometer (blue half-filled circles). (b) Mean viscosity results from the optical fibre viscometer (blue circles) and viscosity from literature [175, 176, 179, 180] (open black symbols) from a mass fraction of 0 - 0.1 of propan-1-ol to water.

The data from literature [175, 176, 179, 180] was measured with a number of different schemes, in comparison to that of the method outlined in this thesis, such as Ostwald viscometers, capillary glass viscometers and U-viscometers, all requiring a larger volume than that described here for the optical fibre viscometer.

Table 4.3 outlines the data available for aqueous solutions of propan-1-ol from the literature, which was used as a comparison for the viscosities estimated by the outlined method for propan-1-ol solutions. The data from literature was used to determine the viscosity model for binary solutions of water and propan-1-ol, seen in Figure 4.22, to compare the experimental results to a mathematical model.

Table 4.3: Results from literature for solutions of propan-1-ol¹ in water².

| Mass fraction ¹ | Viscosity (mPa.s) | Reference |
|----------------------------|-------------------|---------------------|
| 0 | 1.02 | Pang et al. [176] |
| 0.016 | 1.34 | |
| 0.032 | 1.9 | |
| 0.07 | 2.2 | |
| 0.091 | 2.5 | |
| 0.13 | 3.2 | |
| 0.231 | 3.1 | |
| 0.412 | 3.1 | |
| 0 | 0.8 | Ling et al [175] |
| 0.0245 | 1.069 | |
| 0.076 | 1.793 | |
| 0.1 | 2.346 | |
| 0.22 | 2.054 | |
| 0.57 | 1.861 | |
| 0.8 | 1.728 | |
| 0 0.895 | | Mikhail et al [180] |
| 0.03 | 1.35 | |
| 0.07 | 1.836 | |
| 0.114 | 2.26 | |
| 0.17 | 2.497 | |
| 0.23 | 2.65 | |
| 0.31 | 2.661 | |
| 0.41 | 2.592 | |
| 0.54 | 2.349 | |
| 0.73 | 2.162 | |
| 0.85 | 2.043 | |
| 1 | 1.938 | |
| 0 | 0.804 | Dizechi et al [179] |
| 0.06 | 1.477 | |
| 0.09 | 1.803 | |
| 0.13 | 2.112 | |
| 0.18 | 2.376 | |
| 0.26 | 2.544 | |

4.3.2 Glucose and Fructose

This section tests the fibres responsiveness to solutions of the mono-saccharides glucose and fructose dissolved in PBS across a range of concentrations. All measurements were made using the temperature control system described previously. Mono-saccharides are ubiquitous in life and food sciences, as a source of energy in living organisms and as a fundamental ingredient in food for the enhancement of flavour or as a preservative. Knowing the viscosity of saccharide solutions, for example, is important for the measurement of the degree of sweetness [122].

The experiments used prepared solutions of glucose and fructose, dissolved in PBS (purchased in tablet form from Sigma Aldrich). The latter was prepared by dissolving one PBS tablet in 200 ml of purified water to obtain 137 mM NaCl, 2.7 mM KCl, and 10 mM phosphate buffer solution. Solutions of D-(+)-Glucose, $\geq 99.5\%$ in PBS and D-(−)-Fructose, $\geq 99\%$ (Sigma Aldrich) in PBS were prepared at concentrations ranging from 10^{-4} M to 1 M.

A model, taken from Aumann et al. [137], was used to estimate the surface tension for each solution, as previously performed for the propan-1-ol and water solutions. The equation for the surface tension analysis of saccharides requires the concentration of the liquid, the surface tension of the solvent and a constant to calculate the surface tension of the binary mixture of saccharide and water, as described in Equation (4.5).

$$\sigma' = (\sigma_w + \frac{\Delta\rho}{\Delta C}C)\cos\theta \quad (4.5)$$

To determine the surface tension σ , the HC-PCF system was calibrated with the solvent only ($C = 0$). This is done by measuring the average flow velocity of the solvent PBS, and calculating the surface tension σ in Equation (2.24). The value found for σ is then inserted into Equation (4.5) to determine the cosine of the contact angle, taking $\sigma_w = 0.0695$ N/m from literature [181]. In this experiment, the angle θ was estimated to be 50° , using our results and known values for PBS [103].

Table 4.4: Experimental data of velocity and viscosity for PBS solutions of glucose and fructose.

| Concentration | Length | Velocity | Surface Tension | Viscosity |
|---------------|--------|--------------------|-----------------|-----------|
| M | m | mm s ⁻¹ | mN/m | mPa.s |
| Glucose | | | | |
| 1 | 0.12 | 0.69 | 46.07 | 1.38 |
| 0.5 | 0.116 | 0.86 | 45.42 | 1.60 |
| 0.1 | 0.115 | 1.00 | 44.90 | 0.98 |
| 0.05 | 0.114 | 1.08 | 44.84 | 0.91 |
| 0.01 | 0.109 | 1.19 | 44.78 | 0.86 |
| 0.006 | 0.114 | 1.00 | 44.78 | 0.98 |
| 0.005 | 0.105 | 1.08 | 44.78 | 0.99 |
| 0.004 | 0.105 | 1.09 | 44.78 | 0.98 |
| 0.003 | 0.122 | 0.94 | 44.77 | 0.98 |
| 0.002 | 0.123 | 1.05 | 44.77 | 0.87 |
| 0.001 | 0.105 | 1.19 | 44.77 | 0.90 |
| 0.0005 | 0.109 | 1.16 | 44.77 | 0.88 |
| Fructose | | | | |
| 1 | 0.118 | 0.59 | 46.07 | 1.69 |
| 0.5 | 0.109 | 1.12 | 45.42 | 0.93 |
| 0.5 | 0.109 | 1.23 | 44.90 | 0.85 |
| 0.1 | 0.112 | 1.06 | 44.78 | 0.94 |
| 0.01 | 0.110 | 1.15 | 44.78 | 0.89 |
| 0.001 | 0.112 | 1.14 | 44.777 | 0.87 |

The average filling velocity was measured for these solutions as a function of concentration, using the fibre length and time taken for each solution to fill the HC-PCF sample. The results are displayed in Table 4.4. For concentrations below 0.01 M, the velocity appears to be constant with an average value of (0.9 ± 0.2) mm s⁻¹. The error was estimated from the uncertainty in measuring length and filling times of the fibre. The random variations of velocity for concentrations below 0.01 M are probably due to temperature fluctuations between measurements or temperature gradients within the set-up. Above this concentration level, surface tension and viscosity values increase rapidly. There is a notable decrease in the average velocity due to the decrease in the ratio of surface tension to viscosity.

The values of viscosity for aqueous solutions of glucose and fructose taken from

Table 4.5: Viscosity values from literature for mono-saccharides glucose and fructose in solution with water.

| Concentration (M) | Viscosity Glucose (mPa s) | Viscosity Fructose (mPa s) | Reference |
|----------------------|------------------------------|-------------------------------|-----------|
| 0.028 | 1.01 | 1.01 | |
| 0.056 | 1.02 | 1.02 | |
| 0.084 | 1.03 | 1.04 | |
| 0.112 | 1.05 | 1.05 | |
| 0.14 | 1.06 | 1.06 | |
| 0.168 | 1.08 | 1.08 | [172] |
| 0.196 | 1.09 | 1.09 | |
| 0.224 | 1.11 | 1.10 | |
| 0.252 | 1.12 | 1.12 | |
| 0.28 | 1.14 | 1.13 | |
| 0.308 | 1.16 | 1.14 | |
| 0.336 | 1.17 | 1.16 | |
| 0 | 1 | | |
| 0.5 | 1.26 | | [182] |
| 1 | 1.59 | | |
| 1.5 | 1.99 | | |
| 0.27 | 1.36 | 1.26 | |
| 0.56 | 1.58 | 1.43 | [173] |
| 1 | 2.13 | 2.09 | |
| 0.56 | 1.07 | 1.02 | [174] |
| 1 | 1.68 | 1.59 | |

the literature, as shown in Table 4.5, were fitted with a well known equation (4.6) [115].

$$\mu(C) = \mu_0 + A\sqrt{C} \quad (4.6)$$

where C is the concentration of the solute in the solvent, A is a parameter determined by the fitting of the data, and μ_0 is the viscosity of the solvent, water in this case.

The value for the viscosity of PBS (μ_0) is taken to be 1.002 mPa.s [183] and A is calculated from literature [172, 173, 174, 182] by fitting Equation (4.6) to the values outlined in Table 4.5. For glucose, $A = 6.08 \times 10^{-4}$ Pa.s/(M^{1/2}) and for fructose, $A = 6.01 \times 10^{-4}$ Pa.s/(M^{1/2}).

The viscosity results for glucose and fructose are very similar as expected due to their similar physical parameters. The concentration dependent viscosity was determined with Equation (4.6), using surface tension values from Auman et

al. [137] with a selection of data from the literature [172, 173, 174, 182], which are represented by the red and blue fitted lines in Figure 4.23 and are outlined explicitly in Table 4.5. The viscosity measurements from the literature were determined at similar temperatures in aqueous solutions, but different experimental approaches were utilized.

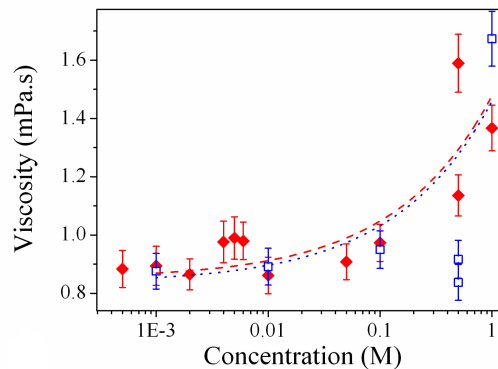


Figure 4.23: Results obtained with the optical fibre viscometer for the measured viscosity, with concentration for the glucose (red, closed diamond symbols) and fructose (blue, open square symbols) in PBS solutions. The red dashed and blue dotted lines are fitted using Equation (4.6) and data from the literature [172, 173, 174, 182], also presented in Table 4.5.

Looking at the trends in Figure 4.23, for low concentrations the changes in viscosity are expected to be within the error limit, as the amount of saccharide added to the solvent is very small. For higher concentrations, however, the viscosity becomes sensitive to the solute concentration. Figure 4.23 illustrates this dependence of the viscosity with increasing saccharide concentrations above 0.1 M, showing that the technique proposed here to determine the solutions viscosity gives similar results for the measurement when compared with other well established techniques. The experimental data in Figure 4.23 (b) has a standard deviation of 0.05 mPa.s for glucose and 0.12 mPa.s for fructose, from the data from literature. The experimental measurements of viscosity for glucose and fructose solutions trend to the values from the literature. The optical fibre viscometer proposed here has the added advantage of small volumes being handled, below 10 nL.

4.3.3 Observations for Saline Solutions

The optical fibre viscometer shows great potential for determining the viscosity of a wide range of solutions over a wide range of concentrations, that preserve the

silica structure of the capillary walls. However, for other solutions, such as saline solutions (e.g., NaCl, NaHCO₃,) ranging from 0.1 mM to 0.1 M, it is observed that the salt reacted with the silica of the fibre, creating deposits on the walls, and resulting in a blockage of the capillaries of the fibre. When examined under the microscope, the fibre ends were contaminated with these deposits and the micro structure of the fibre could no longer be identified.

Further chemical investigations must be realised in order to determine the full limitations of the technique presented here, but the majority of water based solutions, including interstitial fluids, saccharide solutions, and alcohols will be good considerations for analysis.

4.4 Summary

This section outlined the theory and experimental practice behind using the capillary structure and optical properties of HC-PCF as a nano litre optical fibre viscometer. The system was verified to determine its re-usability, error measurement and accuracy in comparison to the capillary model in Chapter 2. The dynamic optical properties of the HC-PCF while filling with a liquid were investigated to understand the optical properties change over the three states of the fibre; empty, core filled and fully filled.

Aqueous solutions of propan-1-ol, glucose and fructose were studied in detail to determine the systems response to different liquids and a wide range of viscosities. These liquids were chosen not only for their versatility, but also due to the availability of data for the viscosity and surface tension over a wide range of concentrations from literature. As a final analysis, the estimations for the solutions viscosities were compared to the literature for all cases, and it was found that the results from the optical fibre viscometer correlated well, within the limits of the error bars, with the results available from the literature.

- The optical fibre viscometer system and experimental set-up was discussed in detail.
 - The alignment was facilitated by a 1060 nm pump wavelength SC source.
 - The experimental laser source and fibre was chosen to optimise the measurements for the PBG shift in the HC-PCF when filling with a

liquid of refractive index (n_{liquid}).

- The temperature control system was implemented utilising copper as a heat transfer material and maintaining temperature with a system of Peltier heaters.
- The timing mechanism for the liquid filling was discussed in detail, showing examples for many different timing experiments.
- The optical nano litre viscometer was tested with solutions of glucose, fructose and propan-1-ol and the results compared to literature.

Chapter 5

Optical Transmission Properties of Liquid Filled Hollow Core Photonic Crystal Fibres

In this chapter the transmission properties of liquid filled hollow core photonic crystal fibres (HC-PCF) are investigated to determine the light guiding properties as the filling state of the fibre changes from empty to core only filled and fully filled. Understanding the constraints of light guiding in HC-PCF is important to characterise the fibres response to liquid insertion over a wide spectral range, from the visible to infrared regions. A full appreciation of the spectral and spatial light guiding properties is used to quantify the HC-PCF for its applicability as a tool for liquid sensing, for a wide variety of applications in viscometry, Raman, fluorescence and absorption or transmission spectroscopy.

To theoretically estimate the light guiding properties of HC-PCF, the wave equations for the periodic micro-structure must be solved numerically. Modelling the propagation properties of these fibres is challenging, requiring demanding computer simulations that employs computationally time expensive techniques, such as the super cell methods [81] and finite element methods [184]. HC-PCF have been studied extensively using these methods [185]. However, at this present time, the light guiding profile of partially or completely filled fibres has received less attention both computationally and experimentally. This is due to the difficulty in distinguishing between the modes generated within the fibre, once the guided light has exited the core. The liquid in the core and the capillaries results in a dynamically changing interface, which increases the difficulty in determin-

ing the modes. Measuring and mapping how the propagation changes over the cross section of the micro-structure when the fibre is filled with liquid will allow a better understanding of how these fibres can be employed optimally for liquid sensing.

There are three filling states of the fibre that are utilised in this thesis for sensing and measurements; (a) an empty fibre, (b) a core only filled fibre, resulting in index guiding [96, 186] and (c) a fully filled fibre, resulting in light guiding by a shift in the photonic band gap (PBG) [93]. These states are used in Chapter 4 to measure the velocity of liquid flow as the propagation properties of the fibre change dynamically while filling with liquid. These states are also used in Chapter 6 and Chapter 7 to generate and collect Raman scatter from liquid samples contained within the capillaries of HC-PCF segments.

To understand the light guiding properties of the fibre experimentally, as the internal refractive index was changed either by selective or by full filling, the fibres were tested and mapped using a broadband light source and an optical spectrum analyser (OSA). This analysis allowed a clear understanding of how wavelengths are guided within the core and the micro-structured cladding, and verified the changes in propagation properties when the fibre is infiltrated with liquids. This was further exemplified using a single laser source, and a Shack-Hartmann interferometer to determine the wavefront of the emitted light for the core only filled and fully filled cases in this chapter. Section 5.3 utilised the information of the propagation properties in both states to estimated the numerical aperture change due to liquid filling.

5.1 Light Transmission Experiments

The light source used in the experimental set-up used to map the transmission spectrum of the fibre was the supercontinuum (SC) source, already described in Chapter 4, generated by a semiconductor pumped Q-switched Nd: YAG laser at 1064 nm (6.85 kHz repetition rate, ~ 0.55 ns pulses, 73.5 mW average power), whose light pumped a non linear PCF (SC-5-1040, Blaze Photonics) to generate a broadband emission between ~ 500 - 1750 nm. The SC source light was collimated using a $\times 40$ infinity corrected lens (L1) and was focused to an empty segment of HC-PCF by another $\times 40$ infinity corrected lens (L2) as shown in Figure 5.1 (a).

HC-1060 fibre segments of 10 cm in length were chosen for experiments, as they

were long enough to enable accurate optical alignment, and did not require filling times greater than five minutes. The fibre tips had their cladding jacket removed, 2 cm from each end, in order to allow cleaving of the ends for better light coupling. The fibre was held horizontally in place by clamps located on two separate xyz nano-positioning stages. These stages were used for the initial alignment of the fibre.

The HC-PCF segment was aligned to the system using the SC source and a bandpass filter at 1050 nm (with 10 nm FWHM), to utilize the fibres PBG as shown in Figure 5.1 (a). A charged coupled detector (CCD) camera (colour sensor Sony ICX204AK) was used to monitor the near field images of the HC-PCF output (not shown in Figure 5.1). The CCD images were recorded via a universal serial bus (USB) at 30 frames/s.

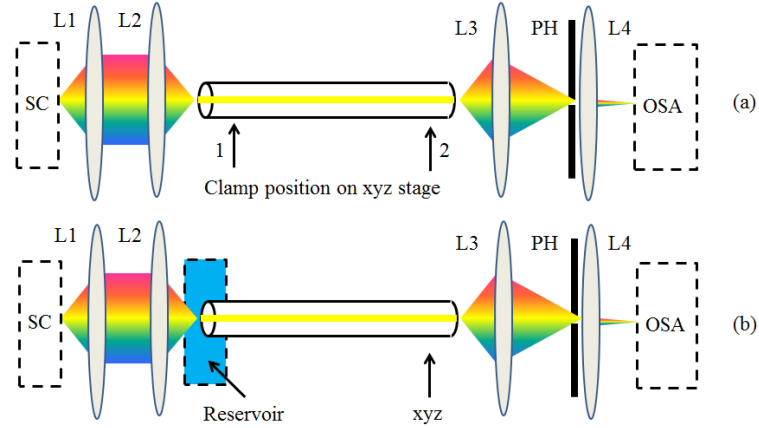


Figure 5.1: Experimental set-up for mapping the transmission properties of the HC-PCF when illuminated with a supercontinuum source (a), and when a reservoir was placed at L2 (b) so that the SC was focused through a PMMA window to the fibre inserted in a liquid filled reservoir. Alignment was facilitated using a motorized xyz stage at the input lens (L2). Transmitted light from the fibre was passed through a pinhole (PH) and collected for analysis by an optical spectrum analyser (OSA). Lenses used in the system were: L1, L2, L4 = $\times 40$ and L3 = $\times 60$ (diagram not to scale).

After alignment, the filter was removed and the entire spectrum was focused to the HC-PCF by L2. The light transmitted through the fibre was then collected by a $\times 60$ infinity corrected lens (L3) which had a focal length of 2.9 mm and passed the light through a circular pinhole (PH) ($100\ \mu\text{m}$ diameter, $0.008\ \text{mm}^2$ area, $12.5\ \mu\text{m}$ thickness), positioned a distance of 10 cm from L3. The PH blocked the majority of the light transmitted from the HC-PCF, to study a small area of the image from L3. The lens, L3 is a complex, infinity correction lens, that consists

of a number of lenses, normally used as a microscope objective lens. However, for these experiments, it is assumed that this complex lens can be simplified to one lens, of focal length 2.9 mm. In this experiment, the image is formed at a distance of 10 cm from the lens, and we assume that due to this large distance, in comparison to the focal length, our assumption to treat this as a one lens system is valid. Therefore, the magnification of the transmitted image was estimated by considering the value of the focal length of L3, and the distance of the PH from L3. A schematic demonstrating the positions of the object, image and focal length is shown in Figure 5.2.

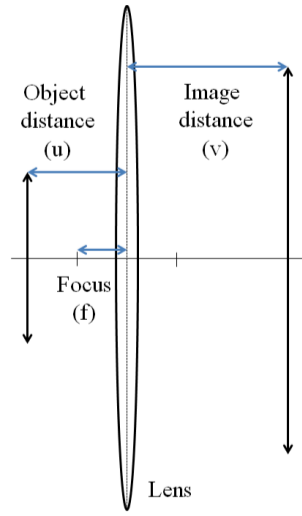


Figure 5.2: Schematic of a simple lens, showing the positions of the object distance, image distance and focal length.

The object distance, (u) could be estimated using the equation for a simple lens;

$$\frac{1}{u} + \frac{1}{v} = \frac{1}{f} \quad (5.1)$$

where u = object distance, v = image distance, and f = focal length of L3. The distance of the object from the lens was therefore determined to be 3 mm. The ratio of the object distance (u) to the image distance (v) gives the magnification of the image, which in this case was estimated to be 33. Therefore the micro-structure of the fibre image had a cross sectional area of 2.13 mm². The 100 μ m PH will allow the transmission of a 3.03 μ m diameter of the HC-PCF, and a 7.2 μ m² area section of the HC-PCF image, when the magnification factor of 33 is taken into account. This is calculated by considering the 100 μ m diameter of the PH, and dividing it by the magnification size to determine the actual diameter of the fibre.

The light allowed through the PH was collected with a $\times 40$ objective lens which focused the light to a multi-mode patch-chord (core diameter $200\ \mu\text{m}$, numerical aperture 0.22) that allowed the signal to be analysed by an optical spectrum analyser (OSA, Ando AQ-6315E, $350\ \text{nm} - 1750\ \text{nm}$, resolution $10\ \text{nm}$, and sweep time $2.5\ \text{s}$). The spectra were collected and sent to a computer via USB. Lens L3 and L4 were mounted on separate xyz stages. This method allowed the mapping and analysis of the empty HC-1060 segment. The measurement procedure is discussed further in Section 5.1.2.

5.1.1 Adaptation of the Experimental Set-Up for Liquid Filled Fibres

The liquid used for these experiments was water, and filled the fibre by capillary action (no over pressure was used). For the experiments with liquid filled fibres, a slight modification of the experimental set-up was required. The liquid fibre needed to be inserted into a reservoir at all times to ensure that the capillaries remained liquid filled, such that there was no leakage of liquid during the measurements which would effect the transmission properties of the HC-PCF. The reservoir was positioned at the input (L2- on the side where the light enters the fibre) and featured a polymethyl methacrylate (PMMA) window ($1\ \text{mm}$ thickness) to facilitate coupling of light to the fibre. Positioning of the reservoir just after L2 leads to initial loss due to non-optimum coupling of SC to the core of the fibre, through the PMMA window of the reservoir. However, reversing the optical system so that the SC source is coupled to the cleaved fibre end and the reservoir positioned at L3 was observed to result in a near identical spectral output detected by the OSA. For all experiments described on this chapter, the reservoir was positioned just after L2, for the duration of the measurements.

For the core only filled state, the fibre sample needed to undergo a further preparation step before being filled with liquid, to ensure that only the core was filled. One end of the fibre was placed in a Fujikura fusion splicer (FSM45PM), and underwent heating to melt the openings of the capillaries, with the exception of the core channel, which was kept open, as described next in Section 5.1.3. The details and parameters used for this method for fibre preparation have been documented previously [104].

5.1.2 Measurement Procedure

The aim of this experiment was to measure the spectra from a small area of the fibre image that was selected spatially by the PH. The experimental measurement proceeded as follows: starting at the edge of the micro-structure, the fibre was scanned in steps by shifting the transmitted image (L3) of the fibre with the xyz nano-positioning stage that held the $\times 60$ lens at the output. The xyz stage at the input lens (L2) remained unchanged in order not to compromise the alignment. One actuator (on the x-axis for L3) was turned at each step by a distance of $x = 2 \mu\text{m}$, which shifted the image of the fibre relative to the PH.

A schematic of the lens system is seen in Figure 5.2. This marks the object position (the end facet of the HC-PCF) and the image position after the lens. The image was formed a distance of 10 cm from the lens, at the PH, as viewed by a CCD camera. Figure 5.3, depicts the ray diagram for the system. Three main rays are used to determine the position of the image after the lens, shown in red, blue and green. The red ray originates from the top of the object, and proceeds horizontally to the central point of the lens, after the lens it passes through the focal position. The blue ray proceeds directly through the centre point of the lens. The green ray proceeds through the focal point before it reaches the lens, and then proceeds horizontally. The point where all three rays meet is the point where the image occurs. This is repeated in this figure for the sections of the object that occur above and below the central axis.

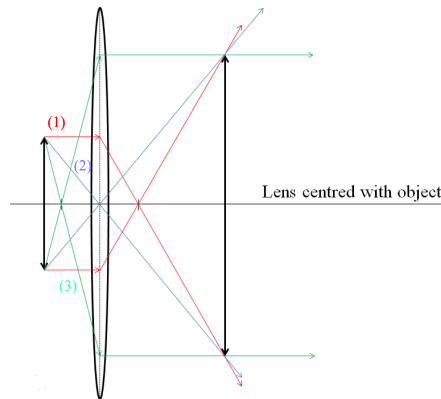


Figure 5.3: Figure showing the position of the object and image formation using a lens. The position of the image is determined using ray tracing methods, outlined in red, blue and green.

When the lens is shifted with respect to the object, the image is also expected to shift. This is demonstrated schematically in Figure 5.4, using the ray diagrams.

These two diagrams show how the image is expected to shift as the lens is moved downwards in steps, as per the experimental method.

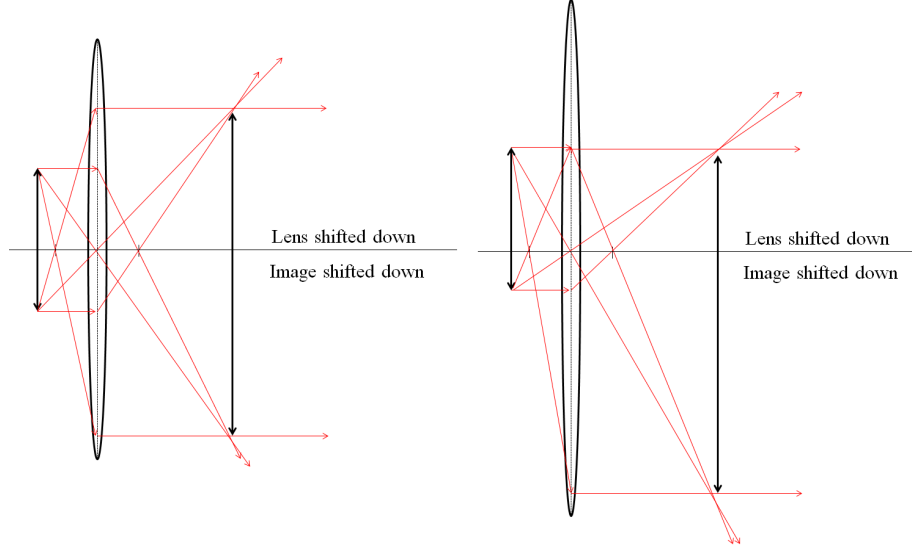


Figure 5.4: Diagram demonstrating the shift of the image as the lens position is changed.

The selection of the image by the PH is exemplified in Figure 5.5. At (a), the portion of the object that is aligned to the centre of the lens is focused through the lens to the PH. The ray that originates from the object (shown by the blue dot), through the centre of the lens and terminates at the image position indicates that this portion of the object shall be positioned at the PH. When the lens is moved downward, by a distance x , the ray that passes through the centre of the lens is now shifted downwards to the red dot, a distance of Δy from the original position. This indicates that another section of the image of the object is focused to the centre of the PH, as shown in Figure 5.5 (b).

The step size of each measurement can be estimated using the ray diagram schematic in Figure 5.5 (c). This schematic shows a triangular interpretation of Figure 5.5 (b). The movement of the lens, x is known, as this is the movement of the actuators on the xyz holding L3. The distance from the lens to the PH is known (10 cm), and the object distance to the lens has been previously calculated (3 mm). To calculate the step size, Δy , of the object, after the lens has been moved by $x = 2 \mu\text{m}$, simple geometry of the image formation is used. The blue triangle traces the ray from the image to the centre point of the original position of the lens, and the red triangle, traces this ray to the object position after the lens has been moved by x . The ratio of the lens step size to the image distance is equivalent to the object step size to the sum of the object and image

distance. The step size (Δy) is therefore the ratio of the lens movement to the image distance multiplied by the sum of the image and object distance, as shown in the equation;

$$\Delta y = \frac{(u + v)x}{v} \quad (5.2)$$

In this way the magnified image was shifted in steps of $2.06 \mu\text{m}$ across the PH, by changing the position of the lens by $2 \mu\text{m}$ for each measurement. Another method that could have been used was the shift of the PH and detection system in steps across the image.

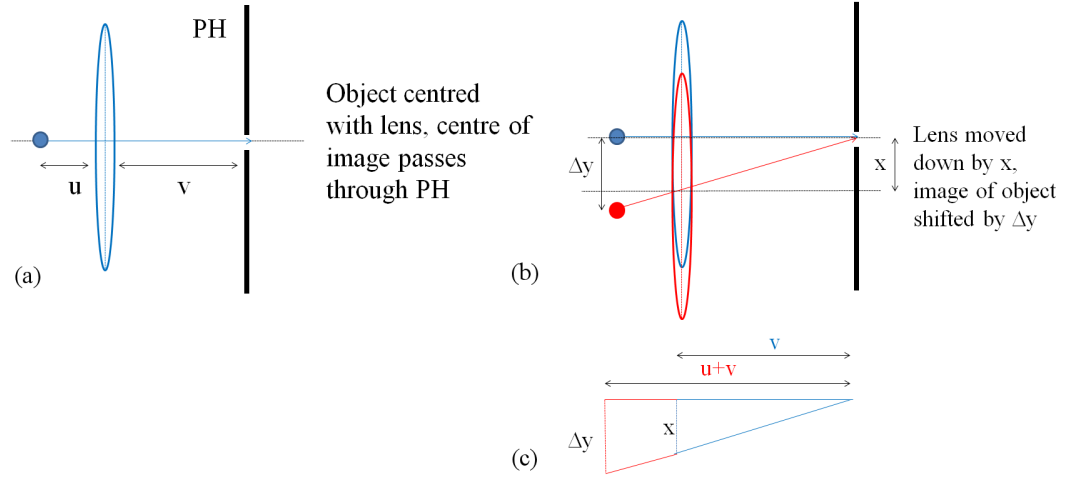


Figure 5.5: Schematic to demonstrate the calculation of the step size of the image, as the lens is moved in steps. (a) indicates the formation of the image of the blue point at the centre of the PH. (b) indicates the formation of the image of the red dot at the centre of the PH. (c) schematically represents the ray diagrams of the object position and image position, using simplified geometric diagrams.

A selection of near field images taken with a CCD, of the output of an empty HC-1060, transmitting the full SC source are shown in Figure 5.6. These images are taken a distance of 10 cm from the L3 lens, and show the magnified image of the core of the fibre and surrounding micro-structure. The image in Figure 5.6 (a) is the position of the fibre, when it is centred with the PH. In this position, the PH will allow the transmission of the spectrum from an area within the hollow core of the fibre. The image in Figure 5.6 (b) shows the same fibre, when the lens L3 has been shifted by $20 \mu\text{m}$ so that the PH records the transmission spectrum from an area of the micro-structure. This demonstrates that using L3 to sweep the image of the fibre across the pinhole, maintains the image information of the transmission of wavelengths and the fibre structure is not deformed. For all measurements and mapping of the transmission spectra, these errors due to non optimum centring of the fibre with L3 are neglected.

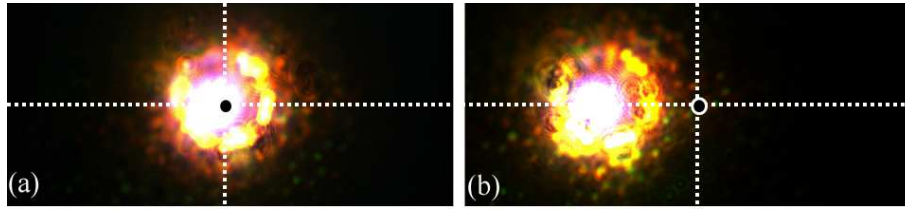


Figure 5.6: Images of an empty HC-1060 transmitting the full SC source when (a) the image is centred with the PH and (b) when the lens is shifted by $20\text{ }\mu\text{m}$, resulting in a change in the image position with respect to the PH. The PH is shown as a black circle at the centre of both images.

Schematically, Figure 5.7 shows the images of the HC-PCF when empty (left), core only filled (centre) and fully filled (right), when no pinhole is used. The images are taken with an optical microscope (Nikon Eclipse ME600). Furthermore, the images in Figure 2.6, demonstrate the propagation of the SC source through an empty, core filled and fully filled fibre respectively. These images illustrate the purpose of the work here, to measure the spatial dependence of the transmission spectrum for the three different states of the fibre for a wide range of wavelengths. This is facilitated using the PH and the OSA to determine the spectral and guidance properties of the HC-PCF over the micro-structure for all three states.

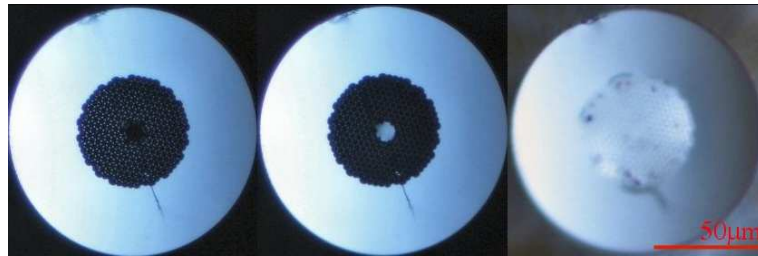


Figure 5.7: Images of all three filling states (left to right: empty, core only filled and fully filled) and guidance properties of the HC-PCF segment. Taken with a Nikon Eclipse Microscope $\times 500$ magnification.

5.1.3 Selective Core Filling

To facilitate the selective filling of the core only, the capillaries in the micro-structure were blocked at one of the end facets, with the core left unblocked. To perform this adjustment to the end facet, there are several methods, many of these are time consuming, and can be found in literature and include side access, polymer curing, and others [68, 107, 187]. There is one method, which is repeatable and that can be performed in minutes. This is satisfactory for

the purposes required here, to block the external capillaries, and leave the core channel open. This method involves the use of a high precision fusion splicer, with adjusted parameters that will melt the external regions of the fibre, causing the capillaries in the micro-structure to collapse and seal, but leaves a narrow opening in the centre of the HC-PCF that allows an access channel to the core of the fibre. With the correct parameters of fusion time and distance, the external melting of the capillaries can be performed repeatedly, and controlled to tailor the radius of collapsed capillaries and the length of the collapsed region of the end facet. To collapse the capillaries of the fibre, leaving the core channel open, a pre-fuse power of 21 bits was applied to both end facets for 180 ms, using the fusion splicer. An example of the collapsed fibres can be seen in Figure 5.8.

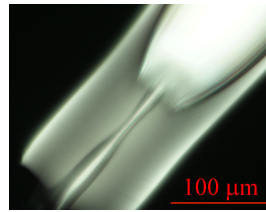


Figure 5.8: Example of the end facet of a HC-1060, after collapsing the capillaries using a fusion splicer. The capillaries are completely sealed, in comparison to an untreated fibre, and the core channel remains open to allow filling of the central channel. Image recorded with a Nikon Eclipse Microscope $\times 500$ magnification.

5.2 Experimental Results

The collection of spectra for each position, recorded by the OSA and the PH was consolidated into a mapping file, that allowed the transmission of spectra to be analysed over the entire micro-structure. Data was collected for a sequence of positions at a distance of $2.06 \mu\text{m}$ across the diameter of the HC-PCF end facet as described in the experimental section, and shown in Figure 5.1. The collected power at each position corresponds to the light transmitted through an area of $7.2 \mu\text{m}^2$ of the micro-structured region. The data was originally measured in units of dBm by the OSA. This method results in the schematic presentation of wavelengths, from -30 dBm to below -75 dBm. The results are shown in two sections, for the empty fibre (Section 5.2.1), and for the liquid filled fibres (Section 5.2.2). The data was analysed first in dBm, as measured by the OSA. It is then

converted to mW, using the equation:

$$P(mW) = 10^{P_{dBm}/10} \quad (5.3)$$

Where P_{mW} is the power in mW and P_{dBm} is the initial measurement in dBm. The data was then normalised to the peak power. Finally the power profiles over the cross section of the micro-structure were analysed to determine the guidance properties of the liquid filled fibres. This is motivated to quantify the fibres use as a liquid sensor, to determine the collection efficiencies of the fibre, and to estimate the change in numerical aperture.

5.2.1 Mapping Distribution of an Empty HC-1060

The mapping profile for the empty HC-1060 (a cross section of HC-1060 is seen in Figure 3.2) is shown in Figure 5.9. The plot was composed using the software Origin Pro 8.0, which uses Delaunay Triangulation to compute and draw the contour lines. The interpolation of the data allows the image to appear continuous, instead of a selection of points, which gives the appearance that there are a greater number of data points. It should be noted, that the points refer to an area of $7.2 \mu\text{m}^2$ at every $2.06 \mu\text{m}$, with a spectral resolution of 0.1 nm .

The y-axis displays the wavelength in nm, the x-axis displays the positioning as a function of distance in μm from the very centre of the fibre (defined as the centre of the hollow core in the micro-structured cross section). The coloured contour plot represents the different power ranges in dBm, of the measured wavelengths over the cross section of the HC-PCF. The hollow core is within the region of $\pm 5 \mu\text{m}$, indicated by the vertical lines in Figure 5.9, and beyond this region is the micro-structure of capillaries. The primary PBG can be seen in the wavelength range from $900 - 1200 \text{ nm}$ and the secondary PBG can also be seen in the range from $700 - 750 \text{ nm}$. There are some asymmetries in the contour plot, which can be explained due to error in the imaging process. Guidance in all cases is mainly confined to the $10 \mu\text{m}$ diameter core, and the surrounding $\pm 5 \mu\text{m}$, with a very low power (-70 dBm) of some wavelengths within the micro-structure. The measurement on the dBm logarithmic scale allows wavelengths at very low intensities to be represented in Figure 5.9.

The data from the OSA measurements was then converted to mW and normalised to the peak point to give a linear definition of the guidance of the broadband SC

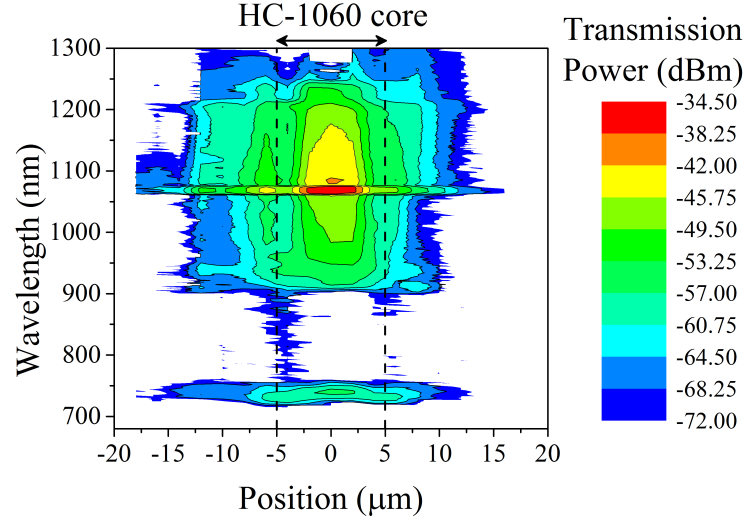


Figure 5.9: Data mapping of the wavelength propagation distribution over the cross section of the HC-PCF in dBm from the OSA, for an empty HC-1060. The data was interpolated to create a continuous contour plot, however, data was taken for an area of $7.2 \mu\text{m}^2$ at every $2.06 \mu\text{m}$, with a spectral resolution of 0.1 nm .

source within the micro structure of the fibre, and the intensities of the transmitted wavelengths. As seen in Figure 5.10 (a), wavelengths from 1060 - 1150 nm for the original PBG are guided within $\pm 4 \mu\text{m}$ of the centre of the core, normalised from 0.2 - 1. There is also weak guidance of light at wavelengths, from 500 - 1200 nm within the core (< 0.2). As expected, the main wavelength range is within the 1060 nm PBG confined tightly to the core of the fibre [160]. The data at 1060 nm is fitted with a Gaussian distribution, as seen in Figure 5.10 (b), to determine the FWHM for the case of the empty HC-PCF, which is $4.51 \mu\text{m}$, with $\sigma = 1.91 \mu\text{m}$. The $1/e^2$ width value for the empty fibre is estimated to be $7.66 \mu\text{m}$, using the relationship

$$width_{1/e^2} = \frac{\sqrt{2} \text{ FWHM}}{\sqrt{\ln 2}} \quad (5.4)$$

Transmission is mostly forbidden in the micro-structured region, as predicted from the theory of the PBG effect, described in Chapter 2. This value for $1/e^2$ can be compared to that from the specification sheet, included in Appendix C. This gives a value of $7.5 \mu\text{m}$ for the mode field diameter.

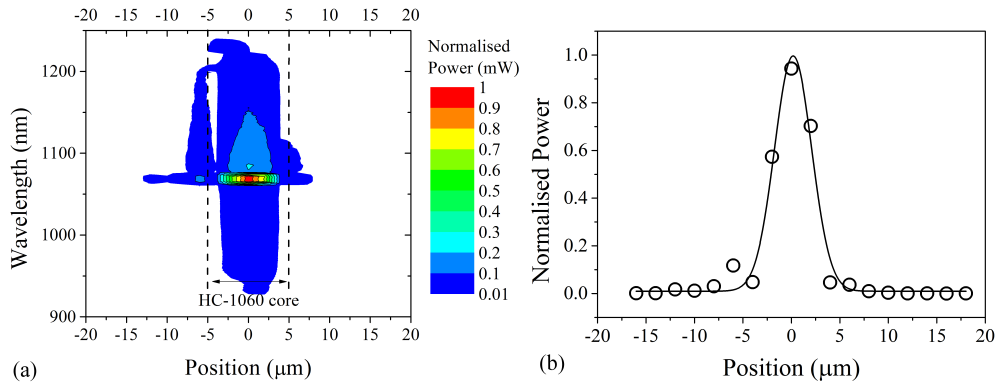


Figure 5.10: Data from the mapping of the cross section of the HC-PCF for an empty HC-1060 in mW. (a) The full spectrum of the PBG. The mode is tightly confined to the centre of the hollow core. (b) Gaussian fit of the data at 1060 nm.

The mapping of the micro-structure in dBm in Figure 5.9 shows a broader confinement of light that spreads to the silica capillaries that surrounds the core. This is also seen in the CCD image in Figure 2.6 (a), where there is propagation of a variety of wavelengths within the silica capillaries. From the CCD images and the mapping in dBm and mW, it is concluded that guidance confinement of greatest power occurs within the hollow core of the HC-PCF for the wavelengths allowed by the PBG. Wavelengths outside this range are filtered by the PBG and scattered into the micro-structure. Some of these forbidden wavelengths can become partially guided within the silica bridge surrounding the core, however, there is no evidence of these wavelengths within the periodic micro-structure. This is confirmed by the mapping of wavelengths within the cross section of the HC-PCF by the OSA in Figure 5.9 and Figure 5.10.

5.2.2 Mapping Distribution of Liquid Filled HC-1060

In this section the wavelength mapping distribution results for the core only filled and fully filled states shall be presented and discussed. The experimental measurements for the liquid filled fibres have the draw back that the reservoir was placed between the focusing lens (L2) and the fibre, as seen in Figure 5.1 (b), which would result in additional insertion loss. The PMMA window attenuates the SC source in the visible region, as seen in Figure 4.6. However, despite the non optimum alignment, the liquid filled fibres were characterised for both filling states (core and full filled). The reservoir needed to be positioned at L2, as the

mapping distribution of the micro-structure could only be facilitated when there were no objects, such as the reservoir, that would distort the image from the end facet of the HC-PCF to the PH and OSA. Therefore this set-up allowed the guidance properties in the micro-structure of the liquid filled HC-PCF to be mapped by the method described in Section 5.1.2.

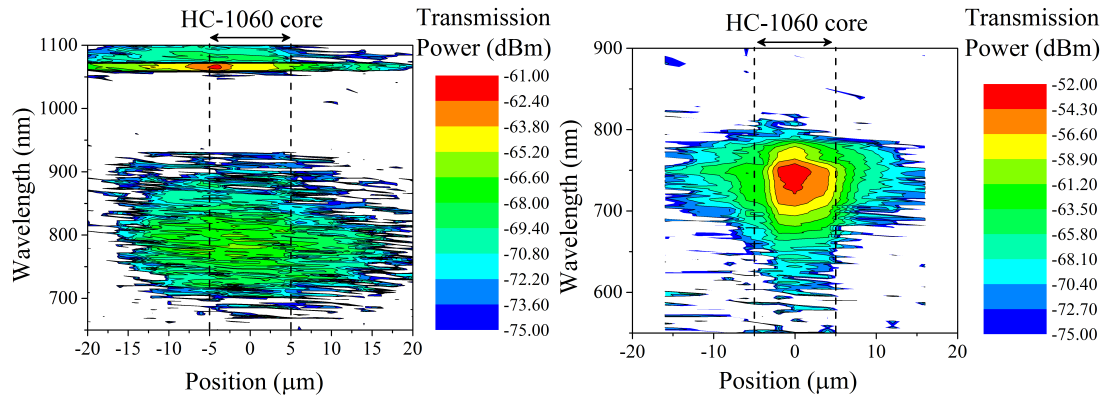


Figure 5.11: Contour plots of the mapping distribution of wavelength transmission for the (left) core only filled with water and (right) fully filled with water, for a HC-1060 fibre 10 cm in length. Both plots are measured in dBm with an OSA.

The contour plots in dBm, measured by the OSA are displayed in Figure 5.11 for the core only filled fibre (left) and the fully filled fibre (right), for a 10 cm HC-1060 sample. In both cases it is concluded that light guiding is shifted toward the visible region, between 700 - 900 nm for the core only filled fibre, and between 600 - 800 nm for the fully filled fibre. The core only filled fibre also guides light at the original PBG at 1060 nm, which is due to the presence of the air filled micro-structure surrounding the water filled core. This retains the features of the original PBG, and results in a hybrid guidance of PBG and index guiding in the core only filled case. These contour plots are in agreement with the transmission spectra accumulated for the entire micro-structure in Chapter 4, Figure 4.5. It was also observed that the core only filled fibre had a peak measurement at -61 dBm, which is 9 dBm lower than the fully filled case. This is due to the collapsing of the capillaries that is required to ensure that only the core is filled. This process changes the structure of the fibre, so that initially, light is coupled to a water core, surrounded by collapsed silica capillaries, which results in a loss of coupling efficiency. After ~ 5 mm, the structure changes to water core surrounded by an air silica cladding, resulting in index guiding and PBG guidance.

The contour plots show very different guidance properties when compared side by side, as seen in Figure 5.11. The fully filled fibre (right) guides by the shifted

PBG effect. As a result, the highest transmission power is seen at the centre of the core of the HC-PCF, and decays quickly with distance from the centre to the micro-structured region. This is similar to the empty HC-PCF mapping distribution, seen in Figure 5.9. The core only fibre guides by a modified index guiding. As such, the fibre exhibits a broad guidance of wavelengths at similar intensities within the core region, and also maintains the original PBG at 1060 nm due to the empty micro-structure cladding surrounding the liquid core.

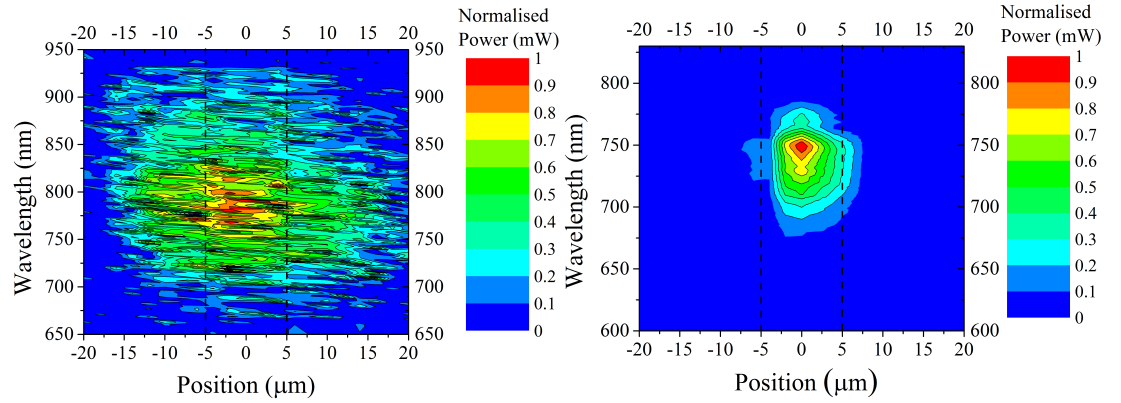


Figure 5.12: Contour plots of the transmission mapping distribution of the (left) core only filled with water and (right) fully filled with water, for a HC-1060 fibre 10 cm in length. Both plots are in units of normalised mW.

The data in Figure 5.11 was converted to mW and was normalised to the peak power. This is seen in the contour plots in Figure 5.12, for the core only filled fibre (left) and the fully filled fibre (right). These plots demonstrate that the fully filled fibre (right) exhibits fibre core centred propagation in the visible region. The core only filled fibre (left) exhibits the propagation of a wider spread in guided wavelengths and spatially a wider spread of guidance over the core area and micro-structure of the HC-PCF.

A histogram of the power transmitted at the peak of power, averaged over 765 - 785 nm for the core only filled fibre and 745 - 755 nm for the fully filled fibre is shown in Figure 5.13.

The open circles represent the data for the liquid core (red- left) case and the fully filled (blue- right) case. It is evident that the power transmitted by the fully filled fibre (right) is strongly confined to the core, whereas the core only filled fibre (left) has a broader guidance that spans the whole core, and leaks partially into the surrounding micro-structure, assuming single mode propagation and Gaussian-like modes. The data for the liquid core fibre was fitted with a second order polynomial, and the data for the fully filled fibre was fitted with a Gaussian

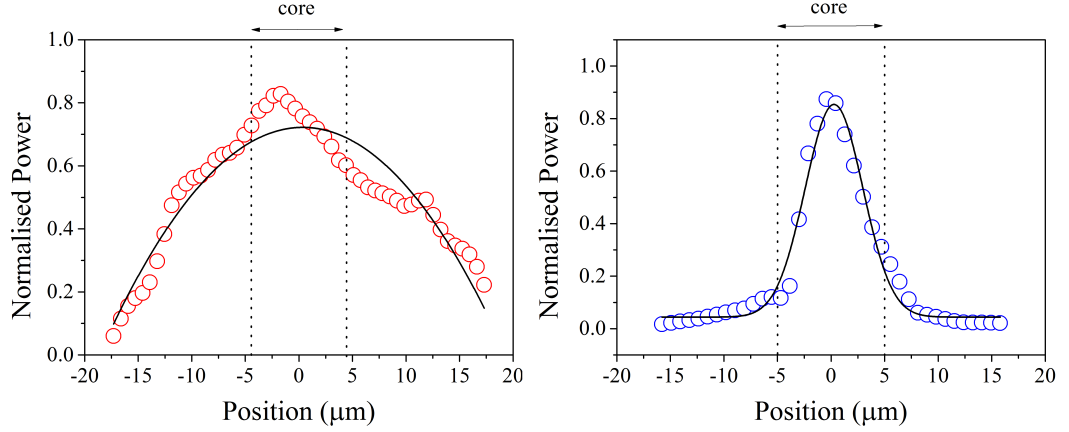


Figure 5.13: Data (open circles) from the three dimensional plots in mW intensities, averaged over 765 - 785 nm for the core only filled fibre (red- left) and 745 - 755 nm for the fully filled fibre (blue- right). A second order polynomial was fitted to the core only filled case and a Gaussian was fitted to the fully filled case.

distribution.

$$F(x; \mu_{mean}, \sigma_{dev}^2) = \frac{1}{\sqrt{2\pi\sigma_{dev}^2}} e^{-\frac{1}{2} \frac{(x-\mu_{mean})^2}{\sigma_{dev}^2}} \quad (5.5)$$

For the core only filled state, the FWHM was estimated to be $27.2 \mu\text{m}$. The fully filled state has an estimated FWHM of $6.3 \mu\text{m}$, and a $1/e^2$ value of $10.7 \mu\text{m}$ (which can be compared with the $1/e^2$ value given for the empty HC-1060 in the data sheet located in Appendix C). This clearly shows the spread in light propagation across the entire core and beyond for the core only filled fibre segment.

For the generation of Raman signal scatter, the intensity of the wavelength and the area of excitation are two important parameters. From examination of the power plots in Figure 5.13, both fibres show great potential for the generation and collection of Raman signal scatter within the liquid filled core due to the guidance properties observed. The fully filled state had a transmission power that was 10 dBm greater than the core only filled fibre. However, this could have been a feature of the non-optimum alignment, due to the positioning of the reservoir at L2, and the initial coupling to the collapsed end of the core only filled fibre. To determine which configuration was optimum for Raman detection, the core only filled and fully filled fibres will be compared in Chapter 7.

Another vital parameter of the guidance properties is the point where the liquid filled fibre will no longer guide light in the visible regime. The broadband source used for the experiments begins to decay in the regime of 500 nm, and at shorter wavelengths cannot be used to measure the transmission properties of the HC-

PCF. However, as seen in Figure 4.5, both the core only filled and fully filled source guide light at shorter wavelengths. To determine the shortest wavelength guided in the core only filled fibre, the radiation line of water can be considered [74, 96]. When the value of λ/Λ becomes greater than the refractive index of water, guidance will no longer occur within the core [96]. For HC-1060, with $\Lambda = 2.75 \mu\text{m}$, this value is 365 nm. For the fully filled fibre, the cut-off wavelength can be estimated using the shifted PBG scalar equations, discussed in Chapter 2. For water filled HC-1060, this is estimated to be 560 nm [148].

5.2.3 Measurements with a Shack-Hartmann Wavefront Sensor

(The following results were measured at C.I.T. with a Shack-Hartmann wavefront sensor, in collaboration with CAPPA, Dr. Milosz Przyjalowski and Dr. Guillaume Huyet.)

To verify the results seen for the mapping distribution, using the PH and OSA, the measurements were repeated using a Shack-Hartmann wavefront sensor (Thorlabs Shack-Hartmann wavefront sensor, 1.3 megapixel resolution WFS150-5C, aperture dimensions: $5.95 \text{ mm} \times 4.76 \text{ mm}$, 39×31 lenslets (lens diameter $146 \mu\text{m}$) with a pitch of $150 \mu\text{m}$). The SC source begins to decay in the regime of short wavelengths (below 650 nm), due to the properties of the non linear PCF which generates the source, as described in Section 4.1. To verify that the mapping distribution seen for longer wavelengths using the OSA is the same at shorter wavelengths, the distribution of a 532 nm and 632.8 nm laser source over the micro-structure of the HC-1060 was captured using a Shack-Hartmann wavefront sensor. A liquid core filled and fully filled fibre were measured to determine the wavefront of the transmitted light for both laser sources. The set-up is similar to that shown in Figure 5.1 (b), with the exception that the PH, L4 and OSA are replaced with the wavefront sensor.

A schematic for the Shack-Hartmann wavefront sensor is shown in Figure 5.14 (a). This figure depicts a wavefront (red) incident on an array of lenses. The transmitted wavefront at each planar convex spherical lens is focused to a detector screen, which is a CCD in this case. Depending on the wavefront, each spot is offset from the centre of the lens, as shown by the red spot. The distortion is compared to a planar wave to reconstruct the wavefront of the incident wave.

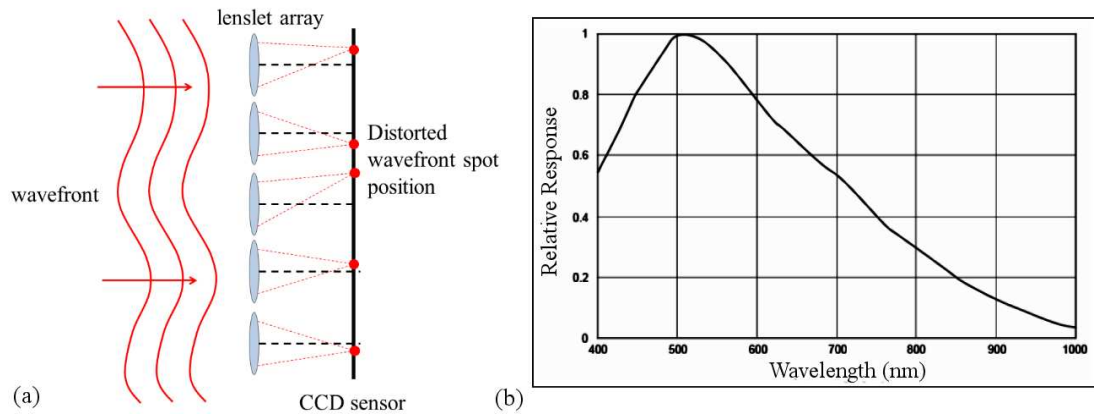


Figure 5.14: A schematic of the Shack-Hartmann wavefront sensor, from Thorlabs Inc. Diagram (a) depicts the set-up of the Shack-Hartmann sensor as a wavefront (red) passes through an array of lenslets and focused to the CCD detector screen (indicated by a black vertical line in the figure). The focused point of each section of the wavefront is indicated by a red dot on the CCD screen. The black dashed lines show the centre of the lenslets. The response curve of the CCD to wavelength is shown in (b) and is courtesy of Thorlabs - Inc.

The typical response of the CCD camera to wavelengths is shown in Figure 5.14 (b), and shows that the camera is most sensitive in the visible wavelength regime.

The two lasers used for the experiments were a frequency doubled Nd:YAG at 532 nm (continuous wave, 4 mW) and a HeNe at 632.8 nm (continuous wave, 1 mW). The HC-1060 sample was aligned to the system for each measurement, as described previously in this chapter. For each of the cases, the wavefront is captured by the wavefront sensor and the result is an accumulation of ten images taken in sequence, with an integration time of 0.1 s. To protect the wavefront sensor from saturation, a selection of neutral density filters were placed in between the fibre output and the detector. The wavefront data taken by the Shack-Hartmann was then used to determine the width of the transmission of the liquid filled fibre. A cross section diameter of the HC-1060 was selected and fitted with a Gaussian to compare the core only and fully filled states, and to determine the width of the wavefront, for the 532 nm and 632.8 nm sources.

The wavefront profiles are shown in Figure 5.15, which are measured as a function of intensity by the CCD sensor. Plot (a) compares the transmitted wavefront of the 532 nm source from the liquid core (red) and fully filled fibre (blue). The open circles are the data taken by the wavefront sensor, and the line represents the fitted Gaussian. Plot (b) compares the transmitted wavefront of the 632.8 nm source for the core filled (red) and fully filled (blue) states, where the open

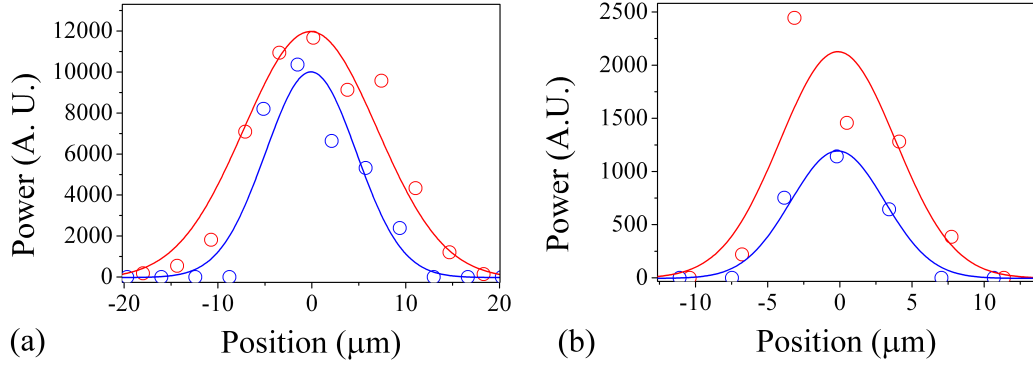


Figure 5.15: Plots of the wavefront transmission of a 532 nm laser source (a) and a 632.8 nm laser source (b) for the core filled (red) and fully filled (blue) states. The open circles in all cases refer to the raw data collected by the Shack- Hartmann wavefront sensor, and the lines are the fitting of a Gaussian distribution to the raw data.

circles and line are the raw data points and Gaussian fit respectively. The data for Figure 5.15 (a) and (b) show that the core only filled state has a broader Gaussian distribution than the fully filled state. This correlates with the measurements previously obtained using the PH mapping method and the SC source. This also verifies that the both lasers at short wavelengths are guided within the core of the fibres in both filled states, which is important for the generation and collection of Raman scatter. This will be examined further in Chapter 6 and Chapter 7.

The width of the Gaussian distribution for the FWHM and $1/e^2$ values for all cases is outlined in Table 5.1. The data for the Shack-Hartmann method is compared to the PH method. As expected for the core filled case, the Gaussian is broader than the fully filled case for all measurements. The PH method contains spatial location information of the wavelengths, and the measurements are made in dBm by the OSA. The Shack-Hartmann wavefront sensor can measure intensity and spatial location of the wavefront. Both methods give different information about the transmission in dBm and as a function of the wavefront. The difference in the width of the Gaussian for the fully filled state could be due to the sensitivity of both systems.

Table 5.1: Comparison of the Shack-Hartmann method and PH method, using the FWHM of the transmission distribution to analyse the transmission of the guided wavelength for the core filled and fully filled fibres.

| Method | Filled State | Wavelength nm | FWHM μm | $1/e^2$ width μm | σ_{dev} μm |
|----------------|--------------|------------------|-----------------------|--------------------------------|---------------------------------|
| Shack-Hartmann | Core Only | 532 | 14.2 | 24.1 | 6.0 |
| | Fully Filled | 532 | 9.7 | 16.5 | 4.1 |
| | Core Only | 632.8 | 9.4 | 16.1 | 4.0 |
| | Fully Filled | 632.8 | 7.65 | 13.0 | 3.3 |
| Pinhole | Core Only | ~ 775 | 27.2 | | |
| | Fully Filled | ~ 750 | 6.3 | 10.7 | 2.7 |

5.3 Numerical Aperture of Liquid Filled Fibres

The numerical aperture is an important parameter in optical systems that determines the range of angles that can be collected for maximum coupling efficiency. For an optical fibre sensor the numerical aperture of the system should be quantified to determine the optimum abilities of the sensor.

The liquid core only filled fibre can be assumed to be treated as an index-like guiding fibre, where the core ($n_{core} \sim 1.33$) has a larger refractive index than the cladding ($n_{clad} \sim 1.05$). The numerical aperture can then be estimated using the equation

$$NA = \sqrt{n_{core}^2 - n_{clad}^2} \quad (5.6)$$

The n_{clad} for a HC-PCF was estimated to be 1.17 by Midrio et al. [188]. This can also be estimated by using the air filling fraction of the micro-structured cladding, as discussed in Section 2.1.2 with Equation (2.4). For the HC-1060 the n_{avg} for the cladding is estimated to be 1.05, for an air filling fraction of ~ 0.9 (taken from the specification sheet included in Appendix C). For a water ($n_{water} = 1.33$) core filled fibre, and an empty cladding, the NA can be estimated to be ~ 0.8 . Taking into consideration the width of the transmission profile of light in the liquid core HC-PCF (see Table 5.1), the collection efficiency of the fibre in this state is advantageous for Raman measurements for the collection of scattered light over a large solid angle.

For a fully filled fibre, the numerical aperture can not be approximated by the index guiding method described above. In this case, the method used for cal-

culating the numerical aperture of a fully filled HC-PCF is the same as for an empty HC-PCF, with the appropriate refractive index change. Using the near field Gaussian mode distribution width estimated in the previous section, of $10.7 \mu\text{m}$, the numerical aperture can be estimated using the relation

$$\tan\theta_{1/e^2} = \frac{\lambda}{\pi\varpi} \quad (5.7)$$

where ϖ is the width of the Gaussian distribution, as described in the literature [189, 190]. Using the $1/e^2$ width of the transmission for the fully filled fibre, and a wavelength of 750 nm, the numerical aperture ($\text{NA} \approx \sin \theta$) was estimated to be ~ 0.02 . This low value for the NA will result in a lower collection efficiency for the isotropically scattered Raman signal within the core and cladding of the liquid filled fibre.

5.4 Summary

This chapter examines the guidance properties of liquid filled fibres, by determining the transmission spectra of a broad range of wavelengths over a cross section of the HC-PCF micro-structure, using an OSA and Shack-Hartmann wavefront sensor. From these examinations of a liquid filled HC-PCF, for both cases of core only filled and fully filled states, it was demonstrated that guidance was shifted toward the visible region. This is an attractive feature for sensing applications that require broad guidance in the visible regime, such as Raman spectroscopy, or fluorescence sensing in biological and chemical analysis. These results shall be used in Chapter 6 and Chapter 7 to test the fibres suitability for use as a tool for Raman scatter collection.

The main findings from the chapter can be summarised as follows:

- The core only filled fibre guides a broader range of wavelengths (675 - 925 nm) and also has a broader confinement area (FWHM $27.2 \mu\text{m}$), than the fully filled fibre, in the mW regime. The normalized power is above 0.5 for the entire core region.
- The fully filled fibre guides a range of wavelengths between 675 - 775 nm, has a FWHM of $6.3 \mu\text{m}$ and a $1/e^2$ width of $10.7 \mu\text{m}$. It has a peak power that decays quickly to less than 0.2 within $\pm 5 \mu\text{m}$ of the core position.
- The fully filled fibre has a very narrow Gaussian confinement of wavelengths

in the core, compared to the broad transmission area of the core only filled fibre.

- The core only filled fibre also demonstrates a hybrid guidance of PBG in the empty capillary cladding and index guiding in the liquid filled core.
- By analysing the NA of the liquid filled fibres, the core only filled state was found to have a higher NA (~ 0.8) when compared to the fully filled state ($\text{NA} \sim 0.02$).

The two filled states can be compared by their transmission properties to determine their suitability as a liquid sensor. The width of the transmitted distribution in comparison to the core size of the core only filled fibre and the guidance of the broad wavelength range allows a larger number of molecules to be probed within the liquid core, with a high intensity value and with wide spatial distribution of the pump. The fully filled fibre has a very narrow Gaussian width transmission distribution in comparison to the core size and this results in fewer numbers of molecules being excited by the pump, and a smaller intensity at the edges of the core. There is also a decrease in transmission of wavelengths within the surrounding micro-structure (beyond $\pm 5 \mu\text{m}$) of the fully filled fibre, resulting in the redundancy of the usefulness of filling these capillaries with extra liquid, which requires larger volumes with no return in sensing enhancement.

The Gaussian distribution, measured by the Shack-Hartmann wavefront sensor, has a smaller FWHM measurement for the core filled case, in comparison to the PH measurements, and the Shack-Hartmann FWHM measurements are similar to the PH measurements for the fully filled case. The Shack-Hartmann measurements confirm the results made by the PH, and reassert that at shorter wavelengths (532 and 632.8 nm), light is guided within the core of the liquid filled fibres.

Chapter 6

Viscometer Integrated with Raman Scatter for Simultaneous Analysis

This chapter combines the work described in previous chapters, to measure the viscosity of liquids (Chapters 3, 4) and introduces a new concept to determine the spectral information of the light scattered inelastically (Raman scattering) from the liquid sample contained within the fibre. Further information about the molecular identity of the infiltrated liquid can be obtained from its Raman spectrum, and this is examined here dynamically as the fibre fills.

Raman spectroscopy is a powerful tool for the study of molecules for chemical and medical applications. Combining this technique for molecular identification with the viscosity measurement could result in a multi-analytical sensing procedure that is potentially powerful and time efficient. This could enable integrated analysis for understanding the physical parameters of the liquid and also identifying the molecular composition of solutions.

The signal of Raman scatter is proportional to the intensity of the pump laser, the number of molecules interacting with the pump beam per unit area [139]. The intensity of the scattered light is inversely proportional to the wavelength of the pump by λ^4 , as shown in Equation (2.30). The liquid filled fibre allows wavelengths within the visible regime to propagate within the core of the fibre as shown in Chapter 5. Therefore, the generation of Raman scatter by a pump laser at short wavelengths for the liquid filled HC-PCF and the potentially long interaction lengths, makes HC-PCF advantageous for Raman scatter detection.

The system of this investigation requires a laser that has sufficiently high output power to generate a detectable signal of Raman scatter, and the fibre must be able to propagate a proportion of this scatter to either end facet.

In Chapter 4, monitoring the transmission power of the pump laser was observed in real time and found to increase with filling due to the shift in the guiding properties of the fibre. In this chapter the generation of Raman signal within the HC-PCF is also be monitored dynamically, as the capillaries fill with the solution, and is explored and discussed for different liquid solutions and applications.

6.1 Experimental Set-up

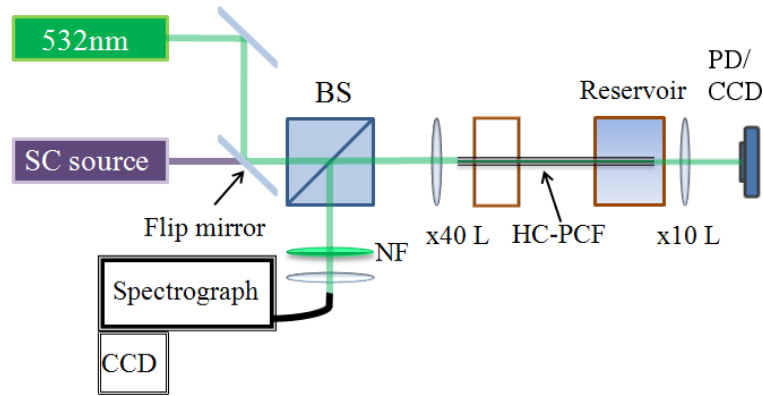


Figure 6.1: Schematic displaying the set-up for the integrated viscometer and Raman measurements (not to scale). The laser sources (SC or 532 nm) are positioned on the left and are focused to the HC-PCF by a $\times 40$ infinity correction lens (L). The backscattered light is transmitted back through the beamsplitter (BS), a notch filter (NF) and collected by the spectrograph for Raman analysis. The forward light from the fibre is transmitted through the reservoir window and detected by the photo-diode (PD).

The experimental set-up was designed to incorporate all aspects of viscosity detection from Chapter 4 and to implement a procedure for the collection of Raman signal. This set-up is shown in Figure 6.1. The supercontinuum (SC) source was used for initial alignment of the HC-PCF (HC-1060) segment with the system, and was focused to the HC-PCF with a $\times 40$ infinity correction lens. The alignment was facilitated by clamping the fibre to a motorised nano-positioning stage at the focusing lens, as described previously in Chapter 4. The end facet of the fibre was placed in a reservoir, the exiting light was collected with a $\times 10$ lens and the image was observed with a CCD camera. A bandpass filter (Thorlabs 1050-10, central wavelength = 1050 ± 2 nm, full width half maximum = $10 \pm$

2 nm) was used to select wavelength ranges from the SC source for optimum alignment of the HC-PCF with the original photonic bandgap (PBG) at 1060 nm.

The pump laser for Raman excitation and the measurement of filling time was a single mode, frequency doubled continuous wave (cw) Nd: YAG laser (4 mW) at 532 nm. It was directed to the input of the fibre, via a flip mirror, shown in Figure 6.1. The transmission was passed through a PMMA window in the reservoir and the signal was collected by a $\times 10$ infinity correction lens. This lens collimated the transmitted light through the HC-PCF onto the detection area (13 mm^2) of a photo-diode (PD). The transmission of the pump laser through the fibre was monitored with a PD at the output of the fibre throughout the experiment. The data was recorded utilising a DAQ and labview program, this method has been described previously in Chapter 4. Also detailed in Figure 4.10 in Chapter 4 is the efficiency and response of the CCD to wavelengths in the visible region. For the 532 nm laser source, the PD has a conversion efficiency of 0.33 A/W.

To measure the backscattered Raman signal generated by a liquid inserted in the capillaries of the HC-PCF, the experimental set-up was changed from that in Chapter 4, Figure 4.8, to accommodate the inclusion of a Raman detection system, complete with a spectrometer. A beam splitter (BS) was placed after the flip-mirror, before the $\times 40$ focusing lens. The backscattered Raman signal generated by the 532 nm pump laser was sent back through the $\times 40$ focusing lens and passed through the beam splitter which separated the incident pump laser source from the backscattered signal. The backscattered signal was then pre-filtered by a notch filter (NF) centred at $532 \pm 17 \text{ nm}$ (suppression 10^{-6}) to block light at the excitation wavelength, and hence avoid saturating the CCD detector of the spectrometer. The scattered light was then focused by a $\times 10$ lens to a guide (fibre bundle with round entrance aperture and slit exit aperture) that was connected to a polychromator (Oriel single grating imaging spectrograph 77480 MS127i) with a back-illuminated and cooled CCD detector (Andor DV401-BV, $-30^\circ \text{ Celsius}$) with a resolution of $\sim 0.22 \text{ nm}$.

The data collected by the cooled CCD was uploaded to the computer via a VGA cable to a PCI card. A software program Andor MCD 2.62 I2C facilitated the acquisition of signal from the cooled CCD camera. The wavelength scale of the spectra were calibrated using a 532 nm laser source, and a Hg-Ar pen ray lamp, with spectral lines at 546 nm, 577 nm and 579 nm to assign a wavelength to each of the 1024 CCD pixel arrays. The Oriel poly-chromator was sensitive over a broad

working range of wavelengths from the ultraviolet region to near infrared (180 - 2500 nm). The wavelength selection of the Oriel poly-chromator was facilitated by a dial, which turned the grating to allow the spectrometer to work over this broad range. As a result, the system was calibrated for every acquisition using the pen ray lamp.

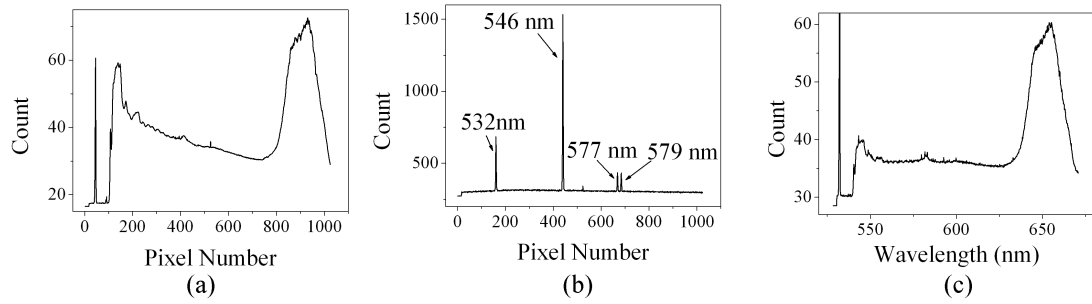


Figure 6.2: Calibration of the pixel array for the CCD camera in the spectrometer. (a) Raman spectrum of water before calibration on a pixel scale, (b) spectrum of the pen ray lamp and the 532 nm laser (c) Raman spectrum of water, with a scale calibrated for wavelength by the Andor software.

The calibration of the pixel array from a sequence of channels to a wavelength scale is shown in Figure 6.2. The Raman spectra for a fibre containing water, are shown in Figure 6.2 before (a) and after (c) the scale has been calibrated. Figure 6.2 (b) shows the spectral lines of the pen ray lamp and the 532 nm laser source. These spectral points are used to assign a wavelength to each of the channels. In the $\sim 530 - 630$ nm range, the CCD camera has a resolution of 0.22 nm.

A HC-1060 segment was used for all measurements, and was cleaved at both ends to facilitate coupling of light. Neither end was further prepared, unlike the preparations that are discussed in Chapter 7 for Raman experimental measurements, as the study in this chapter focused on the dynamic change in Raman signal generation and collection as the capillaries fill in real time.

Once the fibre was aligned to the system using the SC source, the flip mirror was inserted to send the 532 nm pump laser beam through the $\times 40$ focusing lens to the fibre. The time dependent transmission signal and Raman spectra were recorded in real time separately by the Labview program and Andor spectrometer software, when the liquid was added to the reservoir. A kinematic series of 800 Raman backscatter measurements was taken as the fibre was filling, each measurement having an integration time of 1 s. The PD recorded data at a rate of 50 s^{-1} . The experimental measurements were continued until all the capillaries were filled and the signal detection from both sources was stable. The following

sections shall discuss the results for these measurements for a wide range of liquid solutions.

6.2 Proof of Principle Results for Solutions of Glucose

The principle of the dual measurement system was demonstrated with a 12 cm HC-1060 undergoing filling with a 1 M aqueous glucose solution. The power of the transmitted light at 532 nm and the corresponding Stokes Raman spectrum over 4000 cm^{-1} were recorded as a function of time, for each dual viscosity and Raman measurement with a liquid filling HC-PCF, and the results are discussed in this section.

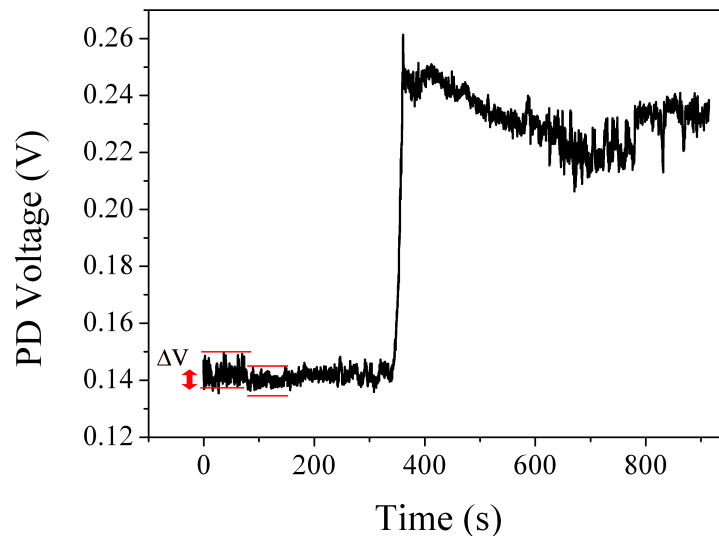


Figure 6.3: Transmission signal measured by the PD for a 532 nm pump source when a HC-1060 was filling with a 1 M aqueous glucose solution. The core filling time was ~ 360 s and the capillaries are filled after 780 s.

The time dependence for the transmission of 532 nm light through the HC-PCF, measured with the PD, is displayed in Figure 6.3. Light at 532 nm is initially outside the fundamental PBG and secondary PBG, as discussed in Section 4.1.2. Therefore, the initial transmission signal (when compared to the voltage as the core filled from 20 - 360 s) is very low ($\Delta V = 0.001$ V) in comparison to the measurements made with the 632.8 nm source (average $\Delta V \sim 0.05$ V), described in Chapter 4. The transmission in Figure 6.3, is plotted in black showing a sharp increase in power at ~ 360 s, due to the core being completely filled. This is in agreement with the investigations in Chapter 4, where it is observed that if the

core only is filled with a fluid, visible light is allowed to propagate by the index guiding effect. The 532 nm signal shows a 20 s rise time, corresponding to the change from almost no guidance to an increase in guidance when the liquid fills the fibre core at ~ 360 s. The 632.8 nm signal shows a much longer rise time of ~ 70 s (see data in Chapter 4, Figure 4.13 and the analysis of the two laser sources for the same experimental conditions in Figure 4.17), and hence the filling time of the core can be determined more accurately using a 532 nm pump, as this wavelength does not fall within the initial PBG of the fibre. It should be noted that the data in Figure 4.13 is for a 0.5 M solution of glucose with an expected viscosity of 1.26 mPa.s, and the data in Figure 6.3 is for a 1 M glucose solution with an expected viscosity of 1.58 mPa.s, which results in a longer filling time in comparison to the solution with a lower concentration, shown in Figure 4.13. This implies that choice of laser source influences the rise time for the determination of the core filling point for the viscosity measurement and results in a change of the characteristic transmission curve of a dynamically filling fibre.

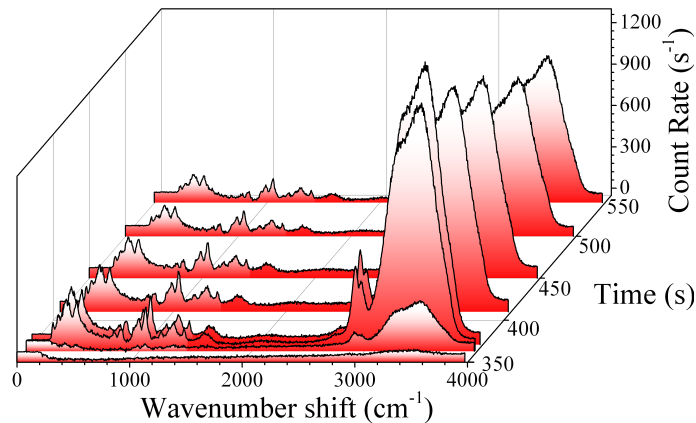


Figure 6.4: The plot shows a selection of sequential Raman spectra with an integration time of 1 s, recorded for a 12 cm HC-1060 as it was filled with 1 M aqueous glucose solution.

Simultaneously with the transmission measurement, the Raman spectra were recorded in real time for the filling of the HC-1060, which are shown in Figure 6.4. In order to understand the changing Raman signal strength, the optical properties of the filling fibre must be considered (Section 4.1.2). The results for the Raman scatter are closely compared with the transmission of the pump laser in Figure 6.3. At ~ 350 s in Figure 6.4 the signal amplitude of the spectra improves markedly until it reaches a maximum at ~ 360 s. At this time, the spectral features are clearly defined, even for the short 1 s integration time used to record these spectra. After ~ 380 s, the signal strength decays, however the spectral features of the liquid solution can still be identified for more than 200 s.

For the Raman measurement, initially no backscattering signal was observed until 350 s. This time corresponds to the core of the fibre being filled by $\sim 90\%$, and the capillaries filling a length of approximately 60%. When the core is filled, broadband propagation of light is enabled. The fact that the Raman signal strength reached a maximum at 360 s, is in agreement with data in Figure 6.3, where a peak in transmission is observed at ~ 360 s. However, the Raman signal decays immediately after this time, until all the capillaries are filled at 800 s. The red trace in Figure 6.5 shows the evolution of the Raman signal at 3500 cm^{-1} (corresponding wavelength $\sim 654\text{ nm}$). In this case, no signal is observed before 350 s, just like the PD signal, which is shown in Figure 6.5 by the grey trace for comparison. After 350 s, a sharp increase in the count rate was measured, again due to the core being fully filled.

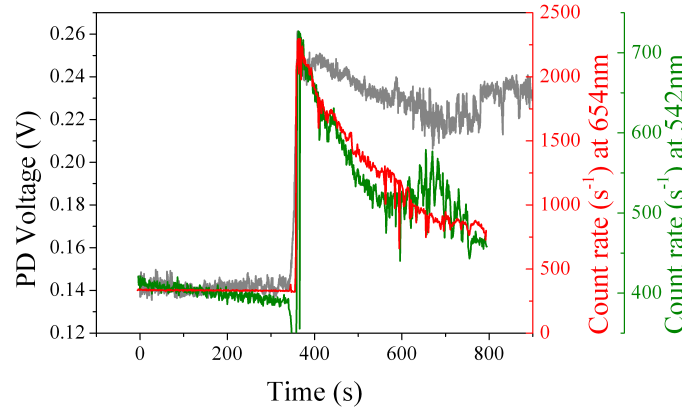


Figure 6.5: Time dependent Raman signal generation at 542 nm (green) and 654 nm (red) in comparison to the PD signal at 532 nm (light grey) for a 1 M aqueous glucose solution filling a 12 cm HC-1060. The left axis is the voltage measured by the PD, while the red and green axis on the right is the Raman count at 654 nm and 542 nm respectively.

Once the core is filled and the capillaries continue to fill, the count rate of the Raman scattered light starts to decrease as the guiding mechanism changes slowly from index-guiding to a shifted PBG (red trace in Figure 6.5). It was observed in Chapter 3, with an optical microscope that the capillaries do not fill uniformly as a function of time. Instead, the filling is gradual after the core fills, with the ring of capillaries closest and furthest to the core filling first. After a certain time, the majority of the capillaries fill, leaving a couple unfilled that will eventually completely fill, as demonstrated in Figure 3.4 and Figure 3.5.

To determine if the time dependence of the signal is similar over the entire spectral range concerned, the intensity at a shift of 350 cm^{-1} (corresponding wavelength 542 nm) is plotted in green in Figure 6.5. A lower count rate is observed, but the

decay in signal is similar to that at 654 nm. There is a slight increase in the green trace around ~ 700 s, by 100 counts per second. This increase can be attributed to the modal competition within the capillaries, that was observed in Chapter 4, and to the spatial filling pattern of the micro-structure.

The decay in the counts of Raman signal is unexpected, as the complete filling of the capillaries results in a larger volume of liquid available within the HC-PCF to generate the Raman signal. The reasons for this decay are explained in Chapter 5 in terms of numerical aperture, collection efficiency and the change in guidance properties between the core being filled and the entire fibre being fully filled. The Raman signal is linearly dependent on the collection efficiency of the system, as discussed in Chapter 2. Nevertheless, from the results, it is clear that an optimum Raman scatter can be obtained from a fibre when only the core is filled, and when the wavelength of the pump light is carefully selected to compliment the guidance specifications of the HC-PCF.

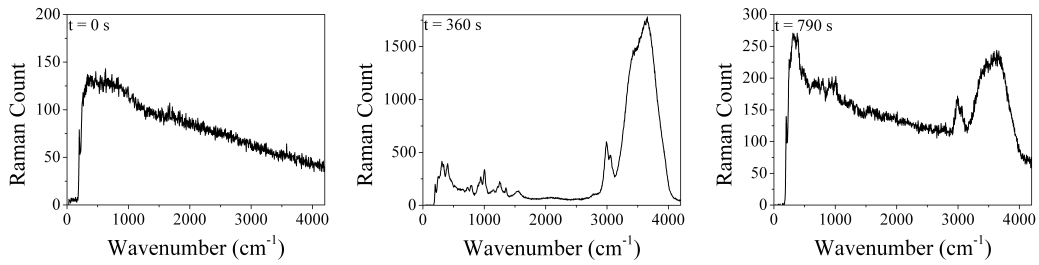


Figure 6.6: Raman spectra generated from a 532 nm light source from a 12 cm HC-1060 when empty at $t = 0$ s (a), core filled at $t = 360$ s (b) and fully filled at $t = 790$ s (c). These spectra are taken during the dynamic filling of the HC-PCF with a 1 M aqueous glucose solution, with an integration time of 1 s.

To further understand the generation of Raman scatter for the three guidance states that occur during the dynamic filling of the fibre, the Raman spectra obtained at all three states are isolated and shown in Figure 6.6 for direct comparison. The spectra for the empty fibre in Figure 6.6 (a) shows a broad, featureless scatter from the silica. The core filled fibre shown in Figure 6.6 (b) shows the Raman features of the glucose solution, and a decrease in the background silica features. The fully filled state in Figure 6.6 (c) shows a significant decrease in the Raman signal from the liquid, by a factor of six at 3500 cm^{-1} , and an increase of the signal from the silica of the fibre, seen in the range $400 - 1000\text{ cm}^{-1}$ wavenumbers. The decay in Raman signal, and in particular the observation of the silica signal in (c) is a result of the PBG guidance mechanism that occurs for fully filled fibres, where there is a greater interaction between the guided light

and the silica micro-structure. This results in an increase in the generation of scatter from the silica, and a decrease in the collection of Raman scatter from the infiltrated liquid sample. The core filled fibre does not feature this scatter signal from the silica as strongly, and it was observed in Chapter 5 that due to the refractive index difference between the core and the surrounding cladding that strong confinement of light occurs within the liquid core.

6.3 Tests with Other Bio-Fluids

In this section the application of the integrated viscometer and Raman detection technique to several biological important fluids, such as aqueous mixtures of creatinine and urea, and aqueous mixtures of glucose and lactate, will be outlined. The velocity of the flow for each solution was studied with the PD, and the Raman signal with an integration time of 1 s per spectrum shall be presented here.

Urea and Creatinine

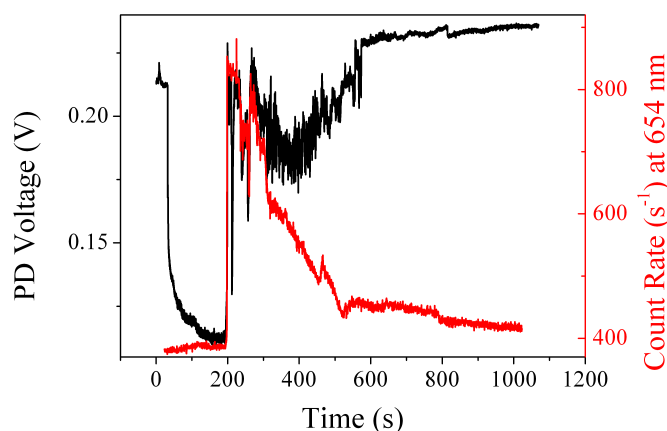


Figure 6.7: Fibre transmission (black, left axis) of light at 532 nm as a function of time (14 cm HC-1060), during the filling with an aqueous solution mixture of 0.3 M urea and 0.05 M creatinine. Change in Raman count (red, right axis) at 3500 cm^{-1} over the filling time from 0 s to 1000 s.

Urea samples and the importance of determining the presence of creatinine within these samples in medical diagnostics are discussed in Chapter 7. Here, an aqueous solution mixture of 0.3 M urea and 0.05 M creatinine is used to examine the physical parameters of the solution and identify the presence of the components of urea and creatinine with the integrated Raman viscometer within a 14 cm HC-1060. Figure 6.7 displays the transmission signal recorded by the PD in black

and the Raman scatter signal at 3500 cm^{-1} in red, over the filling time from 0 s to 1000 s. Alignment of the empty HC-1060 at 532 nm is challenging, and even when using the SC source to utilise the initial PBG, re-adjustments are required to maximise coupling of the 532 nm laser light to the fibre. Hence Figure 6.7 has subtle differences in the transmission curve measured by the PD, than Figure 4.13 from Chapter 4.

Initially, at $t = 0\text{ s}$ in Figure 6.7, a large PD signal (black) is observed (due to the incident light penetrating the silica outer cladding), which rapidly decays as soon as liquid is introduced to the 14 cm fibre. The transmission signal increases again at $\sim 200\text{ s}$, indicating that the core of the fibre has been filled. The transmission signal fluctuates due to modal competition within the fibres core, until the capillaries are filled, after $\sim 600\text{ s}$, resulting in a more stable transmission signal at 532 nm. The Raman count rate (red) also increases at $\sim 200\text{ s}$ when the core is filled. The Raman signal then decays, as previously observed in Section 6.2, resulting in a minimum signal for the Raman scatter when the fibre is fully filled. The average velocity of liquid flow for this sample is estimated to be 8.5 mm s^{-1} , using the length of the fibre and the filling time, as described in Chapter 4.

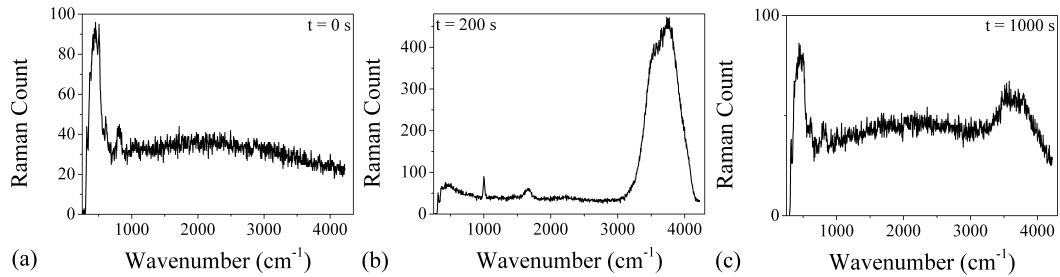


Figure 6.8: Raman spectra of the empty (a), core filled (b) and fully filled (c) 14 cm HC-1060, taken during the filling of the HC-PCF with an aqueous solution of 0.3 M urea and 0.05 M creatinine with an integration time of 1 s per spectrum.

The Raman signal at $t = 0\text{ s}$, 200 s and 1000 s, where the fibre was empty (a), core filled (b) and fully filled (c) respectively is shown in Figure 6.8. Due to incomplete light coupling to the core at 0 s, the Raman scatter from the silica is quite prominent in Figure 6.8 (a) between $400 - 850\text{ cm}^{-1}$. At 200 s, the distinctive Raman signal of urea at 1000 cm^{-1} can be seen in Figure 6.8 (b), however, the characteristic lines of creatinine are difficult to distinguish. To improve the signal to noise ratio, a longer integration time than 1 s was required, and will be examined further in Section 6.4 and Chapter 7. The fibre is fully filled at 1000 s, and the corresponding Raman spectrum shows a strong presence of inelastic scatter from the silica, and weak Raman scatter from the water at $3000 - 4000$

cm^{-1} due to the change in propagation properties from index guiding to guiding by the shifted PBG. The strong silica scattering is reduced in the core filled state, indicating that index guiding results in strong confinement of the laser light within the liquid core, with a minimum guidance of the light at 532 nm within the silica structure of the HC-PCF.

Lactate and Glucose

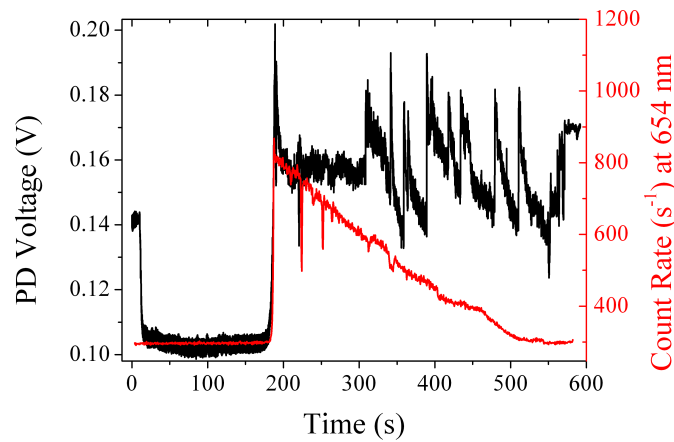


Figure 6.9: Fibre transmission (black, left axis) of light at 532 nm as a function of time (15.5 cm HC-1060) during the filling with an aqueous solution mixture of 50 mM lactate and 10 mM glucose, in comparison to the change in Raman count (red, left axis) as 3500 cm^{-1} over the filling time from 0 s to 600 s.

A solution of 50 mM lactate and 10 mM glucose was tested using the integrated HC-PCF viscometer and Raman detection set-up. Figure 6.9 shows the transmission signal against time (black, left axis) and the Raman scatter signal at 3500 cm^{-1} in red, with time. An initial error in the alignment of the 532 nm source results in a large transmission signal at 0 s. The transmission signal decays rapidly as liquid is introduced to the 15.5 cm HC-1060. Both signals increase at ~ 190 s, indicating that the core of the fibre has been filled. The Raman signal then decays, as observed previously, while the transmission signal decays slightly and fluctuates, due to modal competition within the core, and the initial error in alignment which affected the measurement of the capillary filling. When the capillaries are filled at ~ 570 s, the PD reaches a stable signal without fluctuations for the transmission of 532 nm source, and a minimum count per second for the Raman signal. The average velocity of liquid flow for this sample is estimated to be 8.7 mm s^{-1} .

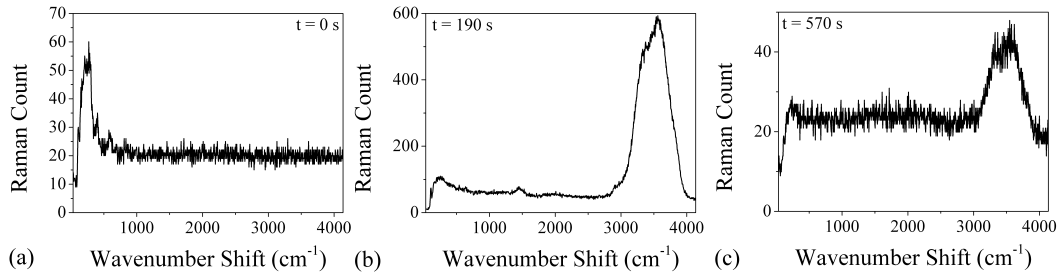


Figure 6.10: Raman spectra of the empty (a), core filled (b) and fully filled (c) 15.5 cm HC-1060, taken during the filling of the HC-PCF with an aqueous solution of 50 mM lactate and 10 mM glucose, with a 1 s integration time per spectrum.

The Raman signal at $t = 0$ s, 190 s and 570 s, where the fibre is empty (a), core filled (b) and fully filled (c) is shown in Figure 6.10. Due to the initial error in alignment at 0 s, the Raman scatter from the silica is quite prominent at $400 - 800 \text{ cm}^{-1}$. At 190 s, the core of the fibre is filled, resulting in an increase in the Raman scatter signal from the liquid contained within the core of the fibre. Due to the short integration time of 1 s and the weak concentration of the solution, the spectral features for lactate and glucose are difficult to distinguish from the background noise. To improve the signal to noise ratio, a longer integration time is required. However, the Raman scatter of the OH stretching vibration of water at 3500 cm^{-1} is clearly visible. At 570 s, the Raman spectra of the fully filled fibre shows a weak glucose and lactate spectra, with the OH stretching vibration the only vibration band clearly visible in the $3000 - 4000 \text{ cm}^{-1}$ region. This band has decayed by a factor of 25. Such a large decay is due to the non optimal alignment of the fibre initially, as previously observed for the PD signal in Figure 6.9.

6.4 Post Analysis of Dynamic Raman Scatter

In the previous section, the Raman scatter as a function of time was used to determine the fibre guidance properties for Raman scatter collection as the HC-PCF filled dynamically. It was seen that the core filled state collected a larger fraction of the scatter than the fully filled state. This was seen as a peak in Raman count at the point where the core filled, followed by a gradual decay in counts per second, as shown in Figure 6.5. A drawback of the dynamic measurement is that each Raman spectra has an integration time of 1 s, which limited the sensitivity of the measurement, due to the short integration time. As such, the

spectrum for aqueous samples with a low concentration of solute have a low count and cannot resolve the individual Raman lines from the background noise for the identification of the molecules.

To overcome this drawback, and still use all recorded data, each spectrum collected over the entire measurement time, from the point where the core was filled to the point where all the capillaries were filled can be added together to increase the count of the Raman scatter and improve the count strength against the background noise. This analysis was completed for each of the samples outlined in this chapter. It must be noted, that as the capillaries of the fibre were filling dynamically, the Raman scatter count strength is not steady and decays over time.

For the 1 M aqueous glucose solution, the spectra over a filling time of 430 s were added together, and the result is shown in Figure 6.11. The increase in Raman count of the features of the spectrum can be seen, for example, at a wavenumber shift of 2998 cm^{-1} , with a count increase from ~ 600 counts to $\sim 3 \times 10^5$ counts. The spectrum in Figure 6.11 clearly shows the typical Raman lines of glucose at 940 , 1000 , 1150 , 1250 and 1350 cm^{-1} , with a higher count (on a scale of $< 10^4$ counts), compared to the background noise (1500 counts), in contrast from that seen previously in Figure 6.6.

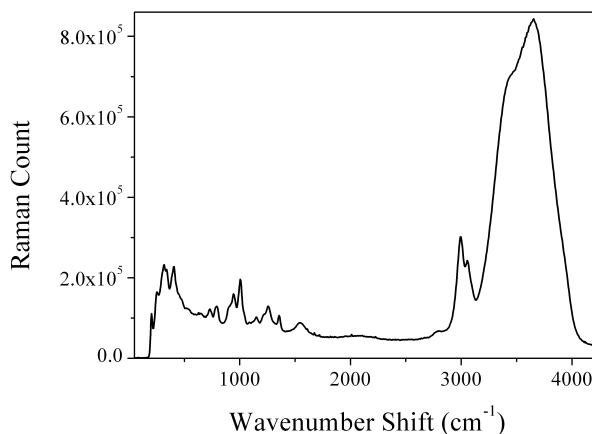


Figure 6.11: Spectrum of 1 M aqueous glucose, compiled using data for the dynamic measurement of Raman scatter from Figure 6.5.

This analysis was also performed for the aqueous solution mixture of 0.3 M urea and 0.05 M creatinine, over a filling time of 800 s, and for the aqueous solution mixture of 0.05 M lactate and 0.01 M glucose, over a filling time of 380 s. Previously in Figure 6.8, the spectral Raman lines of creatinine could not be resolved from the aqueous mixture and the background noise. In Figure 6.8 (b) the feature

of urea at 1000 cm^{-1} can be seen clearly from the spectrum. The post analysed spectrum of the mixture of creatinine and urea, for all spectra collected during the filling time, is seen in Figure 6.12 (a), where the spectral features of the creatinine at 900 and 1150 cm^{-1} and urea at 1000 cm^{-1} can be seen. The urea has a 18000 count at 1000 cm^{-1} , and a background noise of 1000 counts. The ratio of the signal count to the noise is 18 . For the creatinine, the count at 900 cm^{-1} is 1650 and the count at 1150 cm^{-1} is 2250 , giving a signal to noise ratio of 1.65 and 2.25 respectively, for a background noise of 1000 counts.

In Figure 6.12 (b) the post analysed spectrum of the mixture of lactate and glucose, for all spectra collected from the measurement in Figure 6.10 can be seen, where the spectral features of the glucose at 1050 cm^{-1} and 1150 cm^{-1} and lactate at 829 and 1370 cm^{-1} can be seen. For the glucose, the count at 1050 cm^{-1} is 1500 and the count at 1150 cm^{-1} is 1700 , giving a signal to noise ratio of 1.15 and 1.3 respectively, for a background noise of 1300 counts. For the lactate, the count at 829 cm^{-1} is 1000 and the count at 1370 cm^{-1} is 1200 . For the background noise of 1300 counts, this verifies that the Raman lines for lactate cannot be resolved in this spectrum.

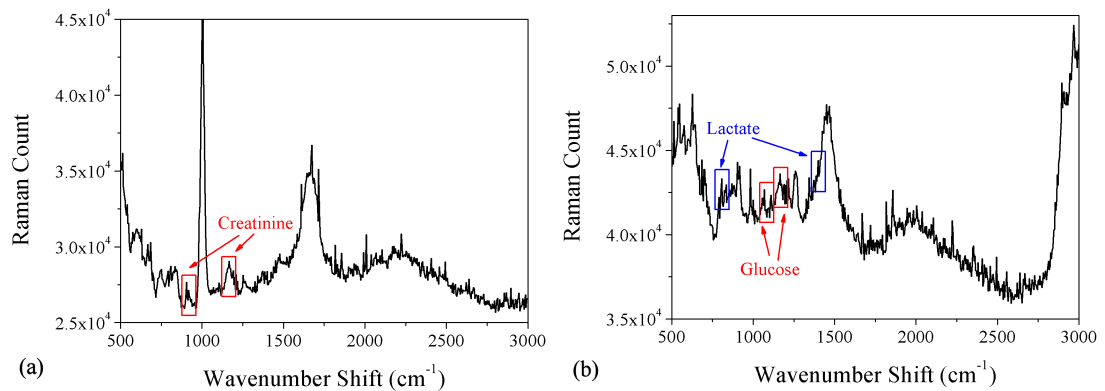


Figure 6.12: Spectra of a mixture of 0.3 M urea and 0.05 M creatinine in aqueous solution (a) and a mixture of 0.05 M lactate and 0.01 M glucose in aqueous solution (b). These spectra are compiled from the results for all the spectra collected as seen in Figure 6.8 for 800 s (a) and Figure 6.10 for 380 s (b).

6.5 Summary

This chapter has conveyed an investigation of the integration of two measurements that can be performed during the dynamic filling of the HC-1060. These measurements are (a) the viscosity measurement procedure outlined in Chapter

4 and (b) the collection of Raman scatter from the liquid contained within the fibre. Raman scatter collection from the HC-PCF will be examined further in Chapter 7. This integrated technique shows that a single measurement of liquid flow through the fibre can determine the physical parameters of the liquid and identify its molecular composition from its unique Raman scatter. In this chapter, the Raman count at a wavenumber shift of 3500 cm^{-1} was used to determine when the core of the fibre has been filled, in combination with the increase of the PD signal. The Raman scatter reaches a maximum value when the core was filled. However, once the capillaries began to fill, the information available from the Raman count becomes limited, and reduces down to a minimum count level similar to that which was present before the filling began.

The continuous filling of the capillaries in the micro-structure after the core fills explains the drop in Raman signal collection. Once the capillaries are filled, the guidance mechanism changes from index guiding to shifted PBG, and effects the collection of the Raman scatter. The collection of the Raman scatter is linearly proportional to the numerical aperture and collection efficiency of the system, as discussed previously in Chapter 5. It can be assumed that the change in guidance mechanism effects these two parameters, and reduces the efficiency of the sensor.

This chapter verified that the viscometer measurements and Raman measurements can be performed simultaneously to determine the physical parameters of the liquid and to identify the chemical structure of the liquid in real time.

Chapter 7

Raman Scatter in Hollow Core Photonic Crystal Fibre

In this chapter, hollow core photonic crystal fibres (HC-PCF) were used for the collection of Raman scattering. The geometry and selective filling of the fibre together with the fibre length and integration time were investigated experimentally, to determine the optimum configuration for the collection of scatter. The merit of utilising HC-PCF for Raman scatter collection is the enhanced collection of scatter, that can provide information of molecules, in samples of nano litre volumes. The Raman spectra of interstitial fluids; saliva and bodily fluids are important in medical diagnostics. The spectra of these fluids can be collected for rapid analysis of disease. These easily accessible fluids are less intrusive to obtain than blood samples, and are often early indicators of many infections, diabetes, liver failure, muscular degenerative diseases. Diabetes in particular is indicated not only by glucose, but by a range of metabolic components in fluids, such as lipids, proteins and amylase [191, 192], which can be identified by their Raman spectra.

Raman scatter is a relatively weak process, as discussed in Chapter 2 and demonstrated in Chapter 6, with a photon conversion efficiency of 10^{-18} [141, 142]. Therefore, to improve the Raman signal strength, the interaction path length between the sample and excitation light can be increased to improve the signal to noise ratio (SNR). Previously Teflon liquid-core fibres have been employed for this purpose [145, 147, 193]. HC-PCF, that are selectively core filled or fully filled are ideal devices for the enhancement and collection of Raman scattered light, similar to the liquid core Teflon fibres. As the HC-PCF has a micro-structure

cladding that is composed of many hollow capillaries, the average index of the empty, air-silica cladding is low, estimated to be ~ 1.05 (depending on the physical parameters of the fibre) [82, 188, 194]. Thus for a liquid core HC-PCF, light guiding in the visible regime will be restricted to the core by modified index guidance [33], due to a large refractive index difference between the aqueous solution within the core and the micro-structured cladding.

The intensity of Raman scatter generated within a liquid waveguide by a single frequency pump source, is proportional to the total number of illuminated molecules per unit length, the intensity of the pump laser, the Raman cross section of the molecule and the collection efficiency. For the purpose of the investigations described in this chapter, the back scattered signal from the liquid fibre is collected for analysis. The Raman back scattered signal (I_R) collected as a function of length (L) is estimated by Equation (7.1) [195]

$$I_R = \frac{I_L}{2\alpha_s} \rho \sigma_s \pi N A (1 - e^{-2\alpha_s L}) \quad (7.1)$$

where I_L is the intensity of the laser light coupled to the waveguide, NA is the numerical aperture of the system, α_s is the loss coefficient of the liquid waveguide, ρ is the number of molecules per unit volume, and σ_s is the scattering cross section of the molecule. The numerical aperture is an important parameter that determines the fraction of the excitation light and Raman scatter that will be propagated and collected by the fibre [194]. This can be estimated for both core filled and fully filled filling states of the fibre using the equations outlined in Section 5.3.

7.1 Experimental Apparatus

Figure 7.1, shows the schematic of the Raman set-up. The system consisted of a frequency doubled continuous wave (cw) Nd: YAG laser (4 mW at 532 nm) and a supercontinuum (SC) source. The choice of a 532 nm source, in comparison with a 632.8 nm source was based on experimental observation of Raman signal generation within the HC-1060. This is discussed further in Section 7.1.1. The specifications of the Oriel poly-chromator, fibre bundle and Andor CCD camera were discussed in Section 6.1. The experimental set-up is similar to that in Chapter 6, with the exception that the end facet of the fibre is not monitored to determine the liquid viscosity with a photodiode (PD).

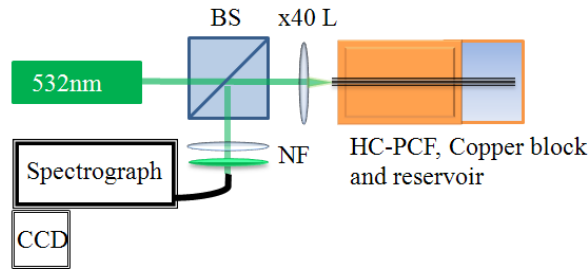


Figure 7.1: Schematic of the Raman signal detection set-up (not to scale). A pump source at 532 nm is focused by a $\times 40$ lens to the HC-PCF, which is inserted in a reservoir at the opposite end. The backscattered Raman signal is sent through the focusing lens, and directed via a beamsplitter (BS) through a notch filter (NF) to the spectrograph via a fibre bundle.

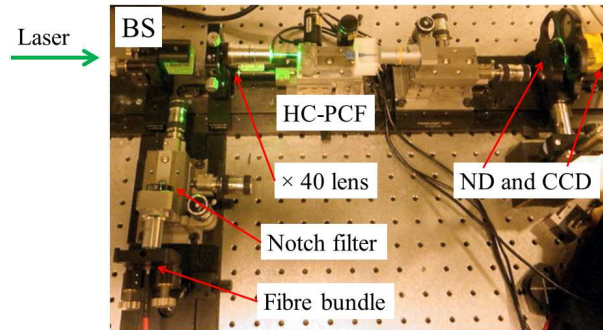


Figure 7.2: Set-up for Raman signal backscatter detection. Inserted to the right is a set of neutral density (ND) filters, a CCD camera and $\times 10$ lens to monitor the alignment of the HC-PCF throughout the experiment.

For the collection of Raman scatter, precise control of the light guidance was crucial. The positioning of the lenses, beam splitter, and the HC-PCF segment in the set-up was adjusted to maximize the collection of the Raman signal. Backscattered Raman signal from the silica cladding can decrease the sensitivity of our measurements, and slight optical misalignments will lead to a significant decrease of the signal-to-noise ratio. Therefore, the alignment of the pump laser to the hollow core required very accurate alignment, and was facilitated using a motorised xyz stage with nm precision actuators. Other stages were aligned manually with μm precision adjusters.

7.1.1 Fibre and Pump Laser Selection

Two liquid filled states; (a) core only filled and (b) fully filled were investigated to determine their effectiveness for the collection of Raman signal with HC-1060, from NKT Photonics A/S. Both these filled states allow the guidance of light in the visible region. The PBG shift for the fully filled fibre state with aqueous

solution was expected to shift to visible wavelengths, ~ 580 nm, as per the scalar equation outlined in Chapter 2, Equation (2.1) and the observations made in Section 4.1.2. The core only filled fibre is expected to guide within the visible regime, and the transmission spectra of both states are seen in Figure 7.3. The results are briefly summarised in Table 7.1.

Table 7.1: Table of properties for core filled and fully filled HC-1060 with water.

| Filled State | Guiding Mechanism | λ_{centre} | 3 dB(FWHM) | 20 dB |
|--------------|-------------------|--------------------|------------|--------|
| Core-only | Index guiding | 810 nm | 150 nm | 440 nm |
| Fully filled | Shifted PBG | 750 nm | 100 nm | 280 nm |

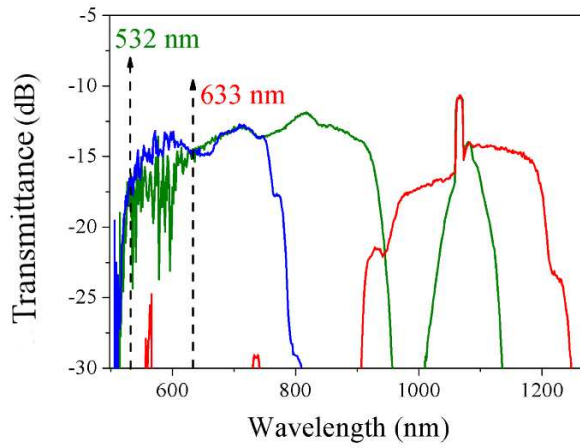


Figure 7.3: Transmission spectra of the empty (red line), core filled (green line) and fully filled (blue line) HC-1060. The emission from the supercontinuum source has been subtracted (on the log scale) from the data to show the guiding properties of the liquid filled HC-PCF states in the short wavelength regime.

The intensity of the Raman scatter scales with the wavelength λ^{-4} as per Equation (2.30), and therefore, shorter wavelengths induce a stronger Raman signal. The transmission spectra of the SC source through 10 cm HC-1060 samples (when empty, core only filled and fully filled with water), are shown in Figure 7.3, where the spectra were normalised to the SC source to determine the light guiding parameters. The spectra shown in Figure 7.3, illustrate that both core only filled (green) and fully filled (blue) fibres guide light in the visible wavelength range. The guided range in both cases is optimum to allow the fibre to guide excitation light and Stokes Raman scattered light. A 532 nm and 632.8 nm laser source were used to generate Raman scatter within a HC-PCF. As seen from Figure 7.3, both of these wavelengths are at the limits of the guidance range for both liquid filled fibres (and the subsequent Stokes Raman scatter generated by the wavelengths is

within the guidance range). This limit is defined as the decay of the transmitted signal below -30 dB from the peak power of the trace in Figure 7.3.

To verify that the generated Raman signal is stronger at a shorter wavelength, even at the edge of the guidance band of the HC-PCF, a water core filled fibre was tested with a 4 mW 532 nm source and a 20 mW 632.8 nm source. The results for the Raman scatter from 3000 - 4000 cm^{-1} in the OH stretching region is displayed in Figure 7.4, for an integration time of 60 s. As it can be seen, the Raman scatter generated by the 532 nm source, displayed in green shows a 23000 count increase in comparison to the signal generated by the 632.8 nm 20 mW pump, despite the greater power of the 632.8 nm source.

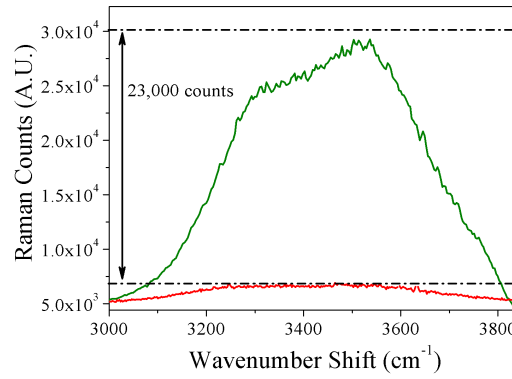


Figure 7.4: A comparison of the OH stretch vibrations for water between 3000 - 4000 cm^{-1} , pumped by a 20 mW HeNe (632.8 nm) source (red) and a 4 mW 532 nm source (green). There is a 23000 count difference in a 60 s integration time between the two Raman signals due to the dependence of the inelastic scattering on wavelength.

To demonstrate the λ^{-4} law, the area under each line was calculated by integrating over the range 3000 - 4000 cm^{-1} for both the 532 nm and 632.8 nm cases:

$$I_{532} = \int_{3000 \text{ cm}^{-1}}^{4000 \text{ cm}^{-1}} \text{Raman counts } d\tilde{\nu} \quad (7.2)$$

The ratio of areas ($I_{532}/I_{632.8}$) was found to be 13.5 for the 532 nm source to the 632.8 nm source, indicating that the 532 nm source generates a larger fraction of Raman scattering.

7.1.2 Background Spectra of Fibres and Preparation of Spectra

To prepare the spectra taken by the Andor spectrometer, first the Raman scatter of the HC-PCF was studied and the background noise was taken into consideration. The silica background of the fibre is shown in Figure 7.5 (a). The vibrational bands and characteristic lines of the silica at 400 - 550 cm^{-1} can be seen in this figure. This spectrum of the silica can be used to understand the surface structure and defects in the silica of the internal walls of the capillaries, which is important for studying the dynamic filling (Section 3.4). These defects are responsible for the increase of filling times for water solutions in Chapter 3 and Chapter 4, as discussed in Section 3.3.4.

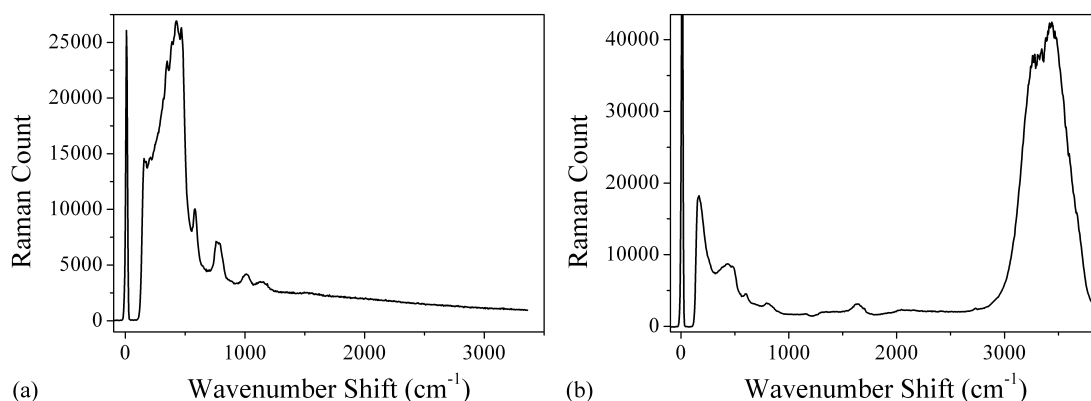


Figure 7.5: Background Raman spectra for silica from the HC-PCF (a) and the aqueous solution in a core only filled fibre (b), integrated over a time of 120 s.

The Raman spectrum for a fibre filled with solvent only, such as water is seen in Figure 7.5 (b). The characteristic bands of water at 3000 - 4000 cm^{-1} and at 1600 cm^{-1} , along with the characteristic silica bands below 1000 cm^{-1} govern the structure of this spectrum. To analyse the spectra of molecules dissolved in aqueous solution, the spectra in Figure 7.5 (b) were subtracted from all the results. This is called the background spectrum and will reduce the noisy signal from the cooled CCD, and take into account any stray backscatter that was produced by the fibres silica walls and the bulk aqueous solution, allowing analysis of the spectra of the molecules in question, with strongly reduced interference from other experimental factors, such as background noise from the CCD, and Raman scatter from the silica and water solution.

Additionally, the residual background noise from the spectra was considered by fitting a Gaussian distribution to the data points taken by the Andor spectrometer

for a 1 s integration time, over a featureless spectrum. The standard deviation was estimated, and the $3\sigma_{dev}$ value of background counts per second was used as a standard error of noise, from which the signal for each line in the Raman scatter spectrum was compared. The $3\sigma_{dev}$ value was calculated separately for each spectra. By comparing the signal of each Raman line to the noise, all data was quantitatively defined by the SNR in this chapter. The SNR is expected to improve with increased integration time.

7.1.3 Comparison of Raman Collection Efficiency in Core Filled and Fully Filled Fibre States

The enhanced collection efficiency of Raman scatter can be demonstrated by comparing the signals of the core filled fibre and fully filled fibre. Figure 7.6 shows the Raman spectra of a core filled and fully filled 10 cm HC-1060, containing a 0.5 M aqueous glucose solution. The integration time per spectrum was 2 s. It can be seen that, with the core filled fibre (top spectrum), a larger Raman count was obtained than with a fully filled fibre (bottom spectrum). There is a 66 % difference in counts between the core filled to the fully filled states at 3500 cm^{-1} .

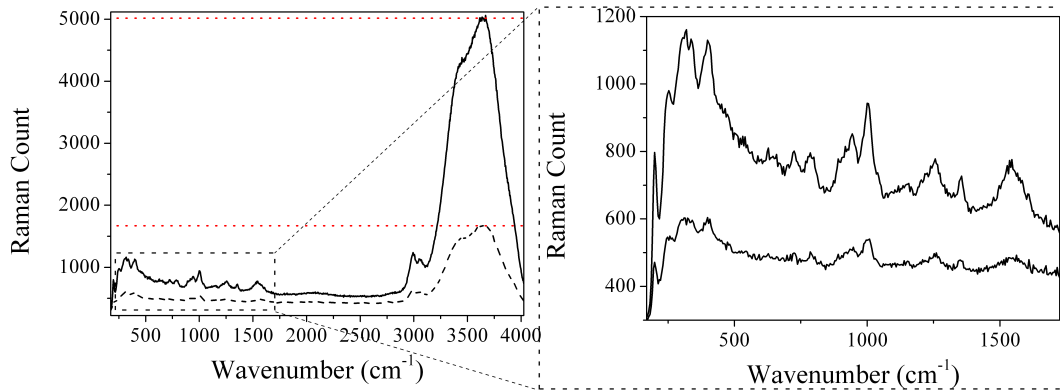


Figure 7.6: Raman scatter collected from a core filled fibre (top spectrum) and a fully filled fibre (bottom spectrum) for a 10 cm HC-1060. The liquid used was a 0.5 M aqueous glucose solution, with an integration time of 2 s. The plot on the right is a magnified insert of the main figure.

In both cases, all experimental parameters have been kept constant, with the exception of the filling state. The fully filled fibre has a larger volume of liquid to generate Raman signal from, yet results in a much lower Raman count in comparison to the core filled state. This is, on the one hand due to the change in light guiding properties from index guiding to a shifted PBG, but, on the other hand, also owing to a change of the numerical aperture of the fibre when liquid

is introduced to all the capillaries (Chapter 5). Both factors lead to a change in the Raman signal count between the two filling states of the fibre. Both of these factors are prominent in Equation (7.1). This was discussed in Chapter 6, when the Raman signal is analysed when filling the fibre in real time, and thus the change in propagation properties for the Raman signal can be observed.

7.1.4 Practical Fibre Length

To investigate the practical length of fibre for Raman backscatter collection, a 0.86 m length of HC-PCF was prepared by collapsing the capillaries at one end of the fibre using the fusion splicer method described in Chapter 5. The fibre was aligned to the laser beam (532 nm, 4 mW), and the collapsed end was inserted to the reservoir. After the core was filled with water through its entire length, the backscatter Raman spectrum was accumulated over a 2 s integration time. The fibre segment was then shortened by 2 cm at the un-collapsed fibre end, and the collection of the Raman backscatter was repeated until the fibre was 3 cm in length. The SNR for the Raman count rate at 3500 cm^{-1} for the OH stretching vibrations was estimated for each length of HC-PCF used.

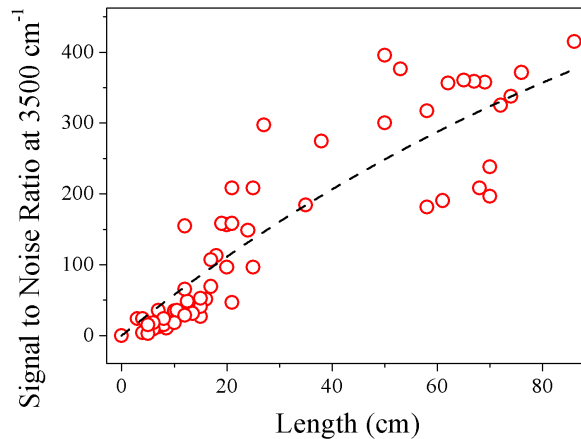


Figure 7.7: Plot of the signal to noise ratio for the Raman count at the OH stretching vibration 3500 cm^{-1} for lengths of core filled HC-PCF from 0.03 m to 0.86 m. The data is fitted with Equation (7.3) (black dashed line) (fitting parameters $b = 6.019$ and $\alpha_s = 0.004$) that has been used previously for Teflon liquid core fibres to model the collection of backscattered Raman signal.

This data is plotted in Figure 7.7 and shows that there is a 400 SNR increase between the 0.03 m and 0.86 m fibre length. This improvement in SNR allows the detection of molecules with a small Raman cross section, and molecules at

very low concentrations within the solvent liquid, at longer fibre lengths. Even for 0.86 m, the amount of sample volume required to make the measurement was 67 nL, for the core filled fibre, and thus the volumes are comparatively small for the enhancement factor that can be obtained with increased interaction length.

To determine the practical length of fibre for Raman backscatter collection, as defined by Altkorn et al. [159], the data was fitted with a model used previously for liquid core Teflon fibres, in the backscatter configuration [195], shown in Equation (7.3):

$$I(L) = \frac{b}{2\alpha_s}(1 - e^{-2\alpha_s L}) \quad (7.3)$$

where $I(L)$ is the Raman count at length (L), b is a parameter of the collection system and $\alpha_s = \alpha_s(\lambda)$ is the combined absorption coefficient of the liquid and loss of the waveguide, and is wavelength dependent. There is a wide fluctuation in the Raman count, particularly for lengths greater than 30 cm, due to the difficulty in fully filling a fibre of this length, and keeping the fibre straight and levelled throughout the experiment.

The practical length for signal collection is defined as the ratio of $1/2\alpha_s$, where the equation reaches approximately e^{-1} value. This determines the length of lossless fibre that has the same signal output as an infinite length of fibre with a loss of α . This model is fitted to the data in Figure 7.7, and is shown as the black dashed line. For our system, the model estimates that the effective fibre length for detection of water is 1.25 m, for $\alpha_s = 0.004 \text{ cm}^{-1}$. The absorption coefficient is wavelength dependent and for pure water is widely known to be 0.002 cm^{-1} at $\sim 600 \text{ nm}$ [196]. Therefore, the waveguide has an additional loss of $\sim 0.002 \text{ cm}^{-1}$. The length for maximum signal collection in the back scattering configuration is infinite [159]. This value is greater than the attenuation length of the system, which is defined as $(1/\alpha_s)$, which is 2.5 m for the HC-1060 filled with water.

The increase in Raman signal is not linear with the increase in fibre length, owing to the increase in other losses of the system. After a certain length, the Raman count begins to trend towards the maximum signal that can be obtained. This is greater than the practical Raman length ($1/2\alpha_s$). For liquids with a larger attenuation coefficient, the practical length will be shorter. For this reason, all Raman experiments were performed using lengths of collapsed HC-1060 between 10 - 30 cm, which is a compromise, as lengths longer than this were not practical for the degree of signal enhancement that could be obtained after the practical length was reached.

7.2 Applications Using Core Only Filled Hollow Core Photonic Crystal Fibre

This section describes a selection of results obtained from utilising the core only filled HC-1060 for Raman scatter collection. A variety of solutions were tested that are prevalent in industry and medical diagnostics to demonstrate the usefulness of HC-PCF as a tool for Raman studies. These molecules include monosaccharides glucose and fructose, and molecules of importance in interstitial fluids, such as glucose, lactate, and creatinine, among others. The system was first considered for the study of glucose and fructose solutions, as investigated previously in Chapter 4. To the best of our knowledge, this is the first time that this work has been shown with HC-PCF, and was subsequently published by Horan et al. [103] and Yang et al. [150]. The application of HC-PCF for Raman collection is extended in the next section to glucose and lactate, creatinine and urea and interstitial fluid characterisation.

7.2.1 Mono-Saccharides: Glucose and Fructose

The importance of glucose and fructose in medical detection and industrial applications was previously discussed in Chapter 4, where the HC-PCF was analysed for viscosity characterisation. In this section, Raman spectra of glucose and fructose are presented and measures to optimise the collection efficiency within a core only filled HC-1060 are discussed.

Figure 7.8 shows the Raman spectra of glucose (red) (a) and fructose (blue) (b) diluted in water inside a core filled HC-PCF. The wavenumber range covered was 290 to 3900 cm^{-1} with an integration time of 60 s. To obtain the spectra in Figure 7.8, the background spectrum for a fibre filled with solvent only was subtracted (as described in Section 7.1.2), accounting for any scattering from the fibre itself and the solvent. The light guiding properties of the fibre may cause the resulting Raman scatter intensities to differ slightly from those acquired with a bulk solution in a cuvette. This is due to the non-consistency of the transmission spectrum over the guidance range, described in Table 7.1 and shown in Figure 7.3. However, the spectral region addressed is within the transmission window of the core filled fibre and comprises the characteristic C-O and C-C stretch vibrations.

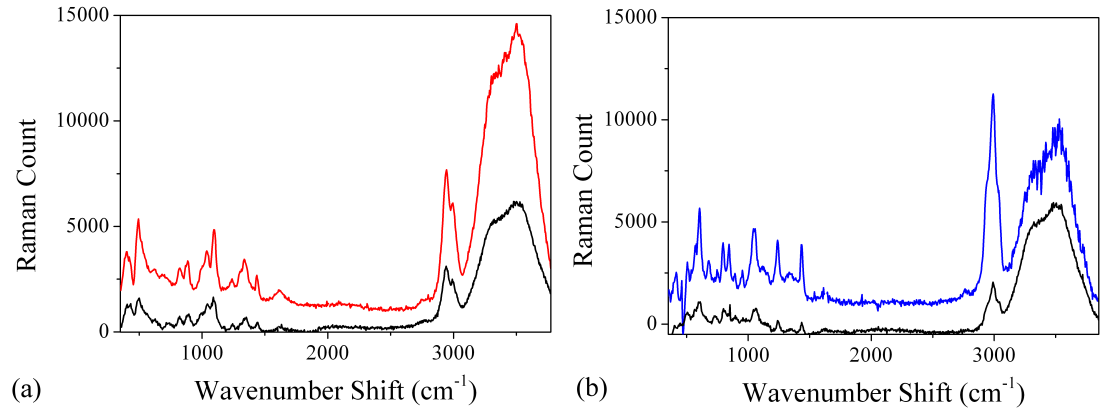


Figure 7.8: Stokes Raman spectra for 1 M aqueous glucose (red) (a) and fructose (blue) (b), measured using a 12 cm core filled HC-1060, integration time 60 s. The black spectra are a comparative measurement for 1 M aqueous glucose (a) and fructose (b) solutions for an integration time of 600 s within a cuvette.

In Figure 7.8 the characteristic vibrational bands of glucose are seen at 900, 1100, and 1350 cm⁻¹ and for fructose at 600, 1230 and 1430 cm⁻¹, allowing the identification of the two mono-saccharides [150, 197]. The Raman spectra in Figure 7.8 are compared to the spectra of the same solutions contained in a cuvette (black spectra), with an integration time of 600 s, which was six times longer than the HC-PCF measurement. This measurement was produced, using the same basic set-up as that in Figure 7.1, with the exception that the $\times 40$ lens was exchanged for a $\times 10$ lens to collect the Raman back scatter and the HC-PCF was replaced with a cuvette. While the two measurement approaches cannot be quantitatively compared, this simple, ad-hoc comparison shows that the use of HC-PCF is advantageous for nano litre volumes and SNR enhancement. This is due to the light guiding properties of the HC-PCF and the longer interaction length offered.

The SNR for the HC-PCF and cuvette approach for a selection of wavelength shifts, is outlined in Table 7.2. The background noise for each spectrum is estimated by fitting a Gaussian distribution to the data, in the featureless section of the spectra from 2400 - 2700 cm⁻¹. The $3\sigma_{dev}$ value for each Gaussian fitting is then considered to be the background noise value of each spectra. This estimation was made for the glucose spectra in Figure 7.8 (a), and the fructose spectra in Figure 7.8 (b), for both cases of cuvette and HC-PCF. Three lines were chosen, 491, 1100 and 2940 cm⁻¹ for glucose and 600, 1430 and 2998 cm⁻¹ for fructose. The results demonstrate that despite the shorter integration time of the HC-PCF method, and the lower sample volume in the fibre (8 nL) compared to

the cuvette, the SNR for the HC-PCF, is considerably greater than the cuvette measurement, as shown in Table 7.2.

Table 7.2: SNR comparison for a 10 cm HC-PCF, acquisition time 60 s and a 1 cm cuvette, acquisition time 600 s.

| Glucose | | | |
|-------------------|----------------------|-----------------------|-----------------------|
| Wavenumber Shift: | 491 cm ⁻¹ | 1100 cm ⁻¹ | 2940 cm ⁻¹ |
| HC-PCF SNR: | 21.2 | 19.2 | 45.4 |
| Cuvette SNR: | 6.1 | 11.4 | 22.6 |
| Fructose | | | |
| Wavenumber Shift: | 600 cm ⁻¹ | 1430 cm ⁻¹ | 2998 cm ⁻¹ |
| HC-PCF SNR: | 16.1 | 8.6 | 47.5 |
| Cuvette SNR: | 7.1 | 2.9 | 17.4 |

The sensitivity of the system over a range of concentrations for the aqueous glucose solutions was tested with an 11 cm fibre and a 20 s integration time. This is shown in Figure 7.9, as count rate s⁻¹ for different concentrations of aqueous glucose ranging from 0.3 M (a) to 2.5 M (d).

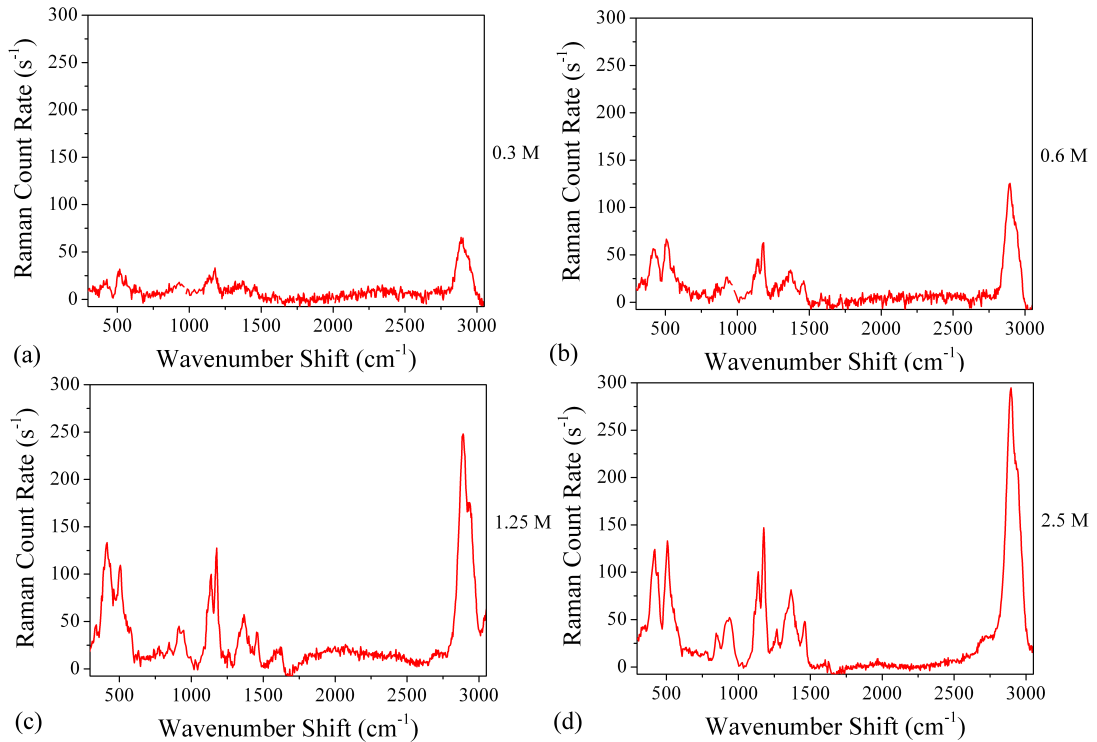


Figure 7.9: (a) 0.3 M, (b) 0.6 M, (c) 1.25 M and (d) 2.5 M aqueous glucose solutions, in core filled only HC-1060, with an integration time of 20 s. All fibres were 11 cm long.

With such short lengths and integration times, solutions at a concentration of 0.3

M could be identified by their Raman spectrum. This is expected to be improved for longer lengths and integration times, as discussed previously.

The noise for each plot was determined using the fluctuations in signal, after the aqueous background was subtracted from each spectra. As described before, the background noise was considered to be the $3\sigma_{dev}$ value of the fluctuations in signal, calculated by fitting a Gaussian distribution to the data at a featureless wavenumber range in the spectrum. The SNR for a selection of lines was then determined for each concentration of aqueous glucose solutions. These lines are at 500, 1180 and 2940 cm^{-1} and are used to determine how the increase in Raman signal behaves with increased concentration. The results for the SNR are outlined in Table 7.3.

Table 7.3: SNR comparison for 0.3 M, 0.6 M, 1.25 M and 2.5 M aqueous glucose solutions in core filled HC-PCF, acquisition time 20 s.

| Wavenumber Shift: | 500 cm^{-1} | 1140 cm^{-1} | 2940 cm^{-1} |
|-------------------|----------------------|-----------------------|-----------------------|
| 0.3 M SNR: | 2.9 | 2.3 | 5.61 |
| 0.6 M SNR: | 4.1 | 4.9 | 11.4 |
| 1.25 M SNR: | 8.9 | 11.7 | 22.8 |
| 2.5 M SNR: | 11.2 | 13.6 | 27.3 |

The SNR values in Table 7.3 verify that with increasing concentration, the sensitivity of the system increases to determine the presence of the target molecule (glucose) in the solution.

The results of Raman count rate s^{-1} are displayed in Figure 7.10 for the four concentrations for the three selected wavenumbers; 500 cm^{-1} (green diamonds), 1140 cm^{-1} (red circles) and 2940 cm^{-1} (blue squares). The limit of the detection of the system is determined by the $3\sigma_{dev}$ value of the noise fluctuations. This is seen in Figure 7.10 as a black dashed line. Each point is assumed to have an error of 20 counts s^{-1} , which is the $3\sigma_{dev}$ value of the noise (which cannot be seen from the figure, due to the scale). The results show that the count rate increases linearly below 2 M, above which, the result is non-linear. This is due to an error in the measurement, probably a misalignment of the fibre, as the Raman count is expected to increase linearly for increasing concentration. A linear function (black dotted line) is fitted to each wavenumber as a function of increasing concentration, and the lines are extrapolated to the 0 intercept to determine where the Raman count intercepts the noise limit. This is at 0.2 M s^{-1} at 2940 cm^{-1} , for an 11 cm core only filled fibre, and is considered the limit of the detection system.

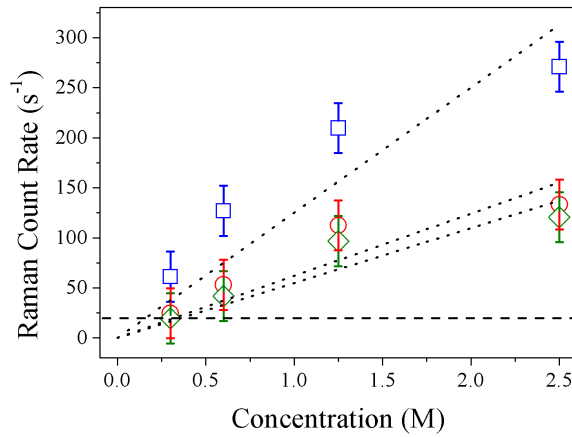


Figure 7.10: Raman count rate with molecular concentration of aqueous glucose. The data for 500 cm^{-1} (green diamonds) 1140 cm^{-1} (red circles) and 2940 cm^{-1} (blue squares) is taken from Figure 7.9 (a-d), and each wavenumber shift is analysed with a linear fit as a function of increasing concentration (black dotted lines). The $3\sigma_{dev}$ noise level is determined from the graphs in Figure 7.9, and plotted as a black dashed line to indicate the detection limit of this system.

The integration time, optimum fibre length and concentration of the sample are important factors that need to be considered for the sensitivity and limits of Raman detection for the collection of Raman scatter from a liquid core waveguide. To detect a molecule at a particular concentration and level of sensitivity, these factors can be balanced to achieve an optimum system, depending on the detection required.

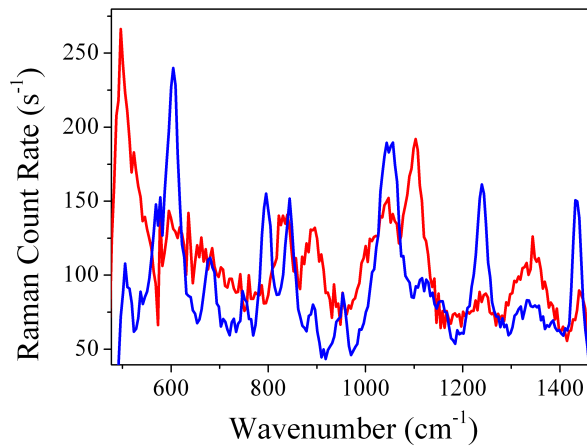


Figure 7.11: Comparison of Raman spectra for 1 M glucose (red) and fructose (blue), in the region $500 - 1500\text{ cm}^{-1}$. Differences in the vibrational structure of the mono-saccharide molecules are seen here.

The mono-saccharides glucose and fructose have very similar physical properties, as discussed in Section 4.3.2. Both have the molecular formula $\text{C}_6\text{H}_{12}\text{O}_6$, with the

difference being that glucose has a six member carbon ring, and fructose has a five member carbon ring [198]. Due to their different fundamental vibrations, the resulting Raman spectra are different in the anomeric region ($600 - 950 \text{ cm}^{-1}$) and the fingerprint region ($950 - 1200 \text{ cm}^{-1}$). While the two molecules were indistinguishable from viscosity measurements (see Figure 4.23), the differences in the Raman spectra allow the molecules to be identified, as illustrated in Figure 7.11.

Identifying Glucose and Fructose

A solution containing the two saccharides at similar concentrations can also be identified by the Raman backscattering. In Figure 7.12, a 0.1 M solution of glucose (red) (a) and a 0.1 M solution of fructose (blue) (b) are shown respectively with a mixed solution of 0.05 M glucose and 0.05 M fructose in water (black) (c), which results in a 0.1 M solution of mono-saccharide. All spectra were taken with an integration time of 20 s. They are compared side by side to determine the presence of the relevant bands in the spectrum.

The presence of glucose is verified by the red dashed lines in Figure 7.12 at 400, 1100, 1300 and 2810 cm^{-1} . The presence of fructose is verified by the blue dashed lines in Figure 7.12 at 520, 730, 1080, 1200, 1370 and 2870 cm^{-1} . In Figure 7.12 (c) the presence of both glucose and fructose is verified by the vibrational bands present at the wavenumbers defined in (a) and (b). Here the Raman count rate is lower in (c), due to the decreased concentration of the glucose and fructose sample in the aqueous solution. The SNR for all solutions at the wavenumbers identified in this paragraph is shown in Table 7.2. This result verifies the presence of both glucose and fructose in the solution in Figure 7.12 (c) and that the Raman scatter from a liquid contained within the HC-PCF can be used to identify the solution, even at low concentrations of 50 mM.

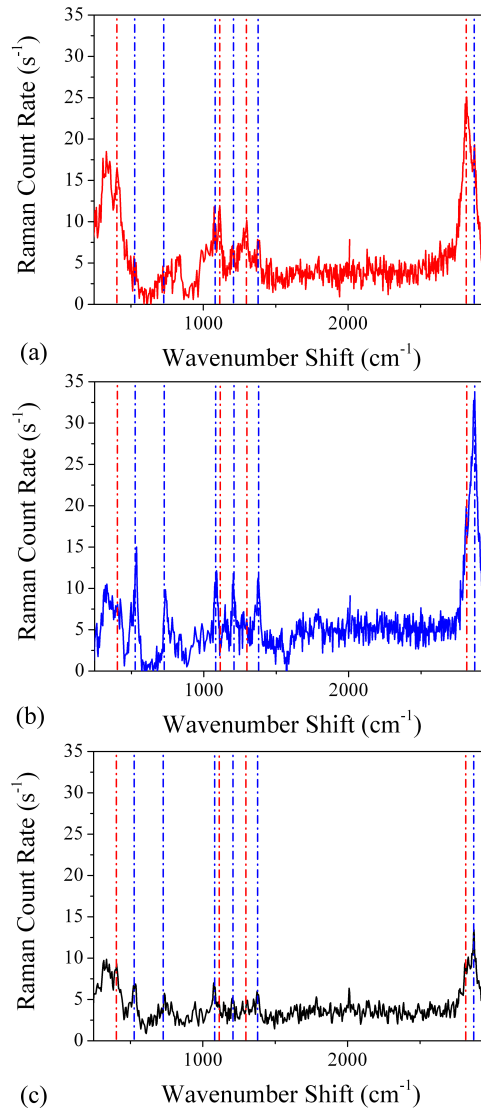


Figure 7.12: 0.1 M glucose spectrum (a) (red) and 0.1 M fructose spectrum (b) (blue) are compared to determine their unique vibration shifts. Then a 0.05 M glucose and 0.05 M fructose aqueous solution (c) is tested to determine if the mixture of glucose and fructose can be identified by their characteristic vibrational bands and intensities, all taken with an integration time of 20 s.

Table 7.4: SNR comparison for 0.1 M aqueous glucose solution, 0.1 M aqueous fructose solution and a mixture of 0.05 M glucose and 0.05 M fructose in aqueous solution, for a number of wavenumbers, verifying the presence of both species in the mixture, for a core filled HC-PCF, for an acquisition time of 20 s.

| Wavenumber | 0.1 M Gluc. | 0.1 M Fruc. | 0.05 M Gluc. and 0.05 M Fruc. |
|-----------------------|-------------|-------------|-------------------------------|
| 400 cm^{-1} | 1.65 | | 3.1 |
| 530 cm^{-1} | | 4.2 | 2.6 |
| 730 cm^{-1} | | 2.3 | 1.2 |
| 1080 cm^{-1} | | 2.4 | 2.6 |
| 1100 cm^{-1} | 2.4 | | 0.9 |
| 1200 cm^{-1} | | 1.9 | 1.3 |
| 1300 cm^{-1} | 1.5 | | 0.9 |
| 1370 cm^{-1} | | 2.4 | 1.9 |
| 2810 cm^{-1} | 6.1 | | 3 |
| 2870 cm^{-1} | | 8.3 | 5.1 |

7.3 Other Applications

The applications of a HC-PCF for the detection of Raman backscatter are numerous in the medical, forensic and industrial industries. A small selection of applications for the sensor are outlined here, which have particular importance in biological and medical applications.

7.3.1 Glucose and Lactate

Glucose and lactate are vital for the metabolism of energy in living organisms. These molecules are complementary during exercise, where glucose is metabolised to produce lactic acid within active muscles [199, 200]. The study of the production of lactic acid in interstitial fluid is an important study in sports science [201]. Furthermore, the understanding of how the concentrations of these molecules in interstitial fluid and in blood plasma change in real time is vital for understanding the bodies recovery to exercise and movement [202, 203].

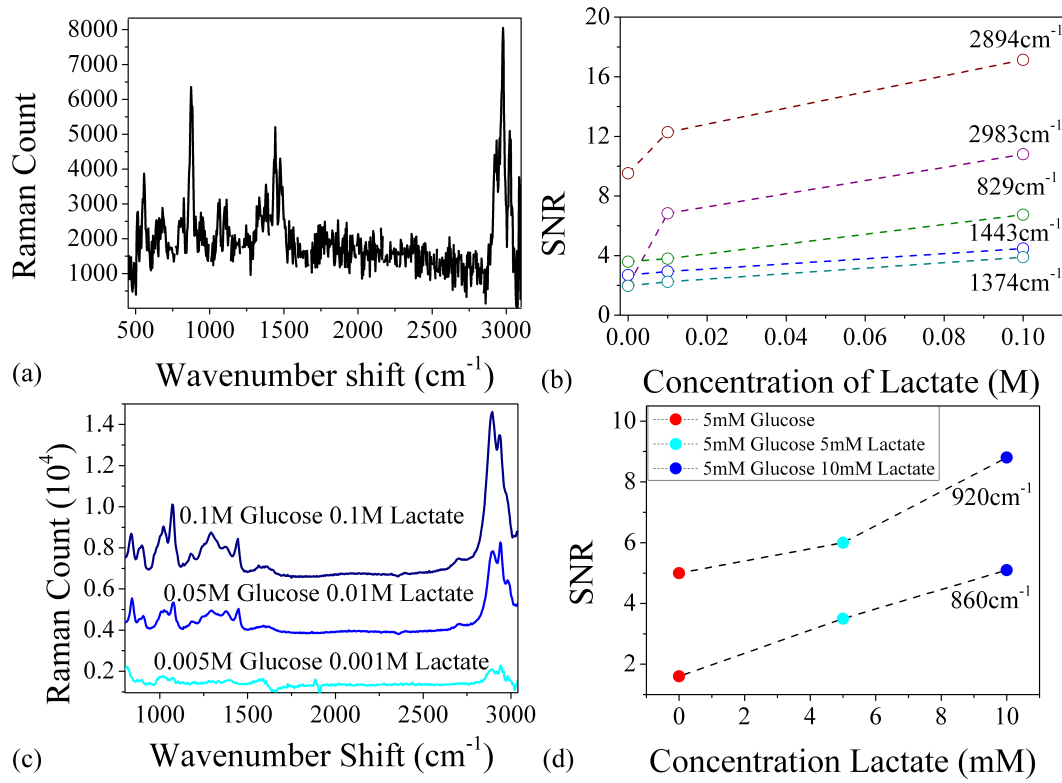


Figure 7.13: Investigations of glucose and lactate at levels of 5 mM to 0.1 M. (a) Raman spectra of a 0.1 M aqueous solution of lactate within a 15 cm HC-1060, integration time 60 s. (b) SNR of lactate Raman spectra lines for three different concentrations. (c) Raman spectra of solutions of glucose and lactate for increasing concentrations, with a 360 s acquisition time. (d) Addition of lactate to a 0.005 M solution of glucose investigated for 860 and 920 cm⁻¹.

Figure 7.13, shows a selection of results for lactate and glucose solutions examined for their Raman spectra within liquid core HC-PCF. The Raman spectra of lactate and glucose were tested for different sample concentrations, to determine how lactate reacted to the presence of glucose. Figure 7.13 (a) shows the Raman spectrum of a 0.1 M aqueous solution of lactate within a 15 cm HC-1060. This spectrum was acquired for 60 s, and the background signal was subtracted. The spectra of lactate has several distinctive Raman lines at 829, 1374, 1443, 2894 and 2983 cm⁻¹, as seen in the literature [204]. The Raman spectra were recorded for three different concentrations, and the results are shown in Figure 7.13 (b). This information could then be used to analyse the addition of lactate to glucose solutions.

Aqueous mixtures of glucose and lactate solution were studied and the results are shown in Figure 7.13 (c-d) at physiological concentrations. Glucose is present

in the human body at concentrations of 4-7 mM, but can be much higher in diabetic patients [45, 50]. Lactate is present in concentrations between 2 - 8 mM within the blood before and during exercise [205, 206]. The Raman spectra 0.1 M solution of glucose and lactate, contained within the core of a HC-1060, was acquired over 360 s. The solution was then diluted to 0.05 M and the Raman spectra recorded. The solution was diluted further to 0.005 M to push the limits of the detection to physiological levels. As can be seen for Figure 7.13 (c) the spectrum of lactate can be distinguished from that of glucose at 829, 1443 and 2983 cm^{-1} . Figure 7.13 (d) features a 0.005 M solution of glucose that has lactate at 0.005 M and 0.01 M added to it. Two Raman lines are examined at 860 and 920 cm^{-1} . It is seen in the figures that the SNR increases with increasing lactate concentration by a ratio of 1 - 3 per 0.005 M increase for a 60 s integration time.

7.3.2 Creatinine and Urea

Creatinine is the break down product of creatine, a nitrogenous organic acid that provides energy to muscle groups within living organisms. Creatinine is not absorbed in the body, but is a waste product that is filtered through the renal system. The functional properties of the kidneys are determined by testing the amount of creatinine present in bodily fluids [207]. An increase in the creatinine levels indicates a malfunction of the kidneys and renal system. A decrease in creatinine can also be indicative of muscular disease. The use of Raman spectroscopy for the study of the presence of creatinine in bodily fluids has potential powerful applications [208].

The Raman spectra for increasing concentrations of creatinine in aqueous solution were measured in a 15 cm core filled HC-1060. In Figure 7.14 (a) a typical creatinine Raman spectrum is shown, with the main vibrational bands marked by coloured dashed lines. This spectra for creatinine is comparable to that seen in the literature [209]. This vibrational structure of creatinine was identified in spectra for a wide range of concentrations from 0.5 - 500 mM in aqueous solutions, the results of the SNR (with the lowest SNR value being 1.5) are shown in Figure 7.14 (b). The Raman spectra of a 0.3 M urea solution is shown in Figure 7.14 (c) showing a strong Raman line at 1000 cm^{-1} . In Figure 7.14 (d) the 0.3 M solution of urea also contains a 0.01M solution of creatinine (at typical physiological levels), and the Raman spectra accumulated over 360 s. Despite the dominance of the of the urea features in the spectrum, the creatinine can still be detected. This is more evident in the magnified section of the spectrum

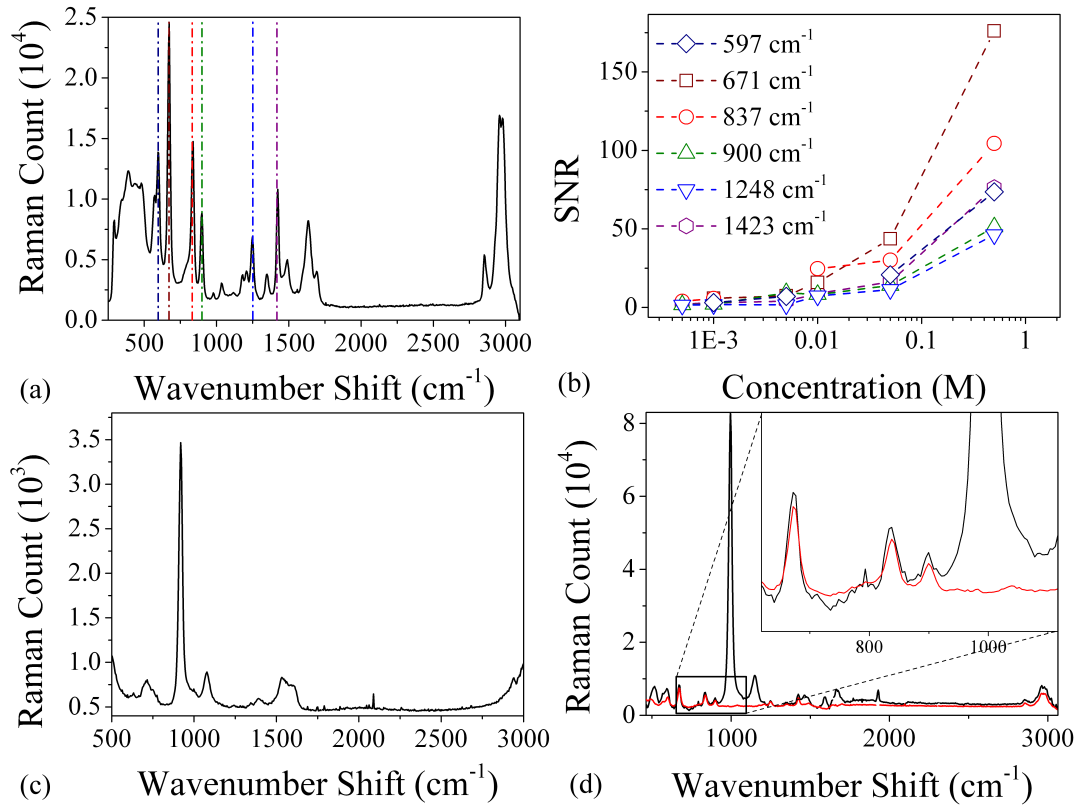


Figure 7.14: (a) 0.5 M aqueous solution of creatinine, displaying the characteristic lines at 597, 671, 837, 900, 1248, 1423 cm^{-1} , that will be used to identify the presence of creatinine in solutions of urea. (b) Analysis of the SNR of the characteristic wavelength shifts of creatinine at different concentrations ranging from 0.5 - 500 mM. All SNR are above 1.5. (c) Raman spectra of an aqueous solution of 0.3 M urea taken for a time of 20 s. (d) Aqueous solution of 0.3 M urea (black) and 0.01 M creatinine (red). Inset: the presence of creatinine (red line) is clearly seen in the urea sample at 671, 837 and 900 cm^{-1} .

between 600 - 1100 cm^{-1} , inset in Figure 7.14 (d), where the mixture of urea and creatinine in black is compared to a 0.01 M solution of creatinine in red.

7.3.3 Interstitial Fluids

In this section, the Raman spectra of solutions of lactic acid, glutamic acid and lysine at concentrations of 0.05 M are presented and discussed. Spectra were taken with an integration time of 20 s using 20 cm core only filled HC-PCF. Figure 7.15 (a-c) shows different Raman spectra for aqueous solutions of interstitial liquids. In Figure 7.15 (d) a Raman spectrum is shown where all three components were mixed. This spectrum contains all the vibrational structure of the three inter-

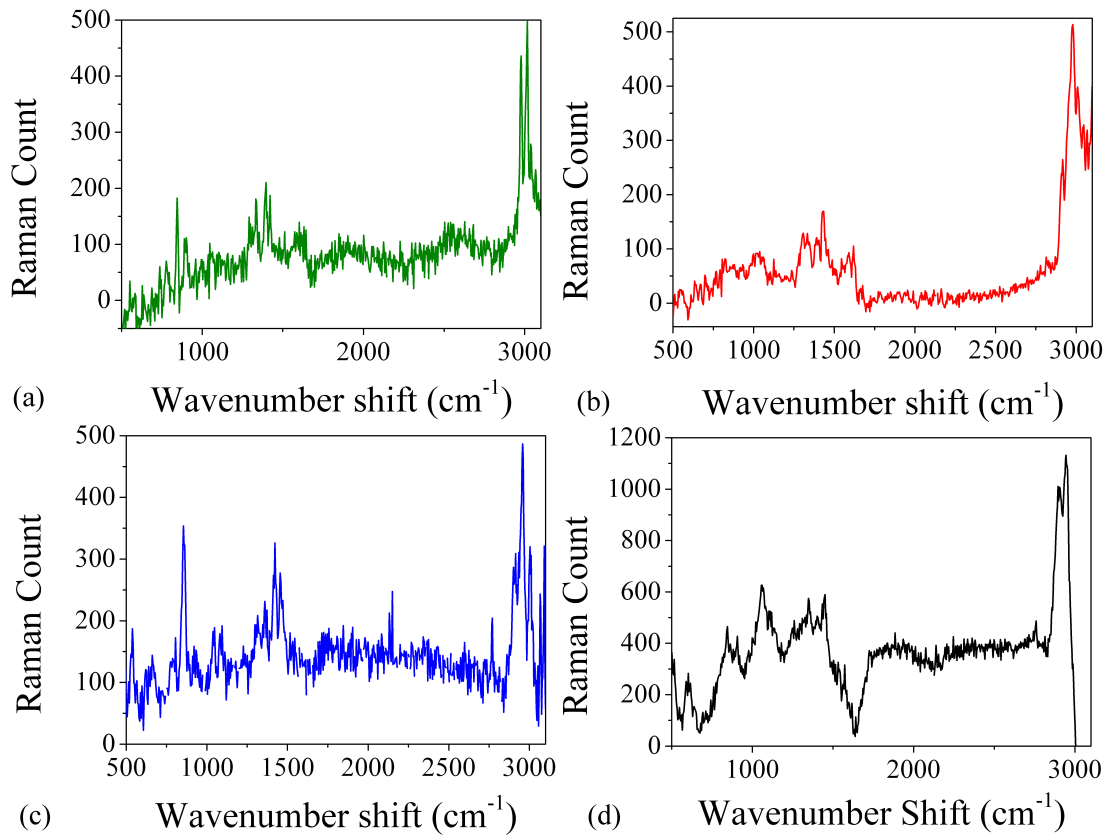


Figure 7.15: The Raman spectra of three different components of interstitial fluids, and a Raman spectra of the combined fluids, contained in a 20 cm core filled HC-PCF. The spectra were integrated over 20 s for aqueous solutions of (a) 0.05 M glutamic acid (b) 0.05 M lysine (c) 0.05 M lactic acid (d) 0.05 M solution of all three components.

stitial components, however, the SNR of each line is reduced due to the nature of the mixed solution. The vibrational bands for each interstitial component are within the same region, resulting in a broadening of the features, and difficulty separating the three components. With longer integration times and longer fibre lengths, the SNR would increase, allowing a thorough identification of the Raman lines of the separate molecules of glutamic acid, lactic acid and lysine.

To our knowledge at this time, some of these results presented here, have not been studied or published before utilising HC-PCF for Raman backscatter collection. The Raman cross section of these substances, such as glucose, lactic acid and lysine are very small, on a range of $10^{-30} \text{ cm}^2 \text{ molecule}^{-1} \text{ sr}^{-1}$ [210]. As a result the use of Raman for their detection and study is not widely utilised, despite the wealth of information that can be determined from this technique.

7.4 Summary

This chapter demonstrates the use of HC-PCF as a tool for the collection of Raman scatter from liquids contained within the hollow capillaries. From experimental observations, it was shown that core only filled fibres are more appropriate for the measurement of Raman spectra than fully filled fibres.

The most practical length of HC-PCF for experimental measurements was determined and the data was fitted with a model to determine the length required to provide enhanced collection of the Raman signal, depending on the absorption coefficient of the Raman generating material and the loss of the fibre. This scales as $1/2\alpha_s$, and the most practical length was determined to be 1.25 m for a water core HC-PCF.

By optimising the length, integration time, pump laser wavelength and strength, the HC-PCF can be used as an optimum device for the collection of Raman scatter, with nano litre volume samples. This has many promising applications in a wide range of sensing procedures, such as industry, medical diagnostics and liquid identification, some of which are briefly investigated in this chapter.

- The limits of detection depend on the cross section of the molecule, and for an 11 cm core only filled fibre was 0.2 M s^{-1} at 2940 cm^{-1} for glucose.
- The system can be optimised for time, fibre length, laser source and strength to collect the Raman signal and enhance the sensitivity of the system.
- The measurement of Raman scatter with HC-PCF was applied to bio-fluids, such as glucose and lactate, creatinine and urea, and a range of interstitial fluids.
 - Bio-fluids require measurements to be made for nano litre volumes.
 - These fluids are present in mM concentrations.
 - Creatinine was detected in this chapter, with an SNR of 3.9 at a concentration of 0.5 mM, at 837 cm^{-1} , for an integration time of 360 s, fibre length 15 cm.
- High intensity laser sources degrade the molecules [211, 212], therefore, low intensity lasers can be used with HC-PCF, compensating for the low power with longer interaction lengths and longer integration times.

Chapter 8

Conclusions

The aim of this thesis was to explore the use of hollow core photonic crystal fibre as a tool for sensing nano litre volumes of liquid samples. This was investigated for the purpose of determining the viscosity, by measuring the liquids flow velocity, and to identify the molecular components of the liquid solution, by the collection of Raman scattering. Hollow core photonic crystal fibre was utilised for sensing liquids of industrial and biological importance, such as mono-saccharide solutions and interstitial fluids, over a wide range of combinations and concentrations. The scope of applications for hollow core fibre can therefore be extended to the food industry and medical diagnostics, especially where nano litre volumes of sample are used and required.

Hollow core photonic crystal fibre waveguides comprise a unique structure that is remarkably suitable for liquid sensing. This is due to the guidance and physical properties of the fibre, which allows the insertion of liquid to the core, and surrounding capillaries. These properties enable high overlap of the liquid sample with the optical field, in particular for the liquid core only filled case, and can be used to monitor the transmission properties, excite the sample, and transport the transmitted signal to the end facets. Employing hollow core photonic crystal fibre for sensing purposes in industry and bio-medical diagnosis has the potential for simple, rapid and continuous monitoring of low volume liquid samples.

Chapter Summary

In the initial chapters of this thesis, Chapter 3 and Chapter 4, the dynamic flow of liquids through the capillaries of the fibre was studied, first with a microscope

to understand the filling pattern, and secondly with a specifically selected laser source. The microscope set-up allowed the filling pattern to be studied to determine experimentally how the light guiding properties of the fibre will change dynamically. It was observed that the core of the fibre will always fill first, due to its larger diameter, followed by the capillaries of the micro-structured cladding. The fibres light guiding properties therefore change from original photonic bandgap when empty, to index guiding when the core was filled, and a shifted photonic band gap effect in the fibre portion where the core and cladding capillaries were filled with liquid.

It was shown for the first time in Chapter 4 that by utilising the change in guidance properties of a hollow core fibre when filling dynamically with a liquid, the point where the core fills and where all the cladding capillaries fill can be determined by observing the propagation changes of a laser source. This technique was used to measure the velocity of liquid flow, and subsequently liquid viscosity, using the theory of capillary flow. The concept was tested with aqueous propan-1-ol solutions and mono-saccharides dissolved in PBS. This has been filed for patent applications in Ireland, the U.K. and the U.S. [110].

To further understand the light guiding mechanism of the liquid filled fibres, the transmission properties of a hollow core fibre was investigated over a broad range of wavelengths. The distribution of wavelengths from 500 - 1700 nm over a cross section of a liquid core and fully filled fibre was mapped in Chapter 5. This chapter verifies that the light guidance properties and distribution of light for the core only filled fibre and fully filled fibre are very different. It was observed that the core only filled fibre has a very broad modal distribution, spanning the width of the core, while the fully filled fibre has a much narrower distribution that was narrowly confined to the centre of the core only, despite the liquid filling of all the capillaries.

In Chapter 6, it is shown for the first time that the hollow core photonic crystal fibre can be used as a multi-analytical sensor by determining the viscosity from the transmission of a 532 nm laser and the Raman spectra from the backscatter of the dynamically filling liquid.

In the final Chapter 7, the Raman backscatter collection using hollow core photonic crystal fibres was investigated in detail, to determine the sensitivity of the technique to fibre length, filling profile, integration time and solution concentration. It is demonstrated that by filling the core only of the fibre, and optimising the detection system, mM concentrations of molecules within aqueous solution

can be detected and identified. Spontaneous Raman scatter is a weak event, and due to the low probability of events, measurements are usually made with high intensity laser sources. However, Raman detection of biomolecules is restricted by the intensity, as high powers can lead to degradation of the molecules. The stability and collection efficiency of the hollow core photonic crystal fibre allows lower laser powers to be used over longer interaction lengths and for much longer integration times. This chapter shows for the first time the Raman analysis of biologically important fluids within a core only filled hollow core photonic crystal fibre.

In conclusion,

- This thesis demonstrates the use of hollow core photonic crystal fibres for use as a liquid sensor. The dynamic filling of the fibre was monitored to determine the viscosity of nano litre liquid samples and to investigate the Raman spectra.
 - This is shown for aqueous solutions of glucose, fructose and propan-1-ol.
- The two filling states, core only filled and fully filled are investigated to determine why the core only filled fibre presented a much greater collection of Raman scatter.
 - The core only filled fibre guides light by a modified index guiding effect, resulting in a large value for the numerical aperture.
 - The fully filled fibre guides light by a shifted photonic band gap effect, resulting in a smaller numerical aperture, than the core only filled fibre.
 - Raman scatter is collected over a greater range of angles due to the large numerical aperture of the core only filled fibre, allowing a larger portion of light to be collected at each end facet.
 - As shown in Chapter 5, the core filled fibre has a wider distribution of the optical field within the core, resulting in a greater number of molecules excited for Raman scatter.
- Interstitial fluid components, with a typically small Raman cross section are investigated utilising core only filled hollow core fibre.
 - The Raman spectra of aqueous solutions of lactic acid, glutamic acid,

lysine and creatinine at physiological levels are measured for the first time in core only filled hollow core photonic crystal fibre.

- A multi-analytical technique for liquid sensing was presented utilising the structure and guidance properties of hollow core photonic crystal fibre.

8.1 Future Work

The work accomplished in this thesis has led to several possible research fields that require further examination. The first is the future development of a nano litre viscometer using hollow core photonic crystal fibre. The concept has been proven here to be sensitive to a wide range of viscosities present in nano litre quantities. There is a demand for such a device, that is light weight, has a simple technique and will achieve rapid viscosity results for nano litre samples. To further develop this concept, a fully temperature controlled and environmentally protected prototype could be fabricated for testing of the measurement technique. Other light sources should be investigated, that allow for the system to be miniaturised and will eventually result in a much less bulky experimental design for the nano litre viscometer prototype.

In this thesis, only Newtonian liquids were investigated. However, non-Newtonian liquids are equally important in medical diagnostics and industrial applications. These liquids have a viscosity that is not constant, and therefore the flow velocity cannot be assumed constant. The liquid flow through the capillaries of the HC-PCF can be monitored externally due to the scatter that occurs when the laser light meets the liquid interface. The change in velocity of the liquid as it travels through the fibre could be measured dynamically by monitoring the interface where light is scattered using a CCD camera, positioned to monitor the side view of the fibre length.

It was demonstrated in this thesis that the hollow core fibre when core only filled is an ideal device for the collection of Raman scatter. There are two possible outcomes from this research. The first is to develop a model that can theoretically determine the guidance and collection properties of liquid filled hollow core photonic crystal fibres, for both states, core only and fully filled. This would require computational analysis of light guidance within a liquid filled hollow core photonic crystal fibre, to determine the optimum Raman signal generation and collection within such a configuration. The second is the design of a fibre that is specifically

for the collection of the Raman scatter within a liquid core, surrounded by an air/silica cladding.

Appendix A

List of Symbols and Acronyms

The list of all acronyms and symbols used throughout this thesis is displayed here

A - area

a_i - parameter for modes

BS - beam splitter

C - concentration

CCD - charge coupled device

d - capillary diameter

D - density of sample

DAQ - data acquisition system

E - electromagnetic wave

f - air filling fraction

F - force

F_c - capillary force

F_f - friction force

F_g - gravity force

F_P - pressure force

FWHM - full width half maximum

$F(x; \mu, \sigma_{dev}^2)$ - Gaussian distribution

g - gravity

HC-PCF - hollow core photonic crystal fibre

I - intensity of scattered wave

I_0 - initial intensity

I_L - intensity of the pump laser

I_R - intensity of Raman signal

A. LIST OF SYMBOLS AND ACRONYMS

k - wavenumber
K - constant of length enhancement for Raman backscatter
KCl - potassium chloride
 k_z - longitudinal component of wavevector
L - length
m - mass
n - refractive index
 n_{air} - refractive index of air ~ 1
 n_{avg} - average refractive index of the fibre cladding
 $n_{cladding}$ - refractive index of the fibre cladding
 n_{core} - refractive index of the fibre core
 n_{eff} - effective refractive index
 n_{liquid} - refractive index of the liquid
 n_{silica} - refractive index of silica ~ 1.45
 Δn - difference in refractive index
NA - numerical aperture
NaHCO₃ - sodium bicarbonate
NF - notch filter
OSA - optical spectrum analyser
P - power
 \vec{P} - electric dipole moment
PBG - photonic band gap
PBS - phosphate buffer saline
PD - photodiode
PH - pin hole
PID - proportional integral device
PMMA - polymethyl methacrylate
 P_P - pressure
q - system co-ordinate
Q - volumetric flow rate
r - radius
 R_L - resistive load
s - second
SC - supercontinuum
SNR - signal to noise ratio
t - time
T - temperature

A. LIST OF SYMBOLS AND ACRONYMS

t_{int} - initial time

T_0 - nominal temperature ~ 298.15 K

u - velocity

USB - universal serial bus

v - velocity

V - volume

x - mass fraction

y - axial distance

α - polarisability

α_{bulk} - bulk modulus of silica

α_L - decay of pump laser

α_s - loss of system

β - propagation constant

\hbar - planks constant

λ - wavelength

λ_0 - initial wavelength

μ - viscosity

μ_{mean} - mean

ν - frequency

$\tilde{\nu}$ - wavenumber

π - universal constant 3.14159

ϖ - width of Gaussian distribution

ρ - density

σ - surface tension

σ_{dev} - standard deviation

σ_s - Raman cross section

σ_w - surface tension of the solvent

Λ - pitch of the hollow core fibre micro-structure

Ω - solid angle

Appendix B

Derivation of the Liquid Flow Velocity Model

To derive the filling model from Equation (2.10), in Chapter 2, the mass is regarded to be a function of volume and density to emulate the previous equations for the four forces, described in the previous section. The velocity is changed to be expressed as a derivative of the length of the capillary with respect to time:

$$\sum \vec{F} = \frac{d(m\vec{v}(t))}{dt} = \frac{d(\rho\pi R^2 \vec{L}(t)\vec{v}(t))}{dt} = \frac{d}{dt} \left(\rho\pi R^2 \vec{L}(t) \frac{d\vec{L}(t)}{dt} \right) \quad (\text{B.1})$$

The sum of all forces with the new expression for Newton's equation is therefore:

$$\frac{d}{dt} \left(\rho\pi R^2 \vec{L}(t) \frac{d\vec{L}(t)}{dt} \right) = 2\pi R\sigma \cos\theta + \Delta P\pi R^2 - 8\pi\mu \vec{L}(t)\vec{v}(t) - \pi\rho g R^2 \vec{L}(t) \quad (\text{B.2})$$

Divide across by $\rho\pi R^2$

$$\frac{d}{dt} \left(\vec{L}(t) \frac{d\vec{L}(t)}{dt} \right) = \frac{2\sigma \cos\theta}{\rho R} + \frac{\Delta P}{\rho} - \frac{8\mu \vec{L}(t)\vec{v}(t)}{\rho R^2} - g\vec{L}(t) \quad (\text{B.3})$$

Let $A = \frac{4\sigma \cos\theta + 2\Delta P R}{\rho R}$ and $B = \frac{8\mu}{\rho R}$ (as per Nielsen) [32].

$$2 \frac{d}{dt} \left(\vec{L}(t) \frac{d\vec{L}(t)}{dt} \right) = A - 2B\vec{L}(t)\vec{v}(t) - 2g\vec{L}(t) \quad (\text{B.4})$$

To solve, the differential expressions in footnotes ¹ and ² are required. Therefore the equation becomes

$$\frac{d^2(\vec{L}(t)^2)}{dt^2} = A - B \frac{d\vec{L}(t)^2}{dt} - 2g\vec{L}(t) \quad (\text{B.5})$$

Gravity is a negligible condition due to scale of radius considered when using a HC-PCF (which is less than $5 \times 10^{-6}\text{m}$), and thus the term can be removed from Equation (B.4). It is also negligible in the experiments that will be outlined, as the fibre will be filled in a horizontal position.

To solve this equation for $\vec{L}(t)$, it is required to format a second order non-linear equation by letting $y = \vec{L}(t)^2$. Therefore $\frac{d^2y}{dt^2} + B \frac{dy}{dt} - A = 0$. This gives an equation, in the form $y'' = f(t, y')$. Note that the function of y is missing from the differential. This lets us solve the equation using an integration factor. In order to do so, let $z = \frac{dy}{dt}$. Thus, a first order differential equation is derived $\frac{dz}{dt} + Bz - A = 0$. A new function $z' = f(t, z)$ is specified, where $B = p(t)$ and $A = q(t)$.

In order to solve an equation like this to determine the roots, an integration constant ³ is required. For the purpose here, the integration constant is chosen to be $h(x) = e^{\int B dt}$. Utilising the integration constant allows the function to be solved as a function of $L(t)$. The function $\frac{dz}{dt} + Bz - A = 0$, is multiplied across by the integration constant, $h(x)$. By applying the product rule in reverse, the left hand side can be written as

$$\frac{dz}{dt} e^{\int B dt} + Bz e^{\int B dt} = \frac{d}{dt} (z e^{\int B dt}) \quad (\text{B.6})$$

and the right hand side can be written as, $A e^{\int B dt}$. This equation then becomes

$$z(t) e^{Bt} = \int A e^{Bt} dt + C \quad (\text{B.7})$$

¹Left hand side:
 $\frac{d^2(f(t)^2)}{dt^2} = \frac{d^2}{dt^2} [f(t)f(t)] = \frac{d}{dt} (f(t)f'(t) + f(t)f'(t)) = 2 \frac{d}{dt} \left(f(t) \frac{df(t)}{dt} \right)$

²Right hand side:

$$\frac{df(t)^2}{dt} = 2f(t)f'(t)$$

³To solve the equation:

$$y'(x) + f(x)y(x) = g(x)$$

Solve using an integrating factor $h = h(x)$, such that using product rule:

$$\frac{d}{dx} (hy) = h \frac{dy}{dx} + y dh dx = hg(x)$$

Dividing through by h gives

$$\frac{1}{y} \frac{dy}{dx} + \frac{1}{h} \frac{dh}{dx} = \frac{g(x)}{y}$$

, with initial condition that $z(0)=0$. Solving gives:

$$ze^{Bt} = \frac{Ae^{Bt}}{B} + C \quad (\text{B.8})$$

Using the initial condition, $C = -\frac{A}{B}$. From before, $z = \frac{dy}{dt}$.

$$\int dy = \int \left(\frac{A}{B} - \frac{Ae^{-Bt}}{B} \right) dt \quad (\text{B.9})$$

$$y(t) = \frac{At}{B} + \frac{Ae^{-Bt}}{B^2} + C \quad (\text{B.10})$$

With initial conditions $C = -\frac{A}{B^2}$ and since $y = L(t)^2$

$$L(t)^2 = \frac{At}{B} + \frac{Ae^{-Bt}}{B^2} - \frac{A}{B^2} \quad (\text{B.11})$$

It is assumed that $e^{-Bt} \rightarrow 0$, which is true when considering the dimensions of the capillaries of the HC-PCF that this model is applied to and the parameters of the fluids that will be considered in this thesis. Equation (B.11) is now in the form of a quadratic formula

$$B^2 L(t)^2 = BA t - A \quad (\text{B.12})$$

This quadratic equation can be solved for B , such that

$$B = \frac{At + \sqrt{A^2 t^2}}{2L^2} \quad (\text{B.13})$$

which gives a value for the ratio of A to B ;

$$\frac{A}{B} = \frac{L^2}{t} \quad (\text{B.14})$$

Considering the constants A and B , defined earlier in this section, the fraction gives the ratio of surface tension to viscosity

$$\frac{A}{B} = \frac{\sigma R}{2\mu} \quad (\text{B.15})$$

This allows the average velocity of the liquid flow through a length of capillary to be related to the viscosity of the fluid (μ), surface tension (σ), radius (R) and

length (L) of the capillary, and the time (t) required to fill the capillary length.

$$v = \frac{L}{t} = \frac{\sigma R}{2L\mu} \quad (\text{B.16})$$

This equation shall be used in the experiments to relate the average liquid velocity to the physical parameters of viscosity and surface tension to characterise liquid samples. The length of a HC-PCF segment can be measured, and experimentally the filling can be timed to determine the average velocity of a liquid sample.

Appendix C

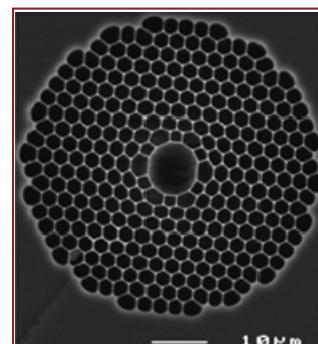
Data Sheets

- HC-1060 data sheet, courtesy of NKT Photonics A/S
- HC-1550 data sheet, courtesy of NKT Photonics A/S

HC-1060-02

Hollow Core Photonic Bandgap Fiber for 1060nm Range Applications

- >95% of optical power located in air
- Quasi-Gaussian fundamental mode
- Can be filled with gas
- Low bend loss down to few mm bend radius
- Fresnel reflection to air at the end faces $<10^{-4}$
- Up to 80% of fiber cross section composed of solid silica, facilitating fusion splicing to conventional fibers
- Undoped silica for good temperature stability



Hollow core photonic bandgap fibers guide light in a hollow core surrounded by a microstructured cladding formed by a periodic arrangement of air holes in silica.

Since only a small fraction of light propagates in glass, the effect of material nonlinearities is significantly reduced and the fibers do not suffer from the same loss limitations as fibers made from all solid material.

Applications include power delivery, pulse shaping and compression, sensors and nonlinear optics.

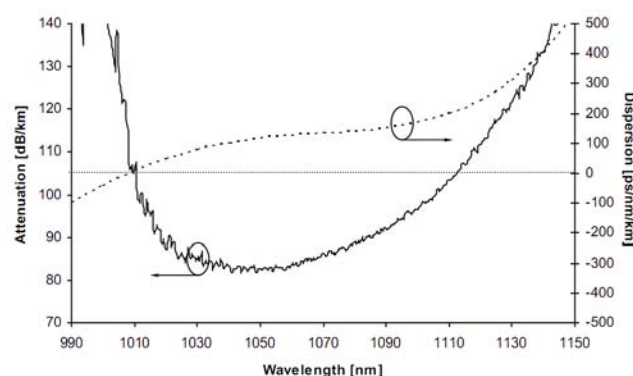
Physical properties

| | |
|--|--------------------------------------|
| Core diameter* | 10 $\mu\text{m} \pm 1 \mu\text{m}$ |
| Pitch | 2.75 μm |
| Air filling fraction PBG region | > 90% |
| Diameter of holey region | 50 μm |
| Cladding diameter | 123 $\mu\text{m} \pm 5 \mu\text{m}$ |
| Coating diameter (single layer acrylate) | 220 $\mu\text{m} \pm 50 \mu\text{m}$ |

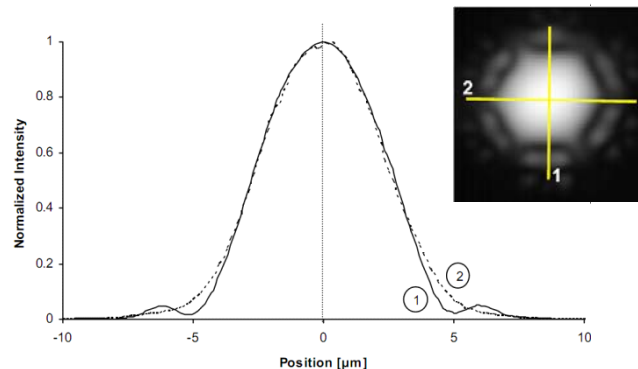
Optical properties

| | |
|--|-------------------------------------|
| Center wavelength | 1060 nm |
| Attenuation @ 1060 nm | < 0.1 dB/m |
| Dispersion @ 1060 nm | 120 ps/nm/km |
| Dispersion slope @ 1060 nm | 1 ps/nm ² /km |
| Dispersion slope @ zero disp. wavelength | 4.4 ps/nm ² /km |
| 10 dB width of transmission band | > 90 nm |
| Fraction of light in air | > 90% |
| Mode field diameter (1/e ²) | 7.5 $\mu\text{m} \pm 1 \mu\text{m}$ |
| Effective mode index | ~0.99 |
| Mode shape overlap with std. SMF | > 90% |

Typical attenuation and dispersion



Typical near field intensity



* Core formed by removing 7 hexagonal unit cells of the cladding



Hollow
Core



Spectral
Filtering

HC-1550-02

Hollow Core Photonic Bandgap Fiber

- < 5% of optical power located in silica
- Gaussian-like fundamental mode
- Can be filled with gas
- Negligible bend loss
- Fresnel reflection of core mode to air <10⁻⁴
- Mode effective index close to unity
- Numerical Aperture ~ 0.2
- Pure silica for good temperature stability

Hollow core Photonic Bandgap Fibers guide light in a hollow core, surrounded by a microstructured cladding of air holes and silica.

Since only a small fraction of the light propagates in silica, the effect of material nonlinearities is insignificant and the fibers do not suffer from the same limitations on loss as conventional fibers made from solid material alone.

Applications

- Fiber optic gyroscopes
- Pulsed lasers (pulse delivery and/or compression)
- Gas spectroscopy
- Low latency communication

Physical properties

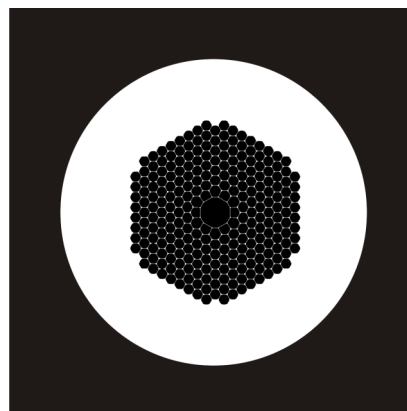
| | |
|------------------------|-----------------------|
| Core diameter | 10 ± 1 µm |
| Cladding pitch | 3.8 ± 0.1 µm |
| Diameter of PCF region | 70 ± 5 µm |
| Cladding diameter | 120 ± 2 µm |
| Coating diameter | 220 ± 30 µm |
| Coating material | Single layer acrylate |

Optical properties

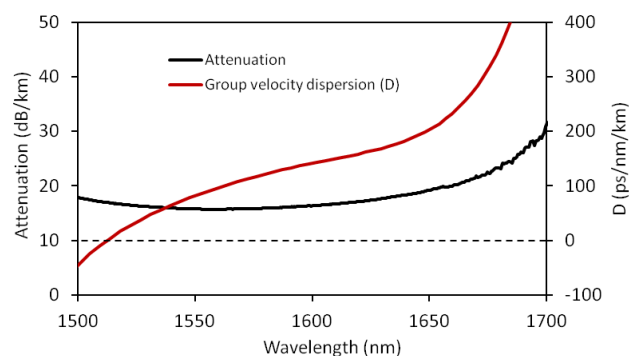
| | |
|--|--------------|
| Design wavelength | 1550 nm |
| Attenuation @ 1550 nm | < 30 dB/km |
| Typical GVD @ 1550 nm | 90 ps/nm/km |
| Operating wavelength ⁽¹⁾ | 1490-1680 nm |
| Mode field diameter @ 1550 nm ⁽²⁾ | 9 ± 1 µm |

1. Over which the attenuation is < 30 dB/km
2. Full 1/e²-width of the near field intensity distribution

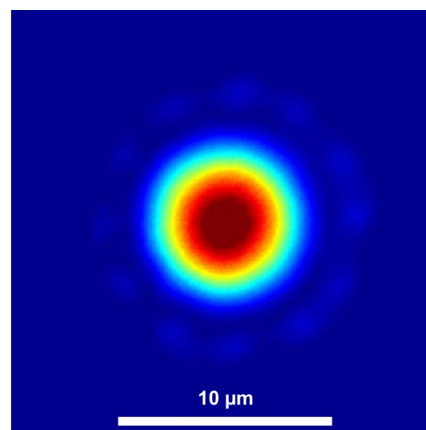
Schematic fiber cross section



Typical attenuation and dispersion



Typical near field intensity profile



HC-1550-02-111221

Bibliography

- [1] E. Hecht, *Optics*. Addison-Wesley Longman, Incorporated, 2002.
- [2] G. Agrawal, *Nonlinear Fiber Optics*. Elsevier, Academic Press, 2007.
- [3] B. Culshaw and A. Kersey, “Fiber-optic sensing: A historical perspective,” *Journal of Lightwave Technology*, vol. 26, pp. 1064–1078, 2008.
- [4] S. W. James, M. L. Dockney, and R. P. Tatam, “Simultaneous independent temperature and strain measurement using in-fibre bragg grating sensors,” *Electronics Letters*, vol. 32, pp. 1133–1134, 1996.
- [5] K. S. C. Kuang, W. J. Cantwell, and P. J. Scully, “An evaluation of novel plastic optical fibre sensor for axial strain and bend measurements,” *Measurement Science and Technology*, vol. 13, pp. 1523–1534, 2002.
- [6] A. J. Rogers, “Distributed optical- fibre sensors for the measurement of pressure, strain and temperature,” *Physics Reports*, vol. 169, pp. 99–143, 1988.
- [7] M. C. Farries, M. E. Fermann, R. I. Laming, S. B. Poole, and D. N. Payne, “Distributed temperature sensor using Nd^{3+} -doped optical fibre,” *Electronics Letters*, vol. 22, pp. 418–419, 1986.
- [8] M. G. Xu, L. Reekie, Y. T. Chow, and J. P. Dalkin, “Optical in-fibre grating high pressure sensor,” *Electronics Letters*, vol. 29, pp. 398–399, 1993.
- [9] B. Culshaw, “The optical fibre sagnac interferometer: An overview of its principles and applications,” *Measurement Science and Technology*, vol. 17, pp. R1–R16, 2006.
- [10] A. D. Kersey, M. A. Davis, H. J. Patrick, M. LeBlanc, K. P. Koo, C. G. Askins, M. A. Putnam, and E. J. Friebele, “Fiber grating sensors,” *Journal of Lightwave Technology*, vol. 15, pp. 1442–1463, 1997.

- [11] K. V. Grattan and T. Sun, "Fiber optic sensor technology: An overview," *Sensors and Actuators*, vol. 82, pp. 40–61, 2000.
- [12] B. Lee, "Review of the present status of optical fiber sensors," *Optical Fiber Technology*, vol. 9, pp. 57–79, 2003.
- [13] Y. J. Rao, "Recent progress in applications of in-fibre bragg grating sensors," *Optics and Lasers in Engineering*, vol. 31, pp. 297–324, 1999.
- [14] O. Strobel, D. Seibl, J. Lubkoll, and R. Rejeb, "Fiber optical sensors-an overview," in *11th International Conference on Transparent Optical Networks*, Azores, pp. 1–6, 2009.
- [15] G. Brambilla, "Microfluidic and bio-applications of optical microfibres," in *Photonics Global Conference, Singapore*, vol. 5706, p. 030 (5 pp), 2010.
- [16] A. K. Sharma, R. Jha, and B. D. Gupta, "Fiber-optic sensors based on surface plasmon resonance: A comprehensive review," *IEEE Sensors Journal*, vol. 7, pp. 1118–1129, 2007.
- [17] M. E. Bosch, A. J. R. Sanchez, F. S. Rojas, and C. B. Ojeda, "Recent developements in optical fiber biosensors," *Sensors*, vol. 7, pp. 797–859, 2007.
- [18] B. Lee, S. Roh, and J. Park, "Current status of micro- and nano-structured optical fiber sensors," *Optical Fiber Technology*, vol. 15, pp. 209–221, 2009.
- [19] M. D. Marazuela and M. C. Moreno-Bondi, "Fiber-optic biosensors-an overview," *Analytical Bioanalytical Chemistry*, vol. 372, pp. 664–682, 2002.
- [20] J. D. Love, W. M. Henry, W. J. Stewart, R. J. Black, and S. Lacroix, "Tapered single-mode fibres and devices. i. adiabaticity criteria," *IEE Proceedings J (Optoelectronics)*, vol. 138, pp. 343–354, 1991.
- [21] M. Sumetsky, "How thin can a microfiber be and still guide light," *Optics Letters*, vol. 31, pp. 870–872, 2006.
- [22] J. Knight, "Photonic crystal fibres," *Nature*, vol. 424, no. 6950, pp. 847–851, 2003.
- [23] K. Kurokawa, K. Nakajima, K. Tsujikawa, T. Yamamoto, and K. Tajima, "Ultra-wideband transmission over low loss pcf," *Journal of Lightwave Technology*, vol. 27, pp. 1653–1662, 2009.

- [24] J. K. Lyngso, C. Jakobsen, H. R. Simonsen, and J. Broeng, "Single-mode 7-cell hollow core photonic crystal fiber with increased bandwidth," *Proceedings of SPIE, 21st International Conference on Optical Fiber Sensors, Ottawa*, vol. 7753, p. 77533Q, 2011.
- [25] P. Roberts, F. Couny, H. Sabert, B. Mangan, D. Williams, L. Farr, M. Mason, A. Tomlinson, T. Birks, J. Knight, and P. Russell, "Ultimate low loss of hollow-core photonic crystal fibres," *Optics Express*, vol. 13, no. 1, pp. 236–244, 2005.
- [26] C. Smith, N. Venkataraman, M. Gallagher, D. Muller, J. West, N. Borrelli, D. Allan, and K. Koch, "Low-loss hollow-core silica/air photonic bandgap fibre," *Nature*, vol. 424, no. 6949, pp. 657–659, 2003.
- [27] F. Benabid, "Hollow-core photonic bandgap fibre: New light guidance for new science and technology," *Philosophical Transactions of the Royal Society A: Mathematical, Physical and Engineering Sciences*, vol. 364, no. 1849, pp. 3439–3462, 2006.
- [28] F. Benabid and P. J. Roberts, "Linear and non-linear optical properties of hollow core photonic crystal fiber," *Journal of Modern Optics*, vol. 58, no. 2, pp. 87–124, 2011.
- [29] T. A. Birks, P. J. Roberts, P. S. J. Russell, D. M. Atkin, and T. J. Shepherd, "Full 2-d photonic bandgaps in silica/air structures," *Electronics Letters*, vol. 31, no. 22, pp. 1941–1942, 1995.
- [30] G. Brambilla, "Optical fiber nanotaper sensors," *Optical Fiber Technology*, vol. 16, pp. 331–342, 2010.
- [31] T. M. Monro, D. J. Richardson, N. G. R. Broderick, and P. J. Bennett, "Holey optical fibers: An efficient modal model," *Journal of Lightwave Technology*, vol. 17, no. 6, pp. 1093–1102, 1999.
- [32] K. Nielsen, D. Noordegraaf, T. Sorensen, A. Bjarklev, and T. Hansen, "Selective filling of photonic crystal fibres," *Journal of Optics A: Pure and Applied Optics*, vol. 7, pp. L13–L20, 2005.
- [33] J. Fini, "Microstructure fibres for optical sensing in gases and liquids," *Measurement Science and Technology*, vol. 15, pp. 1120–1128, 2004.

- [34] C. Martelli, J. Canning, D. Stocks, and M. J. Crossley, "Water-soluble porphyrin detection in a pure-silica photonic crystal fiber," *Optics Letters*, vol. 31, pp. 2100–2102, 2006.
- [35] T. Monro, W. Belardi, K. Furusawa, J. Baggett, N. Broderick, and D. Richardson, "Sensing with microstructured optical fibres," *Measurement Science and Technology*, vol. 12, pp. 854–858, 2001.
- [36] F. Benabid, F. Couny, J. C. Knight, T. A. Birks, and P. S. J. Russell, "Compact, stable and efficient all-fibre gas cells using hollow core photonic crystal fibres," *Nature*, vol. 434, pp. 488–491, 2005.
- [37] Y. L. Hoo, W. Jin, H. L. Ho, J. Ju, and D. N. Wang, "Gas diffusion measurement using hollow core photonic bandgap fiber," *Sensors and Actuators B*, vol. 105, pp. 183–186, 2004.
- [38] Y. L. Hoo, W. Jin, C. Shi, H. L. Ho, D. N. Wang, and S. C. Ruan, "Design and modeling of a photonic crystal fiber gas sensor," *Applied Optics*, vol. 42, no. 18, pp. 3509–3515, 2003.
- [39] J. Jensen, L. Pedersen, P. Hoiby, L. Nielsen, T. Hansen, J. Folkenberg, J. Rishede, D. Noordegraaf, K. Nielsen, A. Carlsen, and A. Bjarklev, "Photonic crystal fiber based evanescent-wave sensor for detection of biomolecules in aqueous solutions," *Optics Letters*, vol. 29, no. 17, pp. 1974–1976, 2004.
- [40] C. Markos, W. Yuan, K. Vlachis, G. E. Town, and O. Bang, "Label-free biosensing with high sensitivity in dual-core microstructured polymer optical fibers," *Optics Express*, vol. 19, no. 8, pp. 7790–7798, 2011.
- [41] D. K. C. Wu, B. T. Kuhlmeier, and B. J. Eggleton, "Ultrasensitive photonic crystal fiber refractive index sensor," *Optics Letters*, vol. 34, pp. 322–324, 2009.
- [42] Y. S. Skibina, V. V. Tuchin, V. I. Beloglazov, and G. Steinmeyer, "Photonic crystal fibers in biomedical investigations," *Quantum Electronics*, vol. 41, no. 4, pp. 284–301, 2011.
- [43] B. Solnica, J. W. Naskalski, and J. Sieradzki, "Analytical performance of glucometers used for routine glucose self-monitoring of diabetic patients," *Clinica Chimica Acta*, vol. 331, pp. 29–35, 2003.
- [44] B. D. Malhotra and A. Chaubey, "Biosensors for clinical diagnostics industry," *Sensors and Actuators B*, vol. 91, pp. 117–127, 2003.

- [45] D. A. Scott, D. E. Renaud, S. Krishnasamy, P. Meric, N. Buduneli, S. Cetinkalp, and K. Z. Liu, "Diabetes-related molecular signatures in infrared spectra of human saliva," *Diabetology and Metabolic Syndrome*, vol. 2, no. 48, p. 9pp, 2010.
- [46] M. Yamaguchi, M. Mitsumori, and Y. Kano, "Noninvasively measuring blood glucose using saliva," *Engineering in Medicine and Biology*, vol. 17, pp. 59–63, 1998.
- [47] M. W. J. Dodds, C. K. Yeh, and D. A. Johnson, "Salivary alterations in type 2 (non-insulin-dependent) diabetes mellitus and hypertension," *Community Dentistry and Oral Epidemiology*, vol. 28, pp. 373–381, 2000.
- [48] O. Abdallah, A. Bolz, J. Hansmann, H. Walles, and T. Hirth, "Design of a compact multi-sensor system for non-invasive glucose monitoring using optical spectroscopy," in *International Conference on Electronics, Biomedical Engineering and its Applications, Dubai*, pp. 310–317, 2012.
- [49] C. E. F. do Amaral and B. Wolf, "Current development in non-invasive glucose monitoring," *Medical Engineering and Physics*, vol. 30, pp. 541–549, 2008.
- [50] S. K. Vashist, "Non-invasive glucose monitoring technology in diabetes management: A review," *Analytica Chimica Acta*, vol. 750, pp. 16 – 27, 2012.
- [51] S. John, "Strong localization of photons in certain disordered dielectric superlattices," *Physical Review Letters*, vol. 58, pp. 2486–2489, 1987.
- [52] E. Yablonovitch, "Photonic band-gap structures," *Journal of the Optical Society of America B*, vol. 10, no. 2, pp. 283–295, 1993.
- [53] E. Yablonovitch, "Inhibited spontaneous emission in solid-state physics and electronics," *Physical Review Letters*, vol. 58, no. 20, pp. 2059–2062, 1987.
- [54] A. Bjarklev, J. Broeng, and A. S. Bjarklev, *Photonic Crystal Fibers*. Kluwer Academic Publishers, 2003.
- [55] J. C. Knight, T. A. Birks, P. S. J. Russell, and D. M. Atkin, "All-silica single-mode optical fiber with photonic crystal cladding," *Optics Letters*, vol. 21, no. 19, pp. 1547–1549, 1996.
- [56] P. S. J. Russell, "Photonic crystal fibers," *Applied Physics*, vol. 299, pp. 358–362, 2003.

- [57] S. E. Barkou, J. Broeng, and A. Bjarklev, "Silica-air photonic crystal fiber design that permits waveguiding by the true photonic bandgap effect," *Optics Letters*, vol. 24, no. 1, pp. 46–48, 1999.
- [58] J. Broeng, D. Mogilevstev, S. E. Barkou, and A. Bjarklev, "Photonic crystal fibers: A new class of optical waveguides," in *Optical Fiber Technology*, 1999.
- [59] R. F. Cregan, B. J. Mangan, J. C. Knight, T. A. Birks, P. S. J. Russell, P. J. Roberts, and D. C. Allan, "Single-mode photonic band gap guidance of light in air," *Science*, vol. 285, no. 5433, pp. 1537–1539, 1999.
- [60] J. C. Knight, T. A. Birks, R. F. Cregan, P. S. J. Russell, and P. D. de Sandro, "Large mode area photonic crystal fibre," *Electronics Letters*, vol. 34, pp. 1347–1348, 1998.
- [61] T. M. Monro, N. G. Broderick, and D. J. Richardson, "Exploring the optical properties of holey fibres," in *NATO Summer School on Nanoscale Linear and Nonlinear Optics, Sicily*, 2000.
- [62] M. N. Petrovich, F. Poletti, A. van Brakel, and D. J. Richardson, "Robustly single mode hollow core photonic crystal fiber," *Optics Express*, vol. 16, no. 6, pp. 4337–4346, 2008.
- [63] F. Benabid and P. J. Roberts, "Guidance mechanisms in hollow-core photonic crystal fiber," *Proceedings of SPIE, Conference on Photonic Crystal Materials and Devices, San Jose*, vol. 6901, p. 69010U, 2008.
- [64] A. S. J. Cequeuira, "Recent progress and novel applications of photonic crystal fibres," *Reports on Progress in Physics*, vol. 73, p. 024401 (21pp), 2010.
- [65] J. C. Knight, T. A. Birks, B. Mangan, and P. S. J. Russell, "New solutions in fiber optics," *Optics and Photonics News*, vol. 13, pp. 26–30, 2002.
- [66] P. S. J. Russell, J. C. Knight, T. A. Birks, B. J. Mangan, and W. J. Wadsworth, "Recent progress in photonic crystal fibres," in *Optical Fibre Conference*, 2000.
- [67] J. D. C. Jones, P. S. J. Russell, J. C. Knight, and T. A. Birks, "Photonic crystal fibres for sensor applications," *Proceedings of IEEE, 15th Conference on Optical Fiber Sensors, Portland*, vol. FB1, pp. 565–568, 2002.

- [68] A. Bozolan, R. M. Gerosa, C. J. S. de Matos, M. A. Romero, and C. M. B. Cordeiro, "Sealed liquid-core photonic crystal fibers for practical nonlinear optics, nanophotonics, and sensing applications," in *Proceedings of SPIE , 2nd Workshop on Specialty Optical Fibers and Their Applications, Oaxaca*, vol. 7839, p. 78390A (4pp), 2010.
- [69] M. E. Bosch, A. J. R. Sanchez, F. S. Rojas, and C. B. Ojeda, "Recent development in optical fiber biosensors," *Sensors*, vol. 7, pp. 797–859, 2007.
- [70] C. M. B. Cordeiro, C. J. S. de Matos, E. M. dos Santos, A. Bozolan, J. S. K. Ong, T. Facincani, G. Chesini, A. R. Vaz, and C. H. Brito-Cruz, "Towards practical liquid and gas sensing with photonic crystal fibres: Side access to the fibre microstructure and single-mode liquid-core fibre," *Measurement Science and Technology*, vol. 18, pp. 3075–3081, 2007.
- [71] J. Jensen, P. Hoiby, G. Emiliyanov, O. Bang, L. Pedersen, and A. Bjarklev, "Selective detection of antibodies in microstructured polymer optical fibers," *Optics Express*, vol. 13, no. 15, pp. 5883–5889, 2005.
- [72] T. Nasilowski, G. Statkiewicz, M. Szpulak, J. Olszewski, G. Golojuch, T. Martynkien, W. Urbanczyk, P. Mergo, M. Makara, J. Wojcik, J. Erps, J. Vlekken, C. Chojetzki, F. Berghmans, and H. Thienpoint, "Sensing applications of photonic crystal fibres," *Proceedings of SPIE, Conference on Lightguides and Their Applications III, Krasnobrod*, vol. 6608, p. 660802 (15pp), 2007.
- [73] E. R. Schartner, H. Ebendorff-Heidepriem, and T. M. Monro, "Low concentration fluorescence sensing in suspended-core fibers," *Proceedings of SPIE, 21st International Conference on Optical Fiber Sensors, Ottawa*, vol. 7753, p. 77534Q, 2011.
- [74] W. Jin, H. F. Xuan, and H. L. Ho, "Sensing with hollow-core photonic bandgap fibers," *Measurement Science and Technology*, vol. 21, p. 094014 (12 pp), 2010.
- [75] F. Couny, H. Sabert, P. J. Roberts, D. P. Williams, A. Tomlinson, B. J. Mangan, L. Farr, J. C. Knight, T. A. Birks, and P. S. J. Russell, "Visualizing the photonic band gap in hollow core photonic crystal fibers," *Optics Express*, vol. 13, pp. 558–563, 2005.
- [76] P. S. J. Russell, "Photonic crystal fibers," *Journal of Lightwave Technology*, vol. 24, pp. 4729–4749, 2006.

- [77] M. A. Duguay, Y. Kokubun, T. L. Koch, and L. N. Pfeiffer, “Antiresonant reflecting optical waveguides in sio2 multilayer structures,” *Applied Physics Letters*, vol. 49, pp. 13–15, 1986.
- [78] S. Guenneau, A. Nicolet, F. Zolla, and S. Lasquellec, “Numerical and theoretical study of photonic crystal fibers,” *Progress in Electromagnetics Research*, vol. 41, pp. 271–305, 2003.
- [79] N. A. Mortensen, “Photonic crystal fibres: Mapping maxwell’s equations onto a schrodinger equation eigenvalue problem,” *Journal of the European Optical Society*, vol. 1, 2006.
- [80] N. Mortensen, M. Nielsen, J. Folkenberg, C. Jakobsen, and H. Simonsen, “Photonic crystal fiber with a hybrid honeycomb cladding,” *Optics Express*, vol. 12, no. 3, pp. 468–472, 2004.
- [81] Z. Wang, G. Ren, S. Lou, and W. Liang, “Investigations of the supercell based orthonormal function method for different kinds of fibers,” *Optical Fiber Technology*, vol. 10, no. 4, pp. 296–311, 2004.
- [82] J. Arriaga, “Effective index model and guided modes in a photonic crystal fiber,” *Physica Status Solidi B: Basic Solid State Physics*, vol. 242, pp. 1868–1871, 2005.
- [83] J. Arriaga, J. C. Knight, and P. S. J. Russell, “Modeling the propagation of light in photonic crystal fibers,” *Physica D: Nonlinear Phenomena*, vol. 189, pp. 100 – 106, 2004.
- [84] F. Fogli, L. Saccomandi, P. Bassi, G. Bellanca, and S. Trillo, “Full vectorial bpm modeling of index-guiding photonic crystal fibers and couplers,” *Optics Express*, vol. 10, pp. 54–59, Jan 2002.
- [85] S. M. Hsu, H. J. Chen, and H. C. Chang, “Finite element analysis of full-vectorial modal and leakage properties of microstructured and photonic crystal fibers,” in *Proceedings of SPIE, Passive Components and Fiber-Based Devices, Beijing*, vol. 5623, 2004.
- [86] H. Uranus and H. Hoekstra, “Modelling of microstructured waveguides using a finite-element-based vectorial mode solver with transparent boundary conditions,” *Optics Express*, vol. 12, no. 12, pp. 2795–2809, 2004.

- [87] O. Frazao, J. L. Santos, F. M. Araujo, and L. A. Ferreira, "Optical sensing with photonic crystal fibers," *Laser and Photonics Reviews*, vol. 2, no. 6, pp. 449–459, 2008.
- [88] R. M. Gerosa, D. H. Spadoti, C. J. S. de Matos, L. de S. Menezes, and M. A. R. Franco, "Efficient and short-range light coupling to index - matched liquid-filled hole in a solid-core photonic crystal fiber," *Optics Express*, vol. 19, pp. 24687–24698, 2011.
- [89] T. Gissibl, M. Vieweg, M. M. Vogel, M. A. Ahmed, T. Graf, and H. Giessen, "Preparation and characterization of a large mode area liquid-filled photonic crystal fiber: Transition from isolated to coupled spatial modes," *Applied Physics B: Lasers and Optics*, vol. 106, pp. 521–527, 2012.
- [90] J. D. Joannopoulos, S. G. Johnson, J. N. Winn, and R. D. Meade, *Photonic Crystals: Molding the Flow of Light*. Princeton University Press, 2008.
- [91] T. Birks, D. Bird, T. Hedley, J. Pottage, and P. S. J. Russell, "Scaling laws and vector effects in bandgap-guiding fibres," *Optics Express*, vol. 12, no. 1, pp. 69–74, 2004.
- [92] J. A. West, C. M. Smith, N. F. Borrelli, D. C. Allan, and K. W. Koch, "Surface modes in air-core photonic band-gap fibers," *Optics Express*, vol. 12, pp. 1485–1496, 2004.
- [93] G. Antonopoulos, F. Benabid, D. M. Bird, J. C. Knight, and P. S. J. Russell, "Experimental demonstration of the frequency shift of bandgaps in photonic crystal fibers due to refractive index scaling," *Optics Express*, vol. 14, no. 7, pp. 3000–3006, 2006.
- [94] F. M. Cox, A. Argyros, and M. C. Large, "Liquid-filled hollow core microstructured polymer optical fiber," *Optics Express*, vol. 14, pp. 4135–4140, 2006.
- [95] J. Sun, C. C. Chan, X. Y. Dong, and P. Shum, "High resolution biochemical sensor by using photonic bandgap fiber," in *International Optical Design Conference, Vancouver*, vol. ME2, p. 2pp, 2006.
- [96] M. Yan and P. Shum, "Guidance varieties in photonic crystal fibers," *Journal of the Optical Society of America B*, vol. 23, no. 8, pp. 1684–1691, 2006.
- [97] A. W. Snyder and J. D. Love, *Optical Waveguide Theory*. Springer, 1983.

- [98] T. A. Birks, J. C. Knight, and P. S. J. Russell, “Endlessly single-mode photonic crystal fiber,” *Optics Letters*, vol. 22, no. 13, pp. 961–963, 1997.
- [99] N. A. Mortensen, J. R. Folkenberg, M. D. Nielsen, and K. P. Hansen, “Modal cutoff and the v parameter in photonic crystal fibers,” *Optics Letters*, vol. 28, no. 20, pp. 1879–1881, 2003.
- [100] J. Knight, J. Broeng, T. Birks, and P. Russell, “Photonic band gap guidance in optical fibres,” *Science*, vol. 282, pp. 1476–1478, 1998.
- [101] C. J. de Matos, C. M. B. Cordeiro, E. M. dos Santos, J. S. Ong, A. Bozolan, and C. H. B. Cruz., “Liquid-core, liquid-cladding photonic crystal fibers,” *Optics Express*, vol. 15, no. 18, pp. 11207–11212, 2007.
- [102] L. E. Horan, A. A. Ruth, and F. C. G. Gunning, “Hollow core photonic crystal fiber based viscometer with raman spectroscopy,” *Journal of Chemical Physics*, vol. 137, p. 224504 (12pp), 2012.
- [103] L. E. Horan and F. C. G. Gunning, “Hollow core photonic crystal fiber as a viscosity sensor,” in *Proceedings of SPIE, 22nd International Conference on Optical Fiber Sensors, Beijing*, vol. 8421, pp. 8421–140, 2012.
- [104] L. Xiao, W. Jin, M. Demokan, H. Ho, Y. Hoo, and C. Zhao., “Fabrication of selective injection microstructured optical fibers with a conventional fusion splicer,” *Optics Express*, vol. 13, no. 22, pp. 9014–9022, 2005.
- [105] L. Xiao, M. S. Demokan, W. Jin, Y. Wang, and C. L. Zhao, “Fusion splicing photonic crystal fibers and conventional single mode fibers: Microhole collapse effect,” *Journal of Lightwave Technology*, vol. 25, no. 11, pp. 3563 – 3574, 2007.
- [106] Y. Huang, Y. Xu, and A. Yariv, “Fabrication of functional microstructured optical fibers through a selective-filling technique,” *Applied Physics Letters*, vol. 85, no. 22, pp. 5182–5184, 2004.
- [107] C. Cordeiro, E. M. dos Santos, C. H. Brito-Cruz, C. J. de Matos, and D. S. Ferreira, “Lateral access to the holes of photonic crystal fibers-selective filling and sensing applications,” *Optics Express*, vol. 14, pp. 8403–8412, 2006.
- [108] M. Rutowska, F. G. Gunning, W. Urbanczyk, and A. Ellis, “Dna immobilisation and hydrogel matrix formation in suspended-core optical fibre,”

- Proceedings of IEEE, Conference on Lasers and Electro-Optics (CLEO Europe)*, vol. CH4.2, 2011.
- [109] L. Xiao, M. Grogan, W. Wadsworth, R. England, and T. Birks, “Stable low-loss optical nanofibres embedded in hydrophobic aerogel,” *Optics Express*, vol. 19, no. 2, pp. 764–769, 2011.
 - [110] M. Rutowska, L. Horan, G. Khara, and F. G. Gunning, “Nanoscale viscometer device,” March 2012.
 - [111] A. A. Ruth, H. Lesche, and B. Nickel, “Temperature dependence of viscosity and density of several commonly used organic solvents,” *Z. Physical Chemistry*, vol. 217, pp. 1–16, 2003.
 - [112] E. Washburn, “The dynamics of capillary flow,” *Physical Review*, vol. 17, no. 3, pp. 273–283, 1921.
 - [113] I. R. Rutgers, “Relative viscosity and concentration,” *Rheologica Acta*, vol. 2, pp. 305–348, 1962.
 - [114] A. Einstein, “On the movement of small particles suspended in a stationary liquid demanded by the molecular-kinetic theory of heat,” *Annalen der Physik*, vol. 322, no. 8, pp. 549–560, 1905.
 - [115] G. Jones and M. Dole, “The viscosity of aqueous solutions of strong electrolytes with special reference to barium chloride,” *Journal of the American Chemical Society*, vol. 51, pp. 2950–2964, 1929.
 - [116] N. P. Singh, M. M. Singh, and P. K. Tikoo, “The coefficients of the jones-doyle equation for the viscosity of solutions of potassium iodide in mixtures of water and dimethylacetamide at 35c,” *Australian Journal of Chemistry*, vol. 30, pp. 2303–5, 1977.
 - [117] C. W. V. D. Elst, A. F. Malan, and H. D. V. Heese, “Blood viscosity in modern medicine,” *South African Medical Journal*, vol. 52, pp. 526–528, 1977.
 - [118] Y. J. Kang, S. Y. Yoon, K. H. Lee, and S. Yang, “A highly accurate and consistent microfluidic viscometer for continuous blood viscosity measurement,” *Artificial Organs*, vol. 34, pp. 944–949, 2010.
 - [119] N. Srivastava, R. D. Davenport, and M. A. Burns, “Nanoliter viscometer for analyzing blood plasma and other liquid samples,” *Analytical Chemistry*, vol. 77, pp. 383–392, 2005.

- [120] J. W. Yarnell, I. A. Baker, P. M. Sweetnam, D. Bainton, J. R. O'Brien, P. J. Whitehead, and P. C. Elwood, "Fibrinogen, viscosity and white blood cell count are major risk factors for ischemic heart disease," *Circulation*, vol. 83, pp. 836–844, 1991.
- [121] B. H. Zimm and D. M. Crothers, "Simplified rotating cylinder viscometer for dna," *Proceedings of the National Academy of Sciences*, vol. 48, pp. 905–911, 1962.
- [122] R. H. Cotton, P. A. Rebers, J. E. Maudru, and G. Rorabaugh, "Use of sugars and other carbohydrates in the food industry," *American Chemical Society*, vol. 12, pp. 3–20, 1955.
- [123] P. J. Cullen, A. P. Duffy, C. P. O'Donnell, and D. J. O'Callaghan, "Process viscometry for the food industry," *Trends in Food Science & Technology*, vol. 11, pp. 451–457, 2000.
- [124] H. A. Barnes, "Rheology of emulsions- a review," *Colloids and Surfaces A: Physicochemical and Engineering Aspects*, vol. 91, pp. 89–95, 1994.
- [125] Y. Zhu and K. Petkovic-Duran, "Capillary flow in microchannels," *Microfluid Nanofluid*, vol. 8, pp. 275–282, 2010.
- [126] E. Livak-Dahl, J. Lee, and M. A. Burns, "Nanoliter droplet viscometer with additive free operation," *Lab on a Chip*, vol. 13, pp. 297–301, 2013.
- [127] F. White, *Viscous Fluid Flow 2nd edition*. New York: McGraw-Hill Education, 1991.
- [128] A. Hamraoui and T. Nylander, "Analytical approach for the lucas-washburn equation," *Journal of Colloid and Interface Science*, vol. 250, pp. 415–421, 2002.
- [129] A. Hamraoui, K. Thuresson, T. Nylander, and V. Yaminsky, "Can a dynamic contact angle be understood in terms of a friction coefficient?," *Journal of Colloid and Interface Science*, vol. 226, pp. 199–204, 2000.
- [130] G. Martic, F. Gentner, D. Seveno, D. Coulon, J. D. Coninck, and T. D. Blake, "A molecular dynamics simulation of capillary inhibition," *Langmuir*, vol. 18, pp. 7971–7976, 2002.
- [131] M. Strange, M. E. Dreyer, and H. J. Rath, "Capillary driven flow in circular cylindrical tubes," *Physics of Fluids*, vol. 15, pp. 2587–2601, 2003.

- [132] N. Ichikawa and Y. Satoda, "Interface dynamics of capillary flow in a tube under negligible gravity condition," *Journal of Colloid and Interface Science*, vol. 162, pp. 350–355, 1994.
- [133] L. O. E. dos Santos, F. G. Wolf, and P. C. Philippi, "Dynamics of interface displacement in capillary flow," *Journal of Statistical Physics*, vol. 121, pp. 197–207, 2005.
- [134] V. D. Sobolev, N. V. Churaev, M. G. Velarde, and Z. M. Zorin, "Surface tension and dynamic contact angle of water in thin quartz capillaries," *Journal of Colloid and Interface Science*, vol. 222, pp. 51–54, 2000.
- [135] G. M. Sreekantath, N. Rajaram, and C. K. Ponnappan, "Simple method for finding the ratio of surface tension to viscosity of a liquid," *Journal of Scientific Instruments*, vol. 36, pp. 378–380, 1959.
- [136] G. K. Batchelor, *An Introduction to Fluid Dynamics*. Cambridge University Press, 1967.
- [137] E. Aumann, L. M. Hildemann, and A. Tabazadeh, "Measuring and modelling the composition of temperature- dependence of surface tension for organic solutions," *Atmospheric Environment*, vol. 44, pp. 329–337, 2010.
- [138] J. R. Ferraro, K. Nakamoto, and C. W. Brown, *Introductory Raman Spectroscopy*. Elsevier, Academic Press, 2003.
- [139] R. L. McCreery, *Raman Spectroscopy for Chemical Analysis*. John Wiley & Sons, Inc., 2005.
- [140] C. V. Raman, "A new radiation," *Indian Journal of Physics*, vol. 2, pp. 387–398, 1928.
- [141] C. L. Evans and X. S. Xie, "Coherent anti-stokes raman scattering microscopy: Chemical imaging for biology and medicine," *Annual Review of Analytical Chemistry*, vol. 1, pp. 883–909, 2008.
- [142] P. M. Conn, *Imaging and Spectroscopic Analysis of Living Cells: Optical and Spectroscopic Techniques*. Academic Press, 2012.
- [143] W. Demtroder, *Laser Spectroscopy: Basic Concepts and Instrumentation*. Springer, 1981.

- [144] S. C. Pinzaru, I. Pavel, N. Leopold, and W. Kiefer, "Identification and characterization of pharmaceuticals using raman and surface enhanced raman scattering," *Journal of Raman Spectroscopy*, vol. 35, pp. 338–346, 2004.
- [145] G. E. Walrafen and J. Stone, "Intensification of spontaneous raman spectra by use of liquid core optical fibers," *Applied Spectroscopy*, vol. 26, pp. 585–589, Nov 1972.
- [146] S. D. Schwab and R. L. McCreery, "Versatile, efficient raman sampling with fiber optics," *Analytical Chemistry*, vol. 56, pp. 2199–2204, 1984.
- [147] R. Altkorn, I. Koev, R. P. V. Duyne, and M. Litorja, "Low-loss liquid-core optical fiber for low-refractive-index liquids: Fabrication, characterization, and application in raman spectroscopy," *Applied Optics*, vol. 36, no. 34, pp. 8992–8998, 1997.
- [148] M. Naji, A. Khetani, N. Lagali, R. Munger, and H. Anis, "A novel method of using hollow-core photonic crystal fiber as a raman biosensor," in *Proceedings of SPIE, Conference on Nanoscale Imaging, Sensing and Actuation for Biomedical Applications, San Jose*, vol. 6865, pp. 68650E(1–8), 2008.
- [149] H. Yan, J. Liu, C. Yang, G. Jin, C. Gu, and L. Hou, "Novel index guided photonic crystal fibre surface enhanced raman scattering probe," *Optics Express*, vol. 16, pp. 8300–8305, 2008.
- [150] X. Yang, C. Shi, D. Wheeler, R. Newhouse, B. Chen, J. Z. Zhang, and C. Gu, "High sensitivity molecular sensing using hollow core photonic crystal fiber and surface enhanced raman scattering," *Journal of the Optical Society of America*, vol. 27, pp. 977–984, 2010.
- [151] Y. Zhang, C. Shi, C. Gu, L. Seballos, and J. Z. Zhang, "Liquid core photonic crystal fibre sensor based on surface enhanced raman scatter," *Applied Physics Letters*, vol. 90, pp. 193504–193503, 2007.
- [152] Y. Han, M. K. K. Oo, Y. Zhu, L. Xiao, M. S. Demohan, W. Jin, and H. Du, "Index-guiding liquid-core photonic crystal fiber for solution measurement using normal and surface-enhanced raman scattering," *Optical Engineering*, vol. 47, p. 040502 (3pp), 2008.
- [153] F. M. Cox, A. Argyros, J. M. C. Large, and S. Kalluri, "Surface enhanced raman scattering in a hollow core microstructured optical fiber," *Optics Express*, vol. 15, pp. 13675–13681, 2007.

- [154] J. Irizar, J. Dinglasen, J. B. Goh, A. Khetani, H. Anis, D. Anderson, C. Goh, and A. S. Helmy, “Raman spectroscopy of nanoparticles using hollow-core photonic crystal fibers,” *Special Topics in Quantum Electronics*, vol. 14, pp. 1214–1222, 2008.
- [155] S. Yiou, P. Delaye, A. Rouvie, J. Chinaud, R. Frey, G. Roosen, P. Viale, S. Fevrier, P. Roy, J. L. Auguste, and J. M. Blondy, “Stimulated raman scattering in an ethanol core microstructured optical fiber,” *Optics Express*, vol. 13, p. 4786, 2005.
- [156] K. Fujiwara, J. B. Simeonsson, B. W. Smith, and J. D. Wineforder, “Waveguide capillary flow cell for fluorometry,” *Analytical Chemistry*, vol. 60, pp. 1065–1068, 1988.
- [157] Y. Ruan, E. Schartner, H. Ebendorff-Heidepriem, P. Hoffmann, and T. Monro, “Detection of quantum-dot labeled proteins using soft glass microstructured optical fibers,” *Optics Express*, vol. 15, no. 26, pp. 17819–17826, 2007.
- [158] W. J. Parak, D. Gerion, T. Pellegrino, D. Zanchet, C. Micheel, S. C. Williams, R. Boudreau, M. A. L. Gros, C. A. Larabell, and A. P. Alivisatos, “Biological applications of colloidal nanocrystals,” *Nanotechnology*, vol. 14, pp. R15–R27, 2003.
- [159] R. Altkorn, M. D. Malinsky, R. P. V. Duyne, and I. Koev, “Intensity considerations in liquid core optical fiber raman spectroscopy,” *Applied Spectroscopy*, vol. 55, no. 4, pp. 373–381, 2001.
- [160] NKT Photonics, *HC-1550-02. Hollow Core Photonic Bandgap Fiber*, 2012.
- [161] NKT Photonics, *HC-1060-02. Hollow Core Photonic Bandgap Fiber for 1060nm Range Applications*, 2012.
- [162] M. Rutowska, L. Horan, and F. G. Gunning, “Photonic crystal fibres: Selective fillings delays,” *Proceedings of IEEE, European Conference on Lasers and Electro-Optics and the European Quantum Electronics Conference (CLEO - EQEC Europe), Munich*, vol. CH3, 2009.
- [163] W. H. Zachariasen, “The atomic arrangement in glass,” *Journal of the American Ceramic Society*, vol. 54, pp. 3841–3851, 1932.

- [164] R. H. French, R. Abou-Rahme, D. J. Jones, and L. E. McNeil, "Absorption edge and bandgap of SiO_2 fused silica glass," *The American Ceramic Society*, vol. 28, pp. 63–80, 1992.
- [165] E. M. Dianov, V. M. Mashinsky, V. B. Neustruev, O. D. Sazhin, A. N. Guryanov, V. F. Khopin, N. N. Vechkanov, and S. V. Lavrishchev, "Origin of excess loss in single-mode optical fibers with high GeO_2 -doped silica core," *Optical Fiber Technology*, vol. 3, no. 1, pp. 77–86, 1997.
- [166] A. V. Amosov and A. O. Rybaltovsky, "Oxygen deficient centers in silica glass: A review of their properties and structure," *Journal of Non-Crystalline Solids*, vol. 179, pp. 75–83, 1994.
- [167] M. Stapelbroek, D. L. Griscom, E. J. Friebele, and G. H. Sigel, "Oxygen-associated trapped hole centers in high purity fused silicas," *Journal of Non-Crystalline Solids*, vol. 32, pp. 313–326, 1979.
- [168] D. R. Lide, *Handbook of Chemistry and Physics*. CRC, 1994.
- [169] P. S. Nikam, L. N. Shirsat, and M. Hasan, "Density and viscosity studies of binary mixtures of acetonitrile with methanol, ethanol, propan-1-ol, propan-2-ol, butan-1-ol, 2-methylpropan-1-ol and 2-methylpropan-2-ol at (298.15, 303.15, 308.15, and 313.15)," *Journal of Chemical Engineering Data*, vol. 43, pp. 732–737, 1998.
- [170] T. A. Birks, M. D. W. Grogan, Z. Chen, L. M. Xiao, and S. G. Leon-Saval, "Modifying photonic crystal fibres," in *14th OptoElectronics and Communications Conference, Hong Kong*, 2009.
- [171] J. Chirife and M. P. Buerea, "A simple model for predicting the viscosity of sugar and oligosaccharide solutions," *Journal of Food Engineering*, vol. 33, pp. 221–226, 1997.
- [172] R. Mathpal, B. K. Joshi, and N. D. Kandpal, "Intermolecular forces of sugars in water," *Monatshefte fuer Chemie Chemical Monthly*, vol. 137, pp. 375–379, 2006.
- [173] M. Migliori, D. Gabriele, R. D. Sanzo, B. D. Cindio, and S. Correra, "Viscosity of multicomponent solutions of simple and complex sugars in water," *Journal of Chemical Engineering Data*, vol. 52, pp. 1347–1353, 2007.

- [174] V. R. N. Telis, J. Telis-Romero, H. B. Mazzotti, and A. L. Gabas, "Viscosity of aqueous carbohydrate solutions at different temperatures and concentrations," *International Journal of Food Properties*, vol. 10, pp. 185–195, 2007.
- [175] T. Ling and M. V. Winkle, "Properties of binary mixtures as a function of composition," *Journal of Chemical Engineering Data*, vol. 3, no. 1, pp. 88–95, 1958.
- [176] F. M. Pang, C. E. Seng, T. T. Teng, and M. H. Ibrahim, "Densities and viscosities of aqueous solutions of 1-propanol and 2-propanol at temperatures from 293.15 k to 333.15 k," *Journal of Molecular Liquids*, vol. 136, no. 1-2, pp. 71–78, 2007.
- [177] G. Vazquez, E. Alvarez, and J. M. Navaza, "Surface tension of alcohol and water from 20 to 50 degrees c," *Journal of Chemical Engineering Data*, vol. 40, no. 3, pp. 611–614, 1995.
- [178] R. B. Maximino, "Surface tension and density of binary mixtures of monoalcohols, water and acetonitrile: Equation of correlation of the surface tension," *Physics and Chemistry of Liquids*, vol. 47, no. 5, pp. 475–486, 2009.
- [179] M. Dizechi and E. Marschall, "Viscosity of some binay and ternary liquid mixtures," *Journal of Chemical Engineering Data*, vol. 27, no. 3, pp. 358–363, 1982.
- [180] S. Z. Mikhail and W. R. Kimel, "Densities and viscosities of 1-propanol - water mixtures," *Journal of Chemical Engineering Data*, vol. 8, no. 3, pp. 323–328, 1963.
- [181] A. T. Palasz, J. Thundathil, R. E. Verrall, and R. J. Maplettoft, "The effect of macromolecular supplementation of the surface tension of tcm-199 and the utilization of growth factors by bovine oocytes and embryos in culture," *Animal Reproduction Science*, vol. 58, no. 3-4, pp. 229–240, 2000.
- [182] J. F. Comesana, J. J. Otero, E. Garcia, and A. Correa, "Densities and viscosities of ternary systems of water + glucose + sodium chloride at several temperatures," *Journal of Chemical Engineering Data*, vol. 48, pp. 362–366, 2003.
- [183] R. A. Serwaym and J. W. Jewett, *Physics for Scientists & Engineers*. Cengage Learning, 4th ed., 2010.

- [184] B. M. A. Rahman, A. K. M. S. Kabir, M. I. Ahmed, M. Rajarajan, and K. T. V. Grattan, "Modal solutions of photonic crystal fibers by finite element method," in *Proceedings of SPIE, Photonic Crystal Materials and Nanostructures, Strasbourg*, vol. 5450, pp. 207–216, 2004.
- [185] F. Couny, F. Benabid, P. Roberts, M. Burnett, and S. Maier, "Identification of bloch modes in hollow core photonic crystal fiber cladding," *Optics Express*, vol. 15, pp. 325–338, 2007.
- [186] J. M. Fini, "Water-core microstructure fiber for optical sensing," *Proceedings of IEEE, Conference on Optical Fiber Communication, Los Angeles*, vol. 2, p. MF3, 2004.
- [187] R. M. Gerosa, A. Bozolan, C. J. S. de Matos, M. A. Romero, and C. M. B. Cordeiro, "Novel sealing technique for practical liquid-core photonic crystal fibers," *IEEE Photonics Technology Letters*, vol. 24, no. 3, pp. 191–193, 2012.
- [188] M. Midrio, M. P. Singh, and C. G. Someda, "The spatial filling mode of holey fibers: An analytical vectorial solution," *Journal of Lightwave Technology*, vol. 18, no. 7, pp. 1031–1037, 2000.
- [189] N. A. Mortensen, "Effective area of photonic crystal fibers," *Optics Express*, vol. 10, no. 7, pp. 341–348, 2002.
- [190] N. A. Mortensen, J. R. Folken, P. M. W. Skovgaard, and J. Broeng, "Numerical aperture of single-mode photonic crystal fibers," *IEEE Photonics Technology Letters*, vol. 14, no. 8, pp. 1094–1096, 2002.
- [191] K. Virkler and I. K. Lednev, "Forensic body fluid identification: The raman spectroscopic signature of saliva," *Analyst, The Royal Society of Chemistry*, vol. 135, pp. 512–517, 2010.
- [192] A. Zalewaska, K. Zwierz, K. Zolkowski, and A. Gindzienski, "Structure and biosynthesis of human salivary mucins," *Acta Biochimica Polonica*, vol. 47, no. 4, pp. 1067–1079, 2000.
- [193] M. Holtz, P. K. Dasgupta, and G. Zhang, "Small-volume raman spectroscopy with a liquid core waveguide," *Analytical Chemistry*, vol. 71, no. 14, pp. 2934–2938, 1999.

- [194] F. Eftekhari, J. Irizar, L. Hulbert, and A. S. Helmy, "A comparative study of raman enhancement in capillaries," *Journal of Applied Physics*, vol. 109, p. 113104 (6 pp), 2011.
- [195] R. Altkorn, I. Koev, and M. Peltier, "Raman performance characteristics of teflon- af 2400 liquid core optical fiber sample cells," *Applied Spectroscopy*, vol. 53, no. 10, pp. 1169–1176, 1999.
- [196] A. Tam and C. Patel, "Optical absorptions of light and heavy water by laser optoacoustic spectroscopy," *Applied Optics*, vol. 18, pp. 3348–3358, 1979.
- [197] S. Soderholm, Y. H. Roos, N. Meinander, and M. Hotokka, "Raman spectra of fructose and glucose in the amorphous and crystalline states," *Journal of Raman Spectroscopy*, vol. 30, pp. 1009–1018, 1999.
- [198] M. J. Clugston and R. Flemming, *Advanced Chemistry*. Oxford University Press, 2000.
- [199] G. Ahlborg and P. Felig, "Lactate and glucose exchange across the forearm, legs, and splanchnic bed during and after prolonged leg exercise," *The Journal of Clinical Investigation*, vol. 69, pp. 45 – 54, 1982.
- [200] J. Wahren, P. Felig, G. Ahlborg, and L. Jorfeldt, "Glucose metabolism during leg exercise in man," *The Journal of Clinical Investigation*, vol. 50, pp. 2715 – 2725, 1971.
- [201] T. D. Noakes and A. S. C. Gibson, "Logical limitations to the "catastrophe" models of fatigue during exercise in humans," *British Journal of Sports Medicine*, vol. 38, pp. 648–649, 2004.
- [202] G. A. Brooks, "The lactate shuttle during exercise and recovery," *Medicine and Science in Sports and Exercise*, vol. 18, pp. 360 – 368, 1986.
- [203] D. A. MacLean, J. Bangsbo, and B. Saltin, "Muscle interstitial glucose and lactate levels during dynamic exercise in humans determined by microdialysis," *Journal of Applied Physiology*, vol. 87, pp. 1483 – 1490, 1999.
- [204] S. Y. Wang, C. E. Hasty, P. A. Watson, J. P. Wicksted, R. D. Stith, and W. F. March, "Analysis of metabolites in aqueous solutions by using laser raman spectroscopy," *Applied Optics*, vol. 32, pp. 925 – 929, 1993.
- [205] V. Billat, P. Sirvent, P.-M. Lepretre, and J. P. Koralsztein, "Training effect on performance, substrate balance and blood lactate concentration at max-

- imal lactate steady state in master endurance runners,” *European Journal of Physiology*, vol. 447, pp. 875 – 883, 2004.
- [206] B. C. Bergman, E. E. Wolfel, G. E. Butterfield, G. D. Lopaschuk, G. A. Casazza, M. A. Horning, and G. A. Brooks, “Active muscle and whole body lactate kinetics after endurance training in men,” *Journal of Applied Physiology*, vol. 87, pp. 1684 – 1696, 1999.
- [207] M. Wyss and R. Kaddurah-Daouk, “Creatine and creatinine metabolism,” *Physiological Reviews*, vol. 80, pp. 1107 – 1213, 2000.
- [208] D. Qi and A. J. Berger, “Chemical concentration and measurement in blood serum and urine samples using liquid-core optical fiber raman spectroscopy,” *Applied Optics*, vol. 46, pp. 1726 – 1734, 2007.
- [209] J. W. McMurdy and A. J. Berger, “Raman spectroscopy based creatinine measurement in urine samples from a multipatient population,” *Applied Spectroscopy*, vol. 57, pp. 522–525, 2003.
- [210] K. E. Shafer-Peltier, C. L. Hynes, M. R. Glucksberg, and R. P. V. Duyne, “Toward a glucose biosensor based on surface enhanced raman scattering,” *Journal of the American Chemical Society*, vol. 125, pp. 588–593, 2003.
- [211] S. M. Som and B. H. Foing, “Thermal degradation of organic material by portable laser raman spectroscopy,” *International Journal of Astrobiology*, vol. 11, pp. 117–186, 2012.
- [212] G. J. Puppels, J. H. F. Olminkhof, G. M. J. Segers-Nolten, C. Otto, F. F. M. D. Mul, and J. Greve, “Laser irradiation and raman spectroscopy of single living cells and chromosomes: Sample degradation occurs with 514.5 nm but not with 660 nm laser light,” *Experimental Cell Research*, vol. 195, pp. 371–367, 1991.